Mag.rer.nat Michaela Ellmeier

Evaluation of the Optical Path and the Performance of the Coupled Dark State Magnetometer

DISSERTATION

zur Erlangung des akademischen Grades

Doktorin der Naturwissenschaften

eingereicht an der

Technischen Universität Graz

Betreuer

Univ.-Prof. Dipl.-Ing. Dr.techn. Laurentius Windholz

Institut für Experimentalphysik
Technische Universität Graz

Zweitbetreuer
Dipl.-Ing. Dr.techn. Roland Lammegger

Graz, August 2019

EIDESSTATTLICHE ERKLÄRUNG

Ich erkläre an Eides statt, dass ich die vorliegende Arbeit selbstständig verfasst, andere als die angegebenen Quellen/Hilfsmittel nicht benutzt, und die den benutzten Quellen wörtlich und inhaltlich entnommenen Stellen als solche kenntlich gemacht habe. Das in TUGRAZonline hochgeladene Textdokument ist mit der vorliegenden Dissertation identisch.

Datum

Unterschrift

Abstract

The Coupled Dark State Magnetometer (CDSM) is an optical magnetometer that is being developed for the measurement of magnetic fields in space. Its measurement principle is based on the coupling of two dark state resonances (CDSM resonance), which are prepared by the Coherent Population Trapping effect. The CDSM resonance is used to determine the magnetic field induced frequency shifts within the hyperfine structure ground states of the ^{87}Rb D_1 line. The CDSM measurement principle compensates for the influence of disturbing frequency shifts on the detected magnetic field by performing a differential measurement.

The main tasks of this thesis were the characterisation of the magnetometer's optical path and investigations of the performance of the CDSM, with special emphasis on the required accuracy of 0.2 nT (1 sigma) for the Jupiter mission of the European Space Agency. In this context, an endurance test with vertical-cavity surface-emitting lasers was performed, two different sensor designs were evaluated and proper optical fibres for the operation in space were selected. In order to improve the accuracy and to optimise the signal-to-noise ratio of the CDSM, the dependence on the following parameters was studied: laser intensity, magnetic field inhomogeneity, buffer gas pressure, sensor cell temperature, combinations of laser current with laser temperature and microwave power level, the optical detuning, the non-linear dependence of the dark state resonance positions on the external magnetic field and the sensor angle.

In the course of these investigations, an imbalance between the single dark state resonance line shapes was discovered and its influence on the CDSM-based compensation effect was evaluated. Based on the obtained results, a new sensor unit with dual laser beam pass through the sensor cell was developed. With the new sensor unit, the line shape imbalance could be reduced across the full sensor angular range. As a result, the compensation of disturbing frequency shifts improved up to a factor of four compared to the original sensor design, which is based on a single laser beam pass.

Furthermore, the CDSM resonance line shapes were optimised for the measurement of magnetic field strengths as low as 150 nT. In this measurement range, the CDSM resonances converge and influence the accuracy of the magnetic field measurement depending on their resonance structures.

These improvements represent an essential step towards highly accurate magnetic field measurements in space.

Kurzfassung

Das Coupled Dark State Magnetometer (CDSM) ist ein optisches Magnetometer, welches für die Magnetfeldmessung im Weltraum entwickelt wird. Das Messprinzip basiert auf der Kopplung von zwei Dunkelzustandsresonanzen (CDSM-Resonanz), die durch den Coherent Population Trapping Effekt erzeugt werden. Mit Hilfe der CDSM-Resonanz werden die durch ein Magnetfeld verursachten Frequenzverschiebungen innerhalb der Hyperfeinstrukturgrundzustände der ^{87}Rb D_1-Linie bestimmt. Durch eine differenzielle Messung kompensiert das CDSM-Messprinzip den Einfluss von störenden Frequenzverschiebungen auf die Magnetfeldmessung.
Die Ziele dieser Dissertation waren den optischen Pfad des Magnetometers zu charakterisieren und das Betriebsverhalten des CDSMs zu untersuchen. Der besondere Schwerpunkt lag hierbei auf der benötigte Genauigkeit von 0.2 nT (1 Sigma) für die Jupiter-Mission der Europäischen Weltraumorganisation. In diesem Zusammenhang wurde ein Dauertest mit Vertical-Cavity Surface-Emitting Lasern durchgeführt, zwei verschiedene Sensordesigns evaluiert und geeignete optische Fasern für den Betrieb im Weltraum selektiert. Um die Genauigkeit und den Signal-Rausch-Abstand des CDSMs zu optimieren wurden die Abhängigkeiten von folgenden Parametern untersucht: Laserintensität, Magnetfeldinhomogenität, Puffergasdruck, Sensorzellentemperatur, Kombinationen von Laserstrom mit Lasertemperatur und Mikrowellenleistungspegel, optische Verstimmung, nichtlineare Abhängigkeit der Dunkelzustandsresonanzen vom äußeren Magnetfeld und Sensorwinkel.
Im Zuge dieser Untersuchungen wurden ungleiche Linienformen der einzelnen Dunkelzustandsresonanzen festgestellt und deren Auswirkung auf den Kompensationseffekt des CDSMs evaluiert. Basierend auf diesen Ergebnissen wurde eine neue Sensoreinheit entwickelt, in welcher der Laserstrahl die Sensorzelle zweimal durchläuft. Mit der neuen Sensoreinheit kann die Ungleichheit der Linienform für den gesamten Sensorwinkel reduziert werden. Dadurch verbesserte sich die Kompensation von störenden Frequenzverschiebungen um bis zu einem Faktor vier im Vergleich zum ursprünglichen Sensordesign, dessen Funktionsweise auf dem Durchgang eines einzelnen Laserstrahls durch die Sensorzelle basiert.
Darüber hinaus wurden die Linienformen der CDSM-Resonanzen für die Messung von Magnetfeldstärken bis zu 150 nT optimiert. In diesem Magnetfeldbereich konvergieren die CDSM-Resonanzen und beeinflussen die Genauigkeit der Magnetfeldmessung in Abhängigkeit ihrer Resonanzstrukturen.

Diese Verbesserungen repräsentieren einen wesentlichen Schritt in Richtung hochgenauer Magnetfeldmessung im Weltraum.

Acknowledgement

I would like to take this opportunity to thank a number of people whose assistance and support was invaluable to this work.

First of all, I want to express my deepest gratitude to my supervisors, Prof. Laurentius Windholz and Dr. Roland Lammegger, for their guidance, their patience and our numerous scientific discussions. Thanks for giving me the opportunity to work on such a diverse and exciting project.

Special thanks to Prof. Svenja Knappe for agreeing to act as external referee for this thesis.

My sincere thanks also go to Dr. Werner Magnes for giving me the opportunity to collaborate with the Space Research Institute. Thanks for always keeping track of the CDSM action items, seeing the bright side during challenging times and all your helpful professional advice.

I would be remiss not to mention the countless contributions of my colleagues from the CDSM team. I really appreciated our constructive discussions, adventurous measurement campaigns and the extraordinary team spirit which made our time in the lab cheerful yet productive.

In addition, I want to thank my colleagues and friends at the Institute of Experimental Physics and the Space Research Institute for the enjoyable coffee breaks, providing positive distraction and encouragement when things did not go as planned.

Also many thanks to my colleagues at the Conrad Observatory and the Technische Universität Braunschweig for their supportive cooperation, scientific exchange and assistance.

Finally, I am utterly grateful for the unconditional encouragement and support of my family and friends during this challenging and exciting time. Thanks for always being there for me, having a sympathetic ear and keeping me in good spirits.

Contents

1. Introduction

The Coupled Dark State Magnetometer (CDSM) is a compact magnetic field measurement device. Its measurement principle was patented by Graz University of Technology in 2008 [1]. Subsequently, the development of a CDSM instrument for space application started in cooperation with the Space Research Institute of the Austrian Academy of Sciences in Graz.
The CDSM belongs to the class of optical magnetometers [2], since the external magnetic field is determined from the interaction of a laser light field with atoms contained in a vapour cell. The CDSM measurement principle is based on the coupling of two dark state resonances (herein called CDSM resonance) which are prepared by the Coherent Population Trapping (CPT) effect [3]. The CPT effect allows the preparation of narrow resonances with line widths of only tens of Hz. In the case of the CDSM, these small line widths enable an accurate determination of the magnetic field induced energy level shift within the hyperfine structure ground states of the ^{87}Rb D_1 line. A further benefit of the CPT effect is that the measurement setup can be miniaturised. Thus, it is applied for, e.g., compact atomic clocks [4][5]. CPT magnetometers have been developed too but these magnetometers typically use only one CPT resonance to determine the external magnetic field [6][7]. This method has the drawback that the CPT resonance position can also be shifted by other effects than the external magnetic field like, e.g., a change of the sensor cell temperature or the laser intensity. Therefore, a precise control of these parameters is required to distinguish a disturbing from a magnetic field induced frequency shift. In order to reduce the influence of such disturbances, the CDSM uses two coupled CPT resonances to determine the external magnetic field strength B by a differential measurement method.

In general, magnetometers are divided into their ability to measure the strength of the magnetic field (scalar magnetometers) or also its direction (vector magnetometers)[8]. Up to now, the CDSM magnetometer belongs to the class of scalar magnetometers but it has the potential to be further developed to a vector magnetometer.

Various types of magnetometers are commonly used for scientific space missions which differ in their characteristics, performances and in their field of application [8][9]. They all have in common that the utilisation in space entails limited resources. As a result, size, mass and power consumption of the instrument are important criteria for the selection of

such a device for space application. Furthermore, the instrument has to work remotely during the whole mission duration with the ability to survive the harsh environment in space including extreme temperatures and high radiation levels.
Benefits of the CDSM are its high dynamic range from $B \approx 10\,\mathrm{nT}$ to $B \approx 100\,\mathrm{mT}$ for the current instrument design and the simple sensor unit design which requires only optical elements for its operation. Furthermore, the use of the CPT effect allows an omni-directional operation of the magnetometer without dead zones with only one sensor unit [10]. Other optical magnetometers circumvent such dead zones by combining at least two sensor units [8] or by a rotation of the polarisation plane by a non-magnetic piezoelectric motor inside of the sensor unit [11].
The first application of the CDSM in space is aboard the China Seismo-Electromagnetic Satellite (CSES) mission launched in February 2018 [12]. Further, the CDSM was selected for the upcoming JUpiter ICy moons Explorer (JUICE) mission by the European Space Agency which will be launched in 2022 [13]. On both missions, the CDSM is applied in combination with two fluxgate magnetometers. Fluxgate magnetometers are vector instruments which measure the magnetic field in three orthogonal directions [9]. During both missions, the fluxgate magnetometers use the CDSM as reference in order to correct temperature and long-term drifts of the vector measurement by in-flight calibration [9].

At the beginning of the CDSM's technological development, the magnetometer was realised by mainly commercial standalone measurement devices in the laboratory. Subsequently, the miniaturisation has advanced and the suitability of the instrument has been proven for the application in space.
As an important element of this process, one part of this thesis aimed at the optimisation of the optical path of the CDSM consisting of the laser unit, a pair of optical fibres and the sensor unit. A description of the electronics unit can be found in [14].
The other part of this thesis comprised investigations of the performance of the CDSM. This included the dependence of the CDSM resonances on its operational parameters, the evaluation and improvement of the CDSM-based compensation of disturbing frequency shifts and the enablement of measurements at magnetic field strengths lower than 150 nT. The influence of operational parameters on the CPT resonances, which are the basis of the CDSM resonances, like, e.g., laser intensity and sensor cell temperature had been characterised before and their behaviour is in principle well known [15]. However, the main focus of investigations in literature was on the CPT resonance which just has a quadratic dependence on the external magnetic field (see section 2.1.2.2). A large section of these results can be transferred to CPT resonances which have also a linear magnetic field dependence but an investigation of the coupled CPT resonances and their dependence on the operational parameters was not done so far. Therefore, this thesis aims at the optimisation of the CDSM's operational parameters and the study of their influence on the measurement accuracy. The emphasis of most investigations was to enable magnetic field measurements with an accuracy of 0.2 nT (1 sigma) for the Jupiter mission.

This thesis is structured as follows. In chapter 2, the CPT effect and its preparation in the hyperfine structure of the ^{87}Rb D_1 line are summarised. In addition, the application of CPT resonances for magnetic field measurements is discussed. Furthermore, the CDSM measurement principle and the CDSM instrument are introduced.
Chapter 3 focuses on the characterisation and optimisation of the optical path which consists of the laser unit, the optical fibres and the sensor unit. The laser unit contains a vertical-cavity surface-emitting laser. The performance of such lasers was tested for its suitability during the Jupiter mission. Additionally, this chapter contains a description of two different sensor designs for the CDSM. The first sensor design was developed for the CSES mission and it is based on a single pass of the laser light through the Rb vapour cell. A second, improved sensor design is under development for the JUICE mission which enables a dual laser beam pass through the Rb vapour cell. Moreover, the selection of optical fibres is discussed for the CDSM including the advantages and disadvantages of using multi-mode fibres instead of single-mode fibres.
Chapter 4 summarises measurements on three different topics. First, the dependence of the CPT and CDSM resonances on the operational parameters of the magnetometer, e.g., laser intensity and buffer gas pressure are discussed. Second, the compensation of disturbing frequency shifts by the CDSM measurement principle is examined. Third, the accuracy in a low magnetic field range ($B < 2\,\mu\mathrm{T}$) is investigated which includes studies of the lower measurement limit of the CDSM.
In chapter 5, the results of chapters 3 and 4 are discussed and summarised. Chapter 6 gives a conclusion and an outlook for upcoming measurements.

2. Measurement Principle of the Coupled Dark State Magnetometer

The measurement principle of the Coupled Dark State Magnetometer (CDSM) [1] is based on a spectroscopic measurement of the hyperfine structure energy level shift within the ^{87}Rb D_1 line due to an external magnetic field. The energy level shift is detected by using the Coherent Population Trapping (CPT) effect [16][3]. The CPT effect enables resonance features with line widths in the range of several kHz to about 30 Hz [17].
One single CPT resonance could be used for the detection of the magnetic field induced frequency shift. However, the energy level shifts within the hyperfine structure are not only influenced by the external magnetic field but also by other unwanted effects like, e.g., the light shift. The separation of these effects from a magnetic field induced frequency shift is required for an accurate magnetic field measurement. For this reason, the CDSM uses coupled CPT resonances to measure the external magnetic field. The coupled CPT resonances allow a reduction or a complete compensation of disturbing energy level shifts which are caused by other effects than a magnetic field change.
The basics of the CPT effect, its experimental realisation as well as its preparation within the ^{87}Rb D_1 line are summarised in sections 2.1 and 2.2. In section 2.3 the application of the CPT effect for magnetic field measurements is discussed and the CDSM measurement principle is introduced. The CDSM instrument designs and the special requirements with regard to the Chinese Seismo-Electromagnetic Satellite (CSES) mission as well as the JUpiter ICy moon Explorer (JUICE) mission are discussed in section 2.4.

2.1. Coherent Population Trapping

Coherent Population Trapping (CPT) is a quantum interference effect, which was discovered in 1976 [3]. This effect can occur in different atomic level configurations consisting of at least three energy levels interacting with two monochromatic light fields. The CPT effect causes a trapping of the atomic population in a so called dark state in which the population can not interact with the resonant light field. As a consequence, a drop in fluorescence and a respective increase in transmission of the exciting light field through

the medium can be detected. This resonance feature has a narrow line width. Therefore, it is ideal for precision measurements of the atomic transition frequencies.
In the next sections, the CPT effect is described with focus on the three level Λ-shaped excitation scheme which is the typical one prepared for the magnetic field measurement of the CDSM.

2.1.1. Coherent Population Trapping in the Three Level Λ System

The three level Λ system consists of two ground states $|1\rangle$ and $|2\rangle$ and one excited state $|3\rangle$ [3][18] (see figure 2.1). The levels $|1\rangle$, $|2\rangle$ and $|3\rangle$ are the eigenstates of the unperturbed atom with their corresponding energy $\mathcal{E}_j = \hbar\,\Omega_j$ $(j = 1, 2, 3)$.

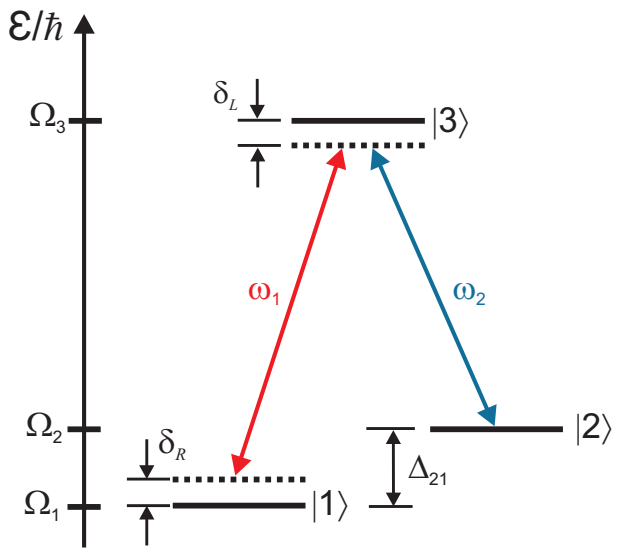

Figure 2.1.: Three level Λ excitation scheme for the CPT resonance preparation: The three level system consists of two ground states $|1\rangle$ and $|2\rangle$ and the excited state $|3\rangle$. The three levels interact with two light fields with the frequencies ω_1 and ω_2. The ground state splitting frequency is labelled with Δ_{21}. The two-photon detuning δ_L and the Raman detuning δ_R are introduced to describe detunings of the laser frequencies from the exact CPT resonance excitation ($\delta_L = 0$ and $\delta_R = 0$).

A coherent pair of monochromatic light fields is required for the formation of the CPT effect. Therefore, two light fields $\mathbf{E_1}$ and $\mathbf{E_2}$ are defined. It is assumed that the light field $\mathbf{E_1}$ can only interact with the transition $|1\rangle \rightarrow |3\rangle$ and excite population from the ground state $|1\rangle$ into the excited state $|3\rangle$ as well as the light field $\mathbf{E_2}$ can only interact with the transition $|2\rangle \rightarrow |3\rangle$ and excite population from the ground state $|2\rangle$ into the excited state

$|3\rangle$. The time dependence of the light fields are of the form

$$\mathbf{E_j} = \mathbf{E}_{0j} \cdot exp\,(-i\,(\omega_j\,t + \varphi_j)), \quad j = 1,\,2\,, \tag{2.1}$$

where $\mathbf{E}_{0j}$ is the amplitude, ω_j is the angular frequency and φ_j is the phase.
Two detunings are defined to describe deviations from the exact CPT resonance excitation: the two-photon detuning and the Raman detuning [18]. The two-photon detuning δ_L describes a common detuning from the respective transition frequencies:

$$\delta_L = \omega_1 - (\Omega_3 - \Omega_1) = \omega_2 - (\Omega_3 - \Omega_2)\ . \tag{2.2}$$

The Raman detuning is defined as the detuning of the light difference frequency from the ground state splitting frequency $\Delta_{21} = \Omega_2 - \Omega_1$:

$$\delta_R = \Delta_{21} - (\omega_1 - \omega_2)\ . \tag{2.3}$$

The interaction of the light field and the atom can be described by using perturbation theory. The light-atom interaction is introduced as a small disturbance via the interaction operator $\hat{V} = -\hat{d}\,\mathbf{E}$ where $\mathbf{E} = \mathbf{E_1} + \mathbf{E_2}$ and $\hat{d}$ is the dipole operator. For the three level system and by the application of the rotating wave approximation, the interaction operator $\hat{V}$ has the following form [3]:

$$\hat{V} = \frac{\hbar g_1}{2}\exp(-i(\omega_1 \cdot t + \varphi_1))|3\rangle\langle 1| + \frac{\hbar g_2}{2}\exp(-i(\omega_2 \cdot t + \varphi_2))|3\rangle\langle 2| + h.c.\ . \tag{2.4}$$

The coupling strength between the light field and an atomic transition is described by the Rabi frequency g_j [18]:

$$g_j = -\frac{d_{3j}E_j}{\hbar}\,, \qquad j = 1, 2\,, \tag{2.5}$$

where d_{3j} is the matrix element of the dipole operator $\hat{d}$ (see also appendix A.1).
The basis system is changed for the further description of the CPT effect. The new basis consists of the excited state $|3\rangle$ and two new states $|\mathrm{C}\rangle$ and $|\mathrm{NC}\rangle$ [3] which are given by

$$|C\rangle \;=\; \frac{1}{g}\;(g_1^*|1\rangle + \;g_2^*|2\rangle)\ , \tag{2.6}$$

$$|NC\rangle \;=\; \frac{1}{g}\;(g_2|1\rangle - \;g_1|2\rangle)\ , \tag{2.7}$$

where $g = \sqrt{|g_1|^2 + |g_2|^2}$. The two states $|\mathrm{C}\rangle$ and $|\mathrm{NC}\rangle$ are linear combinations of the two energy eigenstates (ground states) $|1\rangle$ and $|2\rangle$.
These states develop in time according to [18]:

$$|C\rangle(t) \;=\; \frac{1}{g}\;(e^{-i\Omega_1 t}g_1^*|1\rangle + \;e^{-i\Omega_2 t}g_2^*|2\rangle)\ , \tag{2.8}$$

$$|NC\rangle(t) \;=\; \frac{1}{g}\;(e^{-i\Omega_1 t}g_1|1\rangle - \;e^{-i\Omega_2 t}g_2|2\rangle)\,. \tag{2.9}$$

The transition dipole matrix elements for transitions between the excited state and the coupled $|\mathrm{C}\rangle$ and non-coupled $|\mathrm{NC}\rangle$ states result in [18]

$$\langle 3|\hat{V}|C\rangle = \frac{\hbar}{2g} e^{-i(\Omega_1+\omega_1)t-i\varphi_1} \left(|g_1|^2 + |g_2|^2\, e^{i\delta_R t+i(\varphi_1-\varphi_2)}\right), \tag{2.10}$$

$$\langle 3|\hat{V}|NC\rangle = \frac{\hbar g_1 g_2}{2g} e^{-i(\Omega_1+\omega_1)t-i\varphi_1} \left(1 - e^{i\delta_R t+i(\varphi_1-\varphi_2)}\right). \tag{2.11}$$

If both the Raman detuning and the phase difference $(\varphi_1-\varphi_2)$ are zero, then the transition dipole matrix element of the non-coupled state into the excited state is zero ($\langle 3|\hat{V}|NC\rangle = 0$). In this case, the population of the non-coupled state cannot be excited by the resonant laser light and stays trapped in the non-coupled state. Since the population of the non-coupled state cannot absorb the laser light, the fluorescence light is also reduced. Therefore, this state is called a dark state. On the contrary, the population in the coupled state can still be excited to the level $|3\rangle$.
In order to explain the mechanism of the dark state formation and to describe effects which influence its preparation, relaxation processes have to be considered. This is typically done with the density matrix formalism which allows the description of the simple three level Λ system with decay processes [18]. The time evolution of the system is described by the Liouville equation [19]

$$i\hbar\frac{\partial\hat{\rho}}{\partial t} = [\hat{H},\hat{\rho}] + \hat{R}\hat{\rho}\,, \tag{2.12}$$

where $\hat{\rho}$ is the density operator, $\hat{H}$ is the interaction operator which consists of the sum of the unperturbed Hamilton operator H_0 and the interaction operator $\hat{V}$. Decay processes are introduced by the relaxation operator $\hat{R}$. The eigenstates of the unperturbed atom $|1\rangle$, $|2\rangle$ and $|3\rangle$ are used as basis.
For the three level system, the Liouville equation is given by [20]

$$\dot{\rho}_{nm} = -\frac{i}{\hbar}\sum_{k=1}^{3}(H_{nk}\rho_{km} - \rho_{nk}H_{km}) + (\hat{R}\hat{\rho})_{nm}\,, \qquad n,\, m = 1,\, 2,\, 3\,. \tag{2.13}$$

Depending on the system under investigation, different decay rates are applied. For further discussion, only the following decay rates are mentioned: the decay rates of the population from the excited states into the ground state Γ_{3j} $(j = 1,\, 2)$ and the decay rate of the ground state coherence Γ_{12}.
The obtained differential equations are used to calculate the diagonal elements $\hat{\rho}_{nn}$ which give the population of the state $|\mathrm{n}\rangle$, as well as the off-diagonal elements $\hat{\rho}_{nm}$, which indicate the atomic coherences of the respective states. Nevertheless, the solutions for each element are long and complex. Thus, the calculation is typically performed with some simplifications. An example is the symmetric three level system where equal Rabi frequencies for the two transitions $(g_1 = g_2)$ and equal decay rates from the excited state into the two ground states $(\Gamma_{31} = \Gamma_{32})$ are assumed. A detailed description of the calculation and solutions for the three level system can be found in [16] and [3].

For the detection of the CPT resonances, the coherences ρ_{3j} are of special interest because they are connected with the complex susceptibility ($\chi = \chi' - i\,\chi''$) [3][21], which describes the reaction of the atoms to the exciting field:

$$\chi'(\omega_j) = \frac{N d_{3j}}{\epsilon_0 E_{0j}} \operatorname{Re}(\rho_{j3}) \ , \tag{2.14}$$

$$\chi''(\omega_j) = \frac{N d_{3j}}{\epsilon_0 E_{0j}} \operatorname{Im}(\rho_{j3}) \ , \ j = 1,\, 2\,. \tag{2.15}$$

N gives the number density of atoms, d_{3j} are the dipole matrix elements and E_{0j} are the amplitudes of the electric fields. χ' can be related to the refractive index and χ'' to the absorption coefficient [22].
Typically, CPT resonances are detected via the fluorescence or the transmitted light through the medium. For the simple three level system and low laser intensity, the CPT resonances have a Lorentzian line shape [23]. The smallest attainable line width of the CPT resonance is limited by the decay rate of the ground state coherence Γ_{12} which mainly depends on the lifetime of the selected ground states [18]. Additionally, the measured CPT resonance line width is broadened by other effects like the limited interaction time of the light field with the atoms, atomic collisions, fluctuation of the light field and power broadening [17]. Power broadening will be further discussed in chapter 4.

2.1.2. Coherent Population Trapping in a Multilevel System

In the prior section the CPT effect was introduced with the help of the three level system. Nevertheless, in real atomic systems more energy levels are typically present. In our experiments we use the isotope ^{87}Rb. In general, alkali atoms are often selected for the preparation of the CPT effect because they have two long-lived ground states [18]. The formation of the CPT resonance depends on the ratio of the decay rate of the ground state coherence Γ_{12}, which depends on the lifetime of the ground states, and the decay rate from the excited state Γ [24].
In the following section the most important atomic properties of ^{87}Rb are discussed. Additionally, the hyperfine structure of the ^{87}Rb D_1 line and the influence of an external magnetic field on the atomic levels are briefly summarised. Finally, possible CPT resonance excitation schemes in the hyperfine structure of the ^{87}Rb D_1 line are explained in more detail.

2.1.2.1. Hyperfine Structure of the ^{87}Rb D_1 Line

The element rubidium belongs to the group of the alkali metals. Natural rubidium consists of a mixture of two isotopes: ^{85}Rb and ^{87}Rb. The isotope ^{87}Rb is used for the operation of the CDSM. The Rb atom has 37 electrons but only one valence electron. The nuclear spin quantum number of ^{87}Rb is $I = 3/2$. The ground state is the $5^2S_{1/2}$ state. The first excited state is split into two fine structure levels due to the spin-orbit interaction: $5^2P_{1/2}$ and $5^2P_{3/2}$ states. The transition between the ground state $5^2S_{1/2}$ and the first excited state $5^2P_{1/2}$ is named D_1 line and the transition between the ground state $5^2S_{1/2}$ and the second excited state $5^2P_{3/2}$ is labelled as D_2 line. The transitions have a wavelength of $\lambda \approx 795\,\text{nm}$ for the D_1 line and $\lambda \approx 780\,\text{nm}$ for the D_2 line.
These fine structure levels are further split into the hyperfine structure due to the interaction of the total magnetic moment of the electrons and the magnetic moment of the nucleus. In the case of zero external magnetic field or in the weak magnetic field limit (energy level shift caused by external magnetic field is small compared to hyperfine splitting), the total angular momentum of the electron shell **J** and the angular momentum of the nucleus **I** connect to the total angular momentum **F** [25]:

$$\mathbf{F} = \mathbf{J} + \mathbf{I}\,.$$

Without external magnetic field, the hyperfine structure is split either into $2I + 1$ levels for $J \geq I$ or into $2J + 1$ for $I \geq J$. The states are labelled with the quantum number F of the total angular momentum **F** according to

$$F = |(J - I)|,\ |(J - I + 1)|,\ \ldots,\ (J + I - 1),\ (J + I)\,.$$

Thus, the ground state and the excited state of the D_1 line split into two levels each ($F = 1,\ 2$ and $F' = 1,\ 2$), since $J = 1/2$ and $I = 3/2$. The excited state of the D_2 line, which has $J = 3/2$, consists of four levels ($F' = 0,\ 1,\ 2,\ 3$).
In an external magnetic field, the hyperfine structure levels with quantum number F split into $2F+1$ levels with the corresponding magnetic quantum numbers m_F

$$m_F = -F,\ -(F - 1),\ \ldots,\ (F - 1),\ F\,.$$

As a consequence, the ground state $F = 1$ and the excited state $F' = 1$ separate into three substates each and the states $F = 2$ and $F' = 2$ split into five substates. The resulting hyperfine structure of the ^{87}Rb D_1 line is shown in figure 2.2.
In the case of $J = 1/2$, the hyperfine structure ground state level shift in an external magnetic field can be calculated analytically with the Breit-Rabi formula [26][27]. Two cases are distinguished for the calculation:

- $F = I \pm J$ and $m_F = (I - J),\ \ldots,\ -(I - J)$

$$\Delta E_{HFS,B} = -\frac{h\nu_{HFS}}{2(2I+1)} + m_F \mu_B g_I B \pm \frac{h\nu_{HFS}}{2}\sqrt{1 + \frac{4m_F x_B}{2I+1} + x_B^2}\,, \qquad (2.16)$$

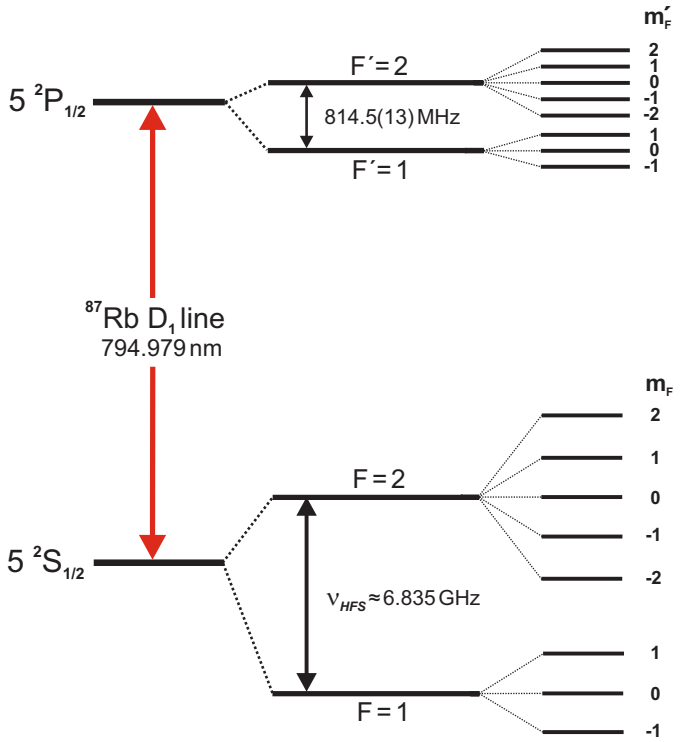

Figure 2.2.: Hyperfine structure of the ^{87}Rb D_1 line: In an external magnetic field, the hyperfine structure levels split into $2F+1$ levels with a shift according to their magnetic quantum number m_F.

- $F = I + J$ and $m_F = \pm(I + J)$

$$\Delta E_{HFS,B} = -\frac{h\nu_{HFS}}{2(2I+1)} + m_F \mu_B g_I B + \frac{h\nu_{HFS}}{2}(1 \pm x_B)\,. \tag{2.17}$$

The parameter x_B is defined as

$$x_B = \frac{(g_j - g_I)\mu_B B}{h\nu_{HFS}}\,. \tag{2.18}$$

The term ν_{HFS} gives the hyperfine splitting of the ground states without external magnetic field (see figure 2.2) which is [28]

$$\nu_{HFS} = 6.834\,682\,610\,904\,290(90)\,\text{GHz}\,. \tag{2.19}$$

Figure 2.3 depicts the shifts of the ground states with the external magnetic field $\Delta E_{HFS,B}$ which were calculated according to equations 2.16 and 2.17. At first, the energy levels shift approximately linear with the external magnetic field but for increasing magnetic field

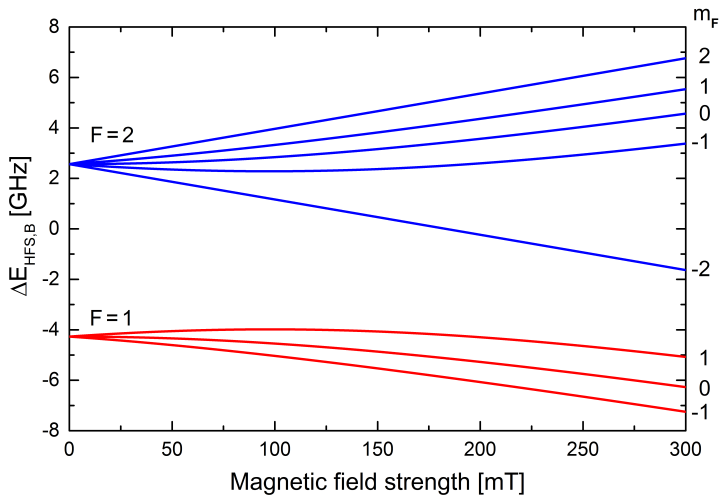

Figure 2.3.: Shift of the hyperfine structure ground state levels with the external magnetic field: The ground state level $F = 1$ splits into three sublevels (red lines) and the level with $F = 2$ splits into five sublevels (blue lines). The levels are shifted with the external magnetic field according to their magnetic quantum number m_F. The shifts were calculated using equations 2.16 and 2.17.

strengths, the quadratic magnetic field dependence becomes visible, except levels with $m_F = \pm 2$ which have no quadratic dependence according to equation 2.17. Typically, the magnetic field strengths measured by the CDSM are less than 0.1 mT. In this magnetic field range, the quadratic magnetic field dependence is still rather low. Nevertheless, for the operation of the CDSM, its influence is usually compensated for magnetic field strengths greater than 0.01 mT (see section 4.1.6).

Transitions can be induced between the ground and excited states according to following selection rules [25]:

$$\begin{aligned} \Delta F &= 0, \pm 1\,, \\ \Delta m_F &= 0 \qquad \text{for linearly polarised light}\,, \\ \Delta m_F &= \pm 1 \qquad \text{for circularly polarised light.} \end{aligned}$$

In figure 2.4 the transmission spectrum of the ^{87}Rb D_1 line is shown. The optical transitions were excited by a Vertical-Cavity Surface-Emitting Laser (VCSEL) which has a typical laser line width of about $50 - 100$ MHz (see section 3.1). The hyperfine structure transitions between the ground states ($F = 1$ and $F = 2$) and the excites states ($F' = 1$ and $F' = 2$) are matched in the transmission spectrum depicted in figure 2.4. The line widths of the optical transitions are Doppler broadened to a width of about 500 MHz [29]. CPT resonances can be prepared with both excited states $F' = 1$ and $F' = 2$. The excited state structure can influence the CPT resonance effect. As a result, the CPT resonances prepared within the D_1 line have, e.g., a better contrast compared to the D_2 line [30][31].

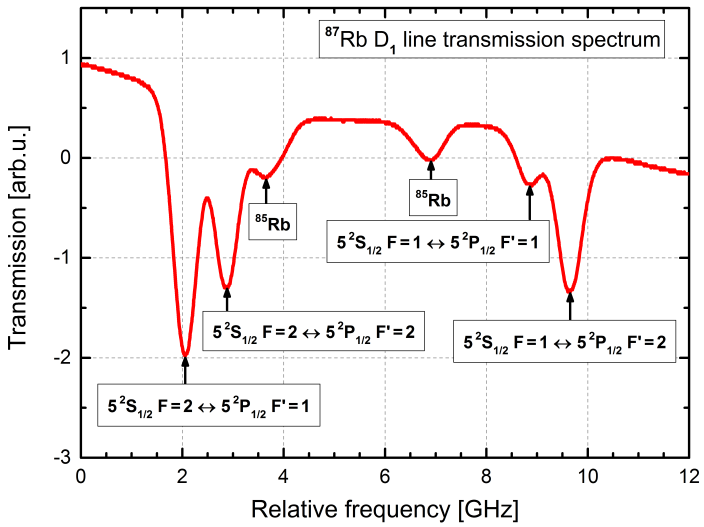

Figure 2.4.: Transmission spectrum of the ^{87}Rb D_1 line obtained with an VCSEL laser and a nearly isotopically pure ^{87}Rb vapour cell.

In this context, the contrast is defined as the ratio of the transmission change at CPT resonance to the maximum absorption [31]. The D_2 line has the drawback that its upper level consists of four excited states ($F' = 0, 1, 2, 3$) where only two levels ($F' = 1, 2$) can be used to prepare the CPT effect. The other two levels ($F' = 0, 3$) act as loss channels, since population of the dark state can be excited by one-photon transitions. Therefore, the decay rate out of the dark state is higher which increases the CPT resonance line width. In contrast, both excited states of the D_1 line can be used for the preparation of the CPT effect. Therefore, the CPT resonance prepared within the hyperfine structure of the D_1 line resulted in a higher contrast and smaller CPT resonance line widths compared to the D_2 line [30][31]. For these reasons, the D_1 line was selected instead of the D_2 line for the operation of the magnetometer.

2.1.2.2. CPT Resonance Preparation in the ^{87}Rb D_1 Line

As described in the previous section, the hyperfine structure of the ^{87}Rb D_1 line splits into $2F + 1$ sublevels in an external magnetic field. These sublevels have a different dependence on the external magnetic field according to their magnetic quantum number m_F (see figure 2.3). Various transitions are allowed between these sublevels depending on the polarisation of the light field and the angle between the light field propagation direction and the magnetic field direction [25]. Henceforth, this angle is labelled as sensor angle ϕ (see also section 4.1.7).
Different transition combinations can be used to establish Λ-shaped excitation schemes

within the hyperfine structure for the preparation of the CPT effect. In total nine CPT resonances can be detected within the ^{87}Rb D_1 line. In our experiments we commonly use circularly polarised light. Therefore, we distinguish the two following cases.
In the first case, the external magnetic field direction is parallel to the laser propagation direction (longitudinal case) which applies for the sensor angles $\phi = 0°$ and $\phi = 180°$. Then, either transitions with $\Delta m_F = +1$ (σ^+ transitions) or $\Delta m_F = -1$ (σ^- transitions) take place depending on the chirality of the light field [25]. In figure 2.5 possible excitation schemes are shown for σ^+ transitions.

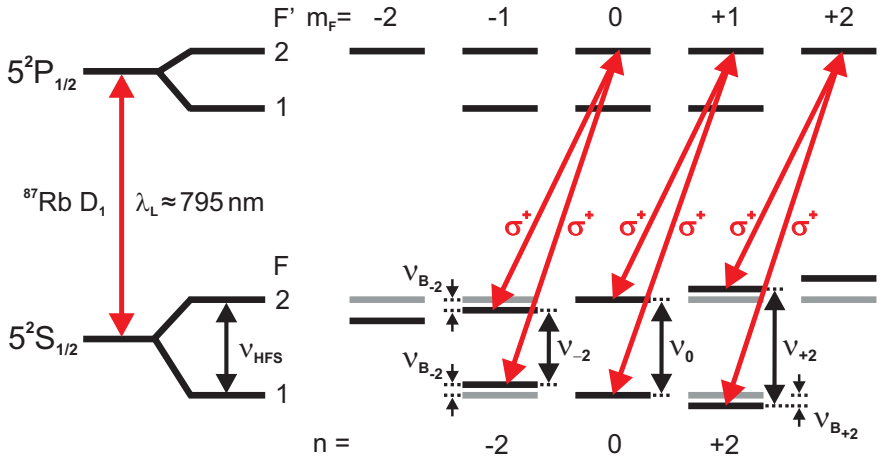

Figure 2.5.: Possible Λ-shaped excitation schemes within the hyperfine structure of the ^{87}Rb D_1 line for σ^+ transitions: The ground states are split due to an external magnetic field[1]. In this case, in total three CPT resonances are established which are labelled with $n = -2$, $n = 0$ and $n = +2$. In an external magnetic field the transition frequencies ν_{-2} and ν_{+2} are shifted by $2{\cdot}\nu_{B_{-2}}$ and $2{\cdot}\nu_{B_{+2}}$ respectively (see equation 2.22).

In this case in total three different CPT resonances with the numbers $n = -2$, $n = 0$ and $n = +2$ can be excited. In general, the CPT resonances are labelled with $n = m_{F1} + m_{F2}$ according to the magnetic quantum numbers of their ground states $(F_1 = 1, m_{F_1})$ and $(F_2 = 2, m_{F_2})$.
In the second case, the external magnetic field direction is perpendicular to the laser propagation direction (transversal case). This condition is fulfilled at the sensor angles $\phi = 90°$ and $\phi = 270°$. Then, transitions with $\Delta m_F = 0$ (π transitions) are allowed [25]. Due to the fact that the linear polarisation state can be thought of as a superposition of the left and right circular polarisation states, several excitation schemes can be realised within the hyperfine structure consisting of σ^-, σ^+ and π transitions. In total six different CPT resonances can be detected: $n = -3$, $n = -1$a, $n = -1$b, $n = +1$a, $n = +1$b and $n = +3$. At lower magnetic field strengths the CPT resonances $n = -1$a and $n = -1$b

[1] The splitting of the excited states is not shown because it only plays a minor part in the CPT resonance preparation by a negligible contribution to the two-photon detuning.

overlap and form the CPT resonance $n = -1$. Equally, the CPT resonances $n = +1a$ and $n = +1b$ build the CPT resonance $n = +1$. The splitting between the single CPT resonances can be detected depending on the external magnetic field strength and the CPT resonance line widths [32] (further discussion below).
In figure 2.6, possible excitation schemes for the six CPT resonances are drawn in for the transversal case. For sensor angles ϕ between these two extreme cases (longitudinal and transversal), all nine resonances can be prepared with varying CPT resonance amplitudes (see section 4.1.7).

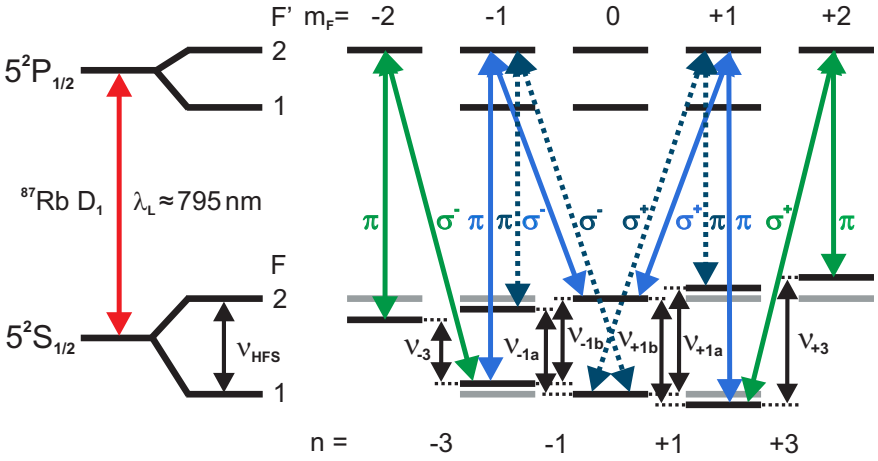

Figure 2.6.: Possible Λ-shaped excitation schemes within the hyperfine structure of the ^{87}Rb D_1 line for linearly polarised light: Linearly polarised light can be interpreted as a combination of left and right handed circularly polarised light. Then six different CPT resonances can be formed. The CPT resonance $n = 0$ is not visible since two possible Λ-shaped excitation schemes with opposite phase relation cancel each other (see discussion in section 4.2.2). Not all possible Λ-shaped excitation schemes are drawn for the respective CPT resonance n, since several combinations of transitions with the same ground states but different excited states can form the same CPT resonance n.

The CPT resonances n have a different dependence on the external magnetic field strength B. As described in section 2.1.1, a CPT resonance n is prepared, when the Raman detuning $\delta_R = \Delta_{21} - (\omega_1 - \omega_2) = 0$ (see equation 2.3). In this case, the two laser frequencies (ω_1 and ω_2) are in resonance with the two transitions of the Λ system and the laser frequency difference matches the difference frequency $\nu_n = \Delta_{21} = \Omega_2 - \Omega_1$ between the two ground states $(F_1 = 1, m_{F_1})$ and $(F_2 = 2, m_{F_2})$. Due to the dependence of the ground state levels on the external magnetic field, also the CPT resonance position shifts with the external magnetic field strength B. The magnetic field induced energy level shift of the ground states can be calculated with the help of the Breit-Rabi formula (see equations 2.16 and 2.17). For the CPT resonances $n = 0$, -1, $+1$, -2 and $+2$, both ground states $(F_1 = 1, m_{F_1})$ and $(F_2 = 2, m_{F_2})$ shift with the external magnetic field according to

equation 2.16. Therefore, the transition frequency ν_n is given by [32]

$$\nu_n = \frac{\mu_B g_I}{h} \Delta m\, B + \frac{\nu_{HFS}}{2} \left[\sqrt{1 + m_{F_1} x_B B + x_B^2 B^2} + \sqrt{1 + m_{F_2} x_B B + x_B^2 B^2} \right] , \quad (2.20)$$

where $\Delta m = m_{F_2} - m_{F_1}$, ν_{HFS} is the ground state splitting frequency (see equation 2.19) and the parameter x_B is defined as $x_B = ((g_j - g_I)\,\mu_B)/(h\,\nu_{HFS})$ [33].
For the preparation of the CPT resonances $n = -3$ and $n = +3$, the ground state (F_1, m_{F_1}), which is either $(F_1 = 1, m_{F_1} = -1)$ for $n = -3$ or $(F_1 = 1, m_{F_1} = +1)$ for $n = +3$, shifts according to equation 2.16 and the second ground state $(F_2 = 2, m_{F_2})$, which is either $(F_2 = 2, m_{F_2} = -2)$ for $n = -3$ or $(F_2 = 2, m_{F_2} = +2)$ for $n = +3$, according to equation 2.17. In this case, the frequency difference is calculated by

$$\nu_n = \frac{\mu_B g_I}{h} \Delta m\, B + \frac{\nu_{HFS}}{2} \left[\sqrt{1 + m_{F_1} x_B B + x_B^2 B^2} + (1 \pm x_B B) \right] . \quad (2.21)$$

In the next step, the terms in the square bracket of equations 2.20 and 2.21 are approximated via a Taylor series. The first- and second-order terms of the Taylor series are further considered for the calculation of the magnetic field induced frequency shift of the ground states difference frequency. Higher order terms are neglected due to their insignificant contributions for the typical measured magnetic field strengths with the CDSM ($B \leq 0.1\,\mathrm{mT}$). As a result, the ground state difference frequency ν_n can be expressed as the sum of the hyperfine structure ground state splitting frequency ν_{HFS} and two times the magnetic field induced frequency shift ν_{B_n} of the two ground states:

$$\nu_n = \nu_{HFS} + 2 \cdot \nu_{B_n} = \nu_{HFS} + 2 \cdot (\delta_{lin} \cdot B + \delta_{quad} \cdot B^2) . \quad (2.22)$$

In addition, the magnetic field induced frequency shift ν_{B_n} is expressed by a linear and a quadratic magnetic field shift coefficient δ_{lin} and δ_{quad} which give the first- and second-order dependence of the respective ground states difference frequency on the external magnetic field. The magnetic field induced shift coefficients of the possible CPT resonances n are listed in table 2.1.
Further on in this thesis, the terms linear and quadratic dependence of the CPT resonance positions on the external magnetic field refers to the dependence of the ground states difference frequency in first- and second-order on the external magnetic field given by the linear and the quadratic magnetic field shift coefficients δ_{lin} and δ_{quad} (see equation 2.22).

Due to the varying magnetic quantum numbers m_F, the respective CPT resonance positions have different magnetic field induced shift coefficients (see table 2.1). The CPT resonance position of $n = 0$ has only a quadratic dependence on the external magnetic field. The magnetic field induced shift increases with the magnetic quantum numbers of the ground states which are used for the CPT resonance preparation. Therefore, the CPT

Table 2.1.: Linear and quadratic external magnetic field frequency shift coefficients δ_{lin} and δ_{quad} of the ground states difference frequencies $((F_1 = 1, m_{F_1}) \longleftrightarrow (F_2 = 2, m_{F_2}))$ involved in the preparation of the CPT resonances n within the hyperfine structure of the ^{87}Rb D_1 (see eqaution 2.22).

n	$F_2 = 2$	m_{F_2}	$F_1 = 1$	m_{F_1}	$2 \cdot \delta_{lin}$ [Hz/nT]	$2 \cdot \delta_{quad}$ [Hz/nT^2]
-3	2	-2	1	-1	-21.015 36	$215.68 \cdot 10^{-10}$
-2	2	-1	1	-1	-14.019 52	$431.36 \cdot 10^{-10}$
-1b	2	0	1	-1	-7.023 69	$503.25 \cdot 10^{-10}$
-1a	2	-1	1	0	-6.995 83	$503.25 \cdot 10^{-10}$
0	2	0	1	0	0	$575.15 \cdot 10^{-10}$
+1a	2	1	1	0	6.995 83	$503.25 \cdot 10^{-10}$
+1b	2	0	1	1	7.023 69	$503.25 \cdot 10^{-10}$
+2	2	1	1	1	14.019 52	$431.36 \cdot 10^{-10}$
+3	2	2	1	1	21.015 36	$215.68 \cdot 10^{-10}$

resonance positions of $n = -3$ and $n = +3$ experience the highest shift with the external magnetic field.
In figure 2.7 the CPT resonance spectrum is depicted for a sensor angle of $\phi = 45°$. Here seven resonances are visible. In the middle of figure 2.7 the CPT resonance $n = 0$ is detected. The CPT resonance position of $n = 0$ is shifted from the hyperfine structure ground state splitting frequency ν_{HFS} (see equation 2.19) due to the use of a buffer gas in the ^{87}Rb vapour cell (see sections 2.3.1 and 4.1.3.3). The CPT resonances, which also have a linear dependence on the external magnetic field, lie symmetrically around the CPT resonance $n = 0$. The CPT resonance amplitudes in figure 2.7 have different amplitudes which can result from different Rabi frequencies of the respective Λ system or due to the optical pumping effect (see section 4).

The applied magnetic field in figure 2.7 is too low to resolve the splitting of the CPT resonances $n = -1$ as well as $n = +1$ into its single CPT resonances $n = +1a$ and $n = +1b$ as well as $n = -1a$ and $n = -1b$. As can be seen from table 2.1, the shift coefficients of the CPT resonances $n = +1a$ and $n = +1b$ as well as $n = -1a$ and $n = -1b$ are very similar [32]. Therefore, for low magnetic field strengths like in figure 2.7, they are not resolved. For higher magnetic field strengths, they split further and the detected CPT resonance signal gets deformed. For this reason, the CPT resonances $n = -1$ as well as $n = +1$ are not well suited for magnetic field measurements over a larger magnetic field range.

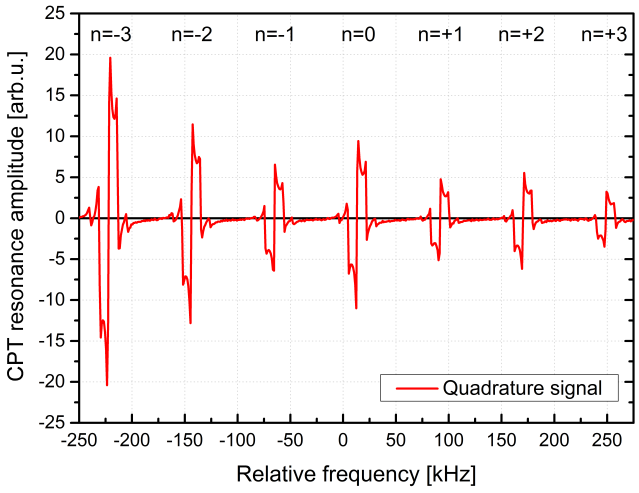

Figure 2.7.: Dispersive CPT resonance spectrum for a sensor angle of $\phi = 45°$: In total seven CPT resonances with $n = -3, -2, -1, 0, +1, +2$ and $+3$ are visible. The frequency on the x-axis is plotted relative to the hyperfine structure ground state splitting frequency ν_{HFS} (see equation 2.19). The measurement was performed with the CSES laboratory model (see section 2.4.3). A magnetic field of B=11.1 µT was applied. The applied magnetic field was too low to resolve the splitting of the CPT resonances $n = +1a$, $n = +1b$, $n = -1a$ and $n = -1b$. The vapour cell had a temperature of $T = 28.1°C$ and contained neon as buffer gas at a pressure of $P_{BG} = 4.0\,\text{kPa}$ (30 Torr). A modulation frequency of $\nu_{B_{FMS}} = 8.680\,\text{kHz}$ was set for the detection with frequency modulation spectroscopy.

2.2. Experimental Setup for CPT Resonance Measurements

In section 2.2.1, a basic experimental setup for the CPT resonance excitation is described. This basic setup was further developed for the operation of the CDSM (see section 2.4). The CPT and CDSM resonances are small compared to the absorption of the optical transitions. Therefore, they are detected by applying frequency modulation spectroscopy (see section 2.2.2).

2.2.1. Basic Setup for the CPT Resonance Preparation

A basic setup for the excitation and detection of CPT resonances is shown in figure 2.8, which is similar to the setup used for the CDSM. First of all, a proper light source is required which allows the generation of the respective frequencies for the excitation of the Λ system. For our setup, which aims at a compact instrument design with low power consumption, a Vertical-Cavity Surface-Emitting Laser (VCSEL) diode was selected (see

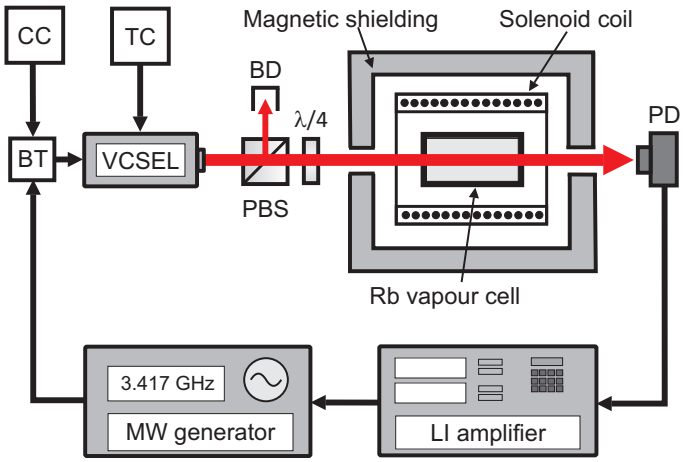

Figure 2.8.: Basic setup for the excitation and detection of CPT resonances: The laser frequency of the VCSEL is set with a Current Controller (CC) and a Temperature Controller (TC). The MicroWave (MW) modulation is combined with the laser supply current within the Bias-T (BT). The emitted laser light is circularly polarised with a Polarising Beam Splitter (PBS) cube and a quarter-wave plate (λ/4). The polarisation component, which is reflected by 90° in the beam splitter cube, is absorbed in a Beam Dump (BD). The transmitted laser light through the Rb vapour cell is detected with a PhotoDiode (PD) and analysed with a Lock-In (LI) amplifier. The Rb vapour cell is mounted in a magnetic shielding can which contains a solenoid coil in order to apply a defined magnetic field.

section 3.1). The laser emits light at a nominal wavelength of $\lambda_L \approx 795\,\text{nm}$ which matches approximately the fine structure transition $5^2S_{1/2} \leftrightarrow 5^2P_{1/2}$ (see figure 2.2). Since the VCSEL is a semiconductor laser diode, the emitted laser frequency can be tuned by either changing the laser temperature or the laser current. Therefore, VCSELs can easily be frequency modulated by applying a modulation via the laser current. Additionally, this laser type has a high modulation bandwidth of several GHz which allows the generation of the required frequency pair for the excitation of the Λ system by a frequency modulation [34]. Therefore, the laser current is modulated by a microwave signal of about half of the ground state splitting frequency ($1/2 \cdot \nu_{HFS} \approx 3.4\,\text{GHz}$). The first-order sidebands, which have a frequency spacing of about 6.8 GHz, are used for the formation of the Λ-shaped excitation scheme. The modulation signal is generated by a MicroWave (MW) generator and combined with the laser supply current in a Bias-T (BT).

There are several other possibilities to generate the required frequencies for the CPT resonance preparation like using two phase-locked lasers [18]. The application of two phase-locked lasers has the benefit that only the required frequency pair is generated which interacts with the Rb atoms. In contrast, frequency modulation generates theoretically an infinite number of frequency sidebands, which can interact with the Rb atoms and influence the CPT transition frequency, e.g., by the light shift (see section 4.1.1.2). Nevertheless, the current modulation has the benefit that it is a pretty simple technique which allows

an easy and compact setup with low power consumption. A further benefit of the current modulation is that the obtained frequency components have a stable phase relation which is required for the preparation of the CPT effect [18] (see equation 2.11).
In our setup, the emitted laser light is linearly polarised by a Polarising Beam Splitter (PBS) cube and then converted into a circular polarisation state with the help of a quarter-wave ($\lambda/4$) plate. Afterwards, the laser light passes a ^{87}Rb vapour cell which contains a mixture of isotopically pure ^{87}Rb and neon as buffer gas. A buffer gas is required to reduce the CPT resonance line width (see section 4.1.3). The vapour cell is placed within a magnetic shielding can, which allows the reduction of the external magnetic field. Inside of the magnetic shielding can a coil allows the application of a defined, homogeneous magnetic field. This magnetic field is used to lift the degeneracy of the energy levels. The laser light can enter and leave the magnetic shielding can by small openings in the can. The transmitted laser light is detected behind the magnetic shielding can by a PhotoDiode (PD) and analysed by a dual-phase Lock-In (LI) amplifier. For the detection of the CPT resonances, frequency modulation spectroscopy is used (see section 2.2.2). An additional modulation is required to enable this method which is typically in the kHz range and provided by the lock-in amplifier.
For the CDSM, this setup was further developed to a compact, robust and lightweight instrument, which fulfils the requirements for a space mission (see section 2.4).

2.2.2. Detection of CPT Resonances by Frequency Modulation Spectroscopy

Frequency Modulation Spectroscopy (FMS) is often used for the detection of CPT resonances [34]. FMS is a sensitive detection technique which also provides information on the absorption and the dispersion behaviour at resonance [35][36]. This technique is required because the reduction of the absorption caused by the CPT effect is very small compared to the absorption background of the optical transitions.
For the application of FMS, the laser current is sinusoidally modulated with the modulation frequency ω_{FMS}. The current modulation results in a frequency modulation of the emitted laser light. Thus, the laser frequency spectrum consists of the laser carrier at the frequency ω_0 and sidebands at integer multiples of the modulation frequency ω_{FMS} apart from ω_0. The emitted light field can be written as [36]

$$E(t) = \frac{E_L}{2} \sum_{m=-\infty}^{\infty} J_m(M) exp\left[\, i(\omega_0 + m\,\omega_{FMS})\, t\,\right] + c.c.\,, \quad (m = 1,\, 2,\, 3, ...)\,, \tag{2.23}$$

where E_L is the electric field amplitude of the unmodulated laser carrier at the frequency ω_0. The amplitude distribution among the carrier and its sidebands depends on the modulation index M. The amplitudes are described by Bessel functions $J_m(M)$ of order m, where $m = 0$ refers to the carrier and $m = \pm 1$ refers to the first-order sidebands [37]. For the following discussion, a modulation index of $M \leq 1$ is assumed. Thus, only the

carrier and the first-order sidebands are considered. The modulated light beam is sent through the Rb vapour cell where each frequency component experiences an attenuation δ_m and a phase shift ϕ_m. The attenuation depends on the absorption coefficient and the phase shift on the refractive index [36]. Under the assumption of small attenuation and phase differences between the carrier and the sidebands ($|\delta_0 - \delta_{+1}|$, $|\delta_0 - \delta_{-1}|$, $|\phi_0 - \phi_{+1}|$ and $|\phi_0 - \phi_{-1}| \ll 1$) following equation is obtained for the transmitted laser beam with the intensity I [35]:

$$I = \frac{cE_0^2}{8\pi} e^{-2\delta_0} \left[1 + (\delta_{-1} - \delta_{+1}) M \cos(\omega_{FMS} t) + (\phi_{+1} + \phi_{-1} - 2\phi_0) M \sin(\omega_{FMS} t)\right] . \tag{2.24}$$

The cosine component contains the information of the attenuation imbalance between both first-order sidebands and the sine component gives the residual imbalance between the first-order sidebands' phase shifts related to the carrier phase shift [35]. The detected signal at the photodiode is analysed with a dual-phase lock-in amplifier where the phase of the reference signal is set such that the absorption signal is displayed in the in-phase signal and the dispersion signal in the quadrature signal. Depending on the ratio of the modulation frequency ω_{FMS} to the width of the spectral feature $\Delta\omega_{sf}$ and the selected modulation index M, three different cases can be distinguished which are applied for the operation of the CDSM.
The first case is $\omega_{FMS} << \Delta\omega_{sf}$ and $M >> 1$ which is selected for the laser frequency stabilisation (see section 2.4.2). For this set of parameters, the detection technique is also called wavelength modulation spectroscopy [38]. In this case the in-phase signal is used for the detection of the resonance feature which is proportional to the first derivative of the absorption in the vapour cell [38]. The amplitude of the detected signal depends on the product $M \cdot \omega_{FMS}$ [38]. The quadrature signal is zero, since the dispersion signal vanishes [38].
The second case is $\omega_{FMS} >> \Delta\omega_{sf}$ and $M \leq 1$. The third case is $\omega_{FMS} \approx \Delta\omega_{sf}$ and $M \leq 1$. These two cases are applied for the detection of the CPT and CDSM resonance features. For the detection of, e.g., a CPT resonance with a setup as described in section 2.2.1, the microwave signal is modulated with a signal with a frequency ω_{FMS}. Thus, the first-order sidebands, which are used for the CPT resonance preparation, have also sidebands at the frequency distance ω_{FMS}. The CPT resonance is prepared when the condition $\delta_R = 0$ is fulfilled (see section 2.3). The detected CPT resonance spectrum can be described with the basic equation of FMS (see equation 2.24). The CPT resonance line shapes have typically a Lorentzian profile [39]. Thus, the obtained spectrum by scanning the carrier frequency also results in Lorentzian line shapes (see figure 4.1). In figure 2.9 calculated CPT resonance spectra are illustrated in order to explain the two different applied cases for the CPT and CDSM resonance detection. For the spectra in figure 2.9,

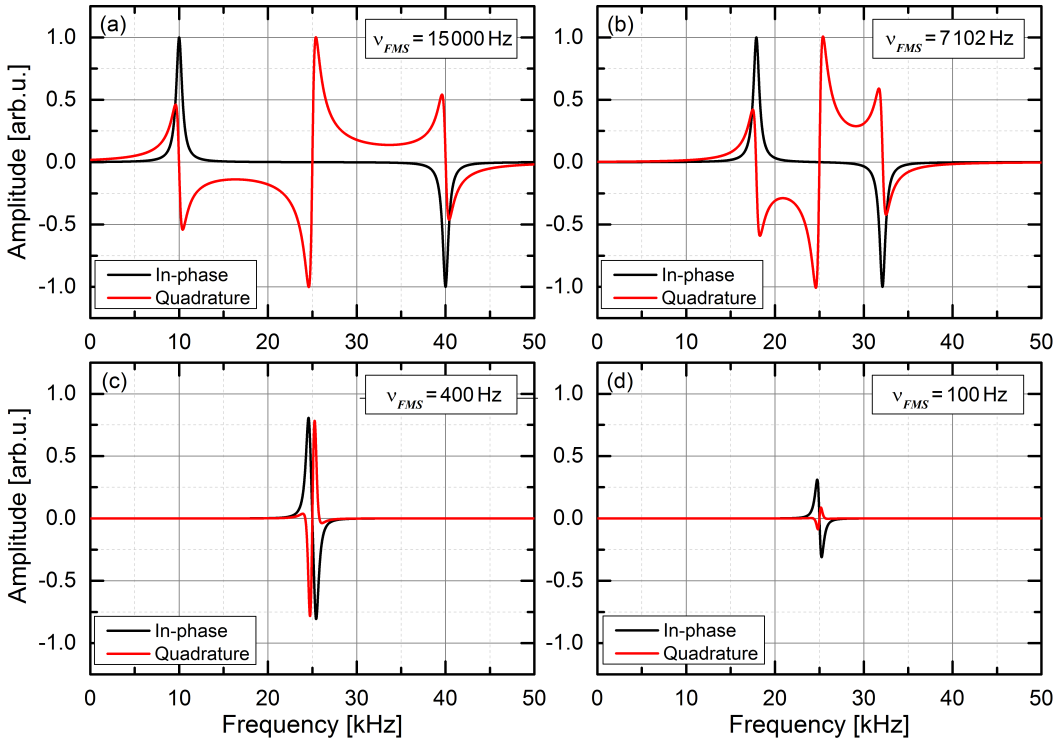

Figure 2.9.: Calculated spectra obtained for resonance features with Lorentzian line shapes like CPT resonances for different modulation frequencies ω_{FMS}: δ_{min} and M were set to 1. The line width of the resonance was set to $\Delta\omega_{CPT} = 2\pi \cdot 800\,\text{Hz}$ and the resonance position to $\omega_{CPT} = 2\pi \cdot 25\,\text{kHz}$. In (a) and (b) the modulation frequencies were higher than the resonance line width: $\omega_{FMS} = 2\pi \cdot 15\,000\,\text{Hz}$ and $\omega_{FMS} = 2\pi \cdot 7\,102\,\text{Hz}$. In (c) and (d) modulation frequencies lower than the line widths of the resonance features were selected: $\omega_{FMS} = 2\pi \cdot 400\,\text{Hz}$ and $\omega_{FMS} = 2\pi \cdot 100\,\text{Hz}$.

the following equations were used in combination with equation 2.24 [35]

$$\delta(\omega) = \delta_{min} \frac{(\Delta\omega_{CPT}/2)^2}{((\omega - \omega_{CPT})^2 + (\Delta\omega_{CPT}/2)^2)}\,, \tag{2.25}$$

$$\phi(\omega) = \delta_{min} \frac{(\Delta\omega_{CPT}/2)(\omega - \omega_{CPT})}{((\omega - \omega_{CPT})^2 + (\Delta\omega_{CPT}/2)^2)}\,, \tag{2.26}$$

where δ_{min} gives the minimum attenuation at the frequency ω_{CPT} and $\Delta\omega_{CPT}$ is the line width of the CPT resonance (see section 4.1).
In the second described case, the modulation frequency ω_{FMS} is larger than the line width of the CPT resonance $\Delta\omega_{CPT}$ ($\omega_{FMS} >> \Delta\omega_{CPT}$) and the condition for the modulation index is $M \leq 1$. If the modulation frequency is high enough, the CPT resonance is prepared three times when the microwave frequency is scanned and the detected signal consists of three substructures (see figure 2.9(a) and (b)). The black and red lines show

the in-phase and the quadrature signal respectively.
In the third case the line width of the CPT resonance is close to the modulation frequency ($\Delta\omega_{CPT} \approx \omega_{FMS}$) and the modulation index is $M \leq 1$. In this case the typical sideband structure vanishes and the spectrum only consists of one remaining resonance feature (see figure 2.9(c) and (d)). Then, the in-phase signal is proportional to the first derivative of the absorption and the detected quadrature signal is proportional to the second derivative of the dispersion [35]. Both signal amplitudes start to decrease when the modulation frequency is smaller than the resonance line width.
Typically, for magnetic fields $B > 2\,\mu\text{T}$, a modulation frequency of several kHz are used for the detection of the CDSM resonances. In contrast, for magnetic fields $B < 2\,\mu\text{T}$, a modulation frequency of only several hundreds of Hz is preferred (see section 4.3).

2.3. Magnetic Field Measurement with CPT Resonances

In general, CPT resonances are well suited for precision measurements due to their narrow line widths (down to several tens of Hz) [18]. As discussed in section 2.1.2.2, in total nine CPT resonances can be prepared within the hyperfine structure of the ^{87}Rb D_1 line whose resonance positions shift with the external magnetic field. As a consequence, the external magnetic field can be determined by measuring their resonance positions in combination with the magnetic field shift coefficients from table 2.1.
In the past, magnetometers were built whose functional principle used one CPT resonance to measure the external magnetic field [6][7]. The benefit of the CPT effect for such applications is that compact setups with low power consumption can be realised. However, the drawback is that the CPT resonance positions are affected by disturbing frequency shifts which cannot be separated from a magnetic field induced shift right away. Therefore, the CDSM uses two coupled CPT resonances to perform a differential measurement of the two coupled CPT resonance positions which reduces or even cancels the influence of disturbing effects.
In section 2.3.1 the magnetic field measurement with a single CPT resonance is briefly described. Additionally, the CDSM measurement principle is summarised in section 2.3.2 and the differences between using either single or coupled CPT resonances for the magnetic field measurement are discussed.

2.3.1. Magnetic Field Measurement with a Single CPT Resonance

The magnetic field measurement with a single CPT resonance can be performed with a setup as described in section 2.2.1. In order to generate the required laser frequencies

to prepare the Λ-shaped excitation scheme, the laser carrier with frequency ν_L is frequency modulated with a modulation signal having the frequency ν_{B_n} (see table 2.1). The frequency ν_{B_n} is adapted such that both first-order sidebands establish the CPT resonance with the number n (see section 2.1.2.2). For example, as shown in figure 2.10, the first-order sidebands ν_{-1} and ν_{+1} of the frequency modulated laser carrier can build the Λ-shaped excitation scheme within the shown hyperfine structure of the ^{87}Rb D_1 line and prepare the CPT resonance $n = +2$.

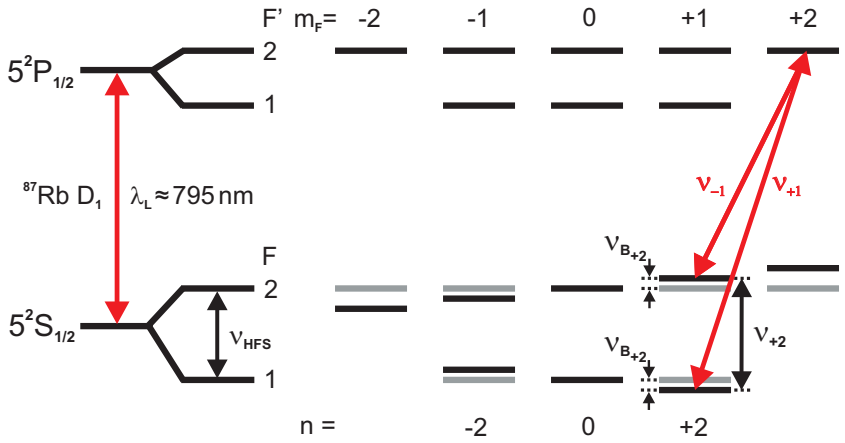

Figure 2.10.: Possible excitation scheme within the hyperfine structure of the ^{87}Rb D_1 line for measuring an external magnetic field with one CPT resonance: The laser frequency ν_L is frequency modulated with a frequency matching $1/2 \cdot \nu_{+2}$ (see section 2.2.1). Then, the first-order sidebands (ν_{-1} and ν_{+1}) establish the Λ system within the hyperfine structure. In an external magnetic field, the measured transition frequency ν_{+2} ideally consists of the ground state splitting frequency ν_{HFS} and an external magnetic field induced frequency shift $\nu_{B_{+2}}$ like $\nu_{+2} = \nu_{HFS} + 2 \cdot \nu_{B_{+2}}$. However, the transition frequency ν_{+2} can also be influenced by disturbing effects like, e.g., the light shift which can affect the accuracy of the magnetic field measurement (see equation 2.27).

In an external magnetic field, the CPT resonance $n = +2$ is established when the laser differential frequency matches the ground state splitting frequency ν_{+2} which is ideally given by $\nu_{+2} = \nu_{HFS} + 2 \cdot \nu_{B_{+2}}$ (see section 2.1.2.2). Therefore, for a magnetic field measurement, the CPT resonance position of $n = +2$ is detected and the external magnetic field is calculated with the help of the shift coefficients in table 2.1.
Nevertheless, the hyperfine structure ground state splitting frequency ν_{HFS} is not only shifted by the the external magnetic field but also by other disturbing effects, e.g., the light shift $\Delta\nu_{LS}$ (see section 4.1.1.2) or shifts introduced by the use of a buffer gas $\Delta\nu_{BG}$ [23]. The buffer gas, which is typically used to obtain narrow CPT resonance line widths, causes a buffer gas pressure dependent and a temperature dependent transition frequency shift (see section 4.1.3). Thus, the CPT resonance n is prepared when the laser difference frequency matches the actual transition frequency ν_n which is given by

$$\nu_n = \nu_{HFS} + \nu_{BG} + \nu_{LS} + 2 \cdot \nu_{B_n} \,. \tag{2.27}$$

The separation of the respective effects would require a profound knowledge of each effect as well as an accurate measurement and control of both the laser intensity and the temperature of the Rb vapour cell. Therefore, measuring magnetic fields with a single CPT resonance and an accuracy better than $\pm 0.2\,\mathrm{nT}$ as required for the JUICE mission (see sections 2.4 and 4.3) would require a huge effort outside of the laboratory.

2.3.2. Magnetic Field Measurement with Coupled CPT Resonances

The CDSM measurement principle reduces the influence of disturbing frequency shifts (see equation 2.27) on the magnetic field measurement by coupling two CPT resonances and measuring the differential shift of their CPT resonance positions [1]. Since all transition frequencies in the hyperfine structure ground states experience about the same adverse frequency shifts by, e.g., the buffer gas $\Delta\nu_{BG}$ (see section 4.1.3), the differential measurement reduces or ideally cancels the influence of these disturbing frequency shifts on the measured magnetic field strength.
For the coupling of the CPT resonances, in total three Λ systems are established within the hyperfine structure of the ^{87}Rb D_1 line. Figure 2.11 shows an example of a circularly polarised light field inducing σ^+ transitions.

The required frequency components for the simultaneous formation of all three Λ systems are achieved by a two-stage modulation process. First, the laser carrier with the frequency ν_L is modulated with ν_{mod_1}. A modulation index $M_{mod_1} \approx 1$ is used. Thus, most of the energy is contained in the carrier and the first-order sidebands. Therefore, higher-order sidebands are not taken into account for the further discussion. As a result, the modulated light field consists of the three frequency components:

$$\nu_{-10} = \nu_L - \nu_{mod_1} \,, \tag{2.28}$$

$$\nu_L = \nu_L \,, \tag{2.29}$$

$$\nu_{10} = \nu_L + \nu_{mod_1} \,. \tag{2.30}$$

In the second step, the first modulation signal with the frequency ν_{mod_1} is phase modulated with an additional signal having the frequency ν_{mod_2}. Therefore, the first modulation signal gets sidebands at multiples of the modulation frequency ν_{mod_2}. Again the modulation index is $M_{mod_2} \approx 1$ and only the first-order sidebands obtained by the second modulation step are further considered. As a result, the double modulated laser light field consists of

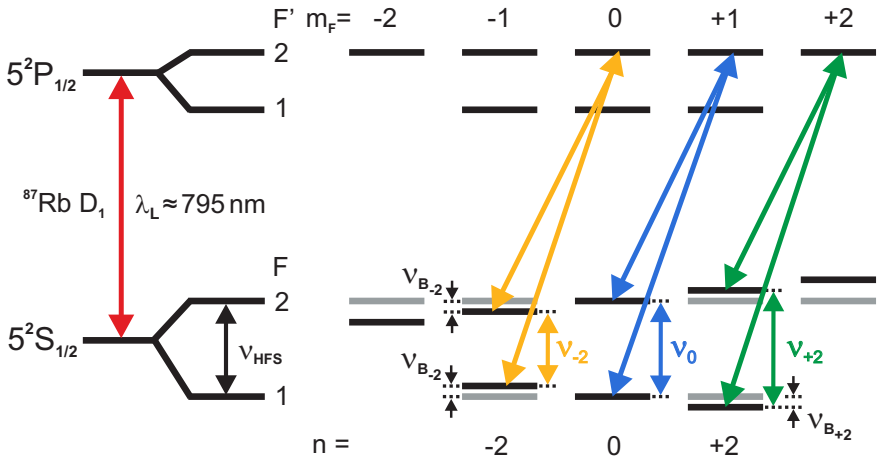

Figure 2.11.: Exemplary excitation scheme within the hyperfine structure of the ^{87}Rb D_1 line for the operation of the CDSM: A two-step modulation process is required to couple the CPT resonances $n = -2$ and $n = +2$. In the first step the laser carrier with the frequency ν_L is frequency modulated with $\nu_{mod_1} = 1/2 \cdot \nu_0$, which is approximately 3.4 GHz. Then, the first-order sidebands establish the centre Λ system (blue arrows). In the second step the first modulation signal is phase modulated with the frequency $\nu_{mod_2} = 2 \cdot \nu_{B_2}$, where $\nu_{B_2} = |\nu_{B_{+2}}| = |\nu_{B_{-2}}|$, which matches the magnetic field induced energy level shift of the CPT resonance positions of $n = -2$ and $n = +2$. As a result, the two outer Λ systems are created (yellow and green arrows).

the following frequency components [1]:

$$\nu_{-1-1} = \nu_L - (\nu_{mod_1} + \nu_{mod_2}) , \tag{2.31}$$

$$\nu_{-10} = \nu_L - \nu_{mod_1} , \tag{2.32}$$

$$\nu_{-11} = \nu_L - (\nu_{mod_1} - \nu_{mod_2}) , \tag{2.33}$$

$$\nu_L = \nu_L , \tag{2.34}$$

$$\nu_{1-1} = \nu_L + (\nu_{mod_1} - \nu_{mod_2}) , \tag{2.35}$$

$$\nu_{10} = \nu_L + \nu_{mod_1} , \tag{2.36}$$

$$\nu_{11} = \nu_L + (\nu_{mod_1} + \nu_{mod_2}) . \tag{2.37}$$

In order to establish the three Λ systems shown in figure 2.11, the modulation frequency ν_{mod_1} is set to $1/2 \cdot \nu_0$. As a result, the first-order sidebands of the first modulation process (ν_{-11} and ν_{10}) establish the centre Λ system (blue arrows) and prepare the CPT resonance $n = 0$.

Subsequently, the second modulation frequency ν_{mod_2} is adapted such that it coincides with $2 \cdot \nu_{B_2} = 2 \cdot |\nu_{B_{+2}}| = 2 \cdot |\nu_{B_{-2}}|$ which is the external magnetic field induced shift of the CPT resonance positions of $n = -2$ and $n = +2$ (see table 2.1). Then, frequency components of the first and second modulation step match the required frequencies for

the excitation of the CPT resonances $n = -2$ and $n = +2$ (yellow and green arrows in figure 2.11).

Originally, in reference [1] the second modulation frequency was set to $\nu_{mod_2} = \nu_{B_2}$ and the first-order sidebands of the second modulation step (ν_{-1-1}, ν_{-11}, ν_{1-1} and ν_{11}) were assumed to prepare the CPT resonances $n = -2$ and $n = +2$ simultaneously (see figure 2.12(a)). However, no coupled CPT resonance was detected with this excitation configuration. The experimental results showed that the simultaneous preparation of the CPT resonances only works with $\nu_{mod_2} = 2 \cdot \nu_{B_2}$. One possible excitation configuration with $\nu_{mod_2} = 2 \cdot \nu_{B_2}$ is shown in figure 2.12(b).

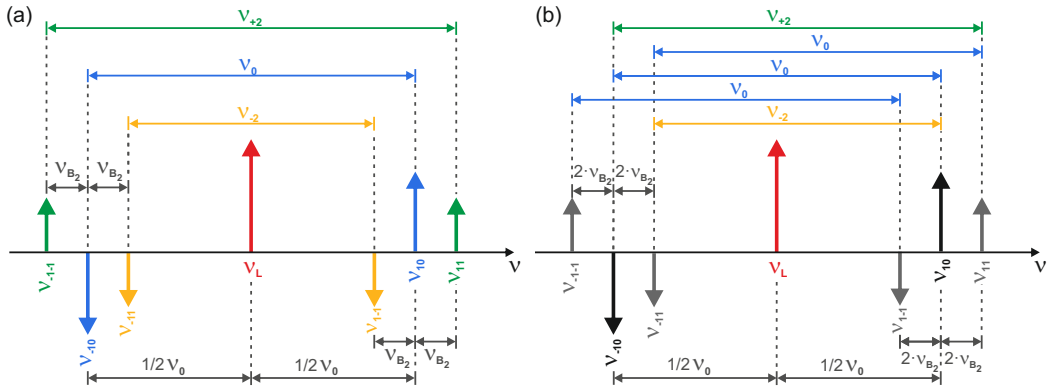

Figure 2.12.: Frequency components of the double modulated laser field for the operation of the CDSM: The light field consists of the laser carrier frequency ν_{L}, its first-order sidebands $\nu_{\pm 10}$ of the first modulation step at a frequency distance of $1/2 \cdot \nu_0$ and the first-order sidebands of the second modulation step. In (a) the second modulation frequency is set to $\nu_{mod_2} = \nu_{B_2}$ and in (b) to $\nu_{mod_2} = 2{\cdot}\nu_{B_2}$. The excitation configuration depicted in (a) did not result in the preparation of coupled CPT resonances. The frequency components shown in (b) match the required frequency components to excite the three CPT resonances $n = 0$, -2 and $+2$ simultaneously (see figure 2.11).

To obtain all three CPT resonances $n = 0$, -2 and $+2$ at the same time, the Raman detunings δ_{R_n} (see equation 2.3) have to be zero for all three Λ-shaped excitation schemes shown in figure 2.11:

$$\delta_{R_0} = \delta_{R_{+2}} = \delta_{R_{-2}} = 0\,. \tag{2.38}$$

Then, the three CPT resonances ($n = 0$, -2 and $+2$) are detected when the respective laser difference frequencies match the ground state transition frequencies ν_n (see figure

2.12 (b)) which are in this case

$$\nu_{-2} = \nu_0 - 2 \cdot \nu_{B_2} \,, \tag{2.39}$$

$$\nu_0 = \nu_{HFS} + \nu_{BG} + \nu_{LS} + \nu_{B_0} \,, \tag{2.40}$$

$$\nu_{+2} = \nu_0 + 2 \cdot \nu_{B_2} \,. \tag{2.41}$$

For the operation of the CDSM, the first modulation signal with the frequency ν_{mod_1} is stabilised to the frequency $1/2 \cdot \nu_0$ with the help of the CPT resonance $n = 0$ (see section 2.4.2). Subsequently, the frequency ν_{mod_2} has to be adapted to match the magnetic field induced shift $2 \cdot \nu_{B_2}$ to obtain the CPT resonances $n = -2$ and $n = +2$ (see figure 2.12). The benefit of this procedure is that the preparation of the CPT resonances $n = -2$ and $n = +2$ gets ideally independent of the disturbing frequency shifts concerning ν_0 (see equation 2.40). Thus, the external magnetic field can be determined directly from the second modulation frequency ν_{mod_2} as will be described in more detail further below.
When the condition $\nu_{mod_2} = 2 \cdot \nu_{B_2}$ is fulfilled, then the Raman detuning is zero for both CPT resonances $n = -2$ and $n = +2$ simultaneously. As a result, a superposition of the CPT resonances $n = -2$ and $n = +2$ is detected. This superposition is called the coupled dark state resonance or the CDSM resonance. In total three CDSM resonances can be prepared in the hyperfine structure of the ^{87}Rb D_1 line as will be discussed further below. A CDSM resonance is detected by using frequency modulation spectroscopy (see section 2.2.2). The zero crossing of the quadrature signal is used to obtain the information about the CPT resonance position which is alao well suited for the realisation of a control loop (see section 2.4.2).
Since the line shape of the single CPT resonances can be approximated by a Lorentzian profile [39], the CDSM resonance detected within the quadrature signal can be approximated by the superposition of two dispersive Lorentzian profiles [1]. In the case of the CPT resonances $n = -2$ and $n = +2$, which each have a dispersive Lorentzian line shape $L_{CPT_{-2}}$ and $L_{CPT_{+2}}$, the resulting CDSM resonance signal L_{CDSM_2} has the following form:

$$\begin{aligned} L_{CDSM_2} &= L_{CPT_{-2}} + L_{CPT_{+2}} \\ &= h_{-2} \cdot \frac{\delta_{R_{-2}} \cdot \Delta\nu_{-2}}{(\delta^2_{R_{-2}} + \frac{1}{4}\,\Delta\nu^2_{-2})} + h_{+2} \cdot \frac{\delta_{R_{+2}} \cdot \Delta\nu_{+2}}{(\delta^2_{R_{+2}} + \frac{1}{4}\,\Delta\nu^2_{+2})} \,, \end{aligned} \tag{2.42}$$

where h_n is the CPT resonance height and $\Delta\nu_n$ is the line width of the respective CPT resonance with the number n. The terms $\delta_{R_{-2}}$ and $\delta_{R_{+2}}$ are the Raman detunings of $n = -2$ and $n = +2$ which are given by

$$\delta_{R_{-2}} = \Delta - 2 \cdot \nu_{B_2} + 2 \cdot \nu_{mod_2} \,, \tag{2.43}$$

$$\delta_{R_{+2}} = \Delta + 2 \cdot \nu_{B_2} - 2 \cdot \nu_{mod_2} \,, \tag{2.44}$$

with the detuning Δ of the first modulation frequency ν_{mod_1} to the transition frequency ν_0:

$$\Delta = \nu_0 - 2 \cdot \nu_{mod_1} \,. \tag{2.45}$$

In order to explain the differential measurement principle of the CDSM and the obtained compensation of disturbing frequency shifts, which affect the single CPT resonance positions (see equation 2.27), two cases are distinguished: $\Delta = 0$ and $\Delta \neq 0$.

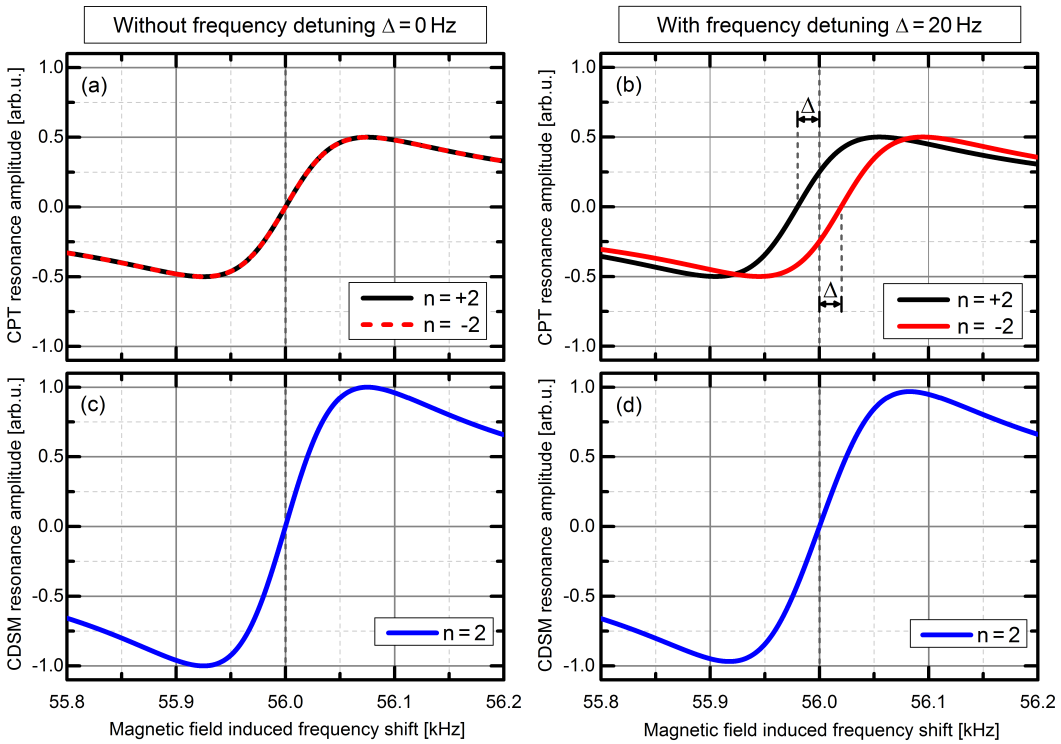

Figure 2.13.: Calculated single CPT resonances and CDSM resonance with and without disturbing frequency detuning Δ: In (a) the single CPT resonances have exactly the same zero crossing frequency as the CDSM resonance (panel (c)). If there is a disturbing frequency detuning, then the CPT resonances are split and shifted in opposite directions (panel (b)). However, the zero crossing frequency of the CDSM resonance is not influenced (panel (d)) and matches the magnetic field induced frequency shift ($2 \cdot \nu_{B_2}$).

For the illustration in figure 2.13, two dispersive CPT resonances are assumed and the CDSM resonance is calculated according to equation 2.42. The two CPT resonance line widths are set to $\Delta\nu_{-2} = \Delta\nu_{+2} = 150\,\text{Hz}$. The peak-to-peak CPT resonance amplitudes are $h_{-2} = h_{+2} = 1$ (see also section 4.1). On the x-axis in figure 2.13 the total magnetic field induced frequency shift $2 \cdot \nu_{B_2}$ of the hyperfine structure ground states difference frequencies is plotted. The magnetic field induced frequency shift is set to $2 \cdot \nu_{B_2} = 56\,000\,\text{Hz}$, which corresponds to an external magnetic field strength of $B = 3\,994\,\text{nT}$ (see table 2.2 below).
In the first case ($\Delta = 0\,\text{Hz}$), the first modulation frequency ν_{mod_1} matches half of the transition frequency ν_0 (see equation 2.45). When the second modulation frequency ν_{mod_2} matches half of the magnetic field induced frequency shift ν_{B_2}, then the Raman detuning

is zero for both CPT resonances $n = -2$ and $n = +2$ simultaneously. As a consequence, the zero crossing frequencies of the CPT resonances $n = -2$ and $n = +2$ coincide at $2 \cdot \nu_{B_2}$ (see figure 2.13(a)).
In the second case ($\Delta \neq 0$), a disturbing frequency shift, for example, due to a change of the sensor temperature (see section 4.1.3.3), causes a detuning between the CPT resonances $n = -2$ and $n = +2$ which shifts their zero crossing frequencies in opposite directions. In figure 2.13(b) a positive detuning of $\Delta = 20\,\text{Hz}$ was assumed. Thus, the CPT resonance $n = +2$ is shifted by Δ to lower frequencies and the CPT resonance $n = -2$ by Δ to higher frequencies (see figure 2.13(b)). For a negative detuning, the CPT resonances would be shifted exactly the other way round. Since the CPT resonances are shifted symmetrically with reference to $2 \cdot \nu_{B_2}$, the opposite amplitude contributions of the single CPT resonances cancel each other out exactly at the magnetic field induced frequency shift value $2 \cdot \nu_{B_2}$ when forming the CDSM resonance. Therefore, the disturbing frequency shift does not affect the magnetic field measurement of the CDSM. However, the compensation behaviour obtained by forming a CDSM resonance crucially depends on the line shapes of the single CPT resonances as will be discussion in section 4.2.

Similar to the CPT resonances $n = -2$ and $n = +2$, the CPT resonances $n = -3$ and $n = +3$ as well as $n = -1$ and $n = +1$ form the CDSM resonances $n = 1$ and $n = 3$ (see figure 2.14). Due to the different magnetic field dependences of the CPT resonance positions (see table 2.1), also the positions of the CDSM resonances ($n = 1$, $n = 2$ and $n = 3$) have different dependences on the external magnetic field. The zero crossing frequency of the CDSM resonance ν_{CDSM_n} shifts with the external magnetic field B according to

$$\nu_{CDSM_n} = 2 \cdot \nu_{B_n} = \delta_{CDSM_n} \cdot B\,, \qquad n = 1,\, 2,\, 3\,, \tag{2.46}$$

where $\nu_{B_n} = |\nu_{B_{+n}}| = |\nu_{B_{-n}}|$ (see section 2.1.2.2) and δ_{CDSM_n} is the linear shift coefficient of the CDSM resonance n with the external magnetic field. The magnetic field shift coefficients δ_{CDSM_n} are listed in table 2.2. The quadratic magnetic field dependence of the CPT resonance positions has to be considered depending on the magnetic field strengths and the required accuracy. For the CDSM operation, the quadratic dependence is typically compensated for magnetic field strengths higher than $10\,\mu\text{T}$ (further discussion see section 4.1.6).

The CDSM resonances with even and odd numbers have different angular dependences on the external magnetic field, which is discussed in section 4.1.7. Switching between the CDSM resonances at certain sensor angles allows an omni-directional magnetic field measurement.

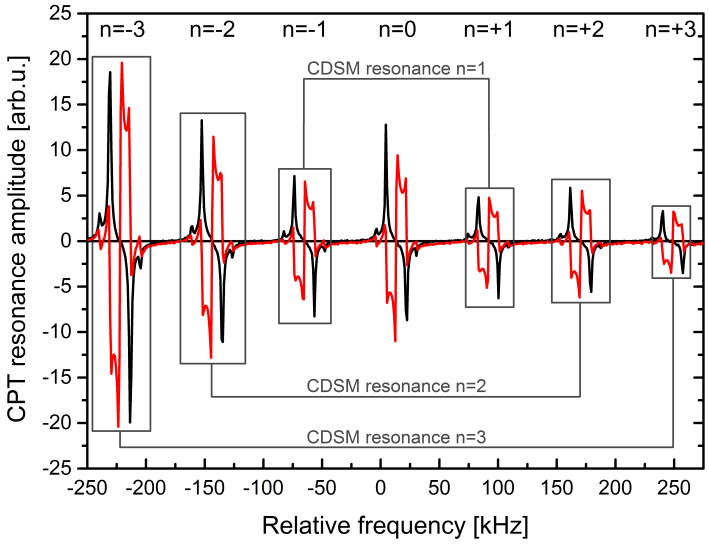

Figure 2.14.: Coupling of single CPT resonances to the CDSM resonances: The CDSM resonances $n = 1, 2, 3$ result from the superposition of the single CPT resonances $n = \pm 1, \pm 2, \pm 3$ which are arranged symmetrically with respect to the CPT resonance $n = 0$. The frequency on the x-axis is plotted relative to the hyperfine structure ground state splitting frequency ν_{HFS} (see equation 2.19). A magnetic field of $B = 11.1\,\mu\text{T}$ was applied. Thus, the single CPT resonances appear at the frequencies $\nu_n = \nu_0 + 2 \cdot \nu_{B_n}$ ($n = \pm 1, \pm 2, \pm 3$). The Rb vapour cell contained neon as buffer gas at a pressure of $P_{BG} = 4\,\text{kPa}$ (30 Torr). For this reason, the position of the CPT resonance $n = 0$ is shifted from ν_{HFS} by ν_{BG} (see equation 2.27).

Table 2.2.: Magnetic field shift coefficients δ_{CDSM_n} of the CDSM resonance positions within the hyperfine structure of the ^{87}Rb D_1 line.

CDSM Resonance n	δ_{CDSM_n} [nT/Hz]
1a	6.995 83
1b	7.023 69
2	14.019 52
3	21.015 36

2.4. The CDSM Instrument

The CDSM instrument was developed for scientific space applications. The first magnetometer prototype was built for the China Seismo-Electromagnetic Satellite (CSES) mission, which was launched in February 2018. The CSES mission investigates the Earth's magnetic field and studies the connection between disturbances in the ionosphere and the

occurrence of earthquakes [40]. For this mission, the CDSM is part of the High Precision Magnetometer package which additionally contains two fluxgate magnetometers [41].
A further CDSM instrument development is ongoing for the upcoming JUpiter ICy moon Explorer (JUICE) mission by the European Space Agency (ESA). This mission will investigate the Jupiter system with special emphasis on the Jupiter moons Ganymede, Europa and Callisto [13].
The requirements on the CDSM instrument differ for the CSES and JUICE missions. The most important differences are compared in section 2.4.1. In section 2.4.2, the CDSM instrument design for the CSES mission is reviewed and the required control loops for the operation of the CDSM are introduced. The CDSM instrument design for the JUICE mission is based on the CSES flight model with adaptations to the specific mission requirements. The different CDSM models, which were build during the development of the CDSM for the CSES and JUICE missions, are summarised in section 2.4.3.

2.4.1. CDSM Requirements for CSES and JUICE Missions

The CSES and the JUICE missions have each distinct requirements on the CDSM which for the most part result from the environmental conditions during the missions. First of all, the measured magnetic field ranges differ. For the CSES mission, the CDSM measures magnetic field strengths in the range of $B = 18-56\,\mu\text{T}$. In contrast, the measured magnetic field values will be much lower during the JUICE mission. For example, during one part of the mission the spacecraft will be orbiting Ganymede at a distance of 500 km. In this orbit, the magnetic field strengths will be in the range of $B = 0.35 - 1.5\,\mu\text{T}$. Each of these two magnetic field ranges have their own challenges in order to keep the accuracy of the magnetic field strengths measured by the CDSM. On the one hand, for the magnetic field strengths during the CSES mission, the quadratic magnetic field dependence of the CPT resonance positions has to be considered (see section 4.1.6). On the other hand, for magnetic field strengths lower than $2\,\mu\text{T}$, the measured magnetic field strength can be influenced by the superposition of the converging CPT and CDSM resonances, if the operational parameters of the CDSM are not selected carefully (see section 4.3).
One further difference between the CSES and the JUICE missions is the temperature at the sensor unit. For CSES, the in-orbit ambient temperature is typically around $T = 12°\text{C}$ [12]. Therefore, the sensor cell has only to be heated to around $T = 25°\text{C}$. For the JUICE mission, the temperature of the sensor unit can get as low as $-150°\text{C}$ [13]. As a consequence, the sensor unit has to be better thermically isolated and the materials thoroughly selected in order to reduce the required heating power (see section 3.3.3). Additionally, the high radiation levels (up to several Mrad) during the JUICE mission affect the selection of the sensor materials (see section 3.3.3) and optical fibres (see section 3.4.2).
Furthermore, the CSES and the JUICE missions have also different durations. CSES has

a mission duration of more than five years [40] while JUICE will have a mission duration of about eleven years, which splits into 7.5 years of transfer and about 3.5 years of science phase in the Jupiter system [13]. Therefore, it had to be demonstrated that all components of the CDSM can survive such a long mission duration. For that reason, an endurance test with VCSELs was performed (see section 3.2).

2.4.2. CDSM Instrument for the CSES Mission

The flight model of the CDSM for the CSES mission is depicted in figure 2.15. Additionally, a block diagram of the CDSM is shown in figure 2.16, which depicts the most important parts of the instrument and its control loops for the operation of the magnetometer. The CDSM instrument consists of the electronics box and the sensor unit which are connected by two optical fibres and a thermal control cable.

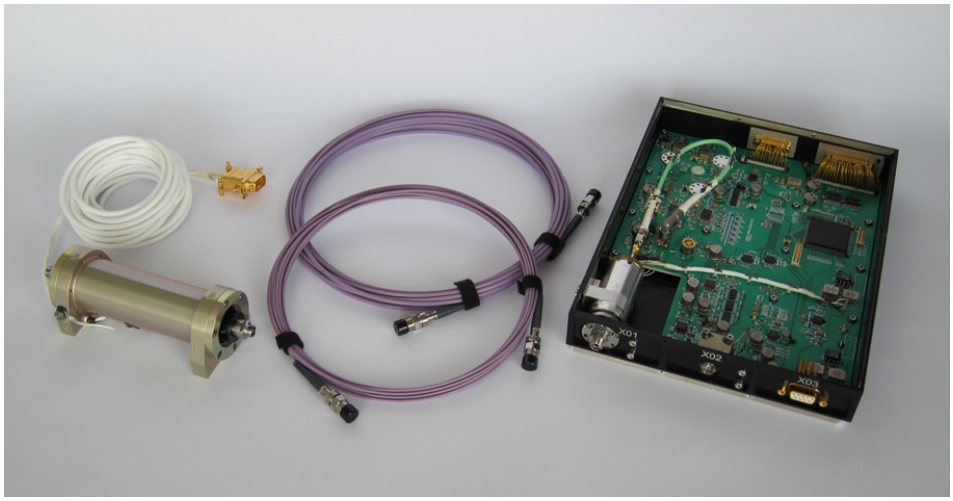

Figure 2.15.: Flight model of the CDSM for the CSES mission [12]: The flight model consists of the sensor unit (left), two optical fibres (middle) and the electronics unit (right).

For the mission, the electronics unit is installed inside of the satellite while the sensor unit is mounted on a boom outside of the spacecraft [41].
The electronics unit consists of the laser unit and the electronics board. Both are mounted in the instrument box (see figure 2.16). The main elements of the electronics board are the control unit and the microwave unit. The microwave unit generates the microwave signal by a phase-locked loop which consists of a Voltage-Controlled Oscillator (VCO) and a fractional-n counter frequency divider plus a Voltage-Controlled Temperature-Compensated Crystal Oscillator (VCTCXO) as a reference oscillator [14]. The microwave signal and the laser current are combined within a Bias-T.

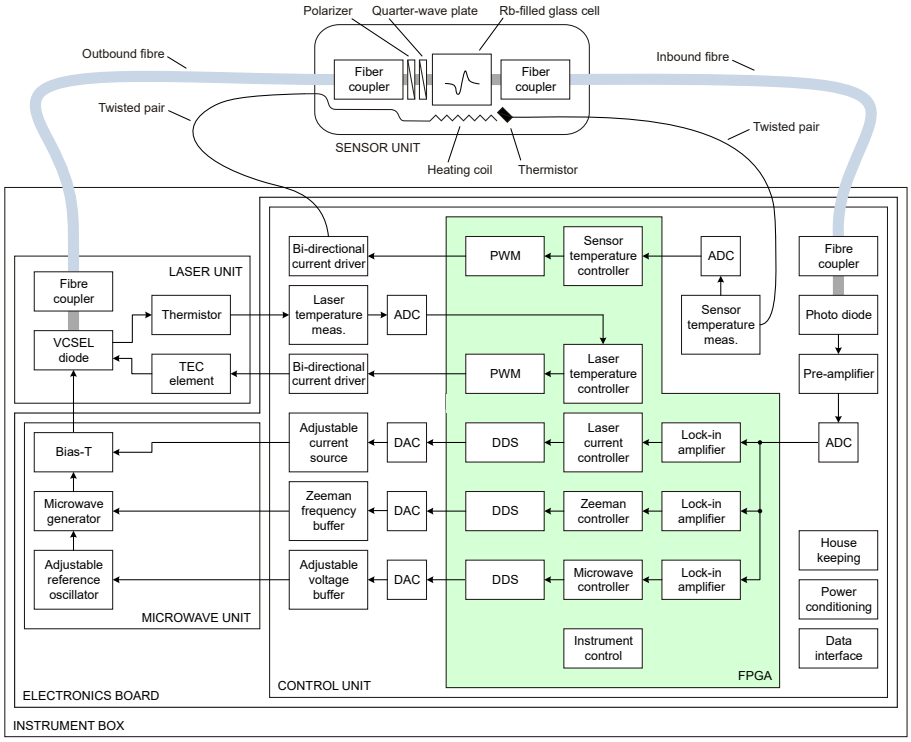

Figure 2.16.: Block diagram of the CDSM instrument for the CSES mission [12]: The electronics board consists of the laser, microwave and control units. The outbound fibre connects the laser unit with the sensor unit. The inbound fibre guides the laser light from the sensor unit to the control unit where the detected light is further processed.

For the CDSM, a VCSEL (see section 3.1) was selected, which provides the carrier frequency ($\lambda \approx 795\,\mathrm{nm}$) of the multi-modulated laser light for the excitation of the CDSM resonances (see section 2.3.2). The VCSEL is mounted in the laser unit including a thermistor and a ThermoElectric Cooler (TEC) in order to temperature control the laser by a control loop.
The emitted laser beam is collimated and coupled into the outbound fibre (see section 3.4) by a fibre coupler. The outbound fibre guides the modulated light field to the sensor unit (see section 3.3). The sensor unit contains the Rb vapour cell and optical components to set the appropriate polarisation state of the light field and couple the light from and back into the optical fibres.
The inbound fibre guides the light back to the electronics board where it is detected by a photodiode. The detected light is analysed by digital lock-in amplifiers which are realised within the Field Programmable Gate Array (FPGA) (see figure 2.16). Therefore, the detected signal is converted to the digital domain by an Analog-to-Digital Converter (ADC). Additionally, the modulation signals for applying FMS (see section 2.2.2) are generated within the FPGA by Direct Digital Synthesis (DDS) as well as both signals to set the

temperature of the laser diode and sensor cell by Pulse Width Modulation (PMW) [12]. The output signals from the FPGA are converted to the analog domain by a Digital-to-Analog Converter (DAC).
In total five control loops are required to operate the CDSM magnetometer [42][12]. The first two of the five control loops stabilise the laser frequency, the third is used to stabilise the microwave generator frequency, the fourth adapts the second modulation frequency to the external magnetic field induced frequency shift and the fifth control loop sets the sensor cell temperature for temperatures lower than 17°C.

The laser frequency has to be stabilised because a drift over time would cause a two-photon detuning δ_L (see equation 2.2). Depending on the used operational parameters, like, e.g., buffer gas pressure, a two-photon detuning of several hundreds of MHz can be accepted and the CPT resonances still be established. However, a two-photon detuning influences the CPT resonance line shapes and also the light shift (see sections 4.1.5 and 4.1.1.2) which both can affect the accuracy of the magnetic field measurement. Thus, a stabilised laser frequency is essential.
The laser frequency can be altered by either changing the laser current or the laser temperature (see section 3.1). Typical values of the laser frequency shift coefficients for the used VCSEL are: current shift coefficient $\Delta\nu/\Delta I \approx -120\,\mathrm{GHz/mA}$ at a laser current of $I_L = 3.5\,\mathrm{mA}$ and temperature shift coefficient $\Delta\nu/\Delta T \approx -27\,\mathrm{GHz/°C}$ [43].
The first control loop of the CDSM sets the laser temperature to a fixed value. The temperature is controlled with the help of a TEC, a pulse width modulated current, a thermistor and a controller in the FPGA [12] (see figure 2.16).
The second control loop of the CDSM sets the laser current. In order to control the laser frequency, the laser temperature is kept constant and a laser frequency change is corrected by adapting the laser current. The appropriate laser current is set via an adjustable current source consisting a constant current source in combination with current sinks [12].
The proper laser frequency is set with the help of the transmission spectrum of the ^{87}Rb D_1 line (see figure 2.4). In order to stabilise the laser frequency to a certain resonance feature, FMS is applied (see first case described in section 2.2.2). Therefore, a modulation frequency of $\nu_{L_{FMS}} = 11.161\,\mathrm{kHz}$ is applied [14] which is much lower than the Doppler broadened line width of the optical transitions ($\approx 500\,\mathrm{MHz}$). Additionally, a modulation index $M >> 1$ is set.
The obtained in-phase signal is depicted in figure 2.17 for two different cases. In the first case the microwave signal is not applied to the laser current (see figure 2.17(a)). Then, the derivative of the transmission spectrum, which is shown in figure 2.4, is detected within the in-phase signal (see figure 2.17(a)).
In the second case the first modulation signal with a frequency of $\nu_{mod_1} \approx 3.4\,\mathrm{GHz}$ was added to the laser current (see figure 2.17(b)). The resulting transmission spectrum consists of contributions from the laser carrier frequency ν_L and its sidebands at integer multiples of ν_{mod_1} exciting the optical transitions of the ^{87}Rb D_1 line hyperfine struc-

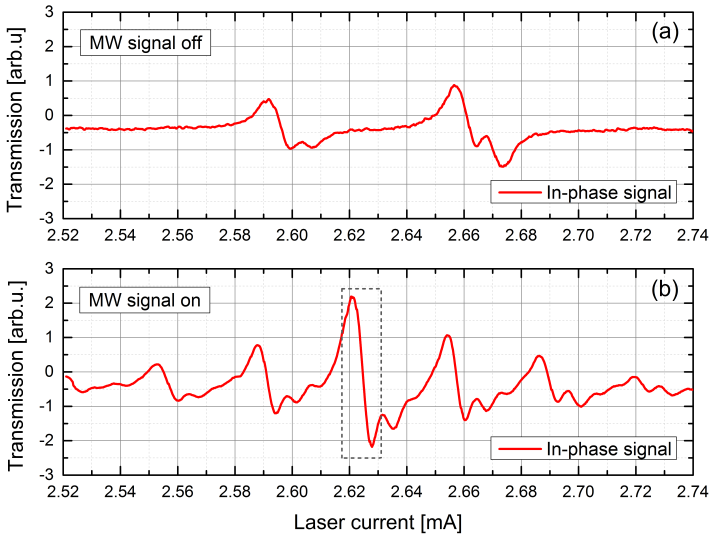

Figure 2.17.: Stabilisation signal used for the laser current control loop: In (a) the derivative of the transmission spectrum of the ^{87}Rb D_1 line is obtained by the application of FMS. In (b) the MicroWave (MW) signal was superposed to the laser supply current (see section 2.2.1). Now the detected signal also consists of contributions from the sidebands with the optical transitions of the D_1 line. The laser current is stabilised to the centre structure (see dashed rectangle in (b)) which appears when both first-order sidebands are in resonance with the transitions forming the Λ excitation scheme for CPT resonance preparation (see section 2.1.1). The measurement was performed with the flight spare electronics (see section 2.4.3.1) and the dual pass sensor (see section 3.3.3). Neon was used as buffer gas which had a pressure of $P_{BG} = 8.0\,\text{kPa}$ (60 Torr).

ture. The centre structure in figure 2.17(b) arises, if both first-order sidebands are in resonance with the same excited state ($F' = 1$ or $F' = 2$) but different ground states ($F = 1$ and $F = 2$). When the laser frequency is stabilised to this centre structure, the frequency difference between the first-order sidebands approximately matches the ground states splitting frequency of about 6.8 GHz (see equation 2.19).
In the next step, in order to prepare a CPT resonance, the modulation frequency ν_{mod_1} is adapted such that the Raman detuning $\delta_R = 0$ (see section 2.1.1). However, stabilising the laser frequency to this zero crossing of the centre structure does not necessarily imply that the two-photon detuning δ_L is also zero. This is due to the fact that the centre structure in the in-phase signal consists of a superposition of two contributions.
The first contribution results when both first-order sidebands are in resonance with the transitions from the ground states ($F = 1$ and $F = 2$) to the excited state $F' = 1$ and form a Λ system for the CPT resonance preparation. Then, both sidebands are absorbed and a dip emerges in the transmission spectrum (see figure 2.4). The minimum of the single dip in the transmission spectrum results in a dispersive signal with a zero crossing at the maximum absorption ($\delta_L = 0$ for CPT resonance preparation with $F' = 1$) in

the derivative of the spectrum detected in the in-phase signal. The second contribution emerges when the first-order sidebands excite transitions from the ground states ($F = 1$ and $F = 2$) to $F' = 2$ and build a Λ excitation system with these two transitions. Then, a second dispersive signal appears in the in-phase signal which has its zero crossing when both optical transitions are in exact resonance ($\delta_L = 0$ for CPT resonance preparation with $F' = 2$).
The second contribution is separated from the first by the hyperfine structure splitting of the excited states ($F' = 1$ and $F' = 2$) which is about 815 MHz (see figure 2.2). Since the transitions from the excited states to the ground states have line widths of about 500 MHz (Doppler broadening) or even higher, if the transitions are broadened due to the use of a buffer gas (see section 4.1.3.1), the two dispersive signals overlap and the zero crossing of the resulting sum signal differs from the condition $\delta_L = 0$ for the CPT resonance preparation with either $F' = 1$ or $F' = 2$.

The third control loop uses the CPT resonance $n = 0$ to stabilise the microwave frequency to $1/2 \cdot \nu_0$ (see equation 2.40) by applying FMS. Therefore, a modulation signal with frequency $\nu_{MW_{FMS}} = 1.906\,\text{kHz}$ is superimposed on the microwave signal [14]. The modulation frequency $\nu_{MW_{FMS}}$ is typically higher than the CPT resonance line width of $n = 0$ and the modulation index is set to $M \leq 1$ (see second case in section 2.2.2). In this case the zero crossing of the quadrature signal is used for the control loop.
The third control loop is required to prevent a detuning Δ (see equation 2.45 and section 2.3.2) which could influence the accuracy of the magnetic field measurement (see section 4.2). A detuning can result from a shift of the CPT resonance positions due to, e.g., a buffer gas induced frequency shift (see section 2.3.1 and equation 2.27) or due to a drift of the microwave generator output frequency.
The control loop can not be operated at all sensor angles ϕ due to the angular dependence of the CPT resonance $n = 0$ (see section 4.1.7). Between the sensor angles of $60° < \phi < 120°$ and $240° < \phi < 300°$ the CPT resonance amplitude $n = 0$ is too small for the operation of the control loop and even vanishes at $\phi \approx 90°$ and $\phi \approx 270°$. As a result, the microwave control loop is not operated at these sensor angles [12]. In these cases, a detuning Δ has to be compensated by the CDSM-based compensation effect as will be further discussed in section 4.2.
Furthermore, this control loop is used to compensate a detuning introduced by the quadratic dependence of the CPT resonance positions on the external magnetic field (see section 4.1.6). Typically, for the CDSM operation, this correction is applied for magnetic field strengths larger than 10 µT.

The fourth control loop adjusts the second modulation frequency ν_{mod_2} to the external magnetic field induced shift $2 \cdot |\nu_{B_n}|$ (Zeeman control loop in figure 2.16). The control loop follows the zero crossing of the quadrature signal obtained by FMS. For CSES, a modulation frequency of $\nu_{B_{FMS}} = 7.102\,\text{kHz}$ [14] was selected which is typically larger

than the CDSM resonance line width (second case described in section 2.2.2). In contrast, for JUICE, modulation frequencies less or equal than the CDSM resonance line widths are preferable in order to keep the measurement accuracy (see third case described in section 2.2.2 and section 4.3).
Depending on the sensor angle ϕ either the CDSM resonance $n = 2$ or $n = 3$ is selected for the magnetic field measurement. An omni-directional magnetic field measurement is enabled by switching between these two resonances (see section 4.1.7 and [10]).
If disturbing frequency shifts cause a detuning between the single CPT resonances (see figure 2.14(b)), the control loop can be operated until a detuning Δ_{max}. Assuming identical single CPT resonance line shapes of the CDSM resonance, Δ_{max} is given by [1]

$$\Delta_{max} = \sqrt{3}/6 \cdot \Delta\nu_{CPT} \approx 0.289 \cdot \Delta\nu_{CPT} \,. \tag{2.47}$$

This limit results from the fact that the zero crossing of the CDSM resonance still exists but the sign of the slope reverses [1]. The proper operation of the control loop requires a zero crossing slope with steady sign. If a detuning exceeds Δ_{max}, the controller does not fail immediately but will drift to another frequency which fulfils the criteria for the operation of the control loop (zero crossing and a slope with required sign). The zero crossing frequency of the new setpoint does not match the external magnetic field induced shift $2 \cdot |\nu_{B_n}|$ and the measured magnetic field strength deviates from the external magnetic field value (see figure 4.29). Therefore, this limit also indicates the maximal detuning which can be accepted by the CDSM-based compensation effect without influence on the magnetic field measurement.

The fifth control loop keeps the temperature of the Rb vapour cell within a certain temperature range which enables the detection of the CDSM resonances with sufficient signal-to-noise ratio (see section 4.1.3.4 and [44]). For the sensor cell heating, a bifilar non-magnetic resistive heating wire is wound around the sensor cell on top of aluminium heater shells (see also section 3.3.1). A bidirectional pulse-width modulated AC current is applied to the heating wire [12] and a non-magnetic thermistor measures the sensor cell temperature.

2.4.3. CDSM Instrument Development

The development of a measuring device for space application typically follows a model philosophy [45]. Commonly, the development starts with a Laboratory Model (LM) which shows the capability of the instrument to measure within the laboratory environment. Afterwards, an Engineering Model (EM) of the instrument is build which has to be electrically representative to the later Flight Model (FM). In the next step, a Qualification Model (QM) is manufactured which is nearly identical to the later FM. The QM is used to qualify the instrument according to the specific requirements of this mission concerning its performance, e.g., in vacuum and at the environmental temperatures in space as well

as its ability to withstand the vibrations during launch. The last model is the FM which is the model that is integrated in the satellite and sent into space. Typically, a second instrument equal to the FM is build as back up called the Flight Spare (FS) model.
The CDSM underwent these development steps for the CSES mission and similarly these models will also be build for the JUICE mission.
Several evaluation and performance tests were accomplished with the different CDSM models which are summarised in chapters 3 and 4. The CDSM models can differ by the used components, number of realised control loops and the selected operational parameters (e.g., buffer gas pressure). As a consequence, the detected CPT resonances and the performance of the magnetometer can vary depending on the used model. The main differences between these models are summarised below.

2.4.3.1. CDSM Models for the CSES Mission

The four different CDSM models listed below were developed for the CSES mission.

- CSES LM
  The CSES LM was the first compact setup of the CDSM, but the laser unit, microwave unit and the control unit were still separated. The LM sensor housing was made of polycarbonate and contained a larger Rb vapour cell compared to the cell in the later CSES sensor models (see section 3.3.1 and appendix A.2). The cell had a length of $l = 36\,\text{mm}$ and a diameter of $d = 25\,\text{mm}$. Neon was selected as buffer gas at a pressure of $P_{BG} = 4.0\,\text{kPa}$ (30 Torr). The control loops to stabilise the laser frequency and the magnetic field control loop were realised. The design of the fibre connectors was adapted such that the connectors are non-magnetic. The typical fibres used for the LM were a graded-index fibre with a core diameter of $d = 50\,\mu\text{m}$ as outbound fibre and a step-index fibre with a core diameter of $d = 100\,\mu\text{m}$ as inbound fibre. The VCSEL was procured from ULM Photonics which afterwards ceased the production of VCSELs emitting at 795 nm. Therefore, the VCSEL for the later models were obtained from a different supplier (see section 3.2).

- CSES EM
  The CSES EM was the first model were all electronics units were miniaturised and integrated in one mounting frame. However,the microwave unit and the control unit were still realised on two individual printed circuit boards. The sensor design was reworked and included smaller dimensions of the Rb vapour cell (optical path length $l = 25\,\text{mm}$ and diameter $d = 12.7\,\text{mm}$). Two buffer gas pressures were commonly used: $P_{BG} = 2.0\,\text{kPa}$ (15 Torr) and $P_{BG} = 5.3\,\text{kPa}$ (40 Torr). PolyEther Ether Ketone (PEEK) and aluminium were tested as housing materials for the sensor unit. Finally, aluminium was selected (see section 3.3.1). The CSES EM sensor design

was used to perform first evaluation tests with respect to the upcoming missions (see section 3.3.2). The typical fibres used for the CSES EM were the same as for the CSES LM. The microwave control loop was realised for the first time but during the performance measurements with the CSES EM depicted in section 4, the control loop was not operated.

- CSES QM
  The CDSM QM consisted of one electronics board containing the laser, microwave and control units. With this model several qualification tests like thermal-vacuum or vibration tests were performed according to the requirements of the CSES mission. The buffer gas pressure was fixed to $P_{BG} = 5.3\,\text{kPa}$ (40 Torr). The typical fibres used for the QM were a graded-index fibre with a core diameter of $d = 50\,\mu\text{m}$ as outbound fibre and a step-index fibre with a core diameter of $d = 400\,\mu\text{m}$ as inbound fibre.

- CSES FM and FS
  The FM and FS are almost identical to the QM. A description of the FM can be found in section 2.4.2 and in reference [12].

2.4.3.2. CDSM Instrument Development for JUICE Mission

For the upcoming JUICE mission, the CSES electronics design is adapted for the requirements of this specific mission. The JUICE mission is a challenging mission due to the cold environment and the high radiation levels in the Jupiter system. For the JUICE mission, a new sensor unit is under development – the dual pass sensor (see section 3.3.3). Furthermore, the optical fibres used for the CSES mission are replaced by more radiation tolerant fibres (see section 3.4.2). Up to now a JUICE LM and JUICE EM of the CDSM have been developed.

3. The Optical Path of the Coupled Dark State Magnetometer

The optical path of the CDSM consists of a laser and a sensor unit as well as two optical fibres and a photodiode. All selected elements of the optical path have to fulfil the requirements according to the respective space mission. In general, the setup should be as light and compact as possible with low power consumption. Additionally, the used materials and components have to withstand the conditions in space.
The laser unit is discussed in section 3.1. For the excitation of CPT resonances, the CDSM requires a proper light source. Several laser types can be used. On the one hand the laser has to meet the requirements of the CPT resonance excitation but on the other hand it has to fulfil the demands for the use in a space application. At the moment the laser of choice is a Vertical-Cavity Surface-Emitting Laser (VCSEL) diode.
Especially, the operational lifetime and the reliability of the VCSEL is essential for space missions with lifetimes of several years. For the JUICE mission, an operational lifetime of more than 17 years had to be proven. Therefore, an endurance test with VCSELs from three different suppliers was performed. The results are summarised in section 3.2.
In section 3.3 the sensor unit is described in detail. First, a sensor unit was developed for the CSES mission. This sensor design is presented in section 3.3.1. A few selected evaluation and performance tests with this sensor unit are summarised in section 3.3.2.
A second sensor design is under development for the JUICE mission. Compared to the CSES sensor which is based on a single pass of the laser beam through the sensor cell, the laser beam in the new sensor design passes the sensor cell twice. Due to the dual pass of the laser beam through the sensor cell, the new sensor unit is named dual pass sensor. Its setup is described in section 3.3.3. The dual pass sensor is developed due to a discovered imbalance between the single CPT resonance line shapes, which build the CDSM resonance. This imbalance reduces the CDSM-based compensation of disturbing frequency shifts compared to the theoretically possible compensation limit (see section 4.2).
In the last section 3.4 of this chapter, the optical fibres are reviewed. Two different multi-mode fibres are utilised within the optical path. The outbound fibre is a graded-index multi-mode fibre and the inbound fibre is a step-index multi-mode fibre. The advantages and disadvantages using multi-mode fibres instead of single-mode fibres are discussed for the CDSM operation.

For the JUICE mission, the optical fibres have to withstand radiation levels up to 10 Mrad. In combination with the prevailing low temperatures during the transfer phase and in the Jupiter system, the selection of appropriate radiation-hard fibres is critical. In section 3.4.2 the most important considerations for selecting optical fibres are summarised.

3.1. Vertical-Cavity Surface-Emitting Laser

The name of the laser results from the fact that in contrast to most laser diodes, the cavity of the VCSEL is vertical to the mirror surface. Thus, the light is emitted typically from the top surface [46]. The whole laser structure only comprises several µm and the active region has just a few tens of nm [47]. The active region contains several quantum wells and is embedded between Bragg reflector mirrors which have a high reflectivity [48]. The high reflectivity mirrors are required because of the low gain per one round-trip. In section 3.1.1 the main properties and the performance of VCSELs for the CPT and CDSM resonance preparation are summarised. Further, the laser unit of the CDSM is described in section 3.1.2.

3.1.1. Properties and Performance

VCSELs can be single-mode or multi-mode devices. The CDSM uses a single-mode VCSEL. Single-mode devices typically have a lower output power compared to multi-mode devices. The emitted light power of a single-mode VCSEL is usually limited to a few hundred µW but this is enough to excite CPT resonances. The inner structure of inherently single-mode VCSELs are designed such that only the fundamental mode is amplified. This is typically achieved by small aperture sizes generated by proton implantation or oxide confinement [49]. Single-mode VCSELs are commonly single-mode within a certain laser current range. For higher laser currents, further modes can be present. It is also possible that VCSELs change the emitting mode over time which can result in polarisation jumps due to the fact that the laser modes can have a different polarisation state (see section 3.5).
The optical power of VCSELs increases linearly above the threshold current. The emitted laser light is typically linearly polarised and has a circular beam profile which allows simple coupling of the light field into optical fibres [48].
Since VCSELs are semiconductor diodes, the emitted laser frequency can be tuned by either changing the laser current or the laser temperature (see section 3.2).
Additionally, VCSELs are well suited for the CPT resonance excitation due to their high modulation bandwidth [34]. The modulation limit is characterised via the relaxation os-

cillation frequency [48]. At the relaxation oscillation frequency the modulation efficiency rapidly decreases.
Typically, the modulation is applied via a modulated supply current [50]. The benefit of the current modulation is that it is simple, it requires less power compared to, e.g., electro-optical modulators, the laser fields frequency components have a stable phase relation and the influence of laser frequency fluctuations is prevented, which would cause a broadening of the CPT resonances [17]. The drawbacks of this method are that theoretically an infinite number of sidebands is generated and that the ±nth-order sidebands have typically different amplitudes due to amplitude modulation [50]. The additional sidebands can influence the measurement accuracy via the light shift (see section 4.1.1.2). Dissimilar laser sidebands can result in asymmetric CPT resonance line shapes (see section 4.1.4) which can also affect the accuracy.
For the CDSM operation, a modulation signal with a frequency of $\nu_{mod_1} \approx 3.4\,\mathrm{GHz}$ is added to the laser current (see section 2.2.1). Additionally, the sideband amplitudes obtained by the second modulation step, which is superposed on the first modulation signal and is required to excite the CPT resonances $n = \pm 2$, increase with the energy in the first-order sidebands from the first modulation step (see section 4.1.4). Thus, ideally most of the energy should be contained within the first-order sidebands obtained by the first modulation step and not the laser carrier which does not contribute to the CPT resonance preparation. The energy distribution between the carrier and the sidebands depends on the modulation index M [37][51]. For low modulation indices, most of the energy is contained in the carrier. With an increasing modulation index the energy in the sidebands increases. Most of the energy is contained in the first-order sidebands at a modulation index of about 1.85. For higher modulation indices, the energy is transferred to higher-order sidebands and thus again lost for the CPT resonance preparation.

In order to determine the modulation index M, the amplitudes of the laser carrier and the first-order sidebands of the first modulation step were measured at the laser output with a Fabry-Pérot Interferometer (FPI). The FPI has a free spectral range of $\delta_{FSR} = 1\,980\,\mathrm{MHz}$ and a finesse of $F \approx 300$. Since the free spectral range is lower than the modulation frequency, an assignment of the lower and upper first-order sideband was not possible. Therefore, they are just labelled with sideband 1 and sideband 2. Nevertheless, this measurement gives a lot of information about the ideal operational current and temperature range of the laser.
In figure 3.1 the measurement results of the distribution of the laser intensity among the carrier and the first-order sidebands are summarised for a constant laser wavelength ($\lambda = const.$). To keep the laser wavelength constant, both laser current and laser temperature were adapted for this measurement. For laser currents below $I_L < 2.4\,\mathrm{mA}$ the second-order sidebands were already clearly present and an assignment of the sidebands was no longer possible.

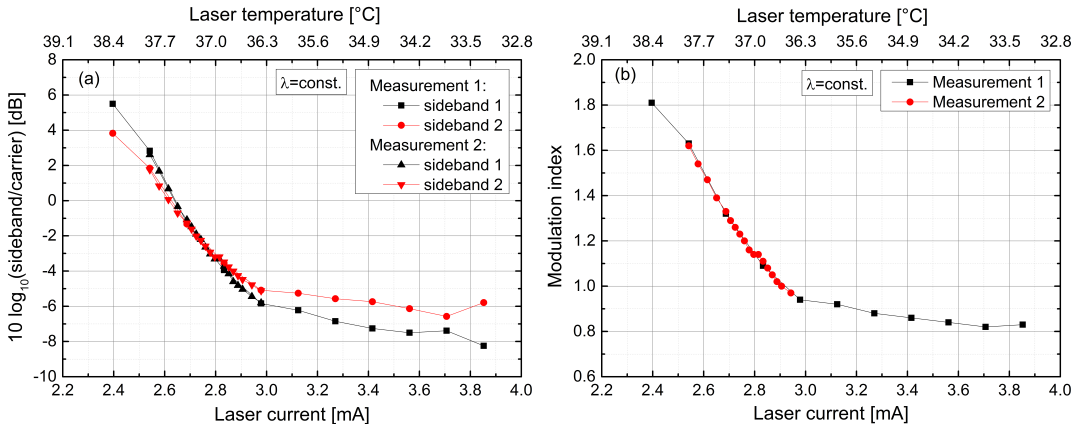

Figure 3.1.: Intensity ratio between the laser carrier and the first-order sidebands for the case of constant laser wavelength ($\lambda = const.$): The measurement was performed with the CSES QM electronics (see section 2.4.3.1) with the maximal possible microwave power level of $P_{MW} = -5.4\,\mathrm{dBm}$. Figure (a) shows the ratios at a constant laser wavelength for different laser current and temperature combinations. Therefore, both, the laser current and the laser temperature, were adapted. In (b) the intensity ratios between the carrier and the mean intensity in the first-order sidebands – determined from the measurement shown in (a) – were used to match modulation indices.

As can be seen in figure 3.1(a), the sideband 1 had a higher amplitude compared to sideband 2 for laser currents $I_L < 2.75\,\mathrm{mA}$. At approximately $I_L = 2.75\,\mathrm{mA}$, both sidebands had the same amplitude. For higher laser currents, the behaviour changed and sideband 2 had a higher amplitude compared to sideband 1.

In figure 3.1(b) the measured intensity ratios between the laser carrier and its sidebands from figure 3.1(a) were used to approximate modulation indices. Therefore, the ratio $\bar{I}_1/I_0$, where $\bar{I}_1$ is the mean intensity of the first-order sidebands and I_0 is the intensity of the carrier [50], was compared to the ratio of the squared amplitudes of the Bessel functions J_1^2/J_0^2 where J_1 is proportional to the amplitude of the first-order sidebands and J_0 to the amplitude of the carrier [52].
As shown in figure 3.1(b), the modulation indices decreased for higher laser currents and lower laser temperature. The determined modulation indices were less than one for laser currents $I_L > 2.9\,\mathrm{mA}$ and increased up to a value of about 1.8 for a laser current of $I_L = 2.4\,\mathrm{mA}$. With the criterion defined above, the magnetometer should be ideally operated at laser currents lower than 2.4 mA. However, for laser currents lower than 2.4 mA, the intensities of the sidebands are unbalanced which can affect the symmetry of the CPT and CDSM resonance line shapes (see section 4.1.4) and the light shift (see section 4.1.1.2). For equal sideband strengths, the CPT resonance line shapes should be symmetric, if the transitions of the Λ system have the same transition strengths (see section 4.1.4).

Therefore, a laser current around 2.75 mA, where both first-order sidebands have the same amplitude, could be preferable for the operation of the magnetometer. Although at this laser current value the modulation index is lower ($M \approx 1.2$).

In figure 3.2 the influence of the laser temperature and the laser current on the modulation behaviour of the laser are discussed separately.

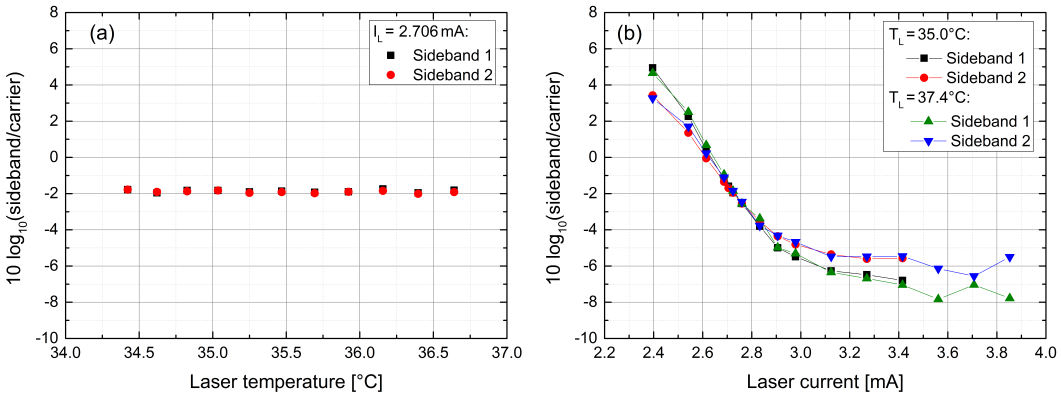

Figure 3.2.: Intensity ratio between the laser carrier and the first-order sidebands: The measurements were performed with the same setup as in figure 3.1. In (a) the dependence of the intensity ratio on the laser temperature is depicted. No change was detected within the measured temperature range. In (b) the ratios are depicted for different laser currents at two different laser temperatures ($T_L = 35.0°C$ and $T_L = 37.4°C$). The laser current had a distinct influence on the modulation properties. At a laser current $I_L \approx 2.7$ mA the first-order sidebands had approximately the same amplitude.

In figure 3.2(a) the laser temperature was varied between $T_L = 34.4°C$ and $T_L = 36.6°C$ at a constant laser current of $I_L = 2.706$ mA. The intensity ratio measurements between the laser carrier and the first-order sidebands revealed no dependence on the laser temperature within the measurement range.

In 3.2(b) the dependence of the intensity ratio on the laser current is shown for two fixed laser temperatures: $T_L = 35.0°C$ and $T_L = 37.4°C$. The characteristic was nearly identical to the one shown in figure 3.1. Thus, the change of the modulation index mainly depends on the laser current. In reference [50] the increase of the modulation efficiency of the laser at lower laser currents was explained by a resonant excitation due to a coincidence of the relaxation oscillation frequency with the modulation frequency.
The influence of the laser parameters on the CPT and CDSM resonances is further discussed in section 4.1.4.

3.1.2. Laser Unit of the CDSM

The main element of the laser unit is the VCSEL. The VCSEL chip is mounted in a TO46 housing. The supply current and the superimposed microwave signal are guided by a microwave suited coaxial cable to the VCSEL housing. The laser temperature is set and measured by a thermoelectric cooler and a thermistor (see section 2.4.2). The emitted laser light is collimated by an aspheric lens with a high numerical aperture $NA = 0.4$ and a focal length of $f = 6.24\,\mathrm{mm}$. The collimated laser light is coupled into the outbound fibre with a fibre coupler. The fibre coupler contains a lens with a focal length of $f = 11\,\mathrm{mm}$ and a numerical aperture of $NA = 0.25$. Coupling efficiencies better than 80% are commonly achieved when coupling into the outbound fibre with a core diameter of $d = 50\,\mu\mathrm{m}$.
At the moment the laser setup is an independent unit that is mounted on the frame of the electronics box (see figure 2.15). A further miniaturisation of the laser unit is planned using a VCSEL with an integrated thermoelectric cooler. The benefit of the integrated thermoelectric cooler is that the laser chip is temperature controlled directly and not the complete housing as in the current laser unit design. Thus, a reduction of the required heating power is expected. However, the modulation capability of the laser might be reduced, since longer bonding wires between the housing and the laser chips are required due to the mounting of the chip on top of the thermoelectric cooler.

3.2. Laser Endurance Test with VCSELs

The following section corresponds to a publication by
M. Ellmeier, C. Hagen, J. Piris, R. Lammegger, I. Jernej, M. Woschank, W. Magnes, E. Murphy, A. Pollinger, C. Erd, W. Baumjohann, L. Windholz
in Applied Physics B, 124(2):18, January 2018 [43].

The author of this thesis was responsible for

- main parts of the electro-optical characterisation
- parts of the laser integration and adjustment for the long-term vacuum test
- main part of the analysis and interpretation of the test results
- authorship of the manuscript.

The contributions of the co-authors are listed below:

- C. Hagen: integration of the lasers for long-term test, data collection and preparation
- J. Piris: integration of the lasers in long-term test, operation and monitoring of the

endurance test in the vacuum chamber
- R. Lammegger: design of experimental setup of the vacuum test, integration of lasers in vacuum chambers, preparation and planning of test, supervision, laboratory, funding
- I. Jernej: part of the theory and calculation of the acceleration factors, preparation and planning of test
- M. Woschank: parts of the electro-optical characterisations.

All other authors contributed by discussion, supervision or/and funding.

3.2.1. Abstract

We performed an endurance test with single-mode Vertical-Cavity Surface-Emitting Lasers (VCSEL) under vacuum condition and increased operational parameters (laser current and laser temperature) to accelerate the ageing of the lasers. During the endurance test the emitted polarisation-dependent and polarisation-independent optical light power from the lasers were detected. Additionally, electro-optical characterisations including measurements of the combination of laser current and laser temperature to excite the ^{87}Rb D_1 transition ($\lambda = 795\,\text{nm}$), the current and temperature tuning coefficients, laser line width, threshold current and the polarisation ellipse were performed for the aged lasers. The test was started with a number of twelve VCSELs consisting of four lasers each from three different suppliers.
The ageing behaviour of VCSELs was investigated with respect to the development of a new optical magnetometer prototype for space missions with a mission duration of up to 17 years. Only a limited change of the electro-optical parameters can be tolerated by the instrument design over the mission duration.
The endurance test and the electro-optical characterisations revealed clear differences in the ageing behaviour of the three suppliers. Lasers from one supplier showed that they can be operated for more than 17 years under vacuum conditions without major degradation of their operational parameters.

3.2.2. Introduction

In the last two decades laser diodes have become important in experimental science. Especially Vertical-Cavity Surface-Emitting Lasers (VCSEL) have a versatile field of application. Compared to other laser diodes VCSELs have low production costs, high modulation efficiency and their circular beam profile allows simple fibre coupling [48]. Therefore, they are widely used in optical fibre communication, in spectroscopy [34] and in consumer elec-

tronics.
VCSELs are also interesting for space applications such as for data communications inside of satellites or new scientific instrument developments [1]. For this application, it has to be demonstrated that VCSELs can tolerate the harsh conditions in space and also provide the required lifetime of several years for space missions.
In this paper we summarise the results of a long-term endurance test under vacuum condition which was accomplished at the Optics- and Opto-Electronics Laboratory (OOEL) [53] of the European Science and Technology Centre (ESTEC) with VCSELs from three different manufacturers. The tested laser diodes were all single-mode VCSELs emitting at a wavelength of 795 nm hermetically sealed in a TO 46 package. The test was carried out under vacuum condition to enable testing as close as possible to the environmental conditions in space. For example, leakages in the sealing of the lasers could occur which would cause a loss of the package atmosphere and thus could have an influence on the lifetime [54].
This test was carried out in the context of the development of a new space magnetometer prototype, the Coupled Dark State Magnetometer (CDSM) [1] [14]. The CDSM is a type of coherently optically-pumped magnetometer. Its functional principle is based on the measurement of the Zeeman energy level shift of the ground state within the Zeeman manifold of the ^{87}Rb D_1 hyperfine structure caused by an external magnetic field. This energy level shift is measured by using a quantum interference effect called Coherent Population Trapping (CPT) [3] [18]. From this shift the external magnetic field can be calculated by means of the Breit-Rabi formula [26].
A prototype has been developed by the Institute of Experimental Physics of the Graz University of Technology (TUG) and the Space Research Institute (IWF) of the Austrian Academy of Sciences.
The first demonstration of this new magnetometer in space will take place aboard the Chinese Seismo-Electromagnetic Satellite (CSES) mission in spring 2018.
The CDSM was also selected for the JUpiter ICy Moon Explorer (JUICE) mission of the European Space Agency (ESA) which will be launched in 2022. This mission will visit the Jovian system and will investigate, among others, the magnetic field around Jupiter's moon Ganymede, which will help studying its inner structure including a presumed subsurface ocean.
For the development of the CDSM, VCSELs are used because their properties fit the requirements for the preparation of the CPT effect and also fulfil those for the use in space applications like small size, low power consumption and robustness. For the excitation of the CPT effect we use a single mode VCSEL emitting a carrier wavelength of $\lambda = 794.979\,\text{nm}$ (vacuum wavelength) [28]. On this carrier frequency we apply a modulation frequency of 3.417 GHz via the power supply current of the VCSEL, which corresponds to the half of the ground state splitting frequency of ^{87}Rb.
Therefore, one of the biggest advantages of the VCSEL for our application is its high modulation ability of several GHz. However, a disadvantage of this laser type for the use

in CPT resonance excitation applications can be its typically higher laser line width of about 50-100 MHz compared to, e.g., DFB lasers (2-5 MHz). The laser line width should be less or equal to the homogeneous line width of the excited optical resonance to allow an efficient preparation of the CPT effect [55] [56]. A further drawback is its high current tuning coefficient (see table 3.5). Compared to edge emitters this coefficient is about a factor of ten higher. Thus, current noise stemming from the laser's constant current source are more efficiently translated into frequency noise leading to a higher noise level in the magnetic field measurement.
For the JUICE mission it is important to prove that the VCSELs can operate for several years (up to 17 years) under vacuum condition and retain their optical properties required for a proper function of the CDSM. Therefore, the VCSELs were artificially aged under vacuum condition to investigate their life time and repeatedly electro-optically characterised in the course of the test [57].
In section 3.2.3 a short summary of VCSEL's reliability testing is given. Sections 3.2.4 and 3.2.5 summarise the test setup and the most important results.

3.2.3. VCSEL Reliability and Test Parameters

In general, there are several reasons for failure of VCSEL diodes. Commonly, they are divided into failures which cause the diodes to malfunction suddenly and those that cause a gradual slow deterioration of the laser properties like optical power [58], which is called wear-out.
Abrupt failure is caused, for example, by growth of dislocation networks often described as dark line defects due to material defects, Electro Static Discharge (ESD) or mechanic damage [59][60].
In general, the lifetime of a VCSEL significantly depends on its parameters of operation [61]. High junction temperatures and high current densities -especially in the active region- reduce the lifetime of a VCSEL. Thus, by increasing the VCSEL's current and temperature compared to their typical operational values I_{op} and T_{op}, the lasers ageing can be accelerated and the VCSELs' behaviour of several years of operation can be studied within a much shorter time. Depending on the chosen test parameters and the design of the VCSEL the lasers are aged at different rates. The factor by which the ageing process is increased is called acceleration factor AF. It is defined as the ratio of the time-to-failure at nominal operation conditions TTF_{op} to that at accelerated operational conditions TTF_{test}.
The acceleration factor reached for the VCSELs is calculated according to following formula [61]:

$$AF = \frac{TTF_{op}}{TTF_{test}} = \frac{I_{test}}{I_{op}^{n} exp(\frac{E_A}{k_B}(\frac{1}{Tj_{op}} - \frac{1}{Tj_{test}}))}. \tag{3.1}$$

Here I_{test} is the applied laser current during the endurance test and I_{op} the typical (nominal) operation current value in our magnetometer application. The exponent n as well as the activation energy E_A are empirically determined by the manufacturer during their reliability testing. k_B is the Boltzmann constant, T_{jop} is the junction temperature for nominal operation and Tj_{test} the junction temperature for the test temperature. However, the junction temperature of the VCSEL cannot be measured directly and is calculated via the relation [48]:

$$Tj_x = T_x + R_{th} \cdot (I_x V_x - P_x). \tag{3.2}$$

The junction temperature depends on the ambient temperature T_x and the heating of the laser chip by electrical power dissipation during its use. The heat that is generated by the laser itself is calculated with the thermal resistance R_{th} and the difference between the introduced electrical power (laser current I_x times laser voltage drop V_x) and the emitted optical power P_x. For the calculation of the acceleration factor the parameters n, E_A and R_{th} were provided by the VCSEL manufacturers [57].
The nominal operational parameters (I_{op} and T_{op}) of each VCSEL were determined during the first electro-optical characterisation. The choice of the operational current was based on the required optical power P_x for the operation of the magnetometer. The corresponding laser temperature T_{op} was determined in order to achieve a wavelength of $\lambda = 794.979\,\text{nm}$ and varies for each laser which influences the obtained equivalent operating life time τ_{eop} (see table 3.2).
The test was planned with four VCSELs at a time from three different suppliers. The abbreviations for the different suppliers which will be used further on and the corresponding part numbers as well as the operational currents I_{op} and the applied current during the endurance test I_{test} are stated in table 3.1.

Table 3.1.: Part numbers, operational laser currents I_{op} as well as laser current during the endurance test I_{test} for the used lasers.

Supplier	Part number	I_{op} [mA]	I_{test} [mA]
A	VIX-795S-0000-G002	1.9	1.9
B	V795-2222-001	2.9	3.0
C	APM2101013300	3.5	4.0

The test duration was first one year and then extended further for two months. The ambient temperature T_x during the vacuum test was set to 70°C, which was the highest possible temperature of the test setup. The applied laser current I_{test} for VCSELs from supplier B and C was set to their maximum rating according to the data sheet. The reached equivalent operating life time τ_{eop} of each tested VCSEL and the mean acceleration factor AF_{mean} can be found in table 3.2.

3.2.4. Laser Endurance Test Description

The main goals of the laser endurance test were to investigate the ageing behaviour of VCSELs under vacuum condition and to determine if the optical and electrical properties of the laser degrade over the achieved lifetime. All used VCSELs are single mode lasers emitting at 795 nm which are hermetically sealed in a TO 46 package.
Before the lifetime test twelve VCSELs in total (four each from supplier A, B and C) were selected and electro-optically characterised. For the vacuum test, the selected lasers were mounted in two separate vacuum chambers at the Optics- and Opto-Electronics Laboratory (OOEL) of the European Science and Technology Center (ESTEC) [53]. Half of the lasers (two from each supplier) were mounted in one vacuum chamber (see figure 3.3) where they remained permanently for the whole vacuum test duration, while the laser in the second chamber were removed twice for electro-optical characterisation.

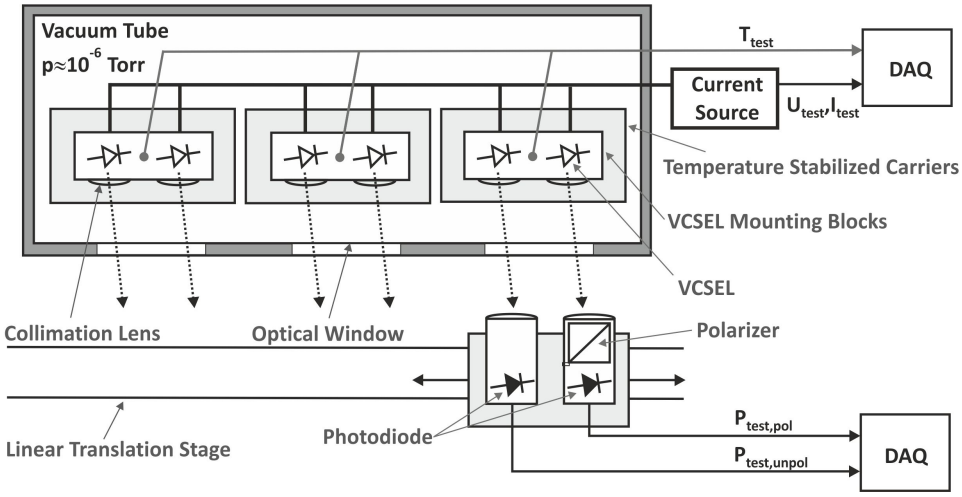

Figure 3.3.: Optical and electrical setup of the endurance test under vacuum condition: The lasers were mounted in mounting blocks on temperature stabilised carriers. The mounting blocks contained lenses for the collimation of the laser beams and a Pt1000 element to measure the temperature. Once per hour the temperature T_{test}, current I_{test} and voltage U_{test} of the lasers as well as the emitted optical power was measured. The polarisation-independent $P_{test,unpol}$ and the polarisation-dependent optical power $P_{test,pol}$ was detected outside of the vacuum chamber by two photodiodes and one additional polariser. Both photodiodes were moved between the windows by a linear translation stage.

Two VCSELs each were assembled in mounting blocks which contained two biconvex lenses in order to form two collimated Gaussian laser beams and a Pt1000 element to measure the temperature of the mounting blocks individually. The mounting blocks were fixed inside the vacuum chamber on temperature stabilised carriers. The mean temperature during the test was (65.6 ± 2.0)°C in vacuum chamber 1 and (66.1 ± 1.8)°C in vacuum

chamber 2. Each VCSEL was supplied with its own custom-made current source providing the predefined currents (see section 3.2.3).
The vacuum chambers have several optical windows which allowed the detection of the optical power outside of the chambers via photodiodes. One photodiode measured the total laser power while the other photodiode detected the laser polarisation-dependent optical power with the help of an additional linear polariser placed in front of the photodiode. Thus, changes in the orientation of the polarisation plane like the unwanted arbitrary polarisation jumps could be measured. All VCSEL were mounted in such a way that the maximum of the linear polarisation state was measured. For these measurements, the two optical detectors were moved from one optical window to the next by a linear translator. Over the whole test duration the laser current I_{test}, laser voltage U_{test}, temperature T_{test}, polarisation-dependent laser power $P_{test,pol}$ and polarisation-independent laser power $P_{test,unpol}$ were measured and logged by a data acquisition system once per hour. The recorded laser power of each laser as a function of test duration is presented in section 3.2.5.1.
For all lasers, the selected electrical and optical parameters were measured before and after the accelerated ageing test (preliminary and final electro-optical characterisation). Additionally, VCSELs mounted in the vacuum chamber number 1 were characterised twice during the accelerated ageing test (intermediate characterisation (IC)). These characterisation measurements were performed outside the vacuum chamber on an optical bench. Therefore, the VCSELs were dismounted from the vacuum chamber mounting blocks and assembled into a laser setup which allowed changing and stabilising both the laser temperature (within ± 1 mK) and laser current. The laser temperature was measured with a Pt1000 element using a four-wire sensing schema and was set with the help of a thermoelectric cooler driven by a temperature control unit (feedback loop). The laser current could be changed by an adjustable constant current source and was monitored with a precision multimeter to an accuracy of ± 10 nA.
The following measurements were performed during the electro-optical characterisation: laser current and temperature combinations for achieving a constant wavelength of $\lambda = 794.979$ nm (vacuum wavelength), current tuning coefficient, temperature tuning coefficient, laser line width, threshold current and polarisation ellipse.
The determination of the emitted laser frequency was calibrated by measuring the resonant excitation inside a glass cell filled with isotopically pure ^{87}Rb. To obtain resonant excitation of the rubidium atoms, a sawtooth-shaped modulation was applied onto the laser current to sweep the laser frequency. During the sweep the transmitted laser light through the cell was measured by a photodiode. The detected photodiode signal was depicted with an oscilloscope showing the ^{87}Rb D_1 spectrum. The ^{87}Rb ($5^2S_{1/2}$ F=2 $\leftrightarrow$ $5^2P_{1/2}$ F=1) transition was used as reference to set the laser frequency. At certain laser current values within the operational range of the laser, the laser temperature was adapted such that this selected transition was excited and the corresponding laser current and temperature values were read.

At the same measured laser current-temperature pairs, also the current tuning coefficient $\Delta\nu/\Delta I$ and the temperature tuning coefficient $\Delta\nu/\Delta T$ were determined. For the measurement of the current tuning coefficient the laser temperature was fixed and the difference of the laser current ΔI required to change the laser frequency from the ^{87}Rb ($5^2S_{1/2}$ F=2 $\leftrightarrow$ $5^2P_{1/2}$ F=1) transition to the ^{87}Rb ($5^2S_{1/2}$ F=1 $\leftrightarrow$ $5^2P_{1/2}$ F=2) transition measured. With the known frequency spacing ($\Delta\nu = 7.650\,\text{GHz}$) between these two transitions, the current tuning coefficient $\Delta\nu/\Delta I$ was calculated.
For the measurement of the temperature tuning coefficient $\Delta\nu/\Delta T$ a similar approach was used. Now, the laser current was fixed and the difference in laser temperature required to change the laser frequency between these two transitions was measured. Again from the known frequency spacing $\Delta\nu$ the temperature tuning coefficient $\Delta\nu/\Delta T$ was calculated.
The laser line width was measured with the help of an optical spectrum analyser. The used device has a free spectral range of $\delta_{FSR} = 1\,980\,\text{MHz}$, finesse of $F \approx 300$ and a thus a resolution of approximately $\delta\nu = 7\,\text{MHz}$. A measurement uncertainty of about $\pm 5\,\text{MHz}$ could be obtained for the laser line width.
The threshold current was determined by making use of the appearance of the speckle pattern when increasing the laser current from zero to above the threshold current. If the laser is operated at a laser current below the threshold current, the laser diode emits virtually incoherent light. At the threshold current the laser starts emitting coherent light and a speckle pattern becomes visible on a rough surface. With the help of an infrared sensitive camera the appearance of the pattern was determined by slowly increasing the laser current from zero up to the threshold current. With this method the threshold current can be determined with an accuracy of $\pm 0.1\,\text{mA}$.
The polarisation ellipse of the linear polarisation state of the laser light was also investigated. The maximum and the minimum of the ellipse were determined with the help of a Glan-Thompson polariser and a power meter.
The obtained results of the electro-optical tests are presented in section 3.2.5.2.

3.2.5. Test Results

3.2.5.1. Long-Term Behaviour of Optical Laser Power under Vacuum Condition and Accelerated Ageing

In total the VCSELs in chamber 1 were operated for 344 days and the VCSELs in chamber 2 for 414 days. For the lasers in vacuum chamber 1, the first intermediate characterisation (1^{st} IC) took place after 114 days and the second one (2^{nd} IC) was carried out after 288 days. Chamber 2 was not opened during the entire test duration.
During the test, all lasers in both chambers were switched off for maintenance for one week each (chamber 1: after 114 days and 275 days, chamber 2: after 147 days and 308

days).
For the illustration of the measurement results in Figure 2, the measured data were smoothed by using a moving average over 20 readings because the raw data were noisy due to the applied measurement method with the linear translator (see section 3.2.4). This artificial noise resulted from slight variations in the position of the detectors and was not caused by the VCSELs itself.
The lasers were labelled with their respective supplier letter (A, B or C) and additionally the two lasers from each supplier which were mounted in vacuum chamber 1 got the numbers 1 and 2 and the two further lasers from the same supplier installed in vacuum chamber 2 received the numbers 3 and 4. Further, the label of the initially mounted lasers ends with a number 1 and the replaced lasers with a number 2. For example, laser number 2 from supplier A which was initially mounted in vacuum chamber 1 was named A2.1 and was replaced by laser A2.2. The Figure 2 includes both the polarisation-independent and polarisation-dependent laser power, which is marked with an additional suffix p.
The laser failure criterion was defined as the reduction of the measured laser power below 50% of its initial value P_I at T_{test}. This power reduction can be tolerated by the setup and allow a proper operation of the magnetometer.
All lasers showed an initial reduction of their optical power when the laser temperature was increased to T_{test} and the vacuum established in the chambers. Within the first few hours the laser power increased again and stabilised. As initial value the optical power after this transient behaviour was taken.
In the course of the intermediate characterisations the functioning lasers were optically and electrically measured and the failed lasers replaced.
The discontinuities of the optical power after the intermediate characterisations in figure 3.4 resulted from the complete dismounting of the lasers from the mounting blocks and a slightly different alignment after reassembly. Due to this discontinuities, the relative changes in optical power after the intermediate characterisation were related to the new starting value after the intermediate characterisation.

In figure 3.4 (a) and (b) the results of the vacuum test for supplier A are summarised. Laser A1.1 showed only minor relative changes of its optical power (about 3%) during the test phases. In contrast the optical power of laser A2.1 started degrading immediately after mounting in the vacuum chamber and failed on the second day of operation in vacuum. Laser A2.1 was replaced during the 1^{st} IC by laser A2.2. The optical power of laser A2.2 behaved quite stable until the last test month where its optical power reduced by about 5%.
Also the laser power of A3.1 only showed reduction of its optical power by about 3% until the 350^{th} day of operation in the vacuum test. Then the laser power decreased faster until the 405^{th} day (in total about 20%) and revealed a polarisation jump. The polarisation jump is visible as a leap in the laser polarisation-dependent optical power and no change in the polarisation-independent power. The polarisation of laser A4.1 revealed in total two

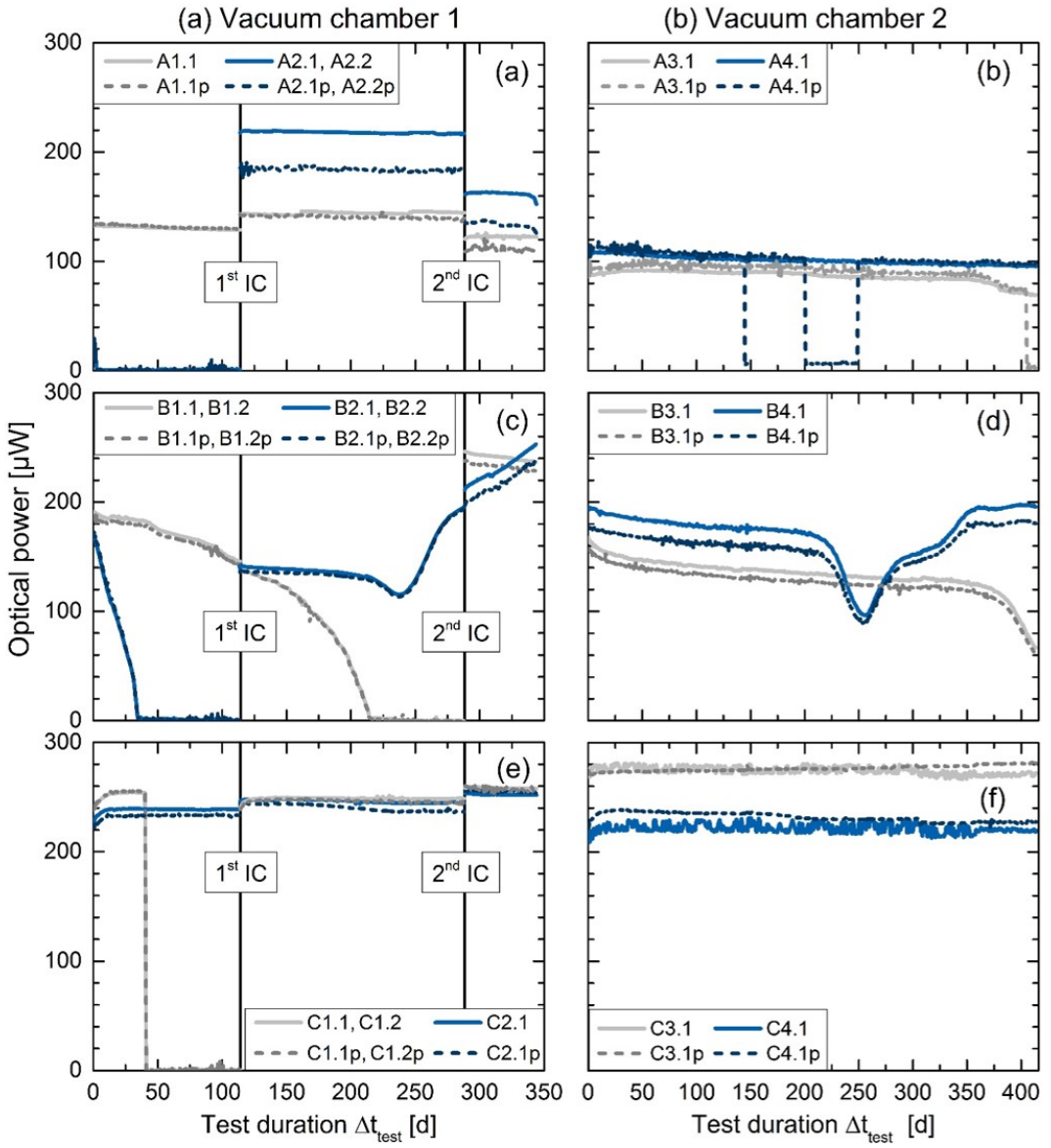

Figure 3.4.: Behaviour of the optical power of all tested lasers during the accelerated endurance test under vacuum condition over the test duration Δt_{test}: The left column contains the results from vacuum chamber 1 and the right column from vacuum chamber 2. Figures (a) and (b) show the long-term behaviour of the optical power of lasers from supplier A, (c) and (d) from supplier B and (e) and (f) from supplier C

polarisation jumps within the whole test period. The first polarisation jump appeared shortly before the first switch off for maintenance after 144 days of operation. After switching-on the lasers again the original polarisation plane was restored. The second polarisation jump appeared after 200 days and returned to its initial polarisation plane on

the 249^{th} day (see figure 3.5). The change of the polarisation state in figure 3.5 took up to 20 h as well as the return to the original polarisation state. The change of the polarisation state of laser A3.1 required as well 20 h. On the contrary, the first polarisation jump of laser A4.1 took only 3 h.
In total, laser A4.1 exhibited a gradual decrease of its optical power by about 9% by the end of the test.

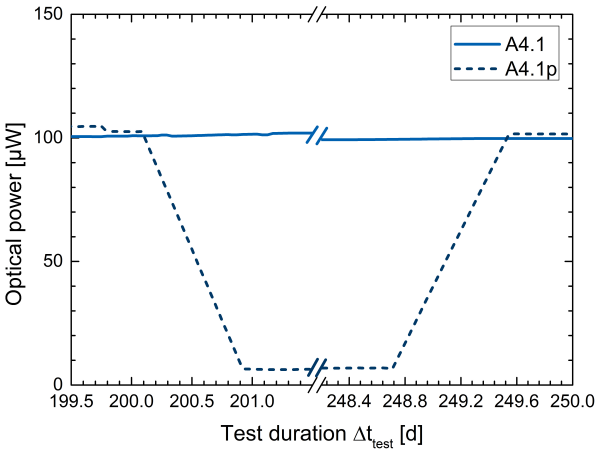

Figure 3.5.: Polarisation jump detected in the run of the optical power of laser A4.1: The polarisation-dependent power was reduced but the polarisation-independent power was unchanged. After 49 days the original polarisation state was restored.

In figure 3.4 (c) and (d) show the long-term behaviour of the optical power under vacuum condition for supplier B. Laser B2.1 started degrading right from the test start and failed after 21 days of operation in the vacuum chamber. It was replaced by laser B2.2 which showed an unusual reduction of its optical power (−16% of initial power $P_I = 142\,\mu W$) with a subsequent increase (+34%) until the 2nd IC. After the 2nd IC the optical power increased further by 20% (initial power after 2nd IC $P_I = 211\,\mu W$). Laser B1.1 gradually degraded within 174 and failed after the 1st IC. The replacement laser B1.2 was operated for 56 days under vacuum and showed a reduction of its optical power of 4%. The optical power of the laser B3.1 decreased over the whole test duration and reduced severely within the last test month. On the 403^{th} day its output power reached values below the defined laser failure limit of 50% initial power and even reduced further to 60% initial power at the end of the test. Laser B4.1 also revealed a significant drop in laser power. The optical power dropped from its initial value of $P_I = 194\,\mu W$ below the failure criterion after 254 days of operation and reached its minimum of 95 µW, which is just below the failure criterion (total reduction of 49.5%). Then the laser power increased again until the end of the test to 196 µW, which is even above the initial value.
Since lasers B4.1 and B2.2 showed a similar laser power variation as laser B3.1, it could be possible that also the optical power of laser B3.1 recovered again but as the test was

not continued further, there is no way of telling.
In figure 3.4(e) and (f) the behaviour of the optical power of lasers from supplier C are outlined. All lasers of supplier C had in common that the optical power started to increase after the beginning of the endurance test (2-7% of P_I) before it stabilised after several days. Therefore, an additional burn-in would help to improve the stability of the optical output power. Laser C1.1 showed proper function until it suddenly failed after 40 days. The failed C1.1 laser was replaced during the 1^{st} IC by laser C1.2 and was sent back to its manufacturer for further investigations.
The variations of the optical power for lasers C2.1 and C1.2 were within 1% of their initial power.
The noise of the polarisation-independent optical power of lasers C3.1 and C4.1, which is not seen in the measurement of the polarisation-dependent optical power, is assumed to be caused by a random misalignment of the laser beam with respect to the optical detector in connection with the repeatedly moved linear translation stage. First both lasers C3.1 and C4.1 showed the typical increase in optical power. Then the optical power of laser C3.1 gradually reduced to approximately its initial value and the optical power of laser C4.1 remained 3% above its initial value after the end of the test.

After the completion of the endurance test the equivalent operating life time τ_{eop} of the tested lasers was calculated with the mean acceleration factor AF_{mean} and the test duration Δt_{test} according to

$$\tau_{eop} = AF_{mean} \cdot \Delta t_{test}. \tag{3.3}$$

For the calculation of the mean acceleration value AF_{mean}, first the acceleration factor of each data point AF_i according to equation 3.2 was calculated and then averaged. In table 3.2 the maximum equivalent operational life time τ_{eop} of each VCSEL is stated which would be reached based on the measurements at the end of this endurance test. Most of the lasers were still working within the defined pass/fail criterion (>50% of initial output power P_I). For those lasers which failed during the test, the maximum reached lifetime was calculated up to the time when they failed. The maximum equivalent operating lifetime τ_{eop} in table 3.2 mainly varies for each VCSEL due to the different operating temperatures T_{op} required to reach the defined laser frequency at the defined operating current I_{op}. Thus, also the maximum equivalent operating lifetime is different for each laser.

3.2.5.2. Test Results from Electro-Optical Characterisations

In this section the results from the electro-optical characterisations are discussed. No results for lasers A2.1, B2.1 and C1.1 are presented in this section, since they have only been characterised once due to their failure prior to the first intermediate characterisation point, and therefore no information on their ageing behaviour could be obtained. The

Table 3.2.: Calculated maximum equivalent operating life time τ_{eop} for all tested lasers at the end of the accelerated ageing test: the factor AF_{mean} is mainly influenced by the different operating temperatures Top of each laser. The * symbol marks the maximum test duration until failure. However, lasers B3.1 and B4.1 were still operating at the end of the test.

Laser	T_{op} [°C]	Δt_{test} [d]	AF_{mean}	max.τ_{eop} [a]
A1.1	24.2	344	21.7	20.5
A2.1	24.2	2*	21.6	20.5
A3.1	26.5	414	17.5	20.5
A4.1	27.3	414	16.3	20.5
A2.2	22.3	230	20.7	20.5
B1.1	19.2	174*	7.1	20.5
B2.1	21.6	21*	5.0	20.5
B3.1	21.3	403*	6.5	20.5
B4.1	22.3	254*	6.5	20.5
B1.2	25.1	56	7.7	20.5
B2.2	28.5	230	6.8	20.5
C1.1	35.1	40*	19.6	20.5
C2.1	37.4	344	16.3	20.5
C3.1	32.2	414	19.4	20.5
C4.1	34.9	414	15.5	20.5
C1.2	38.7	230	20.5	20.5

lasers B3.1 and B4.1 showed a reduction of their optical power of more than 50% but were still working at the time of the electro-optical characterisation and therefore they were also tested. Additionally, lasers C3.1 and C4.1 are not mentioned in the discussion, since a mishandling of the lasers after the endurance test caused a failure of the lasers.
In figure 3.6 an example of the measured laser current and laser temperature combinations to set the wavelength of the ^{87}Rb ($5^2S_{1/2}F = 2 \leftrightarrow 5^2P_{1/2}\ F = 1$) transition as well as in the measurements of the current tuning coefficient are shown for laser A2.2. Both figure 3.6(a) and (b) contain the measurement results from the preliminary ($\tau_{eop} = 0\,\text{a}$), intermediate ($\tau_{eop} = 9.9\,\text{a}$) and the final characterisation ($\tau_{eop} = 13.1\,\text{a}$) of laser A2.2.

In figure 3.6 (a) the laser temperature T_{op} of laser A2.2 showed in total a reduction of ΔT_{op}=(-3.1 ± 0.2)°C between the preliminary and the final characterisation. Also the current tuning coefficient changed for the aged laser by (24 ± 16)% (see Figure 4 (b)). Similar measurements have been carried out for all tested lasers. The change detected in the operational laser temperature T_{op} at I_{op} and the current tuning coefficient are summarised in table 3.5 in the appendix. The change of T_{op} at I_{op} for all lasers is additionally shown in figure 3.7.

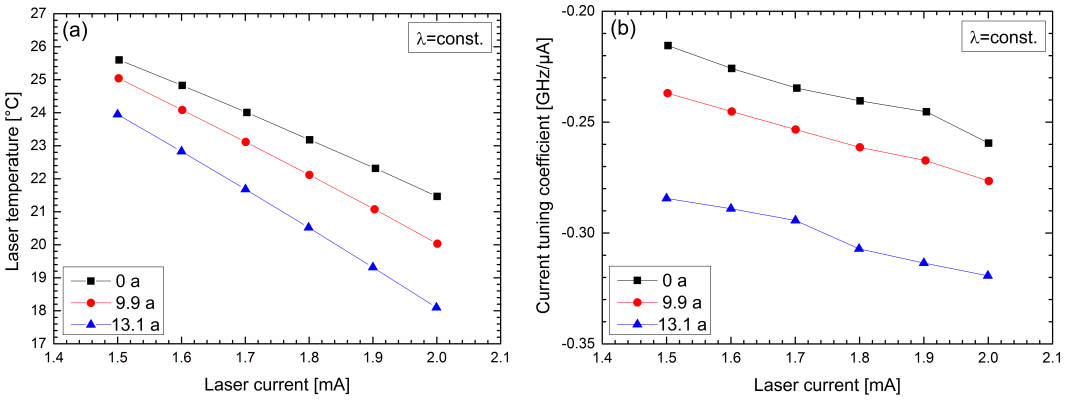

Figure 3.6.: Laser A2.2 (a) Measurements of the laser current and laser temperature combinations to set the defined wavelength (b) Measurements of the current tuning coefficient

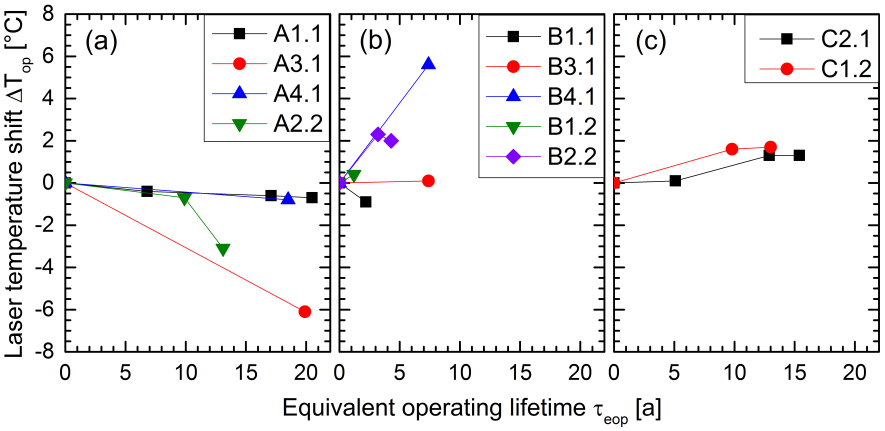

Figure 3.7.: Change of the operational laser temperature T_{op} at I_{op} over the calculated equivalent operating lifetime: (a) Lasers of supplier A, (b) lasers of supplier B and (c) lasers of supplier C.

Since each laser experienced a different ageing in the experiment, the change of T_{op} over the equivalent operational lifetime τ_{eop} is depicted.
All lasers from supplier A (figure 3.7 (a)) showed a reduction of Top over the test duration. The laser temperature Top of laser A3.1 shifted by (-6.1 ± 0.2)°C. Lasers from supplier B showed no clear trend (figure 3.7 (b)). The laser temperature T_{op} of laser B4.1 as well as of laser B2.2 increased during the test but laser B1.1, which failed after the first intermediate characterisation, decreased. Both tested lasers from supplier C showed an increase of T_{op}.

3.2.6. Discussion

The lasers from the three suppliers performed differently during the endurance test and the electro-optical characterisations. Most of the lasers from supplier A and supplier C showed a moderate decrease of their optical power during the lifetime test (<10%). Lasers from supplier B revealed significant variations of their optical power (see figure 3.4). For example, the optical power from laser B4.1 decreased by 50% and increased again to approximately its initial value. Such strong variations in laser power could significantly influence the performance of the magnetometer.
Four lasers in vacuum chamber one completely failed (A2.1, B2.1, C1.1 and B1.1) and were replaced during the intermediate tests. Two lasers in vacuum chamber 2 (B3.1 and B4.4) showed a reduction in laser power more than 50% but were still working at the end of the endurance test and thus they were tested during the final electro-optical characterisation. More lasers failed in vacuum chamber 1 than in vacuum chamber 2. However, all lasers in vacuum chamber 1 and 2 were handled in the same way and powered from identical equipment. There was no known difference between the two vacuum chambers.
Lasers A2.1 and B2.1 failed shortly after test start and laser B1.1 also showed a clear reduction of its optical power right from the start. Most likely these lasers were already damaged at the test start.
However, one laser (C1.1) suddenly failed after 40 days of operation in vacuum chamber 1. This laser was sent back to its manufacturer for further tests on the failure. Investigations by the manufacturer indicated that this laser showed typical features of a laser suffered from an ESD event. Since the high sensitivity of VCSELs on ESD was known, several ESD precautions during handling and operation were made but due to the repeated handling and mounting of the lasers during the test, the risk of ESD damage cannot be eliminated completely. Therefore, the intermediate characterisations with the complete dismounting of the lasers entailed additional risks for ESD damage. Most of the lasers showed only a slight increase or reduction of their optical power after remounting which was explained by a different reassembly. However, a drop in the optical power, which, for example, laser A2.2 showed after the 2^{nd} IC, could also be caused by a prior ESD event.
Due to the failure of the tested lasers, we decided to include measurements of the reverse current-voltage, forward current-voltage as well as the optical power-current characteristics in future test procedures. These additional measurements can help to detect defect or already degraded VCSELs before mounting them in a test setup. Especially, in the reverse current-voltage measurement a degradation, for example, caused by an ESD event, can be identified by a flattening of the originally sharp breakdown voltage [61].
Two lasers from supplier A revealed polarisation jumps (A3.1, A4.1). For applications which use polarisation optics or a polarisation-maintaining fibre the preservation of the polarisation plane is critical. In such applications polarisation jumps could cause severe problems and result in a complete loss of the optical power. This was also one reason why in the CDSM application a multi-mode fibre, which connects the laser unit with the

sensor unit, in combination with polarisation optics at the sensor unit was chosen. After the multi-mode fibre the optical light is nearly unpolarised and the defined polarisation state is obtained with the polarisation optics in the sensor unit. Therefore, optical power is lost at the sensor unit but a failure caused by polarisation jumps is avoided. However, the measurements have shown that the change of the polarisation state could last up to 20 h. Further investigation would be required to study this transition area and to evaluate the influence on the operation of the magnetometer. Additionally, depending on the rate of polarisation jumps they could influence the CPT resonance shape [62][63].
With respect to the JUICE mission it was important to test if a VCSEL laser can operate up to 17 years under vacuum condition. The endurance test allowed us to prove that lasers from at least supplier A and C can reach lifetimes of more than 17 years and still have enough optical power for the operation of the CDSM magnetometer. Lasers A1.1, A3.1 and A4.1 from supplier A as well as lasers C3.1. and C4.1 from supplier C reached an equivalent operational lifetime of more than 17 years. The equivalent operational lifetime for lasers of supplier B was much lower than the lifetime of the two other suppliers A and C. This was due to the fact that the activation energy E_A, which we had received from the manufacturer B, is about half the value of the two other manufacturers. Thus, the calculated equivalent operational lifetime is much lower for lasers of supplier B.
The measurement on the laser temperature T_{op} at the operational laser current I_{op} for the required nominal wavelength of $\lambda = 794.979\,\text{nm}$ (vacuum wavelength) showed different trends for the three manufacturers (see figure 3.7). The laser temperature T_{op} for supplier A decreased for all tested lasers over time. Lasers from supplier B showed both reduction and increase of the laser temperature T_{op}. The tested lasers from supplier C revealed an increase of their laser temperature T_{op} during the test campaign.
Laser A3.1 had the largest operational temperature shift of all tested lasers of $(-6.1 \pm 0.2)°\text{C}$ for an equivalent operational lifetime of about 20 years. The reason for this large change could be caused by a mode jump, which this laser showed several times during the vacuum test. Nevertheless, in the CDSM application such a change of the operational temperature T_{op} can be compensated. However, for different applications enough margins in the design of the instrument should be taken into account.
Also laser B4.1, which failed due to a reduction of its initial power below the defined criterion, showed a large increase of T_{op} at I_{op} of $(+5.6 \pm 0.6)°\text{C}$. However, laser B3.1, which also showed a power reduction of 50% initial power, has no change of its operational temperature. All other lasers showed far less changes of T_{op} at I_{op}.
The current tuning coefficient $\Delta\nu/\Delta I$ for the lasers of manufacturers A, B and C also revealed differences. In general, lasers from supplier C showed the smallest current tuning coefficient and were a factor 2-3 smaller than for suppliers A and B (see table 3.5). A smaller current tuning coefficient is a benefit for the operation of the magnetometer because laser current noise is less efficiently converted into frequency noise. Most of the lasers showed no change of their current tuning coefficient within the measurement accuracy after ageing. However, the current tuning value $\Delta\nu/\Delta I$ of lasers A3.1, A2.2, B1.1

and B3.1 increased (see table 3.5 and figure 3.6). The change of $\Delta\nu/\Delta I$, which is stated in column three of table 3.3, was calculated between the initial characterisation and the final characterisation.

Table 3.3.: Change of the current tuning coefficient $\Delta\nu/\Delta I$ between initial and final electro-optical characterisation: The lasers aged differently and thus they reached a different equivalent operational lifetime τ_{eop}.

Laser	τ_{eop}	Change of $\Delta\nu/\Delta I$ for τ_{eop} [%]
A3.1	19.9	30 ± 23
A2.2	13.1	24 ± 16
B1.1	2.2	11 ± 8
B3.1	7.4	18 ± 8

In the CDSM application an increase in the current tuning coefficient would cause an increase of the noise level and thus in a reduction of the signal-to-noise ratio. The mean temperature tuning coefficient $\Delta\nu/\Delta T$ was identical for the lasers of the three suppliers (see table 3.4). This parameter revealed neither a dependence on the laser current nor on the laser temperature and did not alter for increased operational lifetime.

Table 3.4.: Mean temperature tuning coefficient $\Delta\nu/\Delta T$ for the three different suppliers

Supplier	$\Delta\nu/\Delta T$ [GHz/°C]
A	-26.5 ± 0.6
B	-26.5 ± 0.5
C	-26.5 ± 0.9

The temperature tuning coefficient depends on the change of the average refractive index and the thermal expansion of the cavity with temperature [48]. The equality of the temperature tuning coefficients can possibly be explained by the fact that the material composition of the VCSELs is quite similar and thus they have almost the same linear temperature expansion coefficient. However, the current tuning coefficient seems to depend significantly on the exact inner structure of the lasers (e.g., size of the cavity, number of quantum wells, current confinement) and is thus unequal for the lasers from the three different suppliers.

VCSELs from supplier A showed typical threshold current values between 0.4 mA and 0.6 mA. From supplier C, the threshold current varied in the range from 1.3 mA to 1.5 mA and for supplier B from 0.7 to 0.8 mA. Lasers from supplier A as well as lasers C2.1 and C1.2 showed no change of their threshold current over time within the measurement accuracy. On the other hand, lasers B1.1, B3.1 and B4.1 from supplier B revealed a clear increase of their threshold current over their operational lifetime. The threshold current of VCSEL B1.1 and B3.1 increased from 0.8 mA to 1.3 mA and for laser B4.1 from

0.9 mA to 1.6 mA. An increase of the threshold current can either be a typical result of an aged laser [48] or by ESD driven degradation [64]. Either way it is a hint that the laser structure is already degraded to a certain degree. Lasers from supplier A and B had a typical line width of about 100 MHz and VCSELs from supplier C about 50 MHz. A smaller laser line width is preferable for the CPT resonance excitation (see section 3.2.3). The repeated measurement of the laser line width showed that the theoretical accuracy of ±5 MHz was not reached. Due to the required readjustment of the optical path for this measurement, an experimental accuracy of about ±10 MHz is obtained. Most of the laser line widths showed no significant change for aged lasers except for lasers B1.2, B2.2 and A4.1 which laser line widths' seemed to narrow. The narrowing could also be caused by a back reflection from an optical element into the laser.
The polarisation ellipse was evaluated by measuring its maximum and minimum. The ratio of the maximum to minimum was used to evaluate changes. However, the accuracy of the measurement of the minimum was influenced by background light and therefore here an accuracy of ±2 µW was obtained. Within this limits no significant changes of the ratio were measured during the electro-optical characterisations.
Based on the results from the endurance test and the electro-optical characterisations we decided to further test lasers from supplier C for the CDSM prototype. Both lasers from supplier A and C performed well during the endurance test. However, lasers from supplier C showed several benefits for the CDSM application compared to the other suppliers. They had no polarisation jumps, less changes in the electro-optical parameters compared to the two other suppliers while ageing, a lower current tuning coefficient, typically a two times smaller laser line width and a 2-3 times higher optical power than lasers from supplier A. The obtained output power from laser A was limited by the maximum allowed operational laser current ($I_{max} = 2\,\text{mA}$) according to the data sheet.
An endurance test with a bigger lot of lasers from supplier C will be performed within a new laser vacuum test facility at Graz University of Technology. The benefit of this new test facility is that it allows measurements of the electro-optical characteristic without dismounting the lasers. Additionally, the test facility allows the performance of a further burn-in to stabilise the optical parameters.

3.2.7. Conclusion

In summary 16 VCSEL were tested under accelerated operation conditions under vacuum. Half of the VCSELs were operated for 344 days with two intermediate electro-optical characterisations (vacuum chamber 1) and the other half for 414 days without interference (vacuum chamber 2).
The majority of VCSELS did function well until the end of the test. The optical output power of VCSELs from supplier A and C behaved stable with slight changes during the vacuum test (<10%) except laser A3.1 which showed a decrease of 20%. Lasers from

supplier B showed the greatest variation in optical power during the accelerated ageing test (up to 50%). Such strong variations could influence the performance of our magnetometer. Four lasers in vacuum chamber 1 failed completely (A2.1, B2.1, C1.1 and B1.1).
With the endurance test we were able to show that VCSELs from supplier C can survive more than 17 years of operation with no major degradation of their performance and thus they are well suited for long-term space missions like JUICE. However, a burn-in appeared to be needed for the selected supplier C to stabilise the optical power. For the JUICE application we decided to further test lasers from supplier C and perform an endurance test with a bigger lot in a new laser vacuum test facility at Graz University of Technology. The benefit of this new test facility is that it allows measurements of the electro-optical characteristic in the endurance test setup without dismounting the lasers.

3.2.8. Appendix

In table 3.5 the results on the laser temperature Top at the operational current I_{op} and the current tuning coefficients $\Delta\nu/\Delta I$ at I_{op} are summarised.
With the help of the mean acceleration factor AF_{mean} from table 3.2 and the test duration Δt_{test} until the characterisation, which is stated in column two of table 3.5, the equivalent operational lifetime τ_{eop} for each laser at the time of the characterisation was calculated and is stated in column three of table 3.5.
In the fourth column the measured laser temperature Top at the operational laser current I_{op} for the required nominal wavelength is listed. During the second and fourth electro-optical characterisation, the temperature at the operational laser current was not exactly measured at the defined laser current for lasers of company B. In that case the laser temperature was calculated from a second-order polynomial fit to the measured values [65]. In Table 5 those values are marked with the symbol $*$.
The temperature change ΔT_{op} between consecutive characterisations is given in the fifth column. In the sixth column the calculated current tuning coefficients $\Delta\nu/\Delta I$ for the operational laser current I_{op} are summarised. The current tuning coefficients were calculated for I_{op} using a linear fit to the measured values.

Table 3.5.: Summary of results obtained for the laser temperature T_{op} and current tuning coefficient $\Delta\nu/\Delta I$ at I_{op}.
$*$ Values were determined by polynomial fit

Laser	Δt_{test} [d]	τ_{eop} [a]	T_{op} [°C]	ΔT_{op} [°C]	$\Delta\nu/\Delta I$ [GHz/µA]
A1.1	0	0	24.2 ± 0.1		-0.269 ± 0.001
	114	6.8	23.8 ± 0.1	-0.4 ± 0.2	-0.29 ± 0.04
	228	17.1	23.6 ± 0.1	-0.2 ± 0.2	-0.286 ± 0.018
	344	20.5	23.5 ± 0.1	-0.1 ± 0.2	-0.29 ± 0.03
A3.1	0	0	26.5 ± 0.1		-0.395 ± 0.008
	414	19.9	20.4 ± 0.1	-6.1 ± 0.2	-0.51 ± 0.09
A4.1	0	0	27.3 ± 0.1		-0.336 ± 0.003
	414	18.5	26.5 ± 0.1	-0.8 ± 0.2	-0.38 ± 0.05
A2.2	0	0	22.4 ± 0.1		-0.25 ± 0.03
	230	13.1	19.3 ± 0.1	-2.4 ± 0.2	-0.314 ± 0.022
	174	9.9	21.7 ± 0.1	-0.7 ± 0.2	-0.270 ± 0.010
B1.1	0	0	$19.2 \pm 0.1^*$		-0.265 ± 0.004
	114	2.2	$18.3 \pm 0.3^*$	-0.9 ± 0.4	-0.293 ± 0.021
B3.1	0	0	21.3 ± 0.1		-0.313 ± 0.011
	414	7.4	$21.4 \pm 0.3^*$	0.1 ± 0.4	-0.370 ± 0.021
B4.1	0	0	19.2 ± 0.1		-0.313 ± 0.011
	414	7.4	$24.8 \pm 0.5*$	5.6 ± 0.6	-0.324 ± 0.021
B1.2	0	0	25.2 ± 0.1		-0.292 ± 0.022
	0	0	25.1 ± 0.1	-0.1 ± 0.2	-0.295 ± 0.013
	56	1.2	$25.5 \pm 0.1^*$	0.4 ± 0.2	-0.295 ± 0.015
B2.2	0	0	28.5 ± 0.1		-0.228 ± 0.012
	0	0	$28.3 \pm 0.2^*$	-0.2 ± 0.2	-0.227 ± 0.020
	174	3.2	30.6 ± 0.1	2.3 ± 0.2	-0.227 ± 0.011
	230	4.3	$30.3 \pm 0.2^*$	-0.3 ± 0.2	-0.235 ± 0.015
C2.1	0	0	37.4 ± 0.1		-0.115 ± 0.009
	114	5.1	37.5 ± 0.1	0.1 ± 0.2	-0.115 ± 0.008
	288	12.9	38.7 ± 0.1	1.2 ± 0.2	-0.113 ± 0.005
	344	15.4	38.7 ± 0.1	0.0 ± 0.2	-0.112 ± 0.005
C1.2	0	0	38.7 ± 0.1		-0.124 ± 0.004
	174	9.8	40.3 ± 0.1	1.6 ± 0.2	-0.12 ± 0.04
	230	13.0	40.2 ± 0.1	0.1 ± 0.2	-0.120 ± 0.003

3.3. CDSM Sensor

The CDSM sensor contains the Rb vapour cell and several optical components which are required to prepare the laser light field for the CPT and CDSM resonance excitation. The main benefits of the CDSM sensor design are its simple setup consisting of only optical elements and the ability to omnidirectionally measure magnetic fields with just one sensor cell [10]. The initial CDSM sensor design was developed for the CSES mission which is described in more detail in section 3.3.1. Several tests were carried out to prove the functionality and performance of the design for a space application. These tests are outlined in section 3.3.2.
A new sensor design is under development for the JUICE mission - the dual pass sensor. This design is based on a dual pass of the laser beam through the sensor cell. The dual pass sensor is presented in section 3.3.3.

3.3.1. CDSM Sensor Design for the CSES mission

The sensor design for the CSES mission is based on a single pass of the laser beam through the Rb vapour cell. The main components of the sensor unit are shown in figure 3.8.

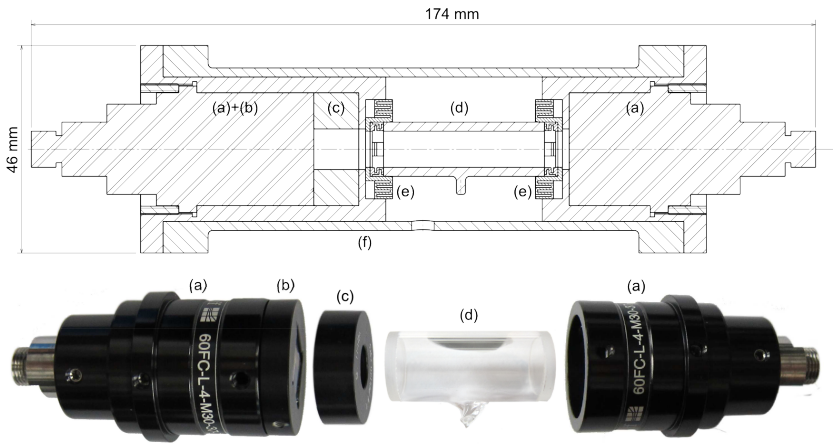

Figure 3.8.: Cross section of the CDSM sensor for the CSES mission and illustration of the optical elements [14]: The outbound fibre is connected to the fibre coupler (a) on the left-hand side of the sensor cell. Then, the light passes the polarisation optics consisting of the polarising beam splitter (b) and the quarter-wave plate (c) to set a defined polarisation state. Further on the circularly polarised light field passes the Rb vapour cell (d). The cell is held by damping elements (e) made of PTFE. The transmitted light is then coupled into the inbound fibre by the second fibre coupler on the right-hand side of the sensor cell (a) which is identical to the first fibre coupler.

The sensor unit contains two commercial fibre couplers (a). The first fibre coupler collimates the laser light after the outbound fibre. An achromatic lens pair with a focal length of $f = 30\,\text{mm}$ is mounted within both fibre couplers. Subsequently, the polarisation state of the laser light is set to a circular polarisation state by a polariser (b) and a quarter-wave plate (c). The polariser is a polarising beam splitter cube with a side length of $l = 10\,\text{mm}$ which has an extinction ratio of $1 : 10^3$.
Then the light field passes the Rb vapour cell (d) which contains isotopically pure ^{87}Rb and neon as buffer gas. The cell has a diameter of $d = 12.7\,\text{mm}$ and an optical path length of $l = 25.2\,\text{mm}$. The windows are coated with an antireflection coating. The cell is held by damping elements made of PolyTetraFluoroEthylene (PTFE) (e). They allow a safe and stable storage of the cell during the launch and cover differences in thermal contraction over large temperature ranges without breaking the glass cell at low temperatures. The transmitted laser light is coupled with the second fibre coupler (a) (on the right-hand side of figure 3.8) into the inbound fibre.
For magnetic field measurements with sufficient signal-to-noise ratio, the temperature of the sensor cell has to be within a certain temperature range. This temperature range is between $T = 18°\text{C}$ and $T = 55°\text{C}$ for the CSES mission [12]. An optimised signal-to-noise ratio is achieved at the sensor cell temperature of $T \approx 45°\text{C}$ (see section 4.1.3.4).
In order to set the sensor cell temperature to a certain temperature, a sensor cell heating is integrated in the sensor unit (see also section 2.4.2). The sensor cell heating consists of a heating wire made of Constantan. Constantan is a copper-nickel alloy which turned out to be non-magnetic. To minimise disturbances from the heating current, the bifilar twisted heating wire is not wound directly onto the sensor cell. Instead, heater shells made of aluminium are glued on the sensor cell and the heating wire is wound around these heater shells.
Two different materials were tested as housing material for the sensor unit: aluminium and Polyether Ether Ketone (PEEK). PEEK is a thermoplastic polymer which has a high temperature and form stability, a temperature expansion coefficient similar to aluminium and it is radiation resistant [66][67]. Initially, glass fibre reinforced PEEK was used for the housing. However, the optical path of the sensor unit suffered from loss of adjustment due to released stress which was induced during the production of the sensor parts. To prevent that, thermal treatment during manufacturing would have been required to release this stress. Finally, the housing was made of aluminium but PEEK is used for sensor parts of the dual pass sensor (see section 3.3.3). The aluminium has the advantage of better mechanical stability and a higher radiation shielding. The total weight of the assembled sensor unit with the aluminium housing is $m = 340\,\text{g}$ [12].
The sensor unit is connected to the electronics unit via a harness which consists of a double twisted pair cable and two optical fibres (outbound and inbound fibre), which are further described in section 3.4. The electrical cable enables the heating of the sensor cell and the temperature measurement required for the operation of the sensor temperature control loop (see section 2.4.2).

3.3.2. Evaluation Tests with the Sensor Unit

The sensor unit has to withstand strong vibrations during launch and the extreme conditions in space. Therefore, typical evaluation tests for space missions like vibration tests and thermal tests were performed corresponding to the mission requirements. For the sake of brevity, only selected tests with the sensor unit are presented in this section. First, in section 3.3.2.1 evaluation tests were performed to determine the coupling tolerances of the CSES sensor unit against a lateral and angular misalignment. Additionally, the polarisation state after the outbound fibre in dependence of the fibre position was investigated and the results are outlined below.
Furthermore, for the upcoming JUICE mission, where extremely low temperatures are expected, a liquid nitrogen test was performed with the sensor unit. During this test the whole sensor unit was tested at different temperatures down to $T = -196°\mathrm{C}$. The test procedure and results are summarised in section 3.3.2.2.

3.3.2.1. Light Coupling and Variation of Polarisation State

The tolerances of the laser light coupling into the inbound fibre were determined for lateral and angular misalignments. The dependence of the coupled optical power on a lateral and angular misalignment is summarised in figure 3.9 and tables 3.6 and 3.7. The tolerances in tables 3.6 and 3.7 refer to a reduction of the optical power to 90% and 50% of the maximum value detected after the inbound fibre.

For these measurements, the optical path of the sensor was reconstructed on an optical bench. The single optical elements were mounted separately on adjustable holders. The outbound fibre was a graded-index fibre with a core diameter of $d = 50\,\mu\mathrm{m}$ and the inbound fibre was a step-index fibre with a core diameter of $d = 100\,\mu\mathrm{m}$. For the measurement of the tolerances, the fibre coupler connected to the inbound fibre was either shifted or tilted and the optical power measured after the inbound fibre with a power meter.
The measurements showed that the sensor design is rather insensitive to a lateral misalignment (see figure 3.9(a)). The fibre couplers can be shifted by several millimetres and still most of the light is coupled into the inbound fibre.
In contrast, the fibre coupling is sensitive to an angular misalignment. In figure 3.9(b) the measured angular tolerance is depicted for two different setups.
First, the angular coupling tolerance was investigated for just the two fibre couplers without all other optical elements of the sensor unit. This measurement was performed with three different inbound fibres which had core diameters of $d = 50$, 100 and $200\,\mu\mathrm{m}$.

Second, the angular tolerance was measured with all optical elements and an inbound

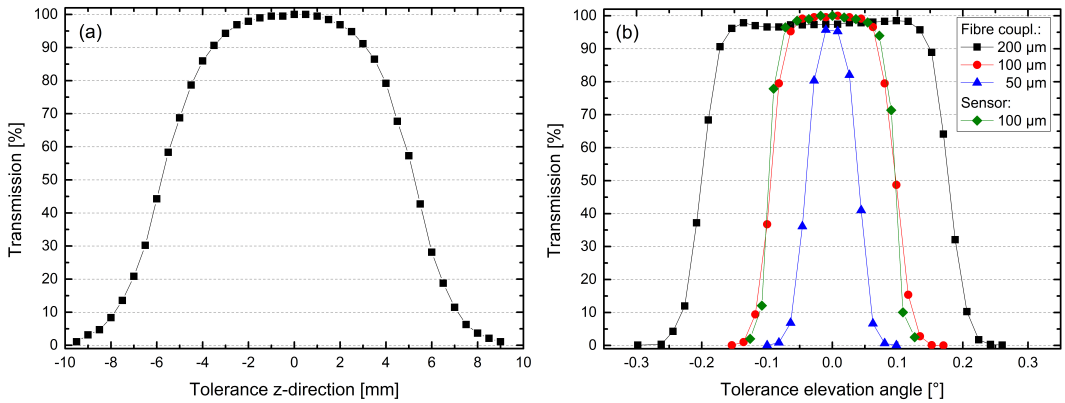

Figure 3.9.: Experimentally determined tolerances of the CSES sensor for lateral and angular misalignment: In (a) the dependence of the light coupling against a lateral misalignment is shown. The fibre couplers can be misaligned by several millimetres and still most of the laser light is coupled into the inbound fibre. In (b) the tolerance of the fibre coupling to an angular misalignment is depicted for three different optical fibres with the following core diameters: $d = 50\,100$ and $200\,\mu m$. Additionally, the angular tolerance was determined for the reconstructed CSES sensor (green diamonds). The angular tolerance of the CSES sensor can be increased by using an inbound fibre with a larger core diameter.

Table 3.6.: Lateral tolerance of the light coupling of the CSES sensor: The lateral tolerances are listed for a reduction of the optical power to 90% and 50% of the maximum coupled optical power. The measurement uncertainty is about $\pm 0.3\,mm$.

Lateral tolerance	
90%	50%
[mm]	[mm]
±3.4	±5.5

fibre with a core diameter of $d = 100\,\mu m$. The determined angular tolerance values are summarised in table 3.7.
The results showed that the angular tolerance can be enhanced by using an inbound fibre with a higher core diameter. Thus, the inbound fibre with a core diameter of $d = 100\,\mu m$ was replaced by a fibre with a core diameter of $d = 400\,\mu m$ in order to increase the angular tolerances with respect to the expected vibration levels for the CSES mission.

Besides the adjustment of the fibre coupling, the changing polarisation state at the output of the outbound fibre has significant influence on the optical power within the sensor unit. Since a multi-mode fibre with a core diameter of $d = 50\,\mu m$ is used as outbound fibre, the polarisation state entering the sensor unit is not fixed. The polarisation state

Table 3.7.: Angular tolerance of the light coupling of the CSES sensor using different inbound fibres with different core diameters: The angular tolerances are listed for an optical power reduction to 90% and 50% of the maximum coupled optical power. The measurement uncertainty is about ±0.01°.

	Core diameter	Angular tolerance 90%	50%
	[µm]	[°]	[°]
Fibre coupling	50	±0.03	±0.05
	100	±0.08	±0.10
	200	±0.19	±0.23
Sensor unit	100	±0.09	±0.11

is influenced by the position of the fibre, its temperature and mechanical stress by, e.g., bending [68]. Thus, to obtain a defined polarisation state at the sensor cell, polarisation optics is used inside of the sensor unit. The drawback of using a multi-mode fibre in combination with polarisation optics is the following. Depending on the difference between the polarisation state of the light field entering the sensor unit and the set polarisation state by the polariser, light intensity is lost at the polarisation optics in the sensor unit. In worst case, if the light field from the optical fibre has a linear polarisation state perpendicular to the set polarisation state by the polariser, then almost all light is lost and the operation of the magnetometer is inhibited.

Therefore, the polarisation state entering the sensor unit was investigated for random fibre movement. In this context, two different tests were performed. First, the change of the polarisation ellipse at the output of the outbound fibre was investigated with the help of an additional polariser (Glan-Thompson prism). Second, the variation of the transmitted optical power through the sensor unit was detected during fibre movement with a power meter and recorded with an oscilloscope. The results of both tests are summarised in figure 3.10.

In figure 3.10(a) a typical polarisation ellipse after the outbound fibre is depicted. The orientation of the polarisation ellipse varied randomly during fibre movement. However, the highest ratio of the axis of the ellipse was 1:3. A linear polarisation state was never detected at the fibre output.

In figure 3.10(b) the variation of the transmitted optical power at the photodiode is shown during fibre vibration. The variation of the optical power is compared for two cases. In the first case, the sensor unit is completely assembled. In the second case, the sensor unit just contains the two fibre couplers. In this case, the polarisation optics and the Rb vapour cell were not mounted. In order to compare the power variations, the respective average detected optical power $\bar{P}$ was subtracted from the measured values and the values normalised with $\bar{P}$. Then, the standard deviation σ was calculated.

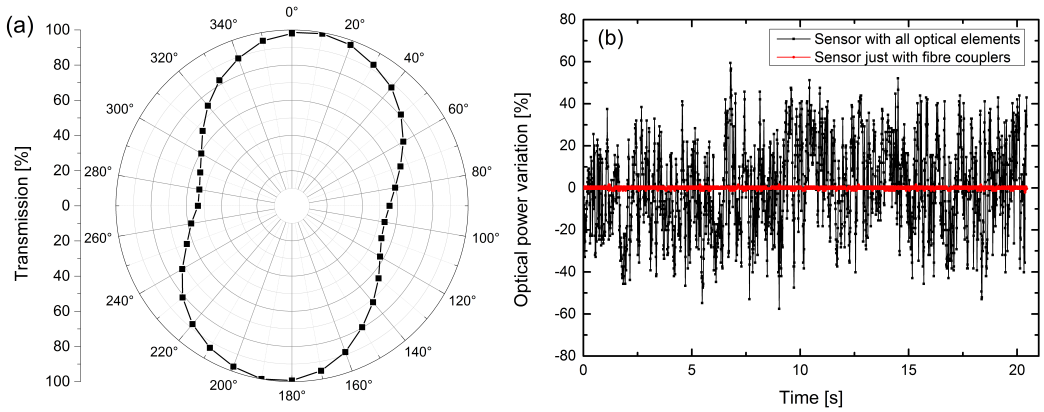

Figure 3.10.: Typical polarisation state after the outbound fibre and variation of the transmitted optical power due to optical fibre movement: In (a) the typical polarisation state after the outbound fibre is elliptical. In (b) the variation of the transmitted optical power through the sensor unit by moving the optical fibre was measured. The red line shows the variation of the optical power for the sensor unit only containing the two fibre couplers. The optical power showed just a slight variation ($\sigma = 0.5\%$) by the fibre movement. For the completely assembled sensor unit including the polarisation optics, the optical power varied significantly ($\sigma = 21.2\%$).

The results revealed a variation of $\sigma = \pm 0.5\%$ for the sensor unit including just the two fibre couplers compared to $\sigma = \pm 21.3\%$ for the completely assembled sensor unit. Besides the high variation of the optical power during the second test, the optical power showed no case were it reduced to zero. Therefore, the fibre movement did not lead to a case where the magnetometer could not have been operated. Nevertheless, the high optical power variation can have an influence on the CPT resonance line shape (see section 4.1.1) as well as the light shift (see section 4.1.1.2) which could affect the performance of the magnetometer.

3.3.2.2. Low Temperature Sensor Test with Liquid Nitrogen

The low temperature sensor test contained four thermal cycles between $T = -20°\mathrm{C}$ and $T = -180°\mathrm{C}$ and a survival test at $T = -196°\mathrm{C}$. In order to prevent condensation of water vapour on the optical elements within the sensor unit during the cooling process, the sensor unit with attached fibres was placed inside of a vacuum bell jar. Then, the chamber was evacuated until a pressure below the vapour pressure of water at room temperature was reached ($P = 31.691\,\mathrm{mbar}$ at $T = 25°\mathrm{C}$ [69]). Subsequently, the chamber was flooded with gaseous nitrogen. The dwell time was $t = 10\,\mathrm{min}$. Afterwards, the sensor was removed from the vacuum bell jar and mounted in a Dewar vessel, which was partly filled with

liquid nitrogen. For the low temperature test, the sensor temperature was adjusted by varying the height of the sensor above the liquid nitrogen level. Two thermistors were used to measure the temperature of the sensor unit. The first one was directly mounted on the Rb glass cell and the second one was attached to the outside of the sensor housing. The optical fibres were connected with the sensor unit during the whole test and the transmitted optical power as well as the measured temperature of both thermistors were recorded. The optical power was measured with a power meter after the inbound fibre. In figure 3.11 the measurement results are summarised.

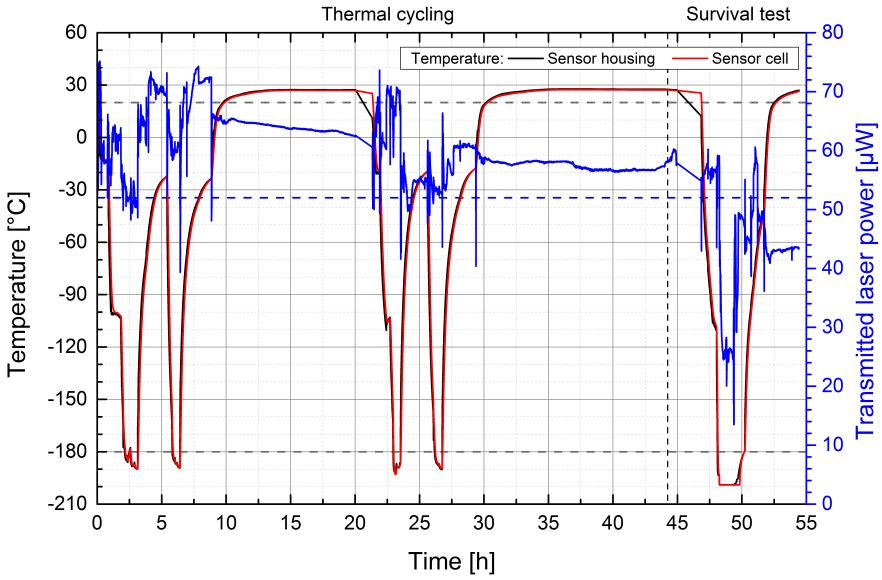

Figure 3.11.: Measurement results of the low temperature test with the CSES sensor: The black and the red lines correspond to the temperature measured on the surface of the Rb vapour cell and on the outside of the sensor housing respectively. The blue line depicts the transmitted optical power after the inbound fibre. First, four thermal cycles were performed. Then, a survival test was conducted where the whole sensor unit with connected fibres was submerged into the liquid nitrogen. The optical power dropped due to liquid nitrogen in the sensor unit but recovered after the sensor unit was removed from the liquid nitrogen.

The red and the black lines in figure 3.11 show the temperature inside and outside of the sensor unit during the test. The blue line indicates the variation of the transmitted optical power. Four thermal cycles between $T = -20°\mathrm{C}$ and $T = -180°\mathrm{C}$ were performed. After the first cooling phase the sensor cell did not reach the upper temperature limit of $T = -20°\mathrm{C}$ but a temperature of $T = -25°\mathrm{C}$ was obtained. After the thermal cycles were completed, a survival test was performed where the sensor unit was submerged into the liquid nitrogen. Thus, the whole sensor unit reached a temperature of $T = -196°\mathrm{C}$. During the survival test, the sensor unit was flooded with liquid nitrogen. Therefore, the transmitted optical power dropped but increased again after removing the sensor unit

from the liquid nitrogen.
A functional check was performed before and after the thermal cycling as well as before and after the survival test. The functional test consisted of an visual inspection of all optical elements, a transmission measurement of the optical power as well as the measurement of the CPT resonance position of $n = 0$. The repeated measurement of the CPT resonance $n = 0$ was used to evaluate the tightness of the Rb vapour cell. A significant change of the transition frequency would indicate a leakage in the sensor cell.
Originally, the whole test was planned to be performed without the optical fibres because they were not qualified for such low temperatures. However, pre-tests showed that the optical fibres could withstand the cold temperatures. Thus, the optical fibres remained connected during the whole test.
As can be seen in figure 3.11 the laser power showed obvious fluctuations. They were caused by the movement of the fibres while adapting the height of the sensor unit. The fibre movement changed the polarisation state after the outbound fibre which in combination with the polarisation optics in the sensor unit resulted in power variations (see section 3.3.2.1).
During the first functional check the received optical power was $P_I = 50\,\mu\text{W}$. Due to fibre movement, the optical power increased during the test up to $P = 72\,\mu\text{W}$ and settled at $P = 46\,\mu\text{W}$ after the survival test. The final power level was just slightly lower than the initial one. Additionally, the visual inspections of the optical elements revealed no damage due to the low temperatures. Moreover, the repeated measurements of the CPT resonance position of $n = 0$ showed no shift during the low temperature test. Thus, the sealing of the cell remained intact and the sensor cell fully functional.

3.3.3. Dual Pass Sensor

A dual pass sensor design is under development for the JUICE mission. The design is based on a dual pass of the laser beam through the Rb cell in contrast to a single pass in the CSES sensor design. For the second pass, the laser beam is reversed after the first sensor cell pass. The dual pass design has some advantages compared to the single pass sensor design. Due to the dual pass the optical path length inside of the sensor cell is doubled. Thus, the CPT and CDSM resonance signals have a higher amplitude (see section 4.1.1). Additionally, the dual pass design has both fibre couplers on the same side which simplifies the handling and mounting of the sensor unit on the satellite boom. Moreover, as discussed in section 4.2, the single CPT resonances do not have the same resonance line shapes for most sensor angles. Thus, the ability to compensate disturbing frequency shifts is reduced at certain sensor angles. With the new design this line shape imbalance can be diminished and the compensation effect obtained by the formation of the CDSM resonances can be improved (see section 4.2.3). Measurements comparing CPT and CDSM resonances prepared by a single or a dual pass of the laser beam through the

sensor cell are included in chapter 4.
A new Rb vapour cell was designed and manufactured which allows the dual pass of the sensor cell without interaction of the two passes (see figure 3.12).

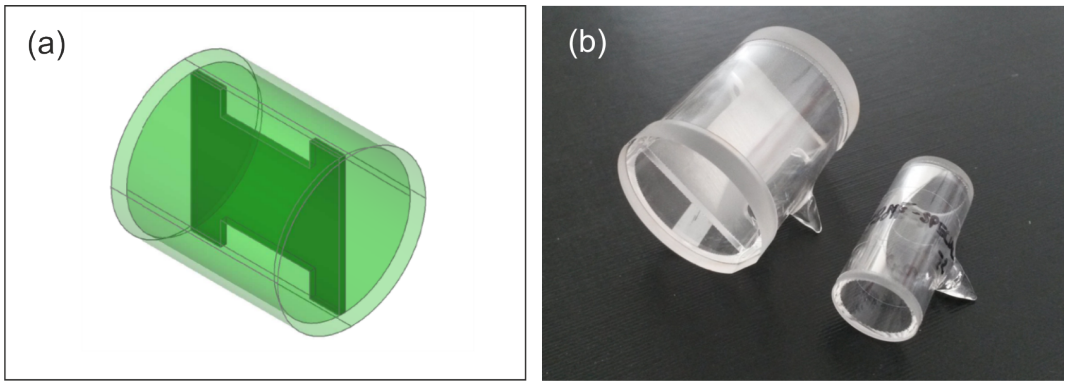

Figure 3.12.: Design of the dual pass sensor cell: In (a) a drawing of the dual pass cell is shown. In the middle of the cell a barrier with cut outs is included to prevent interactions of the atoms prepared by the two separate laser beam passes. In (b) the dual pass cell and the CSES sensor cell are compared. The dual pass cell has about twice the diameter as the CSES sensor cell.

It has a larger diameter ($d = 25\,\mathrm{mm}$) compared to the sensor cell used for the CSES mission ($d = 12.7\,\mathrm{mm}$) (right side of figure 3.12). The larger diameter is required for the dual pass of the laser beam in the both directions without overlap of the two beams. Additionally, a barrier is introduced in the middle of the cell to prevent atoms interacting with one laser beam to immediately interact with the other beam. Thus, possible interference effects are avoided, which might influence the CPT resonance preparation. The barrier has two cut outs lengthwise which guarantee the same temperature and buffer gas pressure on both sides of the barrier. Otherwise the CPT resonance positions would experience different buffer gas induced shifts during the first and second pass. As a result, the CPT resonance positions of the two passes would not match which would influence the measurement accuracy. This fact is also the reason for choosing one bigger cell instead of two independent cells for the dual pass sensor.

With the dual pass cell a new sensor design was developed which partly differs from the CSES sensor design. In figure 3.13 the structure of the dual pass sensor is shown. The laser beam emitted from the outbound fibre is collimated by a fibre coupler containing a best form lens. The fibre couplers used in the CSES sensor are replaced by more compact fibre couplers. The collimated laser beam passes the polarisation optics consisting of a polarising beam splitter and a quarter-wave plate. The polarisation state is set to be circular. For the dual pass sensor design, the polarising beam splitter cube and the quarter-wave plate are combined to one unit. The quarter-wave plate is glued to the polarising beam splitter cube with a spacer in between. Thus, the polarisation state is fixed.

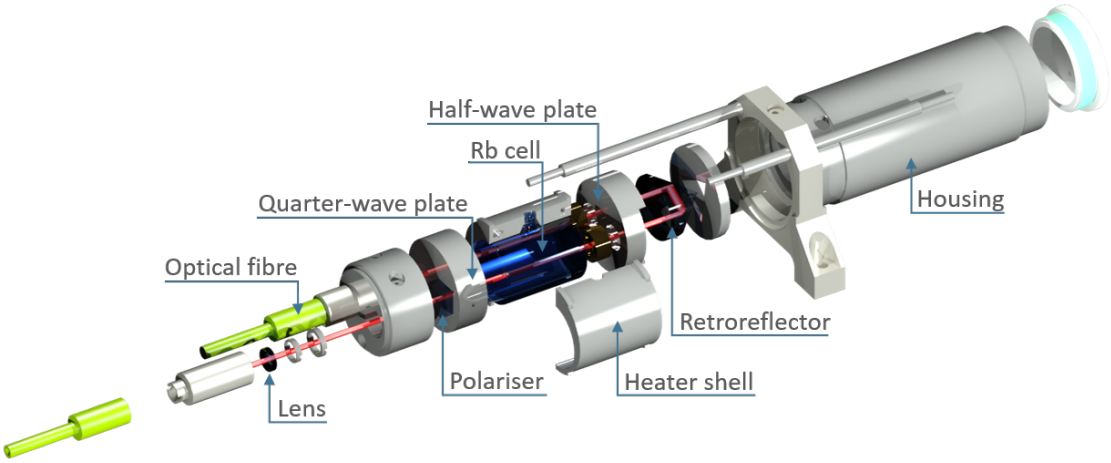

Figure 3.13.: Drawing of the dual pass sensor and its optical elements: The light coming from the outbound fibre is collimated by a best form lens. Then the light beam passes the polarisation optics consisting of a polarising beam splitter cube and a quarter-wave plate. After the polarisation optics the light beam passes the Rb cell for the first time. The transmitted beam is reflected by a retroreflector and passes a half-wave plate before it enters the dual pass cell a second time. After the second pass the laser light is coupled into the inbound fibre.

The polarising beam splitter cube is similar to the one mounted in the CSES sensor. It has a side length of $l = 10\,\text{mm}$ and an extinction ratio of $1 : 10^3$.
Afterwards, the laser beam passes the Rb vapour cell for the first time. The cell has an optical path length of $l = 25\,\text{mm}$ and a diameter of $d = 25\,\text{mm}$. The windows are wedge-shaped (1°).
Then, the transmitted laser beam is reversed by a solid glass retroreflector (corner cube). Compared to a deflecting prism the retroreflector has the benefit that the incoming light beam is reversed by 180° independent of a misalignment. The front surface is anti-reflection coated and has a diameter of $d = 25\,\text{mm}$. The back surface is coated by either silver or aluminium. Without metallic coating the circular polarisation state would be converted into a linear polarisation state after the reflection.
The reversed laser beam is guided through a half-wave plate to reverse the chirality of the circular polarisation state. The compensation of the line shape imbalance between the single CPT resonances is based on the combination of left and right circularly polarised light for the CPT resonance preparation. Thus, the imbalance caused by different transition strengths within the hyperfine structure and the optical pumping effect are reduced (see section 4.2). Therefore, the CPT resonances prepared during the second pass of the laser beam have to be excited by a laser light field with an opposite chirality as compared to the first pass. Without the half-wave plate the same chirality of the circular polarisation state would be given and no equalisation of the CPT resonance spectrum would take

place. After the second pass the laser light is coupled with the second fibre coupler into the inbound fibre.
The materials used in the dual pass sensor are carefully selected regarding their radiation tolerance with respect to the JUICE mission. Depending on the position within the sensor unit, the optical elements experience different total doses. Radiation levels of several hundreds of krad up to a few Mrad are expected within the sensor unit for the JUICE mission. Therefore, most optical elements are made of fused silica which has a good radiation tolerance [70]. Another option would be glass with added cerium oxide to improve the radiation tolerance [71].
The materials for the housing and holders which contain the optical elements were selected according to their radiation tolerances but also on their thermal properties. The temperature range, which the sensor unit has to withstand during the JUICE mission, is between $T = -150°\mathrm{C}$ and $T = 90°\mathrm{C}$ [13]. Most of the holders are made of glass fibre-reinforced PEEK to reduce the thermal conduction compared to aluminium. The housing is made from aluminium. Standoffs made of glass fibre-reinforced PEEK are used to thermally insulate the sensor unit from the satellite boom.

3.4. Optical Fibres

Several different types of fibres were tested during the development of the CDSM. First tests in the laboratory were carried out with a polarisation-maintaining single-mode fibre as outbound fibre. Soon the single-mode fibre was replaced by a graded-index multi-mode fibre in order to improve the reliability. Right from the start, a multi-mode fibre was used as inbound fibre due to their higher core diameter. The requirements on the outbound fibre are higher than on the inbound fibre, since the light field in the sensor cell has to fulfil certain requirements to prepare the CPT effect, e.g., stable phase relation. In contrast, the inbound fibre just has to guide the optical power to the photodiode with little attenuation. In section 3.4.1 the different properties of single-mode and multi-mode fibres are discussed as well as the pros and cons of both fibre types for the application in the CDSM.
Fibre connectors of the type FC-APC are used which is a widely-used configuration. However, the standard commercial fibre connectors are magnetic and would influence the magnetic field measurement. Therefore, the connector was redesigned to be non-magnetic in cooperation with the supplier Schäfter&Kirchhoff GmbH.
Further, when choosing optical fibres for space missions a sufficient performance in harsh environments has to be guaranteed. Especially cold temperatures in combination with high radiation levels are critical for the operation of the fibres. Some aspects which have to be considered when selecting optical fibres for harsh environments are summarised in section 3.4.2.

3.4.1. Single-Mode and Multi-Mode Fibres

The difference between single- and multi-mode fibres is that single-mode fibres only transmit one mode for wavelengths above the cutoff wavelength and multi-mode fibres can guide multiple modes [72]. Single-mode fibres have typically a small core diameter of only a few µm and a step index profile [68]. In contrast, multi-mode fibres have much higher core diameters than single mode fibres and either a step-index or graded-index profile. The benefit of graded-index multi-mode fibres is that they have less intermodal dispersion compared to step-index multi-mode fibres [68]. In our case this fact is important for the outbound fibre. If the intermodal dispersion introduces a phase delay between the light fields exciting the CPT resonances, then the efficiency of the CPT resonance excitation is reduced. A phase difference $\Delta\varphi > \pi/2$ would even destroy the coherence completely [18]. Intermodal dispersion could be prevented by using a single-mode fibre [73].
The intermodal dispersion τ_i of a graded-index fibre can be calculated by [73]

$$\frac{\tau_i}{L} = \frac{(NA)^4}{8\, n_c^3\, c}\,, \tag{3.4}$$

where L is the length of the fibre, NA is the numerical aperture and n_c is the refractive index of the fibre core.
Further, the intermodal dispersion of a step-index fibre can be approximated via the relation [73]

$$\frac{\tau_i}{L} = \frac{(NA)^2}{2\, n_c\, c}\,. \tag{3.5}$$

For comparison, the intermodal dispersions and the resulting phase shifts between the first-order sidebands used for the CPT resonance preparation with a frequency separation of about 6.8 GHz were calculated for a step-index and a graded-index fibre. For this calculation, typical values of fibres applied in the CDSM were used ($n_c = 1.47$ and $NA = 0.20$). The intermodal dispersion resulted in $\tau_i/L \approx 45\,\mathrm{ps/m}$ for a step index fibre and $\tau_i/L \approx 0.2\,\mathrm{ps/m}$ for the graded-index fibre. For a fibre with $L = 10\,\mathrm{m}$, the resulting phase shift for step-index fibre would be too high to prepare the CPT effect. In contrast, the phase shift in a graded-index fibre is about $\Delta\varphi \approx 5°$ which is acceptable for the CPT resonance preparation.
Additionally, the CPT and CDSM preparation requires a defined polarisation state at the sensor cell. The VCSEL emits typically linearly polarised light. However, the polarisation state in a single-mode fibre is not necessarily preserved. In a standard single-mode fibre the core of the fibre has a circular symmetry. Thus, the fundamental mode consists of a superposition of two orthogonally polarised modes which propagate at the same velocity [74]. The energy can be transferred between these two modes and the resulting polarisation state at the end of the fibre is a random combination of these two states. As a

result, a polarisation-maintaining fibre would be required to preserve the coupled polarisation state. In a polarisation-maintaining single mode fibre the two orthogonal modes are forced to propagate at different velocities. Thus, the energy transfer between the two states is prevented. This birefringence is typically obtained by either inducing mechanical stress in the fibre or changing the symmetry of the core [74]. For our preliminary experiments, a PANDA (Polarisation-maintaining AND Absorption-reducing) style fibre was used where rods included in the cladding induced stress to the fibre. Thus, the different propagation velocities were achieved.
However, using a polarisation-maintaining single-mode fibre has disadvantages for the use in the CDSM. The coupling of the laser light into a single-mode fibre is critical considering the expected vibration levels during the rocket launch. Additionally, the stability of the polarisation axes during the mission was a concern. These two issues seemed to be solved by using a multi-mode fibre with additional polarisation optics in front of the Rb vapour cell (see section 3.3).
A multi-mode fibre as outbound fibre also has drawbacks for the application in the CDSM like, e.g., the larger bending radius, the phase shift due to intermodal dispersion and that the polarisation state is not preserved. In order to reestablish the polarisation state, an additional polariser is included in the sensor unit. Due to the changing polarisation state at the multi-mode fibre output, the laser intensity after the polariser is reduced depending on the difference between the obtained polarisation state at the fibre output and the fixed polarisation state at the polariser (see figure 3.10).
Additionally, the transversal laser beam profile after the multi-mode fibre shows no homogeneous intensity distribution and the beam radius varies in dependence on the number and order of transmitted modes. The changing intensity distribution can influence the CPT resonance line shapes depending of the resulting laser beam profile [75], affects the power broadening of the CPT resonances (see section 4.1.1) and can also change the light shift (see section 4.1.1.2).
In order to investigate the intensity dependence of the CPT resonance line shape (see section 4.1.1), the optical intensity I has to be calculated from the measured optical power P. Therefore, the relation $I = P/A$ is used where A is the area of the collimated laser beam in transversal direction. The area A depends on the laser beam profile.
Figure 3.14 shows the resulting transversal laser beam profile for single- and multi-mode fibres. In figure 3.14(a) the obtained laser beam profile is depicted for a single-mode fibre. The selected fibre had a core diameter of $d = 4.7\,\mu\text{m}$ and a numerical aperture of $NA = 0.13$. The laser beam profile after the single-mode fibre was determined by placing a plate with a small slit into the optical path behind the fibre coupler, which is required to collimate the laser beam, and by slowly scanning the laser beam profile transversal to the laser beam propagation direction. The slit is small enough so that the measured profile can be interpreted as a convolution of the original laser beam profile with a delta function. Since only the fundamental mode is transmitted in a single-mode fibre, the resulting laser beam profile is Gaussian-shaped [76]. Thus, a Gaussian fit was applied to the measuring

points which resulted the Gaussian beam radius σ. The Gaussian beam radius is defined as the distance from the maximum intensity at the beam centre to the value where the intensity drops to $1/e^2$ of its maximum value [77].

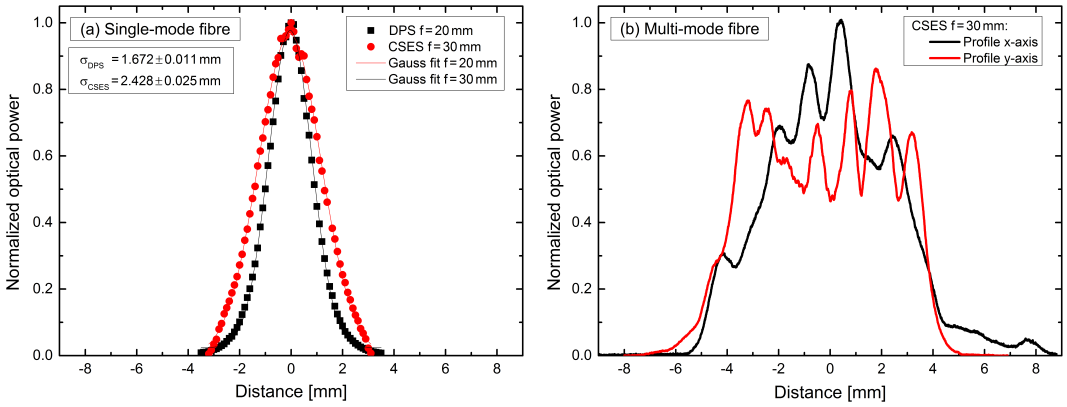

Figure 3.14.: Laser beam radius σ within the CSES sensor and the dual pass sensor for single- and multi-mode fibres: In (a) the transversal laser beam profile is compared for the CSES sensor and the Dual Pass Sensor (DPS) using a single-mode fibre. The CSES sensor contains a lens with a focal length of $f = 30\,\text{mm}$ and the DPS uses a lens with $f = 20\,\text{mm}$. In (b) the transversal laser beam profile was measured using a multi-mode fibre and the fibre coupler of the CSES sensor.

The laser beam profile and the Gaussian beam radius were determined with the fibre couplers of the CSES sensor and dual pass sensor. The lens of the CSES sensor has a focal length of $f = 30\,\text{mm}$ and the resulting Gaussian beam radius was $\sigma_{CSES} = 2.428 \pm 0.025\,\text{mm}$. For the dual pass sensor, a lens with a smaller focal length ($f = 20\,\text{mm}$) was selected. Thus, the measured Gaussian beam radius was also smaller: $\sigma_{DPS} = 1.672 \pm 0.011\,\text{mm}$.

In figure 3.14(b) the laser beam profile after the outbound fibre of the CDSM is depicted using the fibre coupler of the CSES sensor ($f = 30\,\text{mm}$) to collimate the laser beam. The outbound fibre was a graded-index multi-mode fibre with a core diameter of $d = 50\,\mu\text{m}$ and a numerical aperture of $NA = 0.20$. The resulting laser beam profile depends on the actual propagating modes within the fibre, which are influenced by, e.g., the arbitrary position of the fibre, its temperature as well as the bending radius [68]. Thus, the measured laser beam profile deviates from the Gaussian profile shown in figure 3.14(a).

Since the laser beam profile after the multi-mode fibre has no longer a Gaussian profile, a different definition for the laser beam radius is required. There exist different ways to define the laser beam diameter like, e.g., the D4σ-method [78], the width where the intensity drops to a certain level, e.g., $1/e^2$ or the FWHM. For the further discussion, the laser beam radius was calculated from the laser beam diameter which was defined as the width that contains 95% of the total optical power of the measured profile.

The laser beam profiles after a multi-mode fibres were determined with a different method

than for the single-mode fibres. The intensity distribution of the laser beam was detected by a camera with a CMOS sensor [79]. For the evaluation, a picture of the laser beam profile was taken and stored. The measured beam profile was typically elliptical. Therefore, the laser beam diameter was determined for both the major and minor axes of the ellipse. The laser beam profile of the major and minor axis was calculated by a row-wise summation of the intensity information of each pixel of the captured picture. That way two two-dimensional profiles were obtained for the two axes. Then, these laser beam profiles were integrated along the major or minor axis and the laser beam diameters were determined. The laser beam profile measurement was repeated several times for different fibre positions and the resulting mean laser beam radii and standard deviations are listed in table 3.8.

Table 3.8.: Mean laser beam radii of the laser beam profiles obtained with a multi-mode fibre and the fibre couplers of the CSES sensor and the dual pass sensor: The laser beam was collimated with the fibre coupler of either the CSES sensor ($f = 30\,\text{mm}$) or the dual pass sensor ($f = 20\,\text{mm}$). The fibre was a graded-index multi-mode fibre with a core diameter of $d = 50\,\mu\text{m}$ and a numerical aperture of $NA = 0.20$. The radii of the major and minor axes a and b of the elliptical laser beam profile were determined.

Sensor	a [mm]	b [mm]
CSES	4.61 ± 0.13	4.29 ± 0.06
Dual Pass	3.84 ± 0.10	2.97 ± 0.06

For the calculation of the intensity throughout this thesis, an elliptical profile with the area $A = \pi(a \cdot b)$ was assumed where a and b are the radii of the major and minor axes of the ellipse.

3.4.2. Influence of Radiation on Optical Fibres

The selected optical fibres have to withstand the prevailing radiation condition in space. Especially for JUICE a radiation dose of several Mrad is expected at the location of the optical fibres over the whole mission duration. Therefore, it is important to select radiation hardened optical fibres for this mission.
The performance of optical fibres under radiation depends on several factors like the dose rate, the total dose, the wavelength of the transmitted light, the ambient temperature as well as the optical power guided through the fibre [80]. Therefore, the actual performance of the fibre is hard to predict and radiation testing is required with parameters as close as possible to the expected environmental conditions.
In general, radiation can cause Radiation Induced Attenuation (RIA), Radiation Induced

Emission (RIE) and a change of the refractive index [81]. RIA is expected to have the highest impact on the fibre performance for the JUICE mission. RIA is caused by an increase of defects in the glass structure or the activation of pre-existing defects. Thus, RIA typically rises with the dose rate and total dose[81]. Due to the higher absorption inside the fibre, the transmitted optical power is reduced and in worst case no light can be transmitted through the fibre. RIA depends significantly on the operational as well as the environmental conditions of the fibre. At room temperature RIA is commonly lower because the generated defects can anneal but at lower temperatures the annealing process is reduced and thus the RIA is typically higher [82][83]. The optical fibres for the JUICE mission have to be qualified down to temperatures as low as $T = -190°\mathrm{C}$ and in combination with the estimated total dose values of several Mrad, most commercial optical fibres do not meet the requirements. At such low temperatures, the transmitted optical power during the irradiation is crucial for the resulting attenuation because the optical power can cause photobleaching which reduces the RIA [84]. Ideally, the magnetometer should be operated at the maximum laser power which in our case is about $P_{max} \approx 250\,\mu\mathrm{W}$. In contrast, measuring magnetic field strenghts lower than $B < 2\,\mu\mathrm{T}$ requires narrow CDSM resonance line widths which are obtained at low laser intensities (see section 4.3). Here a compromise between the optimised laser intensity value for the magnetic field measurement and the reduction of RIA has to be found.
Further, it was reported that RIA is higher at smaller wavelengths [85][86]. Thus, RIA measurements close to the used wavelength are required to be representative.
Moreover, the radiation tolerance of optical fibres can be improved by carefully choosing the composition of the materials and the manufacturing processes used. It starts already with the preform and the fibre fabrication. The preform deposition process, drawing speed and tension as well as the coating process influence the radiation hardness [80]. Ideally, the optical fibre should have as little as possible defects and impurities within its final structure. Additionally, the selected dopants of the fibre, which enable the light guidance, are very critical for the radiation response. Common materials used within optical fibres are germanium, phosphorous, boron and fluorine [87]. Step-index fibres with a dopant-free core as well as fluorine doped fibres showed the best radiation performance. Germanium doped fibres experienced higher radiation induced attenuation but saturated at a certain RIA level [81]. On the contrary, phosphorus doped fibres showed no saturation of the RIA and thus should be avoided [88].
Further, the hydrogen content within the fibre can improve the radiation tolerance [81].
The CDSM uses a graded-index fibre as outbound fibre which requires doping in the core to obtain the gradual refractive index distribution. A fibre with fluoride as dopant was selected. The inbound fibre is a step-index fibre which can be produced with a pure silica core to obtain low RIA.
RIE is either caused by luminescence from defects or Cherenkov radiation [81]. Compared to RIA, RIE is not expected to influence the performance of the magnetometer significantly because the additional light contributes to the background noise and is largely filtered by

the lock-in detection.
Also the refractive index change due to radiation is supposed to have a small influence on the performance of the magnetometer compared to RIA. The refractive index change can increase the attenuation and the intermodal dispersion, which would reduce the efficiency of the CPT resonance preparation (see section 3.4.1).

4. Parameters Influencing the Performance of the Coupled Dark State Magnetometer

The performance of the CDSM mainly depends on the line shapes of the CPT resonances which build the CDSM resonances. The CPT resonance line shape can be characterised by its amplitude, line width, zero crossing frequency and its symmetry properties. The accuracy of the magnetic field measurement is either influenced by a disturbing frequency shift of the zero crossing frequency or by an asymmetry of the resonance line shape [18][39]. It is assumed that the highest accuracy and best performance of the magnetometer is reached with an optimised amplitude-to-width ratio, symmetric resonance line shapes and by the suppression of disturbing frequency shifts. Therefore, the goal is to characterise parameters which affect the performance of the magnetometer and to optimise them.
The amplitudes and line widths of the CPT resonances are influenced by, e.g., the laser intensity and sensor cell temperature. The symmetry of the CPT resonances can be affected by the operational parameters of the laser (laser current and laser temperature) and an optical detuning of the laser frequency. Their influences on the CPT resonances and as a consequence on the CDSM resonances are discussed in section 4.1.
Additionally, the CDSM-based compensation effect of disturbing frequency shifts (see section 2.3.2) depends critically on the line shapes of the single CPT resonances forming the CDSM resonance. Ideally, the CPT resonances should have the same resonance line shape to obtain the best compensation. Resonance measurements have shown that the single CPT resonance line shapes are different for most sensor angles. Thus, the compensation effect is reduced at these sensor angles. Therefore, the impact of different CPT resonance line shapes on the compensation effect is discussed in more detail in section 4.2.
The optical pumping effect was assumed to mainly cause this imbalance. As a result, this effect is examined more closely and methods are discussed in order to balance its influence on the CPT resonances (see section 4.2.2).
A new sensor design was developed to reduce the influence of the unbalanced single CPT resonance line shapes on the compensation effect – the dual pass sensor (see section 3.3.3). A dual pass sensor unit was produced and first tests were performed. Measurements with both sensor designs, single and dual laser beam pass through the sensor cell (see section 3.3), are shown throughout this chapter.
Finally, this chapter includes investigations of the measurement accuracy in a low magnetic field range (from 0 to 2 µT). In this field range the CPT and CDSM resonances start

to superimpose and influence each other depending on their overall resonance structure. Therefore, the operational parameters of the magnetometer have to be selected carefully in order to keep the measurement accuracy in this low magnetic field range. The laser intensity, buffer gas pressure and the modulation frequency for the phase-sensitive detection of the resonances (see section 2.2.2) have the highest impact on the resonance structure. Additionally, due to the angular dependence of the CPT resonances (see section 4.1.7), the lower limit for accurate measurements showed a dependence on the sensor angle. In section 4.3 measurements performed in this low magnetic field range are summarised.

4.1. Influences on the CPT and CDSM Resonance Line Shapes

Typically, the detected CPT resonance has approximately a Lorentzian line shape [15] or the first derivative of it (see section 2.2.2). The line shape is characterised by its amplitude, line width, zero crossing frequency and the resonance symmetry. For several considerations, the slope at the zero crossing frequency is also analysed. The definitions of resonance amplitude and line width are equal for the CPT and CDSM resonances. Since the CDSM uses the quadrature signal for the measurement of the external magnetic field strength (see section 2.3.2), typically the amplitude and line width of this quadrature signal are analysed. An exemplary CDSM resonance structure is shown in figure 4.1 which was detected by using Frequency Modulation Spectroscopy (FMS) (see section 2.2.2).
In figure 4.1(a) the CDSM resonance structure is depicted which consists of the carrier structure (in the middle) and one sideband each at the modulation frequency $\nu_{B_{FMS}}$ on the left and right side of the carrier structure.
In figure 4.1(b) the carrier structure including the definitions of amplitude and line width is shown. The amplitudes of the CPT resonances Δh_{CPT} and the CDSM resonances Δh_{CDSM} are defined equally as the peak-to-peak distance between the minimum and maximum of the quadrature signal. Further, the line widths of the CPT resonances $\Delta\nu_{CPT}$ and CDSM resonances $\Delta\nu_{CDSM}$ are determined by the frequency spacing between the minimum and maximum of the quadrature signal. For the comparison of specific CPT and CDSM resonances, the height Δh_n and line width $\Delta\nu_n$ are label with their respective resonance number n (see sections 2.1.2.2 and 2.3.2).
The zero crossing frequency of the quadrature signal is used for the detection of the external magnetic field strength. Disturbing influences on the position of the zero crossing frequency cause a shift of the detected frequency and thus add a systematic uncertainty to the determined magnetic field strength. These shifts can result directly from a change in the transition frequency or indirectly by a change of the resonance line shape [18][39]. Therefore, the symmetries of the resonance line shapes have to be considered when investigating the accuracy of the magnetometer.

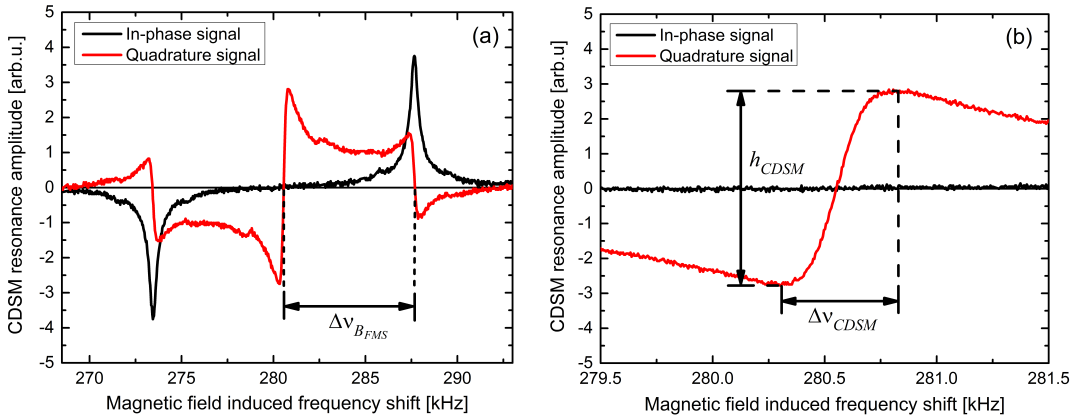

Figure 4.1.: CDSM resonance structure including the definitions of amplitude h_{CDSM} and line width $\Delta\nu_{CDSM}$: In figure (a) the overall CDSM resonance structure consisting of the carrier structure (middle) and two sideband structures at the modulation frequency $\nu_{B_{FMS}} = 7.102\,\text{kHz}$ is illustrated. Figure (b) shows the carrier structure of the CDMS resonance whose zero crossing frequency is used to determine the external magnetic field. The CDSM resonance $n = 2$ was measured with the CSES FS electronics (see section 2.4.3.1) and the dual pass sensor at a sensor angle $\phi = 0°$. A magnetic field of $B = 19.9\,\mu\text{T}$ was applied. The Rb cell contained neon as buffer gas at a pressure of $P_{BG} = 8.0\,\text{kPa}$ (60 Torr). The sensor cell temperature was $T = 24.2°\text{C}$. The intensity was $I \approx 100\,\mu\text{W/cm}^2$.

The symmetry of the CDSM resonance line shape depends on the symmetry of the CPT resonance line shapes, which form the CDSM resonance. Ideally, the CPT resonance line shapes should be symmetric in order to obtain a symmetric CDSM resonance. However, asymmetries of the CPT resonance line shapes can be partially compensated when forming the CDSM resonance (see figure 4.2).
Figure 4.2(a) shows the single CPT resonance structures of $n = -2$ and $n = +2$ which build the CDSM resonance structure $n = 2$ illustrated in figure 4.2(b). The single CPT resonances are measured by introducing such a large detuning Δ that the CDSM resonance splits into its single CPT resonances (see section 2.3.2). The line shape asymmetries of the single CPT resonances are caused either by, e.g., imbalanced Rabi frequencies used for the excitation of the Λ system (see section 4.1.4) or by an optical detuning (see section 4.1.5).

Since the operational parameters of the magnetometer significantly affect the CPT resonance line shapes and as a result the CDSM resonance line shapes, the influence of most important operational parameters is discussed in this section.
First, the impact of the laser intensity on the CPT and CDSM resonance line shapes is described in section 4.1.1. The laser intensity influences the amplitudes, line widths and the zero crossing frequencies by the light shift.

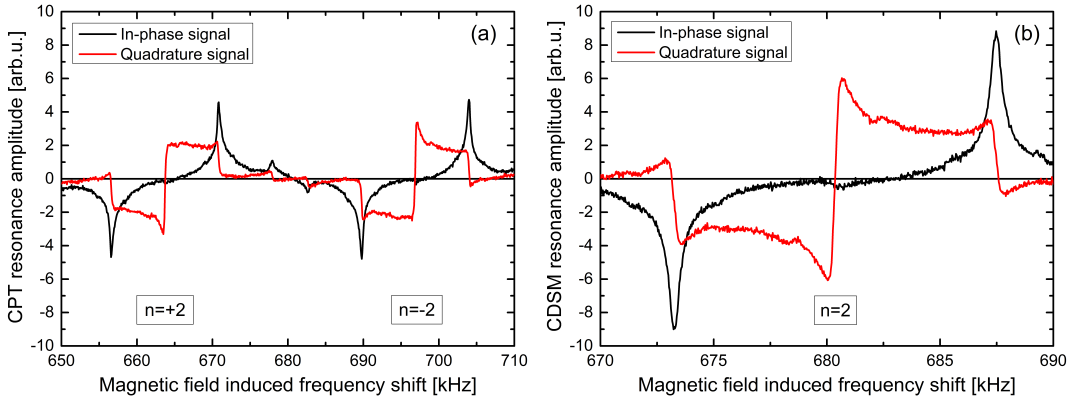

Figure 4.2.: Asymmetrical CPT resonance line shapes forming a symmetrical CDSM resonance line shape: Figure (a) shows the asymmetrical CPT resonance line shapes of $n = -2$ and $n = +2$ which form the symmetrical CDSM resonance line shape $n = 2$ depicted in (b). The resonance line shapes were measured with the dual pass sensor and the CSES QM electronics in Earth's magnetic field ($B \approx 48.5\,\mu T$) at the Conrad observatory (see section A.4.2). The sensor cell contained neon as buffer gas at a pressure of $P_{BG} = 8.0\,kPa$ (60 Torr). A laser power of $P_{PD} = 24\,\mu W$ was detected at the photodiode (see section 2.2.1). The sensor cell was heated to a temperature of $T = 30.8°C$. For the detection, a modulation frequency of $\nu_{B_{FMS}}$=7.102 kHz was applied.

Further, in section 4.1.2 the impact of a magnetic field inhomogeneity on the line shapes of the CPT resonances is briefly discussed.
Then, in section 4.1.3 the effects of the buffer gas on the optical transitions as well as on the CPT and CDSM resonance line shapes are summarised. For the operation of the CDSM, neon is added as buffer gas to narrow the CPT resonance line widths.
In the following section 4.1.4, the impact of the laser operational parameters (laser current and laser temperature) and the microwave power level on the CPT and CDSM resonances is discussed. These parameters can be used to change the intensity distribution in the laser sideband structure. Thus, they affect the amplitudes, line widths, the symmetry as well as the light shift.
Additionally, in section 4.1.5, the influence of an optical detuning on the line shapes is discussed. Especially, the optical detuning impacts the symmetries of the line shapes and the light shift of the CPT and CDSM resonances a(see section 4.1.1.2).
Furthermore, the non-linear dependence of the CPT resonance position on the external magnetic field is outlined in section 4.1.6. The non-linear dependence can have an influence on the measurement accuracy of the CDSM. Therefore, the strategy to compensate its effect on the magnetic field measurement is discussed.
Moreover, the angular dependence of the CPT and CDSM resonance line shapes is reviewed in section 4.1.7. In particular, the change of the CPT and CDSM resonance amplitudes in dependence of the sensor angle is discussed. At certain angles the CDSM resonance

amplitudes vanish. As a consequence, switching between the CDSM resonances is required to obtain an omni-directional magnetic field measurement.

4.1.1. Laser Intensity

The laser intensity I influences the amplitudes, line widths and the zero crossing frequencies of the CPT resonances and as a consequence affects the line shapes of the CDSM resonances. First, the dependence of the resonance amplitude and line width on the laser intensity is discussed. Second, the dependence of the zero crossing frequency on the laser intensity – the light shift – is reviewed.

4.1.1.1. Intensity Dependence of the Resonance Line Shapes

Calculations for the symmetric three level system predict that the theoretical line shape of the CPT resonance is Lorentzian and their amplitude h_{CPT} and line width $\Delta\nu_{CPT}$ are given by [15][23]

$$h_{CPT} \propto n_{Rb}\,\frac{g^4}{\Gamma^2}\,\frac{1}{2\Gamma_{12}+g^2/\Gamma}\,, \tag{4.1}$$

$$\Delta\nu_{CPT} = 2\Gamma_{12} + \frac{g^2}{\Gamma}\,, \tag{4.2}$$

where n_{Rb} is the number density of Rb atoms in the gaseous phase, g is the effective Rabi frequency ($g^2 \propto I$), Γ is the decay rate of the excited state and Γ_{12} is the decay rate of the ground state coherence. The effective Rabi frequency g is given by $g = \sqrt{(g_1^2 + g_2^2)}$ [3] where g_1 and g_2 are the Rabi frequencies of the two transitions forming the Λ system, which are in the symmetric three level system assumed to be equal ($g_1 = g_2$).
Further, the quantity $G{=}g^2/I$ [15] is introduce and equations 4.1 and 4.2 are rearranged to

$$h_{CPT} \propto n_{Rb}\,\frac{G^2I^2}{\Gamma^2}\,\frac{1}{2\Gamma_{12}+(GI)/\Gamma}\,, \tag{4.3}$$

$$\Delta\nu_{CPT} = 2\Gamma_{12} + \frac{G}{\Gamma}\,I\,. \tag{4.4}$$

As can be seen from equation 4.3, for laser intensities $I < \Gamma_{12}\,\Gamma/G$, the CPT resonance amplitude has a square dependence on the laser intensity but for higher intensities, the amplitude increases linearly with the laser intensity [15][89]. Additionally, the amplitude depends on the number density n_{Rb} of Rb atoms in the gaseous phase which contribute to the CPT resonance preparation.

The CPT resonance line width $\Delta\nu_{CPT}$ has a linear dependence on the laser intensity (see equation 4.4). Theoretically, for zero laser intensity, the resonance line width corresponds to two times the decay rate of the ground state coherence Γ_{12}.
During measurements on the intensity dependence, the optical power was detected via the photodiode of the electronics unit (see figure 2.16). The optical power in front of the sensor cell was calculated using a prior measurement where the relation between the optical power in front of the sensor cell and the optical power at the photodiode was determined. Then, the laser intensity in front of the sensor cell was calculated from the optical power as described in section 3.4.1. Therefore, throughout this thesis, the term laser intensity refers to the intensity in front of the sensor cell.

The measurements in this section were performed with a dual pass sensor (see section 3.3.3) and the CSES FS electronics (see sections 2.4.2 and 2.4.3.1). The dual pass sensor was modified such that it allowed either coupling into the inbound fibre after one laser beam pass through the sensor cell or after two passes. Thus, the influence of the second laser beam pass on the resonance line shapes could be studied.
The dual pass cell contained neon as buffer gas at a pressure of $P_{BG} = 8.0\,\text{kPa}$ (60 Torr) (see appendix A.2). For these measurements, the sensor unit was mounted in a magnetic shielding can at the Space Research Institute in Graz (see appendix A.4.1). A magnetic field of $B = 19.9\,\mu\text{T}$ was applied. The magnetic field direction and the laser propagation direction were equal (sensor angle $\phi = 0°$). The light field at the sensor cell was circularly polarised. An additional polarising beam splitter cube was mounted in front of the polarisation optics in the sensor unit in order to reduce the laser intensity. A reduction of the laser intensity is obtained by tilting the additional polarising beam splitter cube. A modulation index of $M_{mod_1} = 1.6$ was measured for the first modulation signal with the set laser parameters ($I_L = 2.620\,\text{mA}$ and $T_L = 39.6°C$) and a microwave power level of $P_{mod_1} = -7.9\,\text{dBm}$ [90] (see sections 2.3.2 and 4.1.4). The modulation index of the second modulation signal was set to $M_{mod_2} \approx 1$.

In figure 4.3 the amplitudes h_n and line widths $\Delta\nu_n$ of the CPT resonances $n = 0$, -2 and $+2$ as well as the CDSM resonance $n = 2$ are shown for a single laser beam pass through the sensor cell. Less data points are depicted for the CPT resonance $n = 0$ than for $n = -2$ and $n = +2$ because for intensities higher than $70\,\mu\text{W/cm}^2$, the resonance line shapes of $n = 0$ were such broadened that the detected carrier structure was no longer well separated from its sideband structures at $\nu_{MW_{FMS}}$. For that reason, the determination of the amplitudes and line widths was not possible at these laser intensities. This influence just affected the CPT resonance line shape of $n = 0$, since a lower modulation frequency is used for the detection of the CPT resonance $n = 0$ via FMS ($\nu_{MW_{FMS}} = 1.905\,\text{kHz}$) compared to the CPT resonances $n = -2$ and $n = +2$ ($\nu_{B_{FMS}} = 7.102\,\text{kHz}$). Thus, for the CPT resonances $n = -2$ and $n = +2$, the carrier and sideband structures are better separated (see figure 4.1(a)).

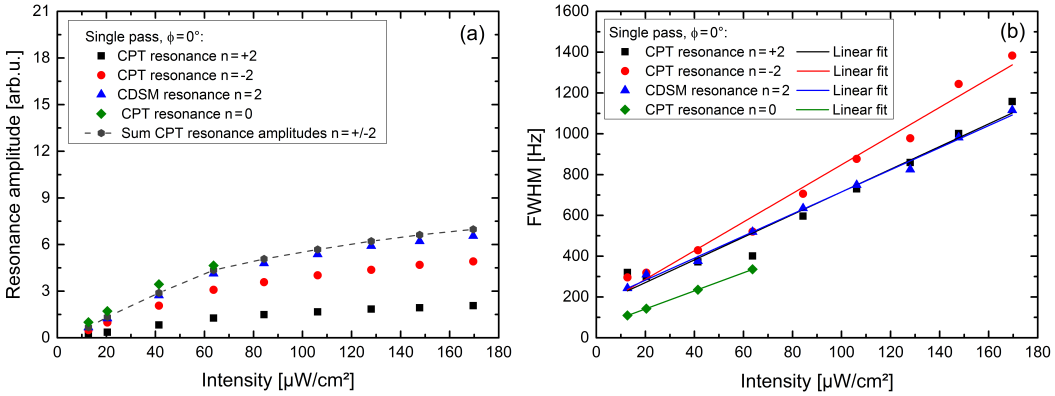

Figure 4.3.: CPT resonance amplitudes and line widths for a single pass through the sensor cell at $\phi = 0°$: In (a) the CPT resonance amplitudes of $n = 0$, -2 and $+2$ as well as the CDSM resonance amplitude of $n = 2$ are depicted in dependence of the laser intensity. In (b) the intensity dependence of the line width is shown for the same set of resonances. The measurement was performed with a dual pass cell containing a buffer gas (Ne) at a pressure of $P_{BG} = 8.0\,\mathrm{kPa}$ (60 Torr). The sensor cell temperature was $T = 24°\mathrm{C}$. A magnetic field of $B = 19.9\,\mu\mathrm{T}$ was applied.

In figure 4.3(a) the amplitudes are shown in dependence of the laser intensity. Further, in table 4.1 the mean CPT resonance amplitude ratios are compared for $n = 0$, -2 and $+2$.

Table 4.1.: Mean CPT resonance amplitude ratios for a single laser beam pass through the sensor cell at a sensor angle of $\phi = 0°$ for the measurements shown in figure 4.3. The CPT resonance amplitudes of $n = 0$, -2 and $+2$ are compared with each other.

n_1	n_2	h_{n_1}/h_{n_2}
0	-2	1.7 ± 0.3
0	$+2$	4.5 ± 0.8
-2	$+2$	2.49 ± 0.14

The CPT resonance amplitude h_0 was higher compared to the amplitudes h_{-2} and h_{+2}, since different laser sidebands are used for the CPT resonance excitation (see section 2.3.2). In contrast, for the excitation of the CPT resonances $n = -2$ and $n = +2$, it is assumed that each resonance is prepared by one sideband from the first and one sideband from the second modulation step. Thus, approximately the same intensities are used for the CPT resonance preparation of $n = -2$ and $n = +2$ and their amplitudes can be compared directly.
The CPT resonance amplitude h_{-2} was about a factor of 2.5 higher than h_{+2} within the measurement range. These deviations can be explained by two possible effects.

First, the effective Rabi frequencies g for the two Λ systems of $n = -2$ and $n = +2$ can vary due to different transition strengths. Information on the effective Rabi frequencies can be gained by measurements on the CPT resonance line width as a function of the laser intensity and by applying a linear fit to the measurement results according to equation 4.2 (see results further below).
Second, as shown in [91], the optical pumping effect can alter the ground states population distribution and thus change the CPT resonance line shapes (see section 4.2.2). Since the CPT resonance amplitudes h_{-2} were higher than h_{+2}, transitions from the ground states to the excited states with a lower magnetic quantum number were excited (σ^- transitions), which also indicates the optical pumping direction. Therefore, more atomic population accumulates in the ground states of the CPT resonance $n = -2$ compared to the ground states of $n = +2$. As a consequence, the CPT resonance $n = -2$ has a higher amplitude. Furthermore, the CPT resonance amplitudes revealed a saturation behaviour with increasing laser intensity (see figure 4.3(a)). This trend deviates from the predictions obtained from the symmetric three level Λ system. In reference [92] a saturation of the CPT resonance amplitude was found as a result of the optical pumping effect in an open system. In terms of CPT resonance preparation, an open system is a system where the population of the three level Λ system interacts with at least one further level which is not required for the CPT effect preparation [92].
The hyperfine structure of the ^{87}Rb D_1 line even consists of 16 energy levels (see figures 2.2 and 2.11). Due to the use of circularly polarised light – in our case here σ^- transitions are induced – the population is pumped to the ground state with the lowest magnetic quantum number ($F = 2$, $m_F = -2$). Thus, the saturation of the CPT resonance amplitudes can be explained by the optical pumping of the ground states population into this natural trapping state where it can no longer contribute to the CPT resonance preparation. As a result, the increase of the CPT resonance amplitudes with the laser intensity is reduced.

In figure 4.3(a) the CDSM resonance amplitude of $n = 2$ is plotted in dependence of the laser intensity. Ideally, the CPT resonance amplitudes of $n = -2$ and $n = +2$ add up to the CDSM resonance amplitude $n = 2$. If the single CPT resonances are split due to a detuning Δ (see equation 2.42 and figure 2.13), the CDSM resonance amplitude should be less than the sum of the two CPT resonance amplitudes. For comparison, the sums of the CPT resonance amplitudes are included in figure 4.3(a)(grey dashed line). The measured CDSM resonances amplitudes were lower by about 6% compared to the calculated CDSM resonance amplitude. This difference can result from the influence of the quadratic magnetic field shift which was not compensated for these measurements (see section 4.1.6) and caused a detuning Δ of about 5.7 Hz.

In figure 4.3(b) the results on the intensity dependence of the line widths $\Delta\nu_n$ are compared for the CPT resonances $n = 0$, -2 and $+2$ as well as the CDSM resonance $n = 2$. The simple three level model predicts a linear increase of the line width with the laser intensity

(see equation 4.4). Therefore, a linear fit was applied to the measurement results according to equation 4.4 and the obtained coefficients are summarised in table 4.2.

Table 4.2.: Linear fit coefficients for a single laser beam pass through the sensor cell at a sensor angle of $\phi = 0°$: A linear fit according to equation 4.4 was applied to the measurement results shown in figure 4.3. That way, the ground state coherence decay rates Γ_{12_n} and the ratio $(G/\Gamma)_n$, which indicates the broadening of the resonance line width, were determined for the CPT resonances $n = 0$, -2 and $+2$ as well as the CDSM resonance $n = 2$.

n	$2{\cdot}\Gamma_{12_n}$ [Hz]	$(G/\Gamma)_n$ [Hz/(μW cm^{-2})]
0	52.7 ± 0.8	4.43 ± 0.02
-2	150 ± 40	7.0 ± 0.4
$+2$	160 ± 40	5.6 ± 0.4
2	174 ± 15	5.41 ± 0.15

The linear fit revealed equal values within the measurement uncertainty for the decay rates of the ground state coherences Γ_{12_n} for the CPT resonances $n = -2$ and $n = +2$ as well as for the CDSM resonance $n = 2$. The values of $\Gamma_{12_{-2}}$ and $\Gamma_{12_{+2}}$ were higher compared to Γ_{12_0}. This can be explained by a magnetic field inhomogeneity in the magnetic shielding can (see section 4.1.2) which broadens the line widths of the CPT resonances $n = -2$ and $n = +2$ compared to $n = 0$.
Further, the line width broadenings with the laser intensity were different for the CPT resonances $n = -2$ and $n = +2$. The CPT resonance line width $\Delta\nu_{-2}$ was more broadened than $\Delta\nu_{+2}$.

In order to explain the different broadenings of the CPT resonance line widths with the laser intensity, all possible Λ excitations schemes for σ^- transitions within the hyperfine structure of the ^{87}Rb D_1 line are listed in table 4.3 including the involved transition strength coefficients $c_{F',m'_F,F,m_F,q}$ and the calculated value G_n for the CPT resonance n (see equation 4.4). G_n was determined with the relation $G_n = g_n^2/I$ where $g_n = \sqrt{g_{1_n}^2 + g_{2_n}^2}$. The coefficients $c_{F',m'_F,F,m_F,q}$ and the Rabi frequencies were calculated as described in the appendix A.1.
In the case of σ^- transitions, the CPT resonance $n = -2$ can only be prepared with the excited state $F' = 2$. In contrast, the CPT resonances $n = 0$ and $n = +2$ can be established either with the excited state $F' = 1$ or $F' = 2$.
In order to compare the calculated values of G_n with $(G/\Gamma)_n$, which were obtained by the linear fit (see table 4.2), the decay rates of the excited states Γ_n have to be considered for the respective CPT resonance n. In the three level system (see section 2.1.1), the excited state decay rate Γ_n consists of the decay rates Γ_{31_n} and Γ_{32_n} of the excited state into the two ground states: $\Gamma_n = \Gamma_{31_n} + \Gamma_{32_n}$.

Table 4.3.: Comparison of possible Λ excitation schemes within the hyperfine structure of the ^{87}Rb D_1 line for σ^- transitions and the resulting values G_n for the respective Λ system. The coefficients $c_{F',m'_F,F,m_F,q}$ are related to the dipole matrix elements (see appendix A.1). The CPT resonances $n = 0$ and $n = +2$ can be formed with both excited states $F' = 1$ and $F' = 2$.

n	Λ	F	m_F	F'	m'_F	$c_{F',m'_F,F,m_F,q}$	G_n
							$[\mathrm{Hz}^2/(\mu\mathrm{W\,cm}^{-2})]$
+2	1	1	1	1	0	$-\sqrt{1/24}$	$14.5 \cdot 10^{-12}$
		2	1	1	0	$+\sqrt{1/8}$	
	2	1	1	2	0	$-\sqrt{1/24}$	$14.5 \cdot 10^{-12}$
		2	1	2	0	$+\sqrt{1/8}$	
0	1	1	0	1	−1	$-\sqrt{1/24}$	$7.3 \cdot 10^{-12}$
		2	0	1	−1	$+\sqrt{1/24}$	
	2	1	0	2	−1	$-\sqrt{1/8}$	$21.8 \cdot 10^{-12}$
		2	0	2	−1	$+\sqrt{1/8}$	
−2	1	1	−1	2	−2	$-1/2$	$29.1 \cdot 10^{-12}$
		2	−1	2	−2	$+\sqrt{1/12}$	

The decay rates of the hyperfine structure levels without external magnetic field can be calculated using equation A.2. In an external magnetic field, the hyperfine structure levels split into substates. In our case, the decay rates between the substates from the excited states to the ground states are mainly caused by collisions of the Rb atoms with the buffer gas atoms [93] (see also section 4.1.3.1). Therefore, they are assumed to be equal for the further discussion. With this assumption, the different line width broadenings of the CPT resonances $n = -2$ and $n = +2$ are mainly caused by the different effective Rabi frequencies.

Considering the CPT resonance preparations with the excited state $F' = 2$ and equal intensities of the laser sidebands preparing the CPT resonances $n = -2$ and $n = +2$, then the ratio G_{-2}/G_{+2} results a value of two. However, the intensities in the sidebands, which are used to prepare the CPT resonances $n = -2$ and $n = +2$, are assumed to be unequal, since the respective Λ system is established by one sideband from the first and one sideband from the second modulation step.

The intensity distribution between the different sidebands of the two modulation steps is estimated from the set modulation index M_{mod_2} which is about one. The amplitudes of the sidebands are proportional to the Bessel function of the first kind (see section 4.1.4). For the set modulation index, the laser intensity in the first-order sidebands of the second modulation step should be about a factor of three lower compared to the first-order sidebands of the first modulation step.

Thus, considering the intensity differences of the sidebands and the excitation scheme

depicted in figure 2.12(b), the ratio G_{-2}/G_{+2} still results a value of two.
Next, the ratio between $(G/\Gamma)_{-2}$ and $(G/\Gamma)_{+2}$ was determined from the fit values listed in table 4.2. The result yielded a value of 1.25±0.12 with the assumption of equal decay rates Γ.
The obtained ratio $(G/\Gamma)_{-2}/(G/\Gamma)_{+2}$ deviates from the estimated value G_{-2}/G_{+2}. This can indicate that the application of the three level model, which neglects the interaction with other levels of the hyperfine structure by, e.g., the optical pumping effect, is not appropriate to interpret the results or that the assumption of equal decay rates from the excited state is not correct or that another effect influenced the measured CPT resonance line widths.
For example, the CPT resonance line shapes of $n = 0$ and $n = +2$ could have been influenced by the formation of a second CPT resonance build with the excited state $F' = 1$ [94] due to the influence of a two-photon detuning ($\delta_L \neq 0$ – see equation 2.2 and section 4.1.5). In case of a two-photon detuning, the respective profile of the detected CPT resonances $n = 0$ and $n = +2$ can consist of a superposition of two CPT resonances (see section 4.1.5). Thus, the detected signal can differ from the predicted line shape by the three level system. In contrast, CPT resonance $n = -2$ can just be prepared with $F' = 2$ (see table 4.3) but its line shape can also be altered by a two-photon detuning [39].
Furthermore, the laser beam profile after the multi-mode fibre typically differs from the ideal Gaussian line profile (see section 3.4.1). This changing transversal laser beam profile can influence the CPT resonance line shape [75].
Therefore, further investigations are required. Especially, the case in which the three level Λ systems are established simultaneously by the multi-modulated laser light field (see section 2.3.2) as well as their possible interactions has to be studied.

In figure 4.4 the amplitudes h_n and line widths $\Delta\nu_n$ of the CPT resonances $n = 0$, -2 and $+2$ and the CDSM resonance $n = 2$ are depicted in dependence of the laser intensity for a dual laser beam pass through the sensor cell at the sensor angle $\phi = 0°$. The dual pass sensor design aims at a balancing of the CPT resonance line shapes by reducing the impact of the optical pumping effect (see section 4.2.2) and by equalising the different Rabi frequencies for the CPT resonance preparation of $n = -2$ and $n = +2$. Thus, the compensation of disturbing frequency shifts by the CDSM resonance should be improved (see also section 4.2).

In figure 4.4(a) the amplitudes h_n are shown in dependence of the laser intensity. Further, in table 4.4 the mean ratios of the CPT resonance amplitudes are compared.
The CPT resonance amplitudes h_{-2} and h_{+2} were more balanced compared to the amplitudes obtained by the single laser beam pass. Additionally, the mean ratios of h_0/h_{-2} and h_0/h_{+2} were equal within the measurement uncertainty.

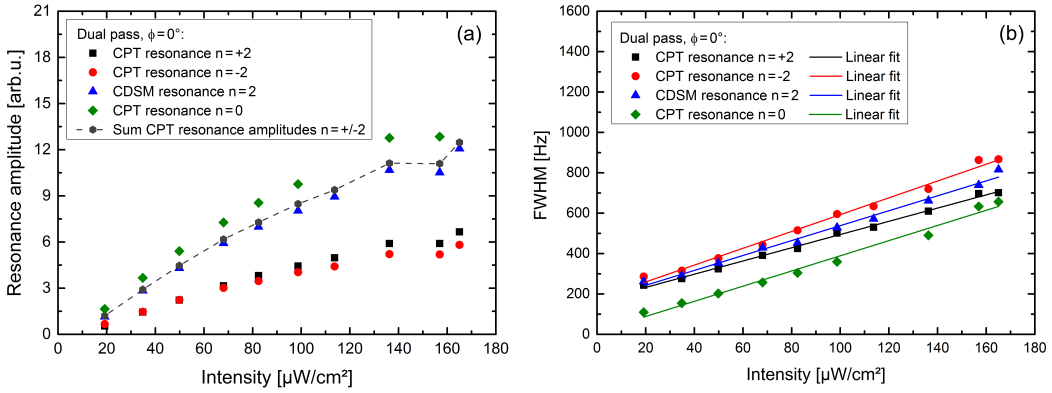

Figure 4.4.: CPT and CDSM resonance amplitudes and line widths for a dual laser beam pass through the sensor cell at the sensor angle $\phi = 0°$: In (a) the resonance amplitudes are shown in dependence of the laser intensity for the CPT resonances $n = 0$, -2 and $+2$ as well as the CDSM resonance $n = 2$. In (b) the line widths of the same set of resonances are depicted. The measurements were performed with the CSES FS model and the dual pass sensor. The sensor cell contained neon as buffer gas at a pressure of $P_{BG} = 8.0\,\mathrm{kPa}$ (60 Torr). The sensor cell temperature was $T = 24°\mathrm{C}$. The sensor was mounted in a magnetic shielding can and a magnetic field of $B = 19.9\,\mu\mathrm{T}$ was applied.

Table 4.4.: Mean CPT resonance amplitude ratios for a dual laser beam pass through the sensor cell at a sensor angle of $\phi = 0°$: The CPT resonance amplitude ratios of $n = 0$, -2 and $+2$ are compared for the measurements shown in figure 4.4.

n_1	n_2	h_{n_1}/h_{n_2}
0	-2	2.45 ± 0.04
0	$+2$	2.4 ± 0.4
-2	$+2$	0.96 ± 0.12

Unexpectedly, the amplitude h_{+2} was slightly higher than the amplitude h_{-2}, since the contribution of the first cell pass should have a higher impact on the total resonance amplitude due to a higher optical intensity in the first pass compared to the second pass. Possible explanations can be that either an intensity imbalance in the laser sideband structure or a higher degree of the circular polarisation in the second pass caused this difference. The polarisation degree in the second pass can be altered due to, e.g., the reflections inside of the retroreflector.
The resonance heights h_n showed a saturation behaviour with increasing intensity similar to the case of the single laser beam pass (see figure 4.3). This is due to the fact that the CPT resonances prepared by each individual laser beam pass still experience the influence of the optical pumping effect. Just its overall effect on the resonance shapes is compensated by the dual laser beam pass through the sensor cell (see section 4.2.2).

Both CPT resonance amplitudes h_{-2} and h_{+2} increased compared to the single laser beam pass because the optical path length within the sensor cell was doubled. As a result, the CDSM resonance amplitudes were also enhanced for a dual pass. At the highest intensity of about 170 µW/cm^2, the CDSM resonance amplitude $n = 2$ was about a factor of two higher compared to the single pass measurement (compare figure 4.3).
In figure 4.4(a) the sums of the CPT resonance amplitudes (grey dashed line) are added to compare them with the measured CDSM resonance. The measured CDSM resonances were about 4% lower than the sum of the single CPT resonances which is again the result of the detuning caused by the quadratic magnetic field shift (see discussion above).

In figure 4.4(b) the resonance line widths $\Delta\nu_n$ are shown in dependence of the laser intensity for a dual laser beam pass through the sensor cell. Again a linear fit was applied according to equation 4.4 and the obtained fit parameters are listed in table 4.5.

Table 4.5.: Linear fit coefficients for a dual laser beam pass through the sensor cell at a sensor angle of $\phi = 0°$. A linear fit according to equation 4.4 was applied to the results depicted in figure 4.4(b). Γ_{12_n} is the ground state coherence decay rate and $(G/\Gamma)_n$ gives the broadening of the resonance line width with the laser intensity.

n	$2{\cdot}\Gamma_{12_n}$ [Hz]	$(G/\Gamma)_n$ [Hz/(µW cm^{-2})]
0	13 ± 18	3.76 ± 0.17
-2	177 ± 14	4.16 ± 0.14
$+2$	167 ± 8	3.27 ± 0.07
2	169 ± 14	3.76 ± 0.17

The ground state coherence decay rates Γ_{12_n} listed in tables 4.2 and 4.5 for a single and a dual laser beam pass through the sensor cell were equal within the measurement uncertainty. The ground state coherence decay rate of the CPT resonances $n = -2$ and $n = +2$ are again affected by a magnetic field inhomogeneity (see section 4.1.2). As will be shown in section 4.1.2, at $\phi = 0°$ the CPT resonance line widths are mainly broadened due to a magnetic field gradient along the optical path. In this case, the CPT resonances experience an almost identical shift by the magnetic field gradient during the first and second laser beam pass through the sensor cell. As a result, the magnetic field inhomogeneity has approximately the same effect on the line width for a single and a dual laser beam pass.
The fit parameters in table 4.5 revealed a lower line width broadening with the laser intensity compared to the values obtained for a single laser beam pass (compare table 4.2). The reduction of the broadening for a dual pass can be explained by an intensity reduction along the optical path due to absorption. Since according to Beer's law the intensity reduces along the optical path, the line width broadening also decreases respectively.

Therefore, the measured line width, which is the mean line width over the whole optical path, was narrower for a dual laser beam pass compared to a single laser beam pass through the sensor cell.
Further, the ratio between $(G/\Gamma)_{-2}$ and $(G/\Gamma)_{+2}$ from table 4.5 results in 1.27±0.06 which is almost equal to the obtained ratio for a single pass (see table 4.2). It was expected that the differential line width broadening of the CPT resonances was more balanced for a dual pass compared to a single pass. By the dual pass, an equalisation of the Rabi frequencies and a compensation the optical pumping effect should be achieved. However, the CPT resonance prepared by each single pass of the sensor cell still experiences the influence of the optical pumping effect and just the overall effect should be compensated. Thus, further investigations are required as was already pointed out during the discussion of the measurement results for a single lase beam pass further above.

In figure 4.5 the amplitudes h_n of the CPT resonances $n = 0$, -2, $+2$, -3 and $+3$ as well as the CDSM resonances $n = 2$ and $n = 3$ are compared for a dual laser beam pass at a sensor angle of $\phi = 45°$. In this configuration σ^-, σ^+ and π transitions are excited simultaneously. Thus, several combinations of transitions can form the same CPT resonance n.

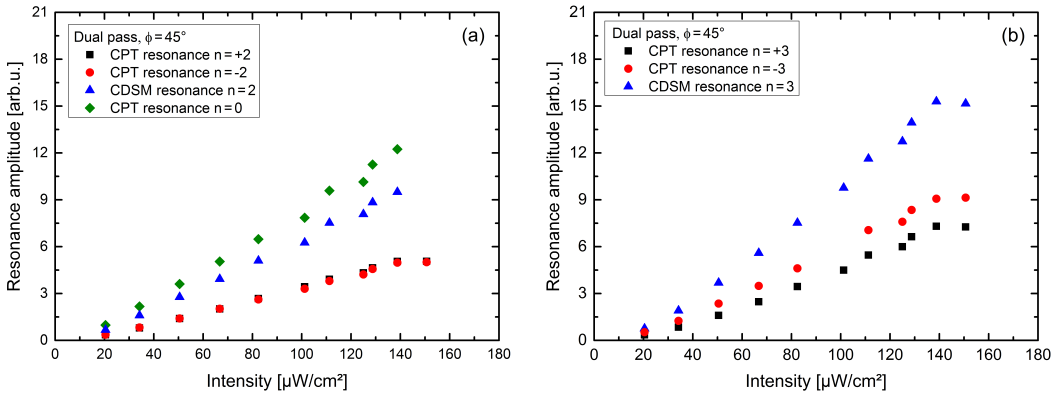

Figure 4.5.: Comparison of the CPT and CDSM resonance amplitudes at $\phi = 45°$ for a dual laser beam pass: In (a) the CPT resonance amplitudes of $n = 0$, -2 and $+2$ and the CDSM resonance $n = 2$ are shown. In (b) the CPT resonance amplitudes $n = -3$ and $n = +3$ as well as the CDSM $n = 3$ are depicted. The dual pass cell contained neon as buffer gas at a pressure of $P_{BG} = 8.0\,\text{kPa}$ (60 Torr). The sensor cell temperature was $T = 24°\text{C}$. A magnetic field of $B = 19.9\,\mu\text{T}$ was applied.

As can be seen in figure 4.5(a), the slight CPT resonance amplitude difference between h_{-2} and h_{+2}, which was seen at $\phi = 0°$ (see figure 4.4(a)), was balanced. In contrast, the CPT resonance amplitudes h_{-3} and h_{+3} shown in figure 4.5(b) revealed an imbalance of about $20 - 30\%$ within the depicted intensity range. Additionally, the CPT resonance amplitudes h_{-3} and h_{+3} were higher compared to the amplitudes h_{-2} and h_{+2} at this

sensor angle. As a result, the CDSM resonance amplitudes h_2 and h_3 differed by about 40% at the highest intensity.
The saturation behaviour of the CPT resonance amplitudes was less pronounced compared to $\phi = 0°$. This is due to the fact that now σ^-, σ^+ and π transitions are excited which reduces the influence of the optical pumping effect.

In figure 4.6 the line widths $\Delta\nu_n$ of the CPT resonances $n = 0$, -2, $+2$, -3 and $+3$ and of the CDSM resonances $n = 2$ and $n = 3$ are compared at a sensor angle of $\phi = 45°$.

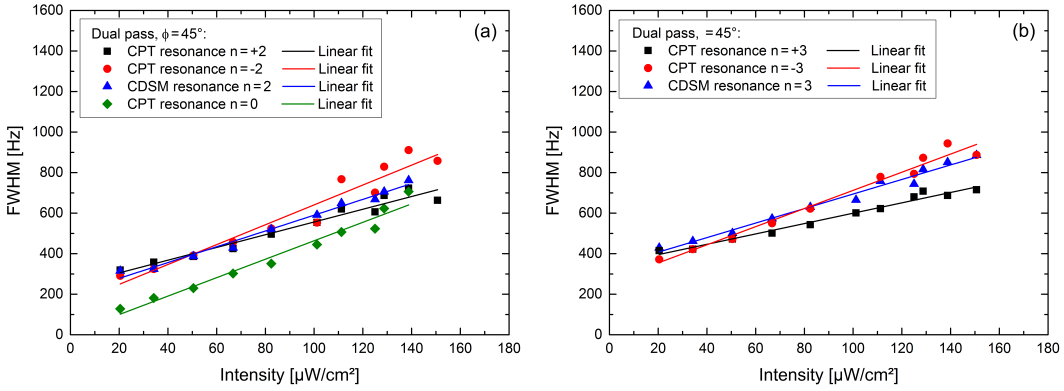

Figure 4.6.: CPT and CDSM resonance line widths for a dual laser beam pass through the sensor cell at $\phi = 45°$: In (a) the measured line widths are depicted for the CPT resonances $n = 0$, -2 and $+2$ as well as the CDSM resonance $n = 2$. In (b) the line widths are shown for the CPT resonances $n = -3$ and $n = +3$ as well as the CDSM resonance $n = 3$. The dual pass cell contained neon as buffer gas at a pressure of $P_{BG} = 8.0\,\text{kPa}$ (60 Torr). The sensor cell had a temperature of $T = 24°\text{C}$. A magnetic field of $B = 19.9\,\mu\text{T}$ was applied.

A linear fit was applied to the measurement results according to equation 4.4. The coefficients of the linear fits are summarised in table 4.6.
The ground state coherence decay rate Γ_{12_n} was higher for the CPT resonances $n = +3$ and $n = -3$ than for the CPT resonances $n = +2$ and $n = -2$ due to a magnetic field gradient which influences the CPT resonances differently depending on their magnetic quantum number m_F (see section 4.1.2). The CPT resonances with a higher magnetic quantum number experience a higher shift with the external magnetic field and hence are also more broadened by a magnetic field inhomogeneity. The line strengths of the CPT resonances are preserved [18]. As a consequence, the amplitudes of CPT resonances with a higher magnetic quantum number are also more reduced.
Although the difference between the amplitudes h_{-2} and h_{+2} vanished at this sensor angle, there was still a different broadening behaviour of the CPT resonances $n = -2$ and $n = +2$ with the laser intensity. The ratio between $(G/\Gamma)_{-2}$ and $(G/\Gamma)_{+2}$ was 1.56 ± 0.20 which was higher than for $\phi = 0°$. Further, the ratio between $(G/\Gamma)_{-3}$ and $(G/\Gamma)_{+3}$ was 1.75 ± 0.14.

Table 4.6.: Linear fit coefficients for a dual laser beam pass of the sensor cell at a sensor angle of $\phi = 45°$ for the measurements shown in figure 4.6.

n	$2{\cdot}\Gamma_{12_n}$ [Hz]	$(G/\Gamma)_n$ [Hz/(μW cm^{-2})]
0	10 ± 30	4.6 ± 0.3
−2	150 ± 50	4.9 ± 0.5
+2	240 ± 30	3.14 ± 0.24
2	200 ± 16	3.90 ± 0.17
−3	270 ± 30	4.48 ± 0.25
+3	344 ± 13	2.56 ± 0.13
3	336 ± 17	3.59 ± 0.17

The optimal laser intensity for the operation of the CDSM is assumed to be the intensity where the slope of the CDSM resonance is highest and thus the highest sensitivity is reached [18]. Additionally, the slopes of the CPT resonances can be used to estimate the efficiency of the CDSM-based compensation (see also section 4.2). Ideally, the CPT resonance line shapes, which build the CDSM resonance, should be identical in order to obtain the best compensation of disturbing frequency shifts.
For the further discussion, the slopes of the CPT resonances were approximated via the ratio of the CPT resonance amplitude h_n and its line width $\Delta\nu_n$. In figure 4.7 the slopes of the CPT resonances $n = -2$ and $n = +2$ as well as the CDSM resonance $n = 2$ are compared for a single and a dual laser beam pass through the sensor cell at $\phi = 0°$.

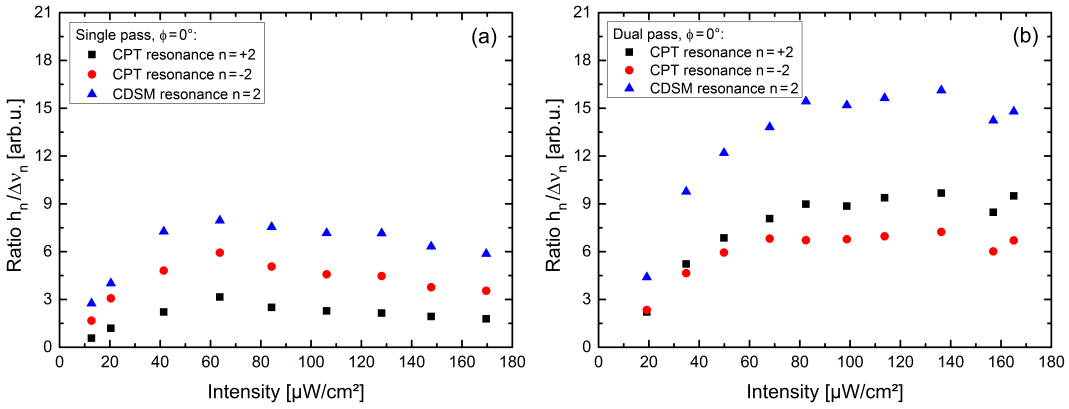

Figure 4.7.: Comparison of the CPT and CDSM resonance slopes for a single and a dual laser beam pass at the sensor angle $\phi = 0°$: The slope was approximated by the ratio of the CPT or CDSM resonance amplitude and its line width. In (a) the measurement results of figure 4.3 were used to estimate the slope of the respective resonances for a single laser beam pass. In (b) the results for a dual laser beam pass from figure 4.4 were used to approximate the slopes.

In figure 4.7(a) the slopes are shown in dependence of the laser intensity for a single laser beam pass. The slopes increased with the laser intensity up to a value of about $60\,\mu W/cm^2$ but then reduced again. Thus, the ideal laser intensity for a single pass is $I_{opt} \approx 60\,\mu W/cm^2$ at $\phi = 0°$. The slope of the CPT resonance $n = -2$ was about $50 - 60\%$ higher than the slope of $n = +2$.
In figure 4.7(b) the slopes of the CPT resonances $n = -2$ and $+2$ as well as the CDSM resonance $n = 2$ are shown for a dual laser beam pass of the sensor cell. For a dual laser beam pass, the slopes increased up to the laser intensity of about $80\,\mu W/cm^2$ and slightly decreased again above $I = 140\,\mu W/cm^2$. Thus, the optimal laser intensity is between $I_{opt} = 80\,\mu W/cm^2$ and $I_{opt} = 140\,\mu W/cm^2$ for a dual pass at $\phi = 0°$.
The slopes of the CDSM resonance $n = 2$ were about a factor of two higher for a dual pass compared to a single pass due to the overall higher resonance amplitudes and the smaller line widths.
The slopes of $n = -2$ and $n = +2$ revealed an imbalance of about $25 - 30\%$ above $80\,\mu W/cm^2$. The imbalance between the slopes of the CPT resonances $n = -2$ and $n = +2$ was reduced by a factor of two for a dual pass compared to a single laser beam pass. Therefore, an improve of the CDSM performance is expected by using the dual pass sensor instead of the CSES sensor, whose functional principle is based on a single laser beam pass design (see section 3.3).

In figure 4.8 the slopes of the CPT resonances $n = -2$, $+2$, -3 and $+3$ as well as the CDSM resonances $n = 2$ and $n = 3$ in dependence of the laser intensity are compared for a dual laser beam pass through the sensor cell at a sensor angle of $\phi = 45°$.

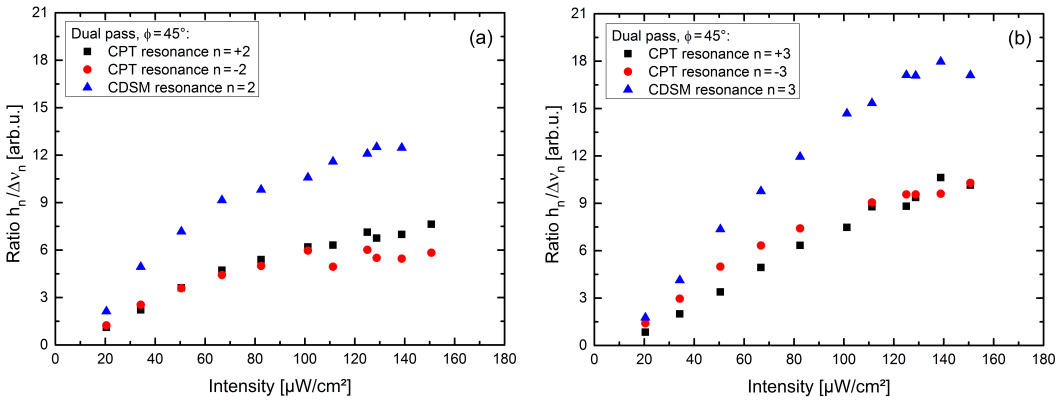

Figure 4.8.: Comparison of the CPT resonance and CDSM resonance slopes at $\phi = 45°$ for a dual laser beam pass: The measurement results from figures 4.5 and 4.6 were used to approximate the slope of the resonances. In (a) the slope of the CPT resonances $n = -2$ and $n = +2$ as well as the CDSM resonance $n = 2$ are shown. In (b) the slope for the CPT resonances $n = -3$ and $n = +3$ as well as the CDSM resonance $n = 3$ are displayed.

As can be seen in figure 4.8(a), the slopes of the CPT resonances $n = -2$ and $n = +2$ as well as the CDSM resonance $n = 2$ increased with the laser intensity until they flattened above $60\,\mu W/cm^2$. In comparison, in figure 4.8(b) the slopes of the CPT resonances $n = -3$ and $n = +3$ as well as the CDSM resonance $n = 3$ showed this flattening at higher laser intensities ($I > 100\,\mu W/cm^2$).
The slopes of the CPT resonances $n = -2$ and $n = +2$ were almost equal until an intensity of about $100\,\mu W/cm^2$. Above this value the slopes revealed an imbalance of about 20%. On the contrary, the slopes of $n = -3$ and $+3$ were unequal at lower intensities and balanced for intensities higher than $I > 100\,\mu W/cm^2$.
The slope of the CDSM resonance $n = 3$ was about 30% higher compared to the slope of $n = 2$. Therefore, the CDSM resonance $n = 3$ would be preferable for the operation of the magnetometer at $\phi = 45°$ for a dual laser beam pass.

4.1.1.2. Light Shift

The shift of the transition frequency due to the interaction of the laser light field with the atom is called light shift [95]. For the symmetric three level Λ system (see section 2.1.1), it is assumed that only two light fields interact with the two transitions of the Λ scheme which also have equal Rabi frequencies. In such a system, the CPT resonance position should be independent of the laser intensity, since the atoms in the dark state do not interact with the light field [18]. Nevertheless, a residual light shift can result either from an imbalance between the Rabi frequencies of the two transitions or due to a laser detuning [96].
The light shift of a single level $\Delta\nu_{LS_i}$ caused by a laser light field with frequency ν_L is given by [29][97]

$$\Delta\nu_{LS_i} = \frac{1}{4}\,|g_{ik}|^2\,\frac{(\nu_L - \nu_{ik})}{(\nu_L - \nu_{ik})^2 + \Gamma^2/4}\,, \qquad (i = 1,\,2),\ (k = 1,\,2)\,, \tag{4.5}$$

where g_{ik} is the Rabi frequency of the considered transition from the ground state $F = i$ to the excited state $F' = k$ with a transition frequency ν_{ik} and Γ is the decay rate of the excited state.
Further, the light shift $\Delta\nu_{LS_{CPT}}$ of the CPT resonance frequency is given by the differential light shift of the two ground states forming the Λ system [97]:

$$\Delta\nu_{LS_{CPT}} = \Delta\nu_{LS_2} - \Delta\nu_{LS_1}\,. \tag{4.6}$$

Actually, the modulated laser light field consists of several frequency components whereby each sideband has an influence on the light shift of the CPT resonance position depending on their Rabi frequency and frequency detuning from resonance [97]. Therefore, the influence of the non-resonant sidebands has to be considered by adding up the contribution of each sideband to the total light shift on the respective level. As a result of this summation,

the light shift was found to consist of one contribution which depends on the optical power and a second contribution which is independent of the optical power but depends on the laser frequency [97].
Furthermore, the light shift can be reduced by choosing an appropriate modulation index [97]. However, the modulation index is influenced by the operational parameters of the laser (see also section 3.1.1). Therefore, stabilising the laser frequency onto the optical transition by either varying the laser current or laser temperature results in a variation of the laser intensity and causes a change of the modulation index by an alteration of the modulation properties of the laser [98]. Additionally, it is shown in [98] that for proper adjustment of the microwave power level the light shift caused by the laser intensity variations due the laser frequency stabilisation and the changed modulation properties can compensate each other.
Furthermore, in reference [99] a continuous reduction of the light shift was realised by adapting the modulation index with a servo loop which has the benefit that also changes of the laser modulation properties due to, e.g., laser ageing can be corrected.
Moreover, in reference [100] a reduction of the light shift was obtained by an increase of the buffer gas pressure due to the broadening of the optical transition.
In sum the compensation of the light shift effect is quite complex, since a number of operational parameters can alter the measured light shift and several transitions with different transition strengths and numerous laser sidebands contribute to this shift. Therefore, typically a reduction of the light shift is obtained by balancing a negative light shift and a positive light shift on the respective transition.
It gets even more complicated considering the case of the coupled CPT resonances of the CDSM. As stated in equation 4.6 the measured light shift of the CPT resonance is the differential light shift of the two ground states of the Λ excitation scheme. Further, the light shift of the CDSM resonance $\Delta\nu_{LS_{CDSM}}$ is given by the differential light shift of the two CPT resonances which form the considered CDSM resonance:

$$\Delta\nu_{LS_{CDSM}} = \Delta\nu_{LS_{CPT_2}} - \Delta\nu_{LS_{CPT_1}} \,. \tag{4.7}$$

Ideally, if both single CPT resonances experience the same light shift, then the measured magnetic field strength of the CDSM should not be influenced by the light shift.
Up to now, no detailed study on the light shift has been carried out for the CDSM resonances. During a test campaign at the Conrad observatory (see appendix A.4.2), the external magnetic field was measured with the CDSM in dependence of the laser intensity but no significant change of the magnetic field strength ($< 0.2\,\mathrm{nT}$) was detected. This could be due to the fact that the light shifts of the single CPT resonances compensated each other and as a result no shift of the magnetic field strength was detected. Therefore, further measurements on the light shift of the single CPT resonances have to be carried out in order to prove this assumption. Furthermore, investigations of the laser frequency dependent light shift which is independent of the optical power, are planned with the CDSM in the future.

4.1.2. Magnetic Field Inhomogeneity

A magnetic field inhomogeneity broadens the CPT resonance line shape by keeping the total line strength constant [18]. Thus, besides the line width broadening, an inhomogeneous magnetic field causes a reduction of the CPT resonance amplitude.
The CPT resonances have different dependences on the external magnetic field according to the magnetic quantum numbers m_F of their ground states (see section 2.1.2.2 and table 2.1). As a result, they are also differently broadened by a magnetic field inhomogeneity [101]. The CPT resonance $n = 0$, which has only a quadratic dependence on the external magnetic field, experiences the lowest influence. Therefore, this CPT resonance is preferred for applications where the magnetic field dependence is disturbing like, e.g., atomic clocks [93].
In order to reduce the influence of an inhomogeneous magnetic field, the CPT resonance line shapes are commonly measured either within a magnetic shielding can or in a magnetic clean environment with low magnetic field gradients like, e.g., at the Conrad Observatory (see appendix A.4.2).
In our laboratory a magnetic shielding can consisting of three layers of mu-metal is used which has a total height of $h = 64\,\mathrm{cm}$ and a diameter of $d = 25.5\,\mathrm{cm}$. Inside the inner layer a solenoid coil (coil windings $N = 640$) is mounted which allows the application of a defined and to a large extend homogeneous magnetic field. Nevertheless, residual inhomogeneities can affect the measurements within the magnetic shielding can.
During test measurements in this magnetic shielding can, several repeated measurements with identical operational parameters revealed different CPT resonance line widths up to a factor of two. Initially, it was assumed that a different sensor positioning in the magnetic shielding can caused this random variation of the CPT resonance line width due to different magnetic field inhomogeneities at the sensor position.
In order to investigate the inhomogeneous magnetic field in the magnetic shielding can, a magnetic field was applied and the magnetic field was measured along the height h of the magnetic shielding can with the help of a fluxgate magnetometer. The magnetic field gradient was calculated from the measured magnetic field strengths at the different heights. This was done for three different cases. In the first case no magnetic field was applied and thus the remanent magnetic field in the shielding can was characterised. In the second case a small magnetic field of about $B \approx 0.37\,\mu\mathrm{T}$ was set and in the third case a magnetic field of $B \approx 7.46\,\mu\mathrm{T}$ was applied. The results are summarised in figure 4.9.
As shown in figure 4.9, the magnetic field inhomogeneity within the magnetic shielding can increased with higher magnetic field strengths. The applied magnetic fields had the highest homogeneity in the range of $h = 40\,\mathrm{cm}$ to $h = 48\,\mathrm{cm}$ and the homogeneity decreased to the ends of the coil. Therefore, the sensor is typically placed in the region with the highest homogeneity for magnetic field measurements. At this sensor position the magnetic field gradient was $\Delta B/\Delta h \approx 0.6 \pm 0.1\,\mathrm{nT/cm}$ for $B \approx 7.46\,\mu\mathrm{T}$ and $\Delta B/\Delta h \approx 0.4\,\mathrm{nT/cm}$ for the lower magnetic field strength $B \approx 0.37\,\mu\mathrm{T}$.

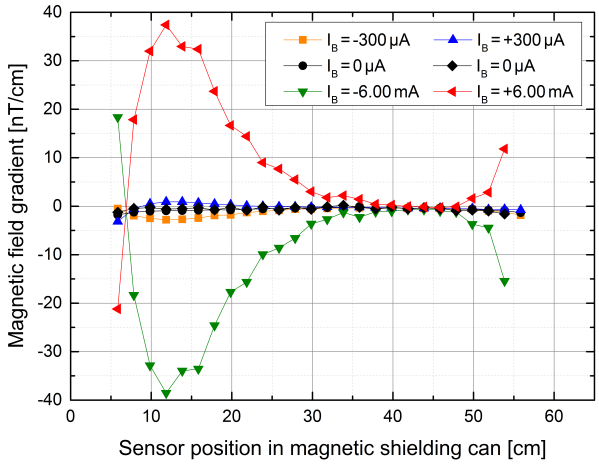

Figure 4.9.: Measured magnetic field gradients in the magnetic shielding can for different applied magnetic fields: The magnetic field inside of the shielding can was measured with a fluxgate magnetometer at several heights in the magnetic shielding can. The applied current on the solenoid coil generated a magnetic field inside of the shielding which can be calculated with the conversion factor: 1244 nT/mA. Thus, a current of $I_B = 300\,\mu\text{A}$ corresponds to a magnetic field of $B \approx 0.37\,\mu\text{T}$ in the magnetic shielding can and $I_B = 6.00\,\text{mA}$ results in magnetic field of $B \approx 7.46\,\mu\text{T}$.

In order to investigate the broadening of the CPT resonance line widths for different magnetic field gradients, the CDSM sensor was positioned at different heights within the magnetic shielding can and the line shapes of the CPT resonances $n = 0$, -2 and $+2$ were measured.
The sensor was positioned along the height of the magnetic shielding can ($\phi = 0°$). For these measurements, the current $I_B = 6.00\,\text{mA}$ was used which resulted in a magnetic field strength of about $B \approx 7.46\,\mu\text{T}$.
These tests were performed with the JUICE EM electronics and the dual pass sensor containing a long dual pass cell with neon as buffer gas at a pressure of $P_{BG} = 8.0\,\text{kPa}$ (60 Torr) (see appendix A.2). The CPT resonances were measured for both single and dual pass of the laser beam through the sensor cell. Therefore, the laser light was coupled into the inbound fibre either after one pass of the sensor cell or after two passes.
In figure 4.10 the CPT resonance line widths of $n = 0$, -2 and $+2$ are depicted for different magnetic field gradients. The magnetic field gradients were approximated from the sensor positions in the magnetic shielding can and the measurements with the fluxgate magnetometer shown in figure 4.9.

The laser intensity in front of the cell varied for measurements with single and dual pass of the laser beam. For the single pass measurement, an intensity of $I \approx 80\,\mu\text{W/cm}^2$ was measured in front of the cell. For the dual pass measurement, a lower intensity of

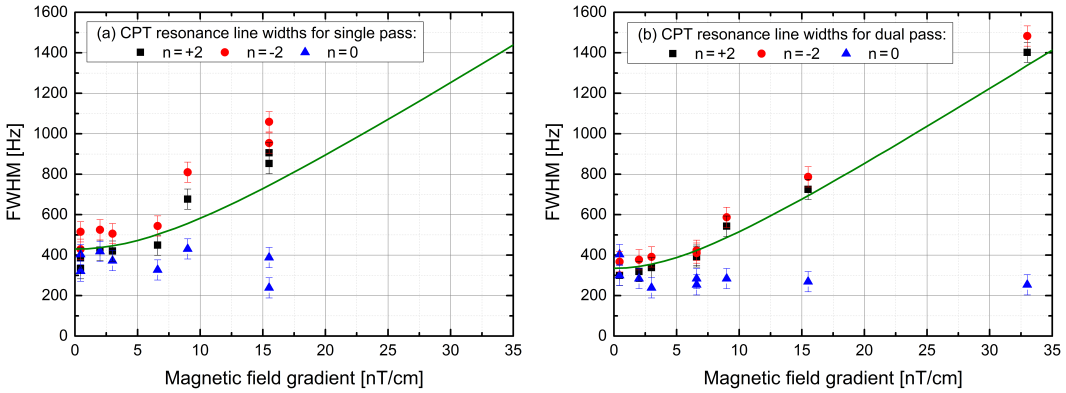

Figure 4.10.: Broadening of the CPT resonance line widths by different magnetic field gradients in a magnetic shielding can: In (a) the line widths of the CPT resonances $n = 0$, -2 and $+2$ are shown for a single pass and in (b) for a dual pass of the laser beam through the sensor cell. The green line gives the simulated broadening of the CPT resonance line widths of $n = -2$ and $n = +2$. A magnetic field of $B \approx 7.46\,\mu\text{T}$ was applied. The JUICE EM electronics and the dual pass sensor were used. The sensor contained a long dual pass cell with neon as buffer gas at a pressure of $P_{BG} = 8.0\,\text{kPa}$ (60 Torr). The sensor cell temperature was $T = 23°\text{C}$. The intensity in front of the cell was $I \approx 80\,\mu\text{W/cm}^2$ for a single pass and $I \approx 70\,\mu\text{W/cm}^2$ for a dual pass.

$I \approx 70\,\mu\text{W/cm}^2$ was detected. Therefore, the line widths of CPT resonances obtained by the single pass were increased due to the higher intensity (power broadening) by about $50 \pm 10\,\text{Hz}$ compared to the dual pass.

In figure 4.10(a) the CPT resonance line widths are compared for a single pass and in (b) for a dual pass of the laser beam through the sensor cell. The CPT resonance $n = 0$ revealed no significant broadening within the obtained measurement uncertainty for both single and dual pass. On the contrary, the CPT resonances $n = -2$ and $n = +2$, which also have a linear dependence on the external magnetic field, showed a clear broadening for increasing magnetic field gradients.

Additionally, the influence of a magnetic field gradient on the CPT resonance line widths of $n = -2$ and $n = +2$ was simulated and the results are included in figure 4.10 (green line). For this simulation, a dispersive Lorentzian function with constant line width (see equation 2.26) was assumed to approximate the CPT resonance line shape. The line widths for single and dual pass were taken from the experimentally obtained CPT resonance line widths shown in figure 4.10 for negligible inhomogeneous magnetic field broadening. A line width of $\Delta\nu_{SP} = 430\,\text{Hz}$ was assumed for a single pass and a line width of $\Delta\nu_{DP} = 335\,\text{Hz}$ was approximated for a dual pass. The detected CPT resonance is assumed to be the superposition of the CPT resonances prepared along the optical path. Thus, for the simulation, the position of the Lorentzian line shape along the optical path was shifted according to the respective magnetic field gradients and the external magnetic field shift coefficients

(see table 2.1). In order to obtain the total resonance line width for a certain magnetic field gradient, the shifted Lorentzian line shapes were added up and the total line width determined.
Just the shift due to a magnetic field gradient along the optical path was considered whereas magnetic field gradients in the two other directions as well as the change of the line width with laser intensity along the optical path were neglected. Despite these simplifications, the line widths obtained by the simulation fit the measured line widths quite well.
From these measurements and further simulations it became clear that the typical magnetic field gradients in the magnetic shielding can can broaden the CPT resonance line width. Especially for CPT resonance line widths $\Delta\nu_{CPT} < 300\,\mathrm{Hz}$, the measured CPT resonance line width can be affected by the inhomogeneity in the magnetic shielding can. However, the influence of the inhomogeneity can be neglected for most common measurement configurations in the magnetic shielding can. Therefore, the randomly detected line width variations, which were mentioned at the beginning of this section, cannot be explained completely by different magnetic field inhomogeneities at the sensor position. In addition, another effect is assumed to influence the line width. The most probable explanation at the moment is the influence of the varying intensity distribution through the multi-mode fibre (see section 3.4.1) but further measurements are required to investigate this influence.

4.1.3. Buffer Gas Pressure and Sensor Cell Temperature

Buffer gases are typically added to the Rb vapour cell to reduce the CPT resonance line width [18]. In a Rb vapour cell without buffer gas the CPT resonance line width is determined by time-of-flight broadening which can be calculated via the relation [102]:

$$\Delta\nu_{tof} = \frac{\sqrt{2}\,ln(2)}{\pi} \cdot \frac{\overline{v}}{d}\,, \tag{4.8}$$

where $\overline{v} = \sqrt{2k_BT/m}$ is the average velocity of the Rb atoms and d is the laser beam diameter. The average velocity is determined by the temperature T of the gas and the mass of the Rb atoms m. As can be seen from equation 4.8, the line width depends on the ratio of the average velocity $\overline{v}$ and the diameter of the laser beam d. Thus, time-of-flight broadening is reduced by increasing the laser beam diameter. With our typical beam diameters of $d \approx 2 - 9\,\mathrm{mm}$, the CPT resonance line widths for an unbuffered Rb vapour cell would be several tens of kHz.
The addition of a buffer gas narrows the CPT resonance line width by a reduction of the mean free path of the Rb atoms due to the collisions and thus increases the interaction time with the laser beam [103]. Typically, inert gases are used as buffer gases due to the fact that the ground state coherence survives millions of collisions with the buffer gas

atoms [104]. In our experiments neon is used as buffer gas. The Rb atoms collide with the neon atoms. These collisions have several effects on the optical transitions as well as on the CPT resonances. First, the buffer gas causes a broadening of the optical transitions (collisional broadening), second a reduction of the CPT resonance line widths and third a shift of the CPT resonance positions depending on the buffer gas pressure and the sensor cell temperature. Additionally, the sensor cell temperature can affect the height and width of the CPT resonance.

4.1.3.1. Broadening of the Optical Transitions

The line width broadening of the optical transitions is caused by phase changing collisions and quenching collisions [77]. The ^{87}Rb D_1 line is broadened by the collisions with the neon atoms at $T = 394\,\mathrm{K}$ [105] by

$$\gamma_{opt,coll} = 9.8 \pm 0.1\,\mathrm{MHz/Torr} \mathrel{\hat{=}} 73.8 \pm 0.8\,\mathrm{MHz/kPa} \tag{4.9}$$

and the transition frequency is shifted by the buffer gas collision according to

$$\Delta\nu_{opt,coll} = -0.90 \pm 0.02\,\mathrm{MHz/Torr} \mathrel{\hat{=}} -6.75 \pm 0.15\,\mathrm{MHz/kPa}\,. \tag{4.10}$$

The natural line width of the ^{87}Rb D_1 line is $\Delta\nu_{nat} = 5.750\,0(56)\,\mathrm{MHz}$ [28] which is further broadened by the thermal motion of the atoms. The typical Doppler line width for ^{87}Rb is about 510 MHz at room temperature [77]. For lower buffer gas pressures, the Doppler width is much higher than the collision induced broadening. Using the broadening factor from equation 4.9, the collisional broadening (homogeneous broadening) and the Doppler broadening (inhomogeneous broadening) [77] are approximately equal at a buffer gas pressure of $P_{BG} \approx 6.9\,\mathrm{kPa}$ (52 Torr). The total optical line width results from a convolution of the homogeneous and the inhomogeneous line profile [77].
The excited state $5^2P_{1/2}$ consists of two hyperfine structure levels with $F' = 1$ and $F' = 2$ which are separated by about 815 MHz [28] (see also figure 2.2). Compared to the ^{87}Rb D_2 line the excited states are well separated but for increasing buffer gas pressure, they start to overlap. CPT resonances can be prepared with both excited states ($F' = 1$ and $F' = 2$). Depending on the optical detuning, CPT resonances are more or less efficiently prepared with both excited states and the measured signal can consist of contributions of two CPT resonances (see sections 4.1.1 and 4.1.5).
With increasing buffer gas pressure not only the line widths of the optical transitions increase but also their heights are reduced. The change of line shapes of the optical transitions is important for the operation of the laser current control loop (see section 2.4.2). This control loop adjusts the laser frequency with the help of the optical transmission spectrum. Therefore, FMS is applied and the derivative of the transmission spectrum of the ^{87}Rb D_1 line is detected in the in-phase signal.

In figure 4.11 the in-phase signal is shown for three different buffer gas pressures: $P_{BG} = 1.0\,\text{kPa}$ (7.5 Torr), $P_{BG} = 4.0\,\text{kPa}$ (30 Torr) and $P_{BG} = 8.0\,\text{kPa}$ (60 Torr). The depicted spectrum resulted from the interaction of the laser carrier and its sideband structure (see figure 2.12 and section 4.1.4) with the optical transitions of the ^{87}Rb D_1 line.

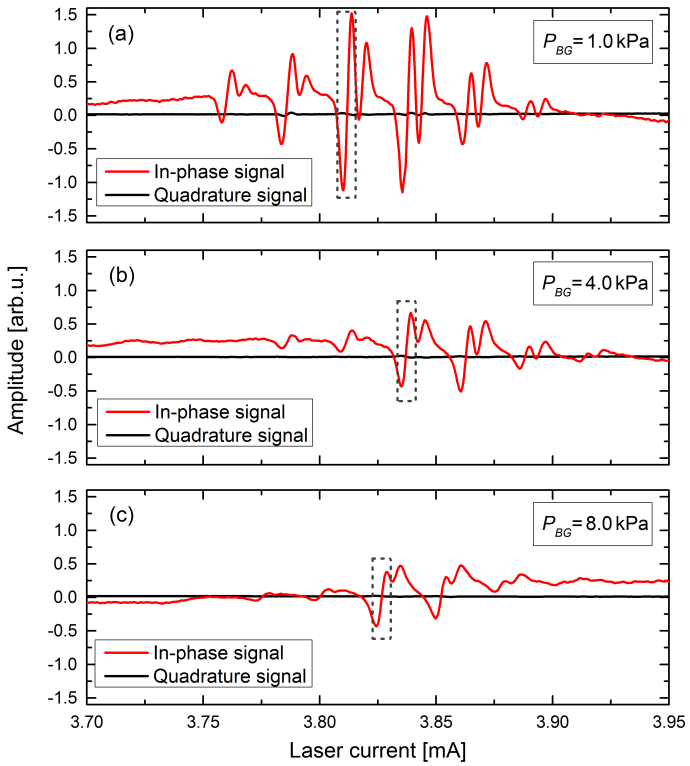

Figure 4.11.: Stabilisation signal used for the laser current control loop for different buffer gas pressures: (a) $P_{BG} = 1.0\,\text{kPa}$ (7.5 Torr), (b) $P_{BG} = 4.0\,\text{kPa}$ (30 Torr) and (c) $P_{BG} = 8.0\,\text{kPa}$ (60 Torr). The slope of the centre structure (dashed rectangle) is used for the operation of the laser current control loop.

In figure 4.11(a) the obtained spectrum showed distinct peaks. Comparing the measured spectra for the buffer gas pressures $P_{BG} \approx 1.0\,\text{kPa}$ (7.5 Torr) and $P_{BG} \approx 8.0\,\text{kPa}$ (60 Torr) revealed a reduction of the peak heights by about a factor of three. Further, the broadening of the optical transitions in figure 4.11(b) and (c) was visible by the reduction of the separation between the single peaks.
Additionally, the transition frequency shift with the buffer gas pressure (see equation 4.10) can be seen in figures 4.11(a) and (b) as the shift of the resonance pattern to higher laser currents. Between the measurements shown in figures 4.11(b) and (c), the laser setup was changed which resulted in a shift of the laser frequency most likely by reflections. Therefore, the shift of the resonance pattern to higher laser currents was not continued in figure 4.11(c).

4.1.3.2. Impact of Collisions on the CPT Resonance Line Shapes

The collisions with the buffer gas influence the CPT resonance line shapes [17]. In general, the CPT resonance amplitudes decrease due to the broadening of the optical transitions (see equation 4.1 and figure 4.27). Additionally, the buffer gas collisions lead to narrowed CPT resonance line widths [103][18] due to the reduction of time-of-flight broadening (see equation 4.8). The reduction is achieved by an increased interaction time of the Rb atoms with the laser light [103]. Due to the frequent collisions of the neon atoms with the Rb atoms, the mean-free path of the Rb atoms is reduced. Without buffer gas, the mean-free path of the Rb atom between Rb-Rb collisions is about $L \approx 4\,\mathrm{m}$ at a temperature of $T = 298.15\,\mathrm{K}$. The mean free path without buffer gas is calculated according to [106]

$$L = \frac{k_B\,T}{\sqrt{2}\,\sigma_{Rb}\,P}\,, \tag{4.11}$$

where σ_{Rb} is the cross section for elastic collisions, which is $13.97 \cdot 10^{-18}\,\mathrm{m}^2$ for Rb-Rb collisions (value according to Massey as cited in [29]), and P is the vapour pressure which is about $53.2 \cdot 10^{-6}\,\mathrm{Pa}$ at $T = 298.15\,\mathrm{K}$ [107].
Additionally, Lamb-Dicke narrowing occurs, which reduces the residual Doppler width, when the mean free path between two collision is much smaller than the wavelength of the hyperfine structure ground states splitting [108][109]. Therefore, the CPT resonance line width in our experiments is typically determined by power broadening.
The CPT resonance line width increases linearly with the laser intensity (see section 4.1.1). As can be seen from equation 4.2, the increase of the CPT resonance line width depends on the decay rate of the excited state and on the ground state coherence decay rate. Both are influenced by collisions. The broadening of the optical transitions with the buffer gas pressure results in a reduced pumping rate [91] which decreases the broadening of the CPT resonance line width with the laser intensity (power broadening) [17].
Further, the ground state coherence decay rate Γ_{12} is influenced by three different types of collisions: the Rb-wall collisions γ_{cw}, Rb-buffer gas collisions γ_{cbg} and Rb-Rb spin-exchange collisions γ_{cse} [29]. These three contributions add up like [23][110]:

$$\Gamma_{12} = (\gamma_{cw} + \gamma_{cbg} + \gamma_{cse})\,. \tag{4.12}$$

The effect of the Rb-wall collisions γ_{cw} can be calculated via [29]

$$\gamma_{cw} = \left[\left(\frac{2.405}{r}\right)^2 + \left(\frac{\pi}{l}\right)^2\right] D_0\,\frac{P_0}{P_{BG}}\,, \tag{4.13}$$

where r is the radius and l is the length of the sensor cell. D_0 is the diffusion constant of the Rb atoms in the buffer gas at the pressure $P_0 = 101.3\,\mathrm{kPa}$. The diffusion constant is $D_0 = 0.31\,\mathrm{cm}^2/\mathrm{s}$ for Rb atoms and Ne as buffer gas [29]. P_{BG} is the buffer gas pressure.
The collision contribution of the Rb atoms with the buffer gas atoms is given via the

relation [29]

$$\gamma_{cbg} = L_0 \, \bar{v}_{r_{RbNe}} \sigma_{BG} \, \frac{P_{BG}}{P_0} \,, \tag{4.14}$$

where L_0 is the Loschmidt constant, $\bar{v}_{r_{RbNe}}$ is the average relative velocity of the Rb atoms and the buffer gas atoms, σ_{BG} is the cross-section of the collisions of the Rb and the buffer gas atoms. The average relative velocity is calculated by the formula [29]

$$\bar{v}_r = \sqrt{(8 \, k_B T / \pi \mu_x)} \,, \tag{4.15}$$

where k_B is the Boltzman constant, T is the temperature and μ_x is the reduced mass of the colliding atoms. The masses of Rb and Ne are $m_{Rb} = 1.443\,160\,769(09) \cdot 10^{-25}$ kg [111] and $m_{Ne} = 0.335\,0(9) \cdot 10^{-25}$ kg [112].
The last collisional contribution of equation 4.12 is the Rb-Rb spin-exchange collisions. They can be calculated by [29]

$$\gamma_{cse} = \frac{6\,I + 1}{8\,I + 4} \, \bar{v}_{r_{Rb}} n_{Rb} \, \sigma_{se} \,, \tag{4.16}$$

where I is the nuclear spin quantum number, which is $I = 3/2$ for ^{87}Rb, $\bar{v}_{r_{Rb}}$ is the average relative velocity for Rb-Rb collisions and n_{Rb} is the number density of the Rb atoms. The number density is calculated with the relation $n = P_{Rb}/k_B\,T$ [29] where P_{Rb} is the vapour pressure of rubidium. For $T = 298.15$ K, the vapour pressure is about $53.2 \cdot 10^{-6}$ Pa [107]. The cross-section σ_{se} of spin-exchanging collisions is $\sigma_{se} = 1.6 \cdot 10^{-14}$ cm^{-2} [113].

These three types of collisions contribute differently to the minimum CPT resonance line width depending on the buffer gas pressure. In figure 4.12, their contributions to the CPT resonance line width are calculated for the dimensions of the Rb vapour cell mounted in the CSES sensor (sensor cell diameter $d = 12.7$ mm, optical path length of $l = 25.18$ mm). According to [23] the minimum line width was calculated by Γ_{12}/π.

As can be seen in figure 4.12 and from equation 4.13 the contribution of the collisions with the cell wall reduces with increasing buffer gas pressure. For the CSES mission, the sensor cell contains Ne as a buffer gas with a pressure of $P_{BG} = 40$ Torr (≈ 5.3 kPa) (see dotted vertical line in figure 4.12). In this case, the collisions with the wall have the highest contribution to the CPT resonance line width.
Measurements on the intensity dependence of the CPT resonance line width of $n = 0$ were performed with the CSES QM, similar to the measurements in section 4.1.1. The sensor unit was mounted within a magnetic shielding can and a magnetic field of $B = 10.0\,\mu$T was applied. A sensor angle of $\phi = 0°$ was set. The minimum line width was determined by applying a linear fit to the measurement results according to equation 4.4 which yielded a value of $\Delta\nu_0 = 45 \pm 4$ Hz. This result is close to the calculated value of $\Delta\nu_{0,calc} \approx 40$ Hz for $P_{BG} = 40$ Torr (5.3 kPa) (see figure 4.12).

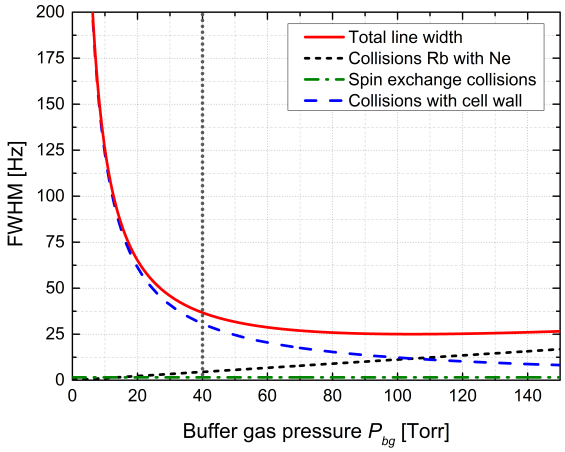

Figure 4.12.: Collisional contributions to the CPT resonance line width in dependence of the buffer gas pressure P_{BG}: The minimum CPT resonance line width depends on the the Rb-wall collisions, Rb-buffer gas collisions and the spin-exchange collisions. Their contributions are calculated for the CSES sensor cell dimensions. Neon is used as buffer gas. The dotted vertical line marks the buffer gas pressure of $P_{BG} = 40\,\text{Torr}$ (5.3 kPa), which is used for the CSES mission.

4.1.3.3. Shift of the CPT Resonance Positions

The shift of the CPT resonance positions increases with the collision rate of the Rb atoms with the Ne atoms [17] and thus increases with the buffer gas pressure [103]. The ground state transition frequency shift $\Delta\nu_{BG}$ [29] due to the buffer gas is approximated by

$$\Delta\nu_{BG} = P_{BG}\left[\beta + \delta\,(T - T_0) + \gamma\,(T - T_0)^2\right], \tag{4.17}$$

where P_{BG} is the buffer gas pressure at the reference temperature T_0 and β is the pressure shift coefficient. The coefficients δ and γ describe the linear and quadratic dependence on the sensor cell temperature T. The coefficients are $\beta = 392 \pm 8\,\text{Hz/Torr}$ and $\delta = 0.26\,\text{Hz/(°C Torr)}$ for Rb and Ne as buffer gas [114][29].
The temperature dependence of the transition frequency is a drawback for many applications which require an accurate determination of the transition frequency like, e.g., atomic clocks. Therefore, either the sensor cell temperature has to be controlled precisely or a mixture of two buffer gases with opposite frequency shift behaviour is selected to reduce the temperature dependence on the CPT resonance positions [115][18].
For the CDSM operation, the CPT resonance positions are assumed to experience the same pressure and temperature shifts. Thus, the differential measurement of the magnetic field strength should not be influenced by the buffer gas induced frequency shifts.
The temperature shifts of the CPT resonance positions $n = 0$, -2, $+2$, -3 and $+3$ were measured. These measurements were performed with the CSES LM but with an external microwave generator (Rhode&Schwarz SMR 20). The CSES LM cell contains Ne as buffer

gas at a pressure of $P_{BG} = 4.0\,\text{kPa}$ (30 Torr) (see appendix A.2). The sensor unit was positioned within a magnetic shielding can (see appendix A.4) and a magnetic field of $B = 11.1\,\mu\text{T}$ was applied. The sensor angle was $\phi = 45°$.
The sensor cell temperature was increased by the sensor cell heating which consisted of a bifilar non-magnetic resistive heating wire wound around the sensor cell. For the shift coefficient measurements, the sensor cell was heated up and then the heating was switched off to prevent disturbances on the CPT resonance positions. During the cooling of the sensor cell the CPT resonance line shapes and their zero crossing frequencies were detected. The drawback of this method is that the sensor cell cooled faster at higher sensor cell temperatures. Therefore, the measurement of the zero crossing frequencies at higher temperatures were less accurate.
The zero crossing frequencies of the CPT resonances showed a linear dependence on the sensor cell temperature. Therefore, the shift coefficients were determined by a linear fit to the measured zero crossing frequencies. The temperature shift coefficient of the respective CPT resonance position are summarised in table 4.7.

Table 4.7.: Linear shift coefficients δ of the CPT resonance positions with the sensor cell temperature T for a buffer gas pressure of $P_{BG} = 30\,\text{Torr}$ (4.0 kPa).

n	$\delta \cdot P_{BG}$ [Hz/°C]
0	7.3 ± 0.2
-2	7.1 ± 0.7
$+2$	8.0 ± 0.8
-3	6.6 ± 0.4
$+3$	7.3 ± 0.3

As can be seen from table 4.7, the shift coefficients of the CPT resonances are very similar. The deviations are supposed to result from the used measurement method which made the zero crossing frequency determination less accurate at higher temperatures (see discussion above).
Calculating the linear temperature shift from the literature value of γ (stated above) results in a shift of about 7.8 Hz/°C for a buffer gas pressure of $P_{BG} = 30\,\text{Torr}$ (4.0 kPa) which is close to the measured values.

During the CDSM operation, the sensor cell temperature is regulated via a control loop (see section 2.4.2). Thus, large temperature changes are prevented. Additionally, the microwave frequency stabilisation control loop operates for most sensor angles (see section 2.4.2). Thus, the influence of a possible detuning Δ (see equation 2.45) introduced by a sensor cell temperature change is reduced. For these reasons, a sensor temperature change should not affect the magnetic field measurement of the CDSM.

4.1.3.4. Line Shape Dependence on the Sensor Cell Temperature

The sensor cell temperature T influences the CPT resonance amplitudes and widths [44] and as a consequence alters the CDSM resonance line shape. As can be seen from equation 4.1, the CPT resonance amplitude depends on the number density n_{Rb} of Rb atoms in the gaseous phase. By heating the sensor cell, the number of atoms in the gaseous phase increases and more atoms can contribute to the CPT effect. Therefore, the CPT resonance amplitudes rise with the sensor cell temperature until they reach a maximum value at a certain temperature, which depends on the sensor cell geometry [44]. Then, the amplitudes reduce again due to the optical thickness effect [44]. A similar trend is also expected for the CDSM resonance amplitudes.
In figure 4.13 the CDSM resonance amplitudes and line widths are depicted in dependence of the sensor cell temperature. These measurements were performed with the CSES EM in the temperature facility at the Space Research Institute (see appendix A.4.1).
The CSES EM cell contained Ne as buffer gas at a pressure of $P_{BG} = 5.3\,\text{kPa}$ (40 Torr). A sensor angle of $\phi = 45°$ was selected in order to determine the CDSM resonance line shapes of $n = 2$ and $n = 3$ simultaneously. A magnetic field of $B = 2.09\,\mu\text{T}$ was applied.

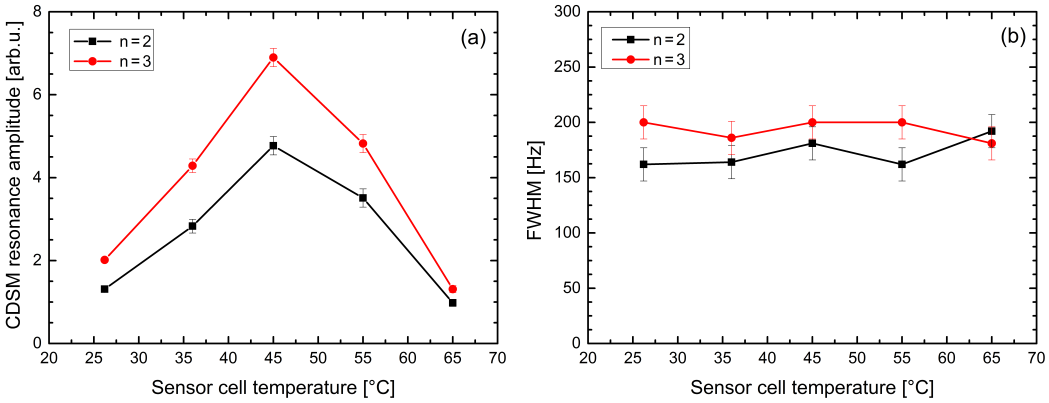

Figure 4.13.: Temperature dependence of the CDSM resonance amplitudes and line widths within the temperature range of $T = 26°\text{C}$ to $T = 65°\text{C}$: In (a) the CDSM resonance amplitudes of $n = 2$ and $n = 3$ are shown. In (b) the behaviour of their line widths are depicted. The CSES EM was used for these measurements. The buffer gas (Ne) had a pressure of $P_{BG} = 5.3\,\text{kPa}$ (40 Torr). The sensor angle was $\phi = 45°$. The applied magnetic field was $B = 2.09\,\mu\text{T}$.

As can be seen in figure 4.13(a) the CDSM resonance amplitudes of $n = 2$ and $n = 3$ increased with the sensor cell temperature until their amplitudes reached a maximum around $T = 45°\text{C}$. Then, they started to decline again due to the mentioned optical thickness effect. The CDSM resonance amplitudes of $n = 2$ and $n = 3$ rose by about a factor of 3.5 due to the increase of the temperature from $T = 26°\text{C}$ to $T = 45°\text{C}$.
The CDSM resonance line widths, depicted in 4.13(b), stayed almost constant within the

tested temperature range. On the one hand, the line width should decrease due to a laser intensity reduction by the increasing optical thickness. On the other hand, the line width should rise due to more frequent spin-exchange collisions (see equation 4.16)[44]. Both contributions seemed to cancel each other within the considered temperature range. Thus, the line width remained nearly constant.
Due to the almost constant line width within the measured temperature range, the optimal operational range for the CDSM magnetometer is determined by the behaviour of the CDSM resonance amplitudes. As a result, the optimal operational range was around $T = 45°\mathrm{C}$ for both $n = 2$ and $n = 3$.

4.1.4. Operational Laser Parameters and Microwave Power Level

The operational laser parameters (laser current I_L and laser temperature T_L) influence the emitted optical power and the modulation properties of the laser. As shown in section 3.1.1, the obtained modulation index depends on the selected laser current.
In total, two modulation steps are required for the operation of the CDSM (see section 2.3.2). Both modulation signals are superimposed on the laser current. The first modulation signal creates sidebands at integer multiples of the modulation frequency ω_{mod_1} around the laser carrier frequency ω_L. Therefore, the emitted laser field is given by [51]

$$E_{L_{mod1}}(t) = \frac{E_L}{2} \sum_{l=-\infty}^{\infty} J_l(M_{mod_1})\, exp\left[\, i\,(\omega_L + l\,\omega_{mod_1})\, t\,\right] + c.c.\,, \tag{4.18}$$

where E_L is the electric field amplitude of the unmodulated laser carrier, J_l is the Bessel function of the lth-order and M_{mod_1} is the modulation index of the first modulation signal. The frequency of the first modulation signal, which is in the microwave regime ($\omega_{mod_1} \approx 2\pi \cdot 3.4\,\mathrm{GHz}$), is generated via a microwave generator (see sections 2.2.1 and 2.4.2). The energy distribution between the laser carrier and its sidebands depends on the microwave power level P_{MW} and thus the obtained modulation index M_{mod_1} [50]. Additionally, the microwave power causes heating of the VCSEL chip which shifts the laser frequency ω_L [110].
For the preparation of the CDSM resonances, the first modulation signal with the frequency ω_{mod_1} is further modulated with a second modulation signal having the frequency ω_{mod_2}. Then, the resulting light field consists of the following frequency components [51][116]:

$$E_{L_{mod2}}(t) = \frac{E_L}{2} \sum_{l,m=-\infty}^{\infty} J_l(M_{mod_1}) J_m(M_{mod_2})\, exp\left[\, i\,(\omega_L + l\,\omega_{mod_1} + m\,\omega_{mod_2})\, t\,\right] + c.c.\,, \tag{4.19}$$

where J_m are the Bessel functions of mth-order and M_{mod_2} is the modulation index of the second modulation signal.

Since the frequency of the first modulation signal is in the microwave regime, its first-order sidebands are labelled as microwave sidebands for the further descriptions to distinguish them from the first-order sidebands generated by the second modulation signal.
The amplitudes of the microwave sidebands are proportional to $J_{\pm1}(M_{mod_1}) \cdot J_0(M_{mod_2})$ (see equation 4.19) and the amplitudes of the first-order sidebands of the second modulation step are proportional to $J_{\pm1}(M_{mod_1}) \cdot J_{\pm1}(M_{mod_2})$.
With increasing microwave power level P_{MW}, the modulation index M_{mod_1} increases. The amplitudes of the microwave sidebands change depending on the set modulation index M_{mod_1}. If the amplitudes of the microwave sidebands are altered, the total energy in the sidebands of the second modulation step is modified too (see equation 4.19) but the modulation index M_{mod_2} stays constant.

The selected operational parameters of the laser and the microwave power level affect the laser frequency stabilisation as well as the CPT and CDSM resonance line shapes. Additionally, this set of parameters influences the light shift as discussed in section 4.1.1.2.
The laser frequency is stabilised by two control loops. The first control loop keeps the laser temperature constant and a frequency change is corrected via a second control loop which adapts the laser current. The laser current control loop uses the ^{87}Rb D_1 line transmission spectrum for its operation (see section 2.4.2).
In figure 4.14 the stabilisation signal to set the appropriate laser current is shown for two different microwave power levels P_{MW}.

The dotted rectangle in figure 4.14 shows the slope of the stabilisation signal used for the laser current control loop. In figure 4.14(a) the applied microwave power level was $P_{MW} = -15.3\,\text{dBm}$, which resulted in a measured modulation index of $M_{mod_1} \approx 0.8$, and in (b) the microwave power level was changed to $P_{MW} = -6.5\,\text{dBm}$, which increased the modulation index to $M_{mod_1} \approx 1.8$ [90]. The height of the slope depends on the microwave power level P_{MW}. For the example shown in figure 4.14, the increase of the microwave power level resulted in a rise of the energy in the microwave sidebands. Thus, the slope enhanced by about a factor of 1.5.

In figure 4.15 measurements on the CPT and CDSM resonance amplitudes are summarised for different laser operational parameters and microwave power levels. In figure 4.15(a) the CPT resonance amplitudes of $n = 0$, -2 and $+2$ as well as the CDSM resonance amplitude $n = 2$ are shown in dependence of the microwave power level P_{MW}. The CPT resonance amplitude of $n = 0$ had a maximum around the microwave power level of $P_{MW} = -7.4\,\text{dBm}$. As can be seen in 4.15(a), the CPT resonance amplitudes $n = -2$ and $n = +2$ showed a similar dependence on the microwave power level as the CPT resonance $n = 0$. The CPT resonance amplitude of $n = 0$ was higher than the amplitudes of the CPT resonances $n = -2$ and $n = +2$, since different sidebands were used for the excitation of the CPT resonances (see section 2.3.2).

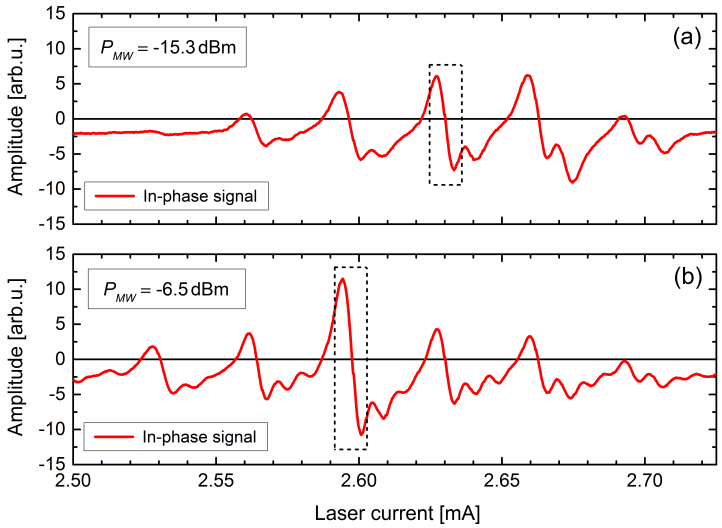

Figure 4.14.: Stabilisation signal used for the laser current control loop for two different microwave power levels P_{MW}: In (a) the stabilisation signal is shown for a microwave power level of $P_{MW} = -15.3\,\mathrm{dBm}$ ($M_{mod_1} \approx 0.8$). In (b) the microwave power level was increased to $P_{MW} = -6.5\,\mathrm{dBm}$ ($M_{mod_1} \approx 1.8$). Therefore, the power in the microwave sidebands was enhanced and the resulting stabilisation signal increased. The dotted area indicates the slope of the stabilisation signal used for the laser current control loop. The CSES FS electronics and the dual pass sensor were utilised. A long dual pass cell was mounted which contained a buffer gas (Ne) at a pressure of $P_{BG} = 8.0\,\mathrm{kPa}$ (60 Torr). The sensor temperature was $T = 24°\mathrm{C}$. The laser intensity in front of the sensor cell was about $I \approx 100\,\mu\mathrm{W/cm^2}$.

The CDSM resonance amplitude $n = 2$ shown in figure 4.15(a) was smaller than the sum of the CPT resonance amplitudes of $n = -2$ and $n = +2$ (grey dashed line). This is due to a detuning caused by the quadratic magnetic field dependence of the CPT resonances which was not compensated for this measurement (see section 4.1.6).
In figure 4.15(b) the CPT resonance $n = 0$ is depicted in dependence of the microwave power level P_{MW} for three different laser current-temperature pairs. The microwave power level at which the CPT resonance $n = 0$ reached its maximum shifted with the set laser current-temperature pair. For $I_L = 2.35\,\mathrm{mA}$ and $T_L = 46.3°\mathrm{C}$, the ideal microwave power level to maximise the CPT resonance amplitude was about $P_{MW} = -7.4\,\mathrm{dBm}$. For the two other laser current-temperature pairs, another microwave power level would be required to optimise the CPT resonance amplitude. This is due to the fact that the modulation efficiency increases for lower laser currents (see section 3.1.1).
In the case of $I_L = 2.43\,\mathrm{mA}$ and $T_L = 46.0°$, an increase of the microwave power would have been required to optimise the CPT resonance amplitude which was not possible, since the maximum output power of the used microwave generator was already reached. For the third current-temperature pair $I_L = 2.15\,\mathrm{mA}$ and $T_L = 47.1°\mathrm{C}$, a microwave power

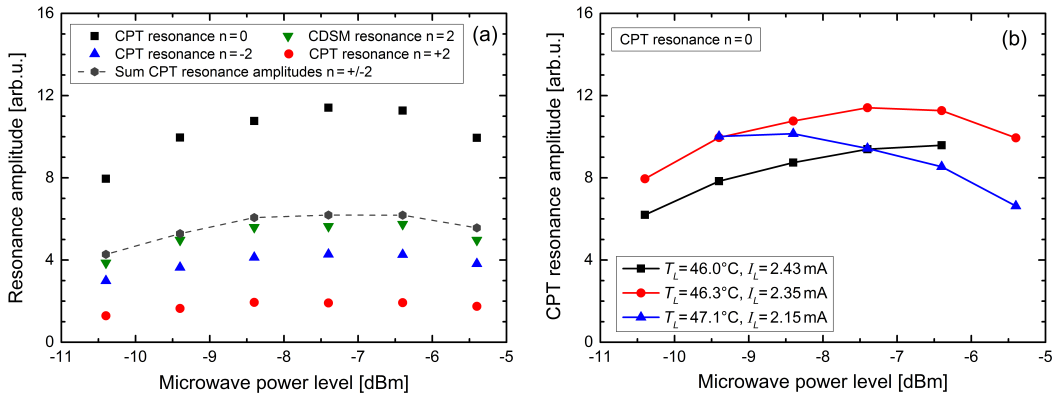

Figure 4.15.: CPT and CDSM resonance amplitudes in dependence of the microwave power level: In (a) a laser temperature $T_L = 46.3°C$ and a laser current $I_L = 2.35\,\text{mA}$ were set. The CPT resonance amplitudes of $n = 0$, -2 and $+2$ as well as the CDSM resonance $n = 2$ are shown. In (b) the CPT resonance amplitude of $n = 0$ is depicted for three different laser current-temperature pairs. The measurements were performed with the CSES QM. The sensor cell contained Ne as buffer gas at a pressure of $P_{BG} = 5.3\,\text{kPa}$ (40 Torr). The laser intensity in front of the cell was about $I \approx 130\,\mu\text{W/cm}^2$. The sensor angle was $\phi = 0°$. A magnetic field of $B = 40.0\,\mu\text{T}$ was applied.

level lower than -9.4 dBm would have been suitable to optimise the resonance amplitude. From this measurement it became clear that the CPT resonance amplitude of $n = 0$ can not be optimised, in respect of the maximum amplitude, when operating the CSES QM at laser currents above $I_L > 2.45\,\text{mA}$.

Furthermore, the selected laser operational parameters influence the symmetry of the CPT resonance line shape. In order to obtain a symmetric CPT resonance line shape, either the Rabi frequencies have to be equal for both transitions forming the Λ excitation scheme or the two-photon detuning has to be zero [117]. Equal Rabi frequencies are obtained in the simplest case, if the two laser sidebands have the same intensity and the two transitions have identical transition strengths.
In figure 4.16 the CPT resonance $n = 0$ is depicted for two different laser current-temperature pairs. In figure 4.16(a) the CPT resonance $n = 0$ is shown for the laser current-temperature pair $I_L = 2.56\,\text{mA}$ and $T_L = 44.6°C$. The measured CPT resonance line shape revealed deviations from the ideal Lorentzian line shape. In figure 4.16(b) the laser current-temperature pair $I_L = 2.35\,\text{mA}$ and $T_L = 46.3°C$ was set which yielded a much more symmetric CPT resonance line shape.
Since both transition matrix elements have the same value for the CPT resonance $n = 0$ (see table 4.3), the CPT resonance should be symmetric when the intensities of the laser sidebands are equal.

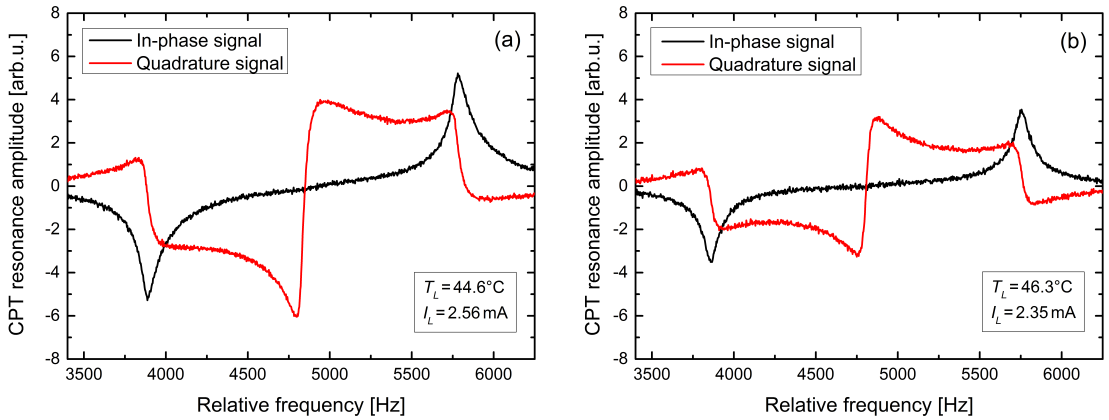

Figure 4.16.: CPT resonance structure of $n = 0$ for two different laser current-temperature pairs: The respective laser operational parameters resulted in (a) an asymmetric CPT resonance line shape and in (b) a symmetric CPT resonance line shape. The same microwave power level was used for the two measurements: $P_{MW} = -5.4\,\mathrm{dBm}$. The measurements were performed with the CSES QM in a magnetic shielding can. A magnetic field of $B = 40.0\,\mu\mathrm{T}$ was applied. The Rb cell contained a buffer gas (Ne) at a pressure of $P_{BG} = 5.3\,\mathrm{kPa}$ (40 Torr). The optical intensity in front of the cell was $I = 130\,\mu\mathrm{W/cm^2}$. The sensor angle was $\phi = 0°$.

Additionally, the line shape could have also been influenced by an optical detuning [39] (see also section 4.1.5). Since the optical detuning during the CDSM operation was not well known (see also 2.4.2), further tests are required to set the ideal values for the optical detuning and laser sideband structure for the operation of the CDSM.

In case of an asymmetric line shape of the CPT resonance $n = 0$, the CPT resonance line shapes of $n = -2$ and $n = +2$ were typically asymmetric too. In order to investigate, if the asymmetric line shapes affect the magnetic field measurement by the CDSM, first test measurements were performed at the Conrad Observatory (see appendix A.4.2) in Earth's magnetic field ($B \approx 48.5\,\mu\mathrm{T}$). The external magnetic fields were measured with the CSES QM and compared to the measured magnetic field strengths of an Overhauser magnetometer over the sensor angle (heading characteristic).
Two different laser current-temperature pairs $I_L = 2.89\,\mathrm{mA}$ and $T_L = 44.5°\mathrm{C}$ with $I_L = 2.48\,\mathrm{mA}$ and $T_L = 46.3°$ were used. The laser temperature T_L was set to the same value as during the measurements in the laboratory, which resulted the CPT resonance line shapes depicted in figure 4.16. However, the resulting laser current I_L deviated from the measurements in the laboratory due to the different surrounding temperature at the observatory ($T \approx 6°\mathrm{C}$). The coaxial cable, which was used to apply the modulated laser current to the VCSEL, was directly connected to the laser housing. The cable, which was at the ambient temperature of the observatory, cooled the laser. The lower temperature

of the laser shifted the laser frequency which was compensated by a change of the laser current. A different laser current results in a changed intensity distribution between the laser frequency components (see figure 3.1).
The difference of the measured magnetic field strengths for the two different current-temperature pairs was lower than 0.2 nT. The asymmetry of the single CPT resonance line shapes seemed to be compensated by building the CDSM resonance (see figure 4.2). Nevertheless, further measurements are planed in order to investigate the influence of the laser operational parameters on the CPT and CDSM resonance line shapes and their effect on the measurement accuracy.

4.1.5. Optical Detuning

In the case of the CDSM, a detuning of the laser frequency causes a detuning of the whole laser frequency sideband structure (see figure 2.12) and thus introduces a two-photon detuning δ_L (see equation 2.2). The two-photon detuning δ_L indicates, as shown in figure 2.1, a deviation of the two laser frequencies (ω_1 and ω_2) from exact resonance with the two optical transitions ($|1\rangle \rightarrow |3\rangle$ and $|2\rangle \rightarrow |3\rangle$) while the condition $\delta_R = 0$ is still fulfilled. For this reason, it is also called optical detuning. An optical detuning affects the line shape of the CPT resonance and causes asymmetries [39].
Since an optical detuning shifts all frequency components of the double modulated laser field equally, the transitions forming the Λ systems for the CPT resonance excitations experience the same optical detuning. Thus, the CPT resonance line shapes of both single CPT resonances, which form the CDSM resonance, are affected similarly by an optical detuning. The resulting line shape asymmetries of the single CPT resonances are largely compensated by forming the CDSM resonance (see figure 4.2). Depending on the single CPT resonance line shapes, the asymmetries can result in a deviation of the symmetric CDSM resonance line shape which shifts the stabilisation point of the control loop and as a consequence the detected magnetic field strength.
Additionally, the CPT resonance line shape can be influenced by the optical detuning by another circumstance. As described in section 4.1.1, CPT resonances can be formed with both excited states ($F' = 1$ and $F' = 2$) which can be simultaneously prepared. Therefore, the detected CPT resonance signal can consist of contributions from two CPT resonances formed each with one of the excited states [94]. The CPT resonance preparation depends on the optical detuning, the frequency difference between the two excited states (≈ 815 MHz), the broadening of the optical transitions by, e.g., collisional broadening (see section 4.1.3.1) and the laser line width [56]. The line shape of the resulting CPT resonance could be asymmetric depending on the individual contribution of the two CPT resonances.
Furthermore, the optical detuning influences the light shift (discussion see section 4.1.1.2) and increases the noise level of the magnetometer due to a conversion of the laser frequency

noise into amplitude noise by the slope of the absorption signal of the two resonant optical transitions preparing the Λ system [15].
During the CDSM operation, the laser frequency is set by two control loops (see section 2.4.2). The laser temperature control loop keeps the laser temperature at a defined temperature and the laser current control loop is used to compensate laser frequency changes by adjusting the laser current. The laser frequency is kept constant with the help of the optical spectrum but the frequency is not exactly stabilised to the condition where the Λ system is prepared by the two ground states and just one of the excited states $F' = 1$ or $F' = 2$ due to the broadening of the optical transitions (see also discussion in section 2.4.2). Thus, the value of the optical detuning is unknown so far and an optical detuning could influence the CDSM resonances line shapes, which could affect the magnetic field measurement.
In order to examine the effect of an optical detuning on the CDSM resonance line shape, the laser frequency was altered while still operating the laser frequency stabilisation control loop. Since the frequency position of the stabilisation point is not exactly known, the term laser frequency detuning is used instead of optical detuning in the further discussion. The laser frequency detuning describes the detuning of the laser frequency from the normally stabilised laser frequency during the operation of the CDSM.
Usually, the laser frequency control loop follows the zero crossing of the stabilisation slope (see figure 2.17). Nevertheless, the laser frequency can be detuned by stabilising the laser frequency not to the zero crossing but to an offset along the edge. The possible offsets – and thus the laser frequency detuning range – are limited by the height and the slope of the stabilisation signal which are influenced by the operational parameters of the magnetometer like, e.g., laser intensity and buffer gas pressure. Thus, the laser frequency detuning cannot be set arbitrarily large while operating the laser current control loop.

In figure 4.17 the CDSM resonance $n = 2$ is depicted for different laser frequency detunings from the usually stabilised laser frequency of the magnetometer. The laser frequency was still stabilised via the control loop – as described above – but the stabilisation point was shifted by a positive or negative offset. The laser frequency detuning was calculated from the shift of the laser current by the set offset and the current shifting coefficient of the mounted laser diode ($\Delta\nu/\Delta I = 104\,\mathrm{GHz/mA}$ at $I_{op} = 2.7\,\mathrm{mA}$) (see also section 3.2).

The laser operational parameters were set such that the CDSM resonance had a symmetric line shape (see section 4.1.4). For positive frequency detunings as shown in figure 4.17(a), the positive peak of the dispersion signal showed a reduction of its amplitude. For a negative detuning as depicted in figure 4.17(b), the negative peak of the dispersion signal showed a deviation from the symmetric line shape.
Changing the laser frequency detuning during the operation of the laser frequency control loop can be used to correct line shape asymmetries and thus optimise the CDSM resonance amplitude or to alter the influence of the light shift (see section 4.1.1.2).

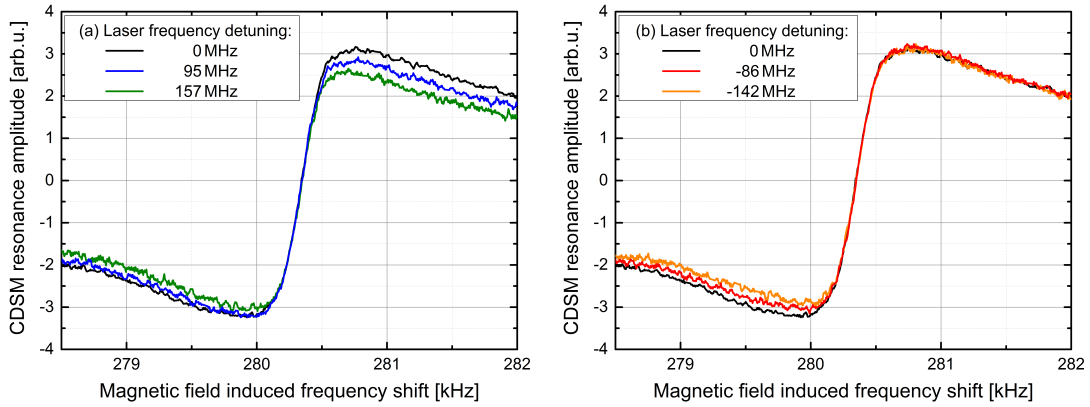

Figure 4.17.: Influence of a laser frequency detuning on the CDSM resonance $n = 2$: In (a) the CDSM resonance $n = 2$ is depicted for positive frequency offsets. In (b) the behaviour of the same CDSM resonance is shown for negative frequency offsets. The measurement was performed with the CSES FS model. The sensor cell contained neon as buffer gas at a pressure of $P_{BG} = 5.3\,\mathrm{kPa}$ (40 Torr). A magnetic field of $B \approx 19.9\,\mu\mathrm{T}$ was applied. The laser intensity in front of the cell was $I \approx 140\,\mu\mathrm{W/cm^2}$. The sensor cell had at a temperature of $T = 25°\mathrm{C}$.

A symmetric CDSM resonance line shape can be achieved even though the single CPT resonances are asymmetric. As described in section 4.1.4, the CPT resonance line shapes are affected by different Rabi frequencies of the transitions forming the Λ systems and by an optical detuning. Thus, the single CPT resonances have to be investigated in order to evaluate line shape asymmetries by, e.g., an optical detuning which can affect the light shift. Ideally, the Rabi frequencies should be equal and the optical detuning $\delta_L = 0$ to reduce the light shift. Thus, further investigations of the line shape asymmetries caused by the optical detuning and their impact on the accuracy of the magnetic field measurement are planned with a well-defined optical detuning.

Additionally, since the laser frequency is set by the zero crossing of the stabilisation signal used for the laser current control loop, disturbances like, e.g., reflections and the possible formation of etalons by two reflecting surfaces, such as, e.g., the sensor cell windows, can shift the zero crossing and thus introduce an optical detuning.
In figure 4.18, the stabilisation signal, which is used for the laser current control loop (see section 2.4.2), is compared for a Rb vapour cell with and without anti-reflective (AR) coating on the sensor cell windows. The uncoated sensor cell windows caused a sinusoidal variation of the detected signal. The disturbing influence depends on the distance of the optical elements and the strength of the reflection. An uncoated optical surface typically reflects about 4% [118]. Depending on the position of the stabilisation signal on the disturbing signal, the zero crossing of the control loop was shifted and consequently the optical detuning changed (up to several hundreds of MHz).

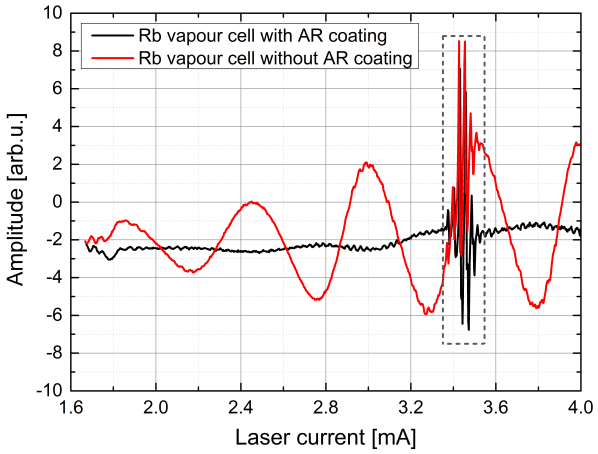

Figure 4.18.: Influence of reflections from uncoated and AR coated Rb vapour cell windows on the stabilisation signal used for the laser current control loop: The dashed rectangle shows the signal used for the laser frequency stabilisation (see section 2.4.2 and figure 2.17). The reflections on the sensor cell windows without AR coating causes a sinusoidal disturbance over the laser current and thus shifts the position of the laser current stabilisation point depending on the shape of this disturbance. The measurement was performed with the CSES QM. A laser intensity of $I = 190\,\mu W/cm^2$ was measured. Both sensor cells had the same size and contained Ne as buffer gas at a pressure of $P_{BG} = 5.3\,kPa$ (40 Torr).

Using AR coating on the windows ($R < 0.5\%$ per surface) reduced these sinusoidal disturbance (see black line in figure 4.18). The optical spectrum measured with the AR coated cell still showed some disturbances coming from reflections and stray light from other optical elements. These influences were further reduced by using AR coatings with less reflectivity and additionally tilting several optical elements slightly. Further, the surrounding areas of the optical elements were black anodised to reduce the influence of stray light.

4.1.6. Quadratic Dependence on the External Magnetic Field

As discussed in section 2.1.2.2, the ground state transition frequencies within the hyperfine structure of the ^{87}Rb D_1 line have also a quadratic dependence on the external magnetic field B. In table 2.1 the quadratic shift coefficients of the ground state transition frequencies and their respective CPT resonance are summarised. Additionally, in figure 4.19 the quadratic shifts with the external magnetic field, which shift the CPT resonance positions by the same value, and their influence on the CDSM resonances are depicted. The quadratic frequency shifts of the CPT resonance positions with the external magnetic field are shown in figure 4.19(a) for the CPT resonances $n = 0$, -2, $+2$, -3 and $+3$.

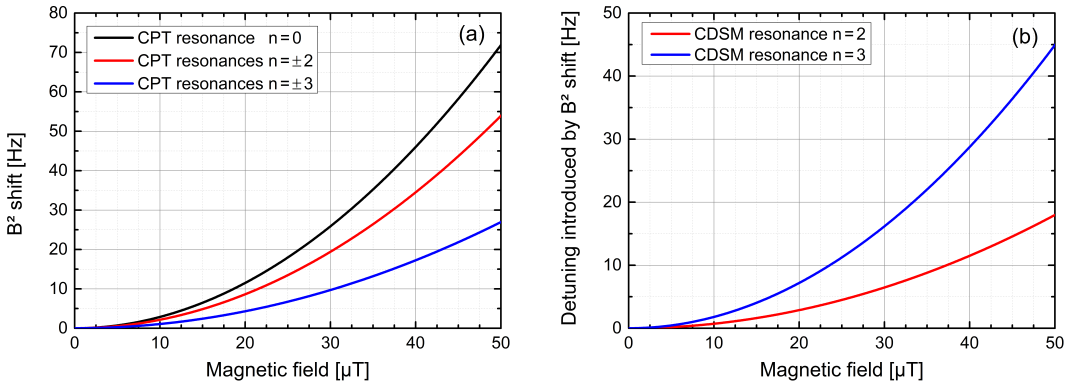

Figure 4.19.: Quadratic dependence of the CPT resonance positions on the magnetic field as well as the introduced detuning for the respective CDSM resonance: In (a) the quadratic shifts of the ground state transition frequencies are depicted, which are used to prepare the CPT resonances $n = 0$, -2, $+2$, -3 and $+3$. In (b) the relative quadratic frequency shifts between $n = 0$ and the CDSM resonances $n = 2$ and $n = 3$, which cause a detuning Δ_{B^2}, are shown.

The CPT resonance $n = 0$ has the highest quadratic dependence on the external magnetic field. The height of the quadratic dependence reduces with increasing CPT resonance number. Thus, the CPT resonances $n = -3$ and $n = +3$ experience a lower quadratic shift compared to $n = -2$ and $n = +2$.
The two CPT resonances ($n = \pm 2$ or $n = \pm 3$), which are coupled to the CDSM resonances ($n = 2$ or $n = 3$), are shifted equally by their quadratic dependence on the external magnetic field. Therefore, the quadratic magnetic field shift would introduce a detuning Δ (see equation 2.45) respective to their quadratic shift coefficient (see table 2.1). However, due to the use of the microwave frequency stabilisation control loop (see section 2.4.2), a detuning of the height of the relative quadratic magnetic field shift values $\Delta\nu_{B^2}$ is introduced instead. The relative quadratic magnetic field shift value $\Delta\nu_{B^2}$ is given by the difference between the quadratic shift coefficients of the CPT resonance $n = 0$, which is used for the stabilisation of the control loop, and the CPT resonance, which is used for the magnetic field measurement. In figure 4.19(b) the resulting detuning $\Delta\nu_{B^2}$ is depicted for the CDSM resonances $n = 2$ and $n = 3$ in dependence of the external magnetic field. Additionally, the differential quadratic magnetic field shift coefficients $\Delta\nu_{B^2}$ are listed in the table 4.8 for the CPT resonances $n = -2$, $+2$, -3 and $+3$. These coefficients were used to calculate the detuning shown in figure 4.19(b).

The detuning Δ_{B^2} can affect the magnetic field measurement, either if the detuning gets larger than the compensation limit (see equation 2.47) or if the two CPT resonance line shapes are different (see section 4.2.1 and figure 4.2). For different line shapes, the measurement accuracy can be influenced depending on the height of the detuning (see figure 4.29).

Table 4.8.: Differential magnetic field shift $\Delta\nu_{B^2}$ of the CPT resonance $n = 0$ and $n = -2$, $+2$, -3 and $+3$: When the microwave control loop is operated, a detuning Δ_{B^2} is introduced between the single CPT resonances $n = \pm 2$ and $n = \pm 3$ (see section 2.3.2).

n	$\Delta\nu_{B^2}$ [Hz/nT^2]
± 2	$-143.8 \cdot 10^{-10}$
± 3	$-359.5 \cdot 10^{-10}$

For the CSES mission, the differential quadratic magnetic field shift is compensated by an alternating mode of the microwave frequency stabilisation control loop [12] which has the following sequence. First, the zero crossing frequency of the CPT resonance $n = 0$ is detected (see also section 2.4.2), second the microwave controller state is preserved, third the determined microwave frequency is corrected by the differential magnetic field shift $\Delta\nu_{B^2}$ of the respective CDSM resonance (see table 4.8) and fourth the external magnetic field strength is detected.
In contrast, for the JUICE mission, where mainly magnetic fields below $B < 2\,\mu\mathrm{T}$ are expected during the main science phase (see also section 4.3), the influence of the quadratic magnetic field is not relevant ($< 0.01\,\mathrm{nT}$ for $n = 3$) and no compensation has to be performed.
Additionally, the introduced detuning influences the CPT resonance line shapes, when it is not compensated. The detuning causes a splitting of the single CPT resonances forming the CDSM resonance (see figure 2.13). Due to this splitting the CDSM resonance amplitude is reduced and the line width broadened.

4.1.7. Angular Dependence on the External Magnetic Field Direction

The angular dependence of the CPT resonance line shapes on the external magnetic field direction is important for the operation of the magnetometer, since during space missions the external magnetic field can have various orientations compared to the mounting of the sensor unit.
The CPT resonance line shapes change with the external magnetic field direction due to altered Rabi frequencies (see equations 4.1 and 4.2) which are determined by the laser intensity and the transition strengths of the selected transitions. Further on, the transition strength depends on the polarisation state of the light field and the angle between the laser propagation direction and the external magnetic field direction, which we label as the sensor angle ϕ. A sensor angle of $\phi = 0^\circ$ corresponds to the case when the laser propagation direction and the magnetic field direction coincide (see longitudinal case in

section 2.1.2.2). Further, a sensor angle of $\phi = 90°$ corresponds to the case when the laser propagation direction and the magnetic field direction are perpendicular (see transversal case in section 2.1.2.2).
Several CPT resonances can be excited within the hyperfine structure of the ^{87}Rb D_1 line depending on the sensor angle ϕ and the set polarisation state of the light field (see figures 2.5 and 2.6). According to the theoretical model in [91], for high buffer gas pressures and circularly polarised light, the angular dependence of the relative CPT resonance line strength S_{rel} is given by:

$$S_{rel} \propto \cos^2(\phi) \qquad \text{for } n = 0, \pm 2\,, \tag{4.20}$$

$$S_{rel} \propto \sin^2(\phi) \qquad \text{for } n = \pm 1, \pm 3\,. \tag{4.21}$$

From equations 4.20 and 4.21 it results that the relative line strengths of the odd and even numbered CPT resonances have a $\pi/2$-shifted angular dependence.
For the operation of the CDSM magnetometer, the angular dependence of the relative line strengths is commonly not investigated. Rather the amplitudes and slopes of the CPT resonances or the line shape imbalance between the single CPT resonances, which are coupled to the CDSM resonance, are examined in dependence of the sensor angle.

In figure 4.20 the CPT resonance amplitudes $n = -2$, $+2$, -3 and $+3$ are depicted for different sensor angles. The CSES EM electronics and the dual pass cell were used but the sensor cell was only passed once by the laser beam and then the beam was coupled into the inbound fibre.
The measurement was performed in the Helmholtz coil system at the Space Research Institute (see appendix A.4.1). The benefit of a coil system compared to a magnetic shielding can are that the optical fibres do not have to be moved during the measurements. Thus, the light properties in the optical fibres are not changed during the experiment. The drawback of the coil system is that disturbing AC and DC magnetic fields, which are present in the laboratory environment, can influence the measurement. Therefore, the magnetic field inhomogeneity is typically higher compared to the magnetic shielding can and the CPT resonance line shapes are broadened. The detected CPT resonances had line widths in the range of $\Delta\nu_{CPT} = 2 - 4\,\text{kHz}$ which were about a factor of two higher compared to the line widths measured in the magnetic shielding can.

In figure 4.20(a) the CPT resonance amplitudes of $n = -2$ and $n = +2$ are shown for several sensor angles between $\phi = 0°$ and $\phi = 180°$. The CPT resonance amplitude of $n = +2$ had an absolute maximum at the sensor angle of $\phi \approx 30°$ and a relative maximum at $\phi \approx 135°$. The CPT resonance amplitude of $n = -2$ had an absolute maximum at a sensor angle of $\phi \approx 150°$ and a relative maximum at $\phi \approx 45°$. Both CPT resonance amplitudes vanished around $\phi = 90°$
In figure 4.20(b) the angular dependences of the CPT resonance amplitudes of $n = -3$ and $n = +3$ are shown. Both resonances were not detectable around the sensor angles of

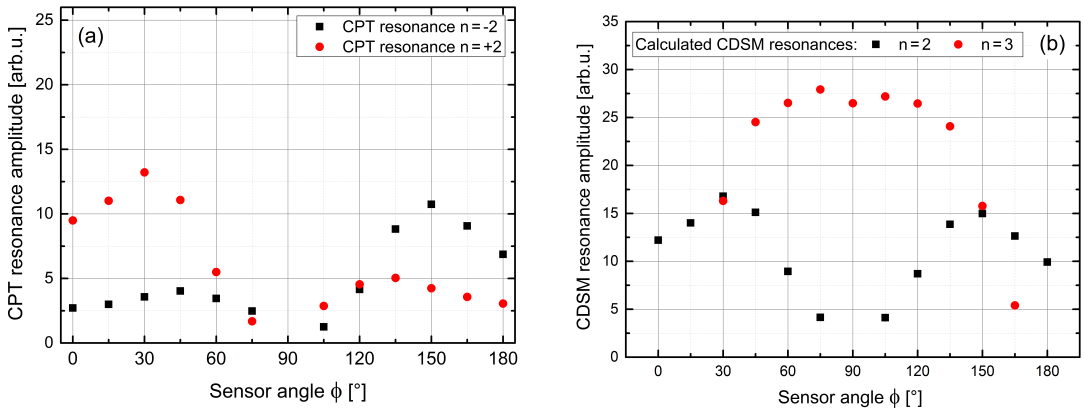

Figure 4.20.: CPT resonance amplitudes in dependence of the sensor angle: In (a) the amplitudes of CPT resonances $n = -2$ and $n = +2$ are depicted. In (b) the CPT resonance amplitudes of $n = -3$ and $n = +3$ are shown. The measurement was performed in a Helmholtz coil system. A magnetic field of $B = 40.0\,\mu T$ was applied. The CSES EM electronics and the dual pass cell were used but the sensor cell only passed once by the laser beam. The sensor cell contained Ne as buffer gas at the pressure of $P_{BG} = 4.0\,kPa$ (30 Torr). The optical intensity in front of sensor cell was $I = 180\,\mu W/cm^2$.

$\phi = 0°$ and $\phi = 180°$. The CPT resonance amplitude of n=−3 increased steadily from $\phi = 30°$ up to a sensor angle of $\phi \approx 135°$ where it had a maximum. The CPT resonance amplitude of $n = +3$ had a maximum at $\phi \approx 45°$ and its amplitudes decreased again for larger angles.
As shown in figure 4.20, the amplitudes of the single CPT resonances, which form the CDSM resonance, revealed dissimilar amplitudes for most sensor angles. As will be further discussed in section 4.2, the imbalanced CPT resonance line shapes reduce the CDSM-based compensation.

The angular dependence of the CDSM resonances results from the angular dependence of the single CPT resonances. Therefore, in figure 4.21 measured CDSM resonance amplitudes are compared with calculated CDSM resonance amplitudes from the CPT resonance amplitudes shown in figure 4.20. The measured and calculated CDSM resonance amplitudes depicted in figure 4.21(a) and (b) can not be compared directly, since different experimental setups and parameters were used. However, the angular characteristics should agree despite the different measurement configurations.

In figure 4.21(a) the angular dependence of the CDSM resonances is depicted for a measurement performed in a Braunbeck coil system (see appendix A.4.3) and an applied magnetic field of $B = 49.00\,\mu T$. The magnetic field direction was rotated in order to obtain the sensor angles between $\phi = 0°$ and $\phi = 180°$.

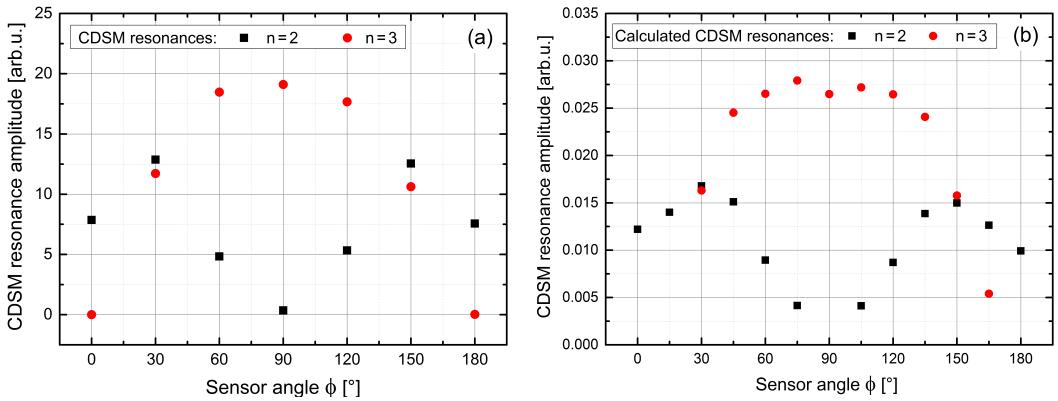

Figure 4.21.: CDSM resonance amplitudes for sensor angles between $\phi = 0°$ and $\phi = 180°$: In (a) the measured CDSM resonances $n = 2$ and $n = 3$ are depicted. In (b) the sums of the single amplitudes of the CPT resonances shown in figure 4.20 are presented. The measurements illustrated in (a) were performed in a Braunbeck coil system. The CSES LM was used with a sensor cell containing a buffer gas pressure of $P_{BG} = 4.0\,\text{kPa}$ (30 Torr). The optical power at the photodiode was $P_{PD} = 57\,\mu\text{W}$. A magnetic field of $B = 49.00\,\mu\text{T}$ was applied.

The angular dependence of the CDSM resonance amplitude of $n = 2$ showed two maxima at $\phi = 30°$ and $\phi = 150°$ which coincides with the angular dependence of the calculated CDSM resonance $n = 2$ in figure 4.21(b).
The CDSM resonance amplitudes of $n = 3$ revealed a maximum at $\phi = 90°$. The angular dependence of the measured CDSM resonance $n = 3$ nearly matched the angular dependence of the calculated CDSM resonance $n = 3$. However, the measured CDSM resonance amplitudes of $n = 3$ were affected by the quadratic dependence of their CPT resonances on the external magnetic field (see section 4.1.6) which was not compensated for this measurement. The quadratic magnetic field dependence introduced a detuning between the single CPT resonances $n = \pm 3$ which led to a reduction of the CDSM resonance amplitudes. The influence of the quadratic magnetic field dependence on the CDSM resonance $n = 2$ is lower compared to $n = 3$. For this reason, the measured CDSM resonance amplitudes of $n = 3$ were more reduced by the quadratic dependence than $n = 2$. In contrast, the calculated CDSM resonances in figure 4.21(b) were not affected by the detuning, since the maxima of the single CPT resonance amplitudes were added up directly.

The CDSM uses the different angular dependence of the even and odd numbered CDSM resonances to obtain an omni-directional magnetic field measurement for the whole sensor angle range [10]. In figure 4.22 the CDSM resonance structures of $n = 1$, 2 and 3 are shown for the sensor angles $\phi = 0°$, 30°, 60° and 90°.

In accordance with the amplitude dependence shown in figure 4.21, at a sensor angle of $\phi = 0°$ only the CDSM resonance $n = 2$ was visible and almost vanished at $\phi = 90°$. The

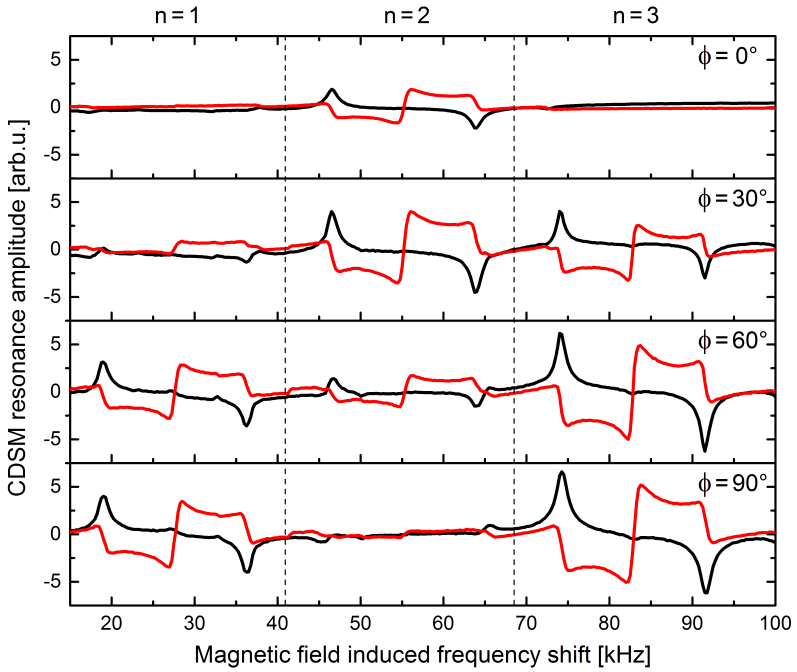

Figure 4.22.: Angular dependence of the CDSM resonances $n = 1$, 2 and 3: The measurements were performed with the CSES LM in a magnetic shielding can. A magnetic field of $B = 3.89\,\mu T$ was applied. The Rb cell contained Ne as buffer gas at a pressure of $P_{BG} = 4.0\,kPa$ (30 Torr). The sensor temperature was $T = 26.5°C$. An optical power of $P = 90\,\mu W$ was measured at the photodiode. A modulation frequency of $\nu_{B_{FMS}} \approx 8.7\,kHz$ was applied.

CDSM resonances $n = 1$ and $n = 3$ had a minimum amplitude at $\phi = 0°$ and a maximum at $\phi = 90°$.

Typically, the CDSM resonances $n = 2$ and $n = 3$ are used for the magnetic field measurement, since they have a higher linear magnetic field shift coefficient δ_{CDSM_n} than the CDSM resonance $n = 1$ (see table 2.2). Additionally, the CDSM resonance $n = 1$ actually consist of two CDSM resonances $n = 1a$ and $n = 1b$ which have a slightly different linear magnetic field shift coefficient. As a result, they split up for increasing external magnetic field strengths which is unwanted for magnetic field measurements over a large dynamic range.

During the operation of the magnetometer, the switching between the CDSM resonances $n = 2$ and $n = 3$ is accomplished at certain sensor angles to obtain an omnidirectional magnetic field measurement. For the CSES mission, the CDSM resonance $n = 2$ is selected for the magnetic field measurement in the sensor angle ranges from $\phi = 300°$ to $\phi = 60°$ and $\phi = 120°$ to $\phi = 240°$ [12]. At the other sensor angles, the CDSM resonance $n = 3$ is used for the magnetic field measurement.

At the sensor angles 60°, 120°, 240° and 300° the CDSM resonances are switched. Therefore, the information on the magnetic field direction has to be known. For the CSES

mission as well as for the JUICE mission, the CDSM is operated in combination with two vector magnetometers (fluxgate magnetometers). The fluxgate magnetometers use the CDSM as reference to correct drifts of the vector measurement by in-flight calibration [9]. In return the CDSM gets the information on the magnetic field direction from the vector magnetometer [12] and then selects the ideal CDSM resonance. The resonance selection could be obtained independently from the vector magnetometer but has not been realised yet.

4.2. CDSM-Based Compensation of Disturbing Frequency Shifts

As discussed in section 2.3.1, the transition frequencies within the hyperfine structure ground states are not only shifted by the external magnetic field but also by, e.g., buffer gas induced shifts (see section 4.1.3) or the light shift (see section 4.1.1.2). The impact of these disturbing frequency shifts on the magnetic field measurement is compensated by building the CDSM resonance (see section 2.3.2). The efficiency of the CDSM-based compensation depends critically on the CPT resonance line shapes. Thus, in order to obtain the best compensation effect, the line shapes of the CPT resonances, which form the CDSM resonance, should be ideally identical. However, measurements with the CDSM have shown that the CPT resonance line shapes are different for most sensor angles. Therefore, the influence of different CPT resonance line shapes on the CDSM-based compensation is discussed in more detail in section 4.2.1.
The optical pumping effect was supposed to cause the imbalanced CPT resonance spectrum. Therefore, the optical pumping effect is reviewed in section 4.2.2 and measurements are summarised which aim at a reduction of its influence on the CPT resonance line shapes. To reduce the impact of the optical pumping effect, a new sensor design was developed - the dual pass sensor (see section 3.3.3). In section 4.2.3 the amplitude ratios of the single CPT resonances, which build the CDSM resonance, are compared for a single and a dual laser beam pass through the sensor cell in dependence of the sensor angle. Additionally, the impact of the CPT resonance line shapes on the CDSM-based compensation of disturbing frequency shifts is investigated for a single and a dual laser beam pass.

4.2.1. Impact of Different CPT Resonance Line Shapes

The compensation of disturbing transition frequency shifts by the formation of the CDSM resonance critically depends on the line shapes of the single CPT resonances which form the respective CDSM resonance (see section 2.3.2). A disturbing frequency shift introduces a detuning of $2 \cdot \Delta$ between the single CPT resonance positions. The detuning was defined as

$\Delta = \nu_0 - 2 \cdot \nu_{mod_1}$ (see equation 2.45). When the microwave frequency stabilisation control loop is active (see section 2.4.2), the microwave modulation frequency ν_{mod_1} is adjusted to half of the transition frequency ν_0 (see equation 2.27) and as a result $\Delta = 0$. However, this control loop cannot be operated at all sensor angles (see section 2.4.2). When the control loop is not operated, a detuning Δ is ideally completely compensated by the CDSM resonance without influence on the detected magnetic field. The theoretical compensation limit of a detuning Δ_{max} (see equation 2.47) is only reached, if the single CPT resonances, which form the CDSM resonance, have the same line shape. However, measurements in dependence of the sensor angle ϕ have shown that the single CPT resonances have different line shapes for most sensor angles (see also section 4.1.7).
In figure 4.23 the amplitude ratios h_{-2}/h_{+2} and h_{-3}/h_{+3} of the single CPT resonances $n = \pm 2$ and $n = \pm 3$ are depicted for sensor angles between $\phi = 0°$ and $\phi = 180°$.

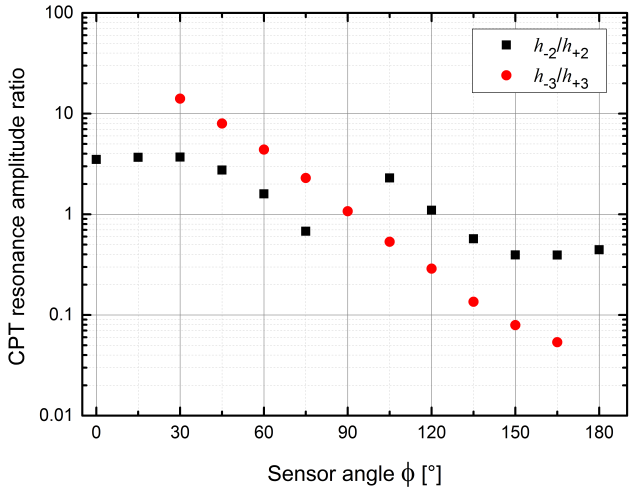

Figure 4.23.: Amplitude ratios of the CPT resonances h_{-2}/h_{+2} and h_{-3}/h_{+3} for different sensor angles between $\phi = 0°$ and $\phi = 180°$: The measurement was performed in a triaxial Helmholtz coil system. A magnetic field of $B = 40.0\,\mu T$ was applied. For this measurement, the CSES EM electronics was used in combination with a dual pass cell but the cell was only passed once by the laser beam. The sensor cell contained Ne as a buffer gas at the pressure of $P_{BG} = 4.0\,kPa$ (30 Torr). The intensity was about $180\,\mu W/cm^2$ in front of the sensor cell.

The amplitude ratios are used as indicator of the similarity between the single CPT resonance line shapes (see also figure A.1). The measurements were performed within a triaxial Helmholtz coil system at the Space Research Institute in Graz (see appendix A.4.1). A magnetic field of $B = 40.0\,\mu T$ was applied and the CSES EM electronics was used. A dual pass cell was mounted which contained Ne as buffer gas at a pressure of $P_{BG} = 4.0\,kPa$ (30 Torr). The laser beam passed the sensor cell only once. The single CPT resonance amplitudes of the same measurement are depicted in figure 4.20.
For sensor angles $\phi = 0°$, 15° and 30°, the amplitude ratios of h_{-2}/h_{+2} were about 3.5.

The CPT resonance amplitudes became more balanced by increasing the sensor angle from $\phi = 30°$ to about $\phi \approx 70°$ where they were approximately equal. Then, the ratio rose again until the CPT resonances vanished around a sensor angle of $\phi = 90°$. The run of the ratio h_{-2}/h_{+2} was almost point symmetric around the sensor angle $\phi = 90°$. The slight deviation from symmetry was assumed to result from a residual inhomogeneous magnetic field in the unshielded environment.
The amplitude ratio of h_{-3}/h_{+3} was balanced at $\phi = 90°$ but rapidly increased for diverging angles. At $\phi = 60°$ the CPT resonance amplitude of $n = -3$ was already a factor of 4.4 higher than the amplitude of $n = +3$. For most sensor angles, the amplitude ratios of h_{-2}/h_{+2} were more balanced than the ratios of h_{-3}/h_{+3} except of sensor angles close to $\phi = 90°$.

The influence of different CPT resonance line shapes on the CDSM-based compensation of disturbing frequency shifts is illustrated in figure 4.24. A disturbing frequency shift introduces a detuning Δ between the zero crossing frequencies of the CPT resonances and the magnetic field induced frequency $2 \cdot |\nu_{B_n}|$ (see table 2.1).
In figure 4.24 the CPT resonance line shapes are approximated by two dispersive Lorentzian functions (see section 2.3.2). The two CPT resonance line widths are set to $\Delta\nu_{CPT_1} = \Delta\nu_{CPT_2} = 150\,\text{Hz}$. The zero crossing frequencies of the CPT resonances without disturbing frequency shift are $2 \cdot |\nu_{B_n}| = 56.000\,\text{kHz}$, which, e.g., corresponds to an external magnetic field strength of $B = 3994.4\,\text{nT}$ for the CDSM resonance $n = 2$. For the example depicted in figure 4.24, the CPT resonances are split and shifted in opposite directions by a detuning of $\Delta = 20\,\text{Hz}$.
Additionally, in figure 4.24(a) the CPT resonance amplitudes are equal $\Delta h_{CPT_1} = \Delta h_{CPT_2} = 1$. Therefore, the two CPT resonances have the identical line shape and the compensation of an unwanted detuning Δ works best. In this case, the opposite contributions of the CPT resonance amplitudes at the magnetic field induced frequency shift $2 \cdot |\nu_{B_n}|$ add up and the resulting CDSM resonance has its zero crossing at the frequency $2 \cdot |\nu_{B_n}|$ (see figure (c) and enlarged in (e)). For identical line shapes and a line width of $\Delta\nu_{CPT} = 150\,\text{Hz}$, the theoretically possible detuning Δ_{max}, which can be compensated without an influence on the measured magnetic field, can be calculated from equation 2.45 which gives $\Delta_{max} \approx 42\,\text{Hz}$.
In figure 4.24(b) the line widths are still the same but the amplitudes are unequal: $\Delta h_{CPT_1} = 1$ (black curve) and $\Delta h_{CPT_2} = 0.3$ (red curve). As a result, the two CPT resonances have different line shapes. In this case, the amplitudes of the two CPT resonances at the magnetic field induced transition frequency $2 \cdot |\nu_{B_n}|$ are dissimilar and the zero crossing frequency of the CDSM resonance is shifted by about 12 Hz in the direction of the single CPT resonance with the higher CPT resonance amplitude (see figure (d) and enlarged in (f)). This frequency shift results in a change of the measured magnetic field by about 0.9 nT for $n = 2$ (see table 2.2).

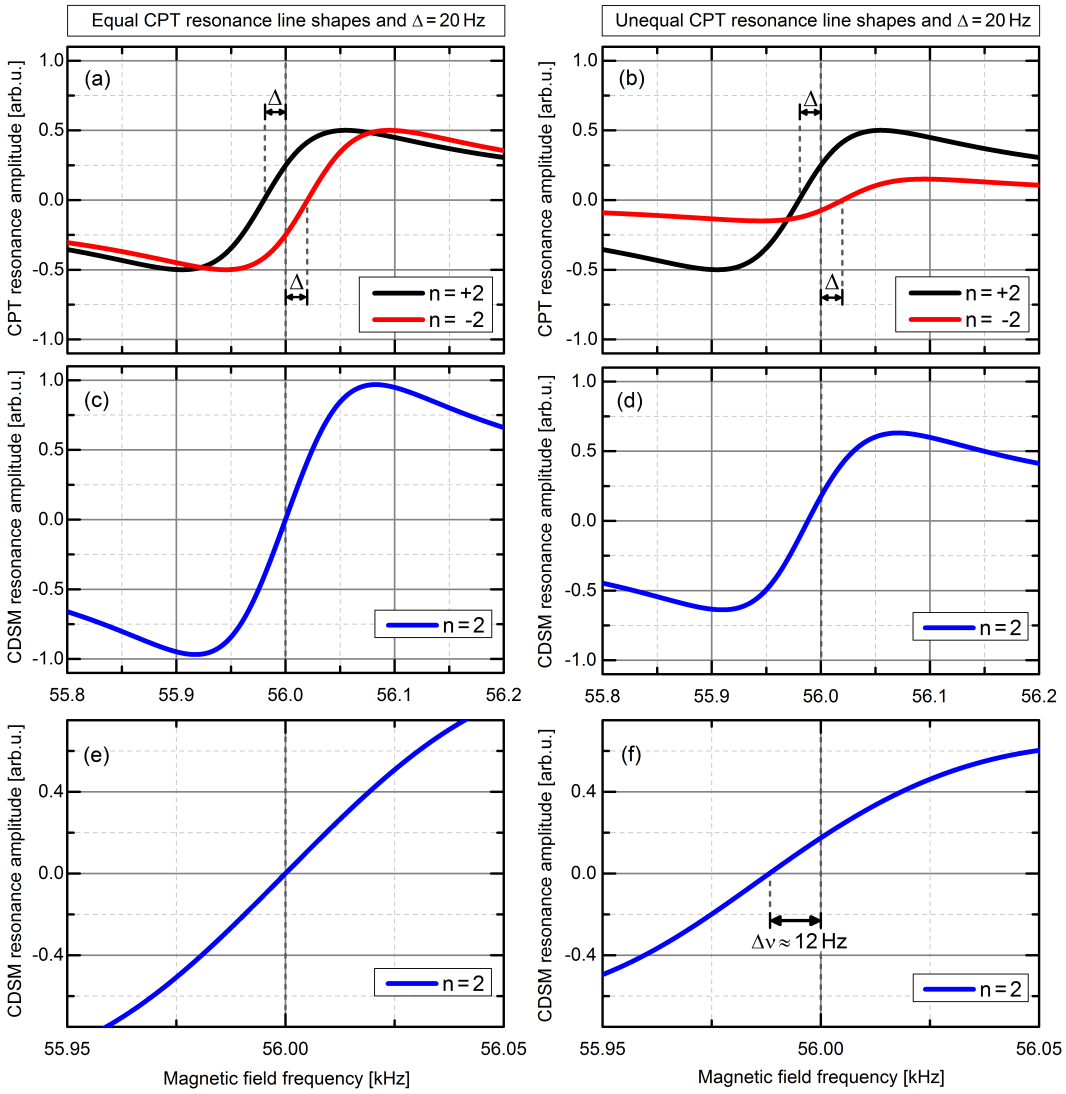

Figure 4.24.: Simulated compensation of a detuning Δ with identical and different single CPT resonance line shapes: In (a) the case of identical single CPT resonance line shapes is shown. The zero crossing of the CDSM resonance in (c) is formed at the magnetic field induced frequency shift $2 \cdot |\nu_{B_n}|$ (enlarged section in (e)). Thus, the magnetic field measurement is unaffected by the detuning Δ. In (b) the case of different single CPT resonance line shapes is depicted for the same detuning Δ as in (a). In (d) the zero crossing frequency of the CDSM resonance is shifted by about 12 Hz towards the single CPT resonance with the higher amplitude (enlarged section in (f)).

Without forming the CDSM resonance, a disturbing frequency shift of 20 Hz would result in a shift of -1.4 nT for using the CPT resonance $n = -2$ to determine the external magnetic field or 1.4 nT for using the CPT resonance $n = +2$. Thus, for different CPT resonance line shapes, the influence of a disturbing frequency shift on the measured magnetic

field strength is still reduced by forming the CDSM resonance. However, the achieved compensation effect is reduced with increasing slope difference between the two CPT resonances (see also section 4.2.3).
A disturbing frequency shift of several Hz can be caused, for example, by a change of the sensor temperature (see section 4.1.3.3) or a drift of the reference oscillator (see section 2.4.2). For sensor angles at which the microwave frequency stabilisation control loop is active, a detuning Δ is compensated. In the angular range where the control loop is not operated (typically between $\phi = 60°$ and $\phi = 120°$ as well as between $\phi = 240°$ and $\phi = 300°$), the similarity of the CPT resonance line shapes is important for the compensation of a detuning Δ. Therefore, the single CPT resonances should have the same line shape for an ideal operation of the CDSM. As a consequence, an equalisation of the CPT resonance line shapes is desirable for the whole sensor angle range.

4.2.2. Optical Pumping Effect

The discovered imbalance between the CPT resonance line shapes (see figure 4.23) is supposed to result from the optical pumping effect [119][104] by a redistribution of the ground state population.
In figure 4.25 the influence of the optical pumping effect is explained for σ^+ transitions.

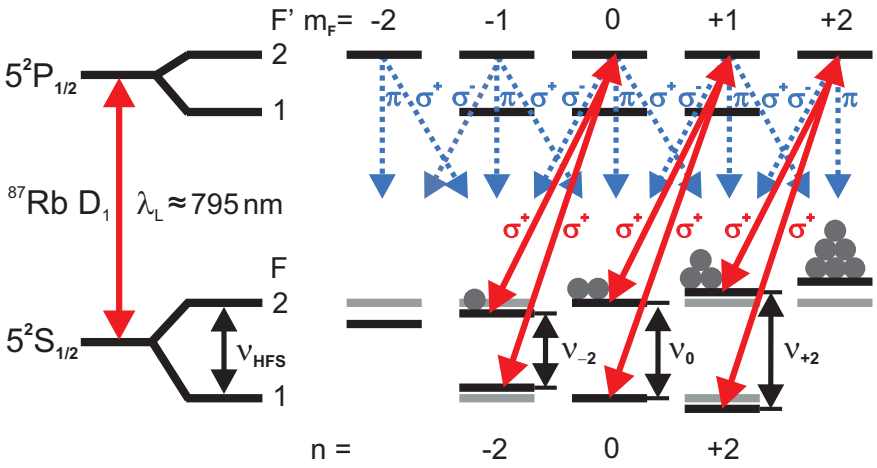

Figure 4.25.: Optical pumping within the hyperfine structure of the ^{87}Rb D_1 line for σ^+ transitions in an external magnetic field: The atomic population is pumped to the ground state with the highest magnetic quantum number m_F. This ground state ($F = 2$, $m_F = 2$) acts as a natural trapping state. The CPT resonance, which is prepared by the ground states with the increased ground state population, has an enhanced CPT resonance amplitude.

In the illustrated case, the circularly polarised light field induces σ^+ transitions from the ground states into the excited states by an increase of the magnetic quantum number m_F by one. When the population relaxes back into the ground state, transitions by emitting light with any polarisation state are possible. Therefore, transitions with $\Delta m_F = 0, \pm 1$ are allowed. Since the cycles of excitation and relaxation from the excited state, which pump the population to the outermost level, are much more frequent than the relaxation of population out of the outermost energy level, most of the population accumulates in the outermost level [92]. Thus, this level can act as natural trapping state and the ground state population distribution is altered compared to the distribution without laser light interaction.
The impact of the optical pumping effect on the ground state distribution depends on the polarisation of the light field as well as the angle between the propagation direction of the light field and the external magnetic field direction, the sensor angle ϕ [119]. For this reason, the CPT and the CDSM resonance preparations are affected differently by the optical pumping effect in dependence of sensor angle. The strongest influence of the optical pumping effect is expected in the case of circularly polarised light and the magnetic field direction parallel to the optical path (longitudinal case - see section 2.1.2.2). In this case, depending on the chirality of the light field, transitions are excited which either increase or decrease the magnetic quantum number by one. Therefore, a change of the population distribution towards the outer sublevels is favoured. As a consequence, the CPT resonances $n = -2$ and $n = +2$ should exhibit the greatest influence of the optical pumping effect at the sensor angles $\phi = 0°$ and $\phi = 180°$.
On the other hand, for the case of circularly polarised light and laser propagation direction vertical to the external magnetic field direction (transversal case), the optical pumping effect should be balanced. In this case transitions with $\Delta m_F = 0$ are allowed and thus no net angular momentum is transferred [119]. As a result, the ground state population is distributed symmetrically around the ground states with $m_F = 0$ where the population has a maximum [55]. Therefore, at the sensor angles $\phi = 90°$ and $\phi = 270°$ the CPT resonance spectrum should be balanced around $n = 0$ and the single CPT resonances, which build the CDSM resonance, should have the same line shapes.

A reduction of the influence of the optical pumping effect on the CPT resonance spectrum was targeted in order to improve the CDSM-based compensation effect. There are three known options to influence the optical pumping effect. First, the dependence of the optical pumping on the polarisation state can be used to balance the ground state population distribution by, e.g., using combinations of different polarisation states [120]. Second, the optical pumping effect can be influenced by the laser intensity and third, its impact can be reduced by increasing the buffer gas pressure [92][91].
The first option can be realised by using a combination of right and left circularly polarised laser light. The simplest way would be to use linearly polarised light, which can be thought of as a combination of right and left circularly polarised light. Nevertheless, the CPT

resonance $n = 0$ can not be prepared with linearly polarised light because no Λ-shaped excitation scheme can be formed between the ground states with a magnetic quantum number m_F=0 and the excited states with $m'_F = 0$ due to selection rules [28]. If the linear polarisation state is again thought of as a superposition of left and right circular polarisation state, then the CPT resonance $n = 0$ can be established with the excited states with either $m'_F = -1$ or $m'_F = +1$. However, in reference [121] it was shown that in the case of linearly polarised light, two dark states are simultaneously prepared with the excited states having $m'_F = -1$ and $m'_F = +1$ which cancel each other due to an opposite phase condition.
A combination of right and left circularly polarised laser light can be used to reduce the optical pumping effect but an additional phase delay of π is required between the two differently polarised light fields. The appropriate phase difference can be obtained by several methods. One approach is to reverse the transmitted laser beam and adapt the phase of the reversed beam [120]. A further method is to use two laser beams with one light field being left and the other right circularly polarised and introducing a stable phase difference between the light fields [122].
When two laser light fields with the respective wave vectors k_1 and k_2 are present in the vapour cell with length L, then interference effects allow even an increase of the CPT resonance amplitude for Rb cells much smaller than $L << \pi/(k_1 - k_2)$ [120]. For Rb, this length would be about $L \approx 22\,\text{mm}$.
The dual pass sensor (see section 3.3.3) also uses the combination of right and left circularly polarised laser light to reduce the influence of the optical pumping effect. In the dual pass sensor design, both passes are separated to prevent interactions between the CPT resonances prepared by the first and second pass which might affect or even destroy the CPT resonance formation. Each single path of the dual pass sensor still experiences the optical pumping effect but the overall effect should be balanced by the reversed dependence of both paths on the optical pumping effect. However, since the laser intensity is not completely equal for both passes due to absorption along the path, some residual effect remains.

The second option to reduce the influence of the optical pumping effect is to lower the laser intensity. As a consequence, the excitation rate into the excited state is decreased [91]. To investigate this behaviour, the amplitude ratio h_{-2}/h_{+2} between the CPT resonances $n = -2$ and $n = +2$ was determined for different laser intensities (see figure 4.26). If the influence of the optical pumping effect reduces with decreasing laser intensity, then the amplitude ratio should be more balanced at lower laser intensities. Additionally, in figure 4.26 the amplitude ratios are compared for a single and a dual pass of the laser beam through the sensor cell. The amplitude ratios in figure 4.26 were calculated from the CPT resonance amplitudes shown in figures 4.3 and 4.4. The sensor angle was set to $\phi = 0°$. As mentioned above, at this sensor angle the optical pumping effect should have the highest impact on the amplitudes of the CPT resonances $n = -2$ and $n = +2$.

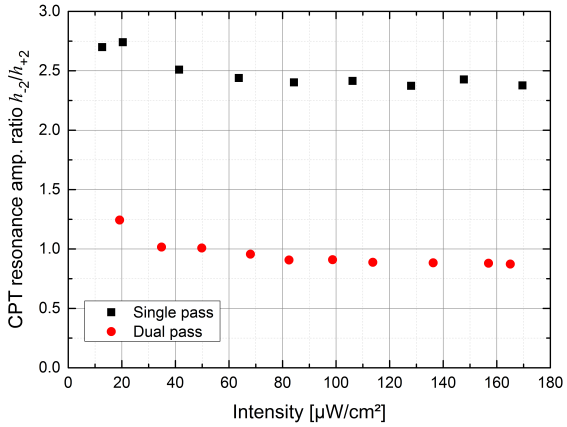

Figure 4.26.: CPT resonance amplitude ratios in dependence of the laser intensity for a single and a dual laser beam pass through the sensor cell: The amplitude ratios h_{-2}/h_{+2} for the single pass had approximately a constant value of 2.4 for $I > 80\,\mu\mathrm{W/cm^2}$. The amplitude ratios for the dual pass were close to the ideal ratio of one. For these measurements, the FS electronics and the dual pass sensor were used. The sensor cell contained neon as a buffer gas at the pressure of $\mathrm{P}_{BG} = 8.0\,\mathrm{kPa}$ (60 Torr). The sensor angle was $\phi = 0°$. A magnetic field of $B = 19.9\,\mu\mathrm{T}$ was applied.

As shown in figure 4.26, for $I > 80\,\mu\mathrm{W/cm^2}$, the amplitude ratio h_{-2}/h_{+2} was about 2.4 for the single pass. For lower laser intensities, the ratio increased but the CPT resonance amplitudes were already low and close to the noise floor. Thus, further measurements with a better signal-to-noise ratio are required in this low intensity range.
Nevertheless, reducing the laser intensity did not result in an equalisation of the amplitude ratios h_{-2}/h_{+2} for a single laser beam pass. On the one hand this may indicate that the optical pumping effect plays a minor part in the imbalance between the CPT resonance line shapes within this intensity range. On the other hand, the obtained results depicted in figure 4.26 may indicate that even the laser intensity at the measurement point with the lowest intensity in figure 4.26 is still high enough to change the ground state population distribution by the optical pumping effect. Thus, the laser intensity would have to be lowered much more to reduce its influence and to obtain an uniform population distribution. However, a further reduction of the laser intensity is not intended for the operation of the CDSM magnetometer because of the low signal-to-noise ratio.
For dual laser beam pass of the sensor cell, the amplitudes of the CPT resonances $n = -2$ and $n = +2$ were much more balanced compared to the single pass measurement. Their amplitude ratios were close to the ideal ratio of one at which the CPT resonance amplitudes are completely balanced. The amplitude ratios also increased for lower intensities but as mentioned above the signal-to-noise ratio was already low in this intensity range.

The third option to reduce the impact of the optical pumping effect is to increase the buffer gas pressure. As described in reference [91], two mechanisms lead to this reduction. On the one hand, the optical transitions are broadened due to the collisions with the buffer gas atoms. Thus, the pumping efficiency of the ground state population into the excited states is reduced. On the other hand, the line widths of the excited states are broadened such that they have a higher overlap. Therefore, the redistribution rate should be more balanced among the ground states.
In figure 4.27 measurements of the CPT resonance amplitudes of $n = -2$, $+2$, -3 and $+3$ and the their ratios h_{-2}/h_{+2} and h_{-3}/h_{+3} are summarised for different buffer gas pressures. The measurements were performed in the triaxial Helmholtz coil system at the Space Research Institute in Graz (see section A.4.1). A magnetic field of $B = 40.0\,\mu\text{T}$ was applied. The CSES EM electronics was used and the sensor unit was rebuilt on an optical bench. Thus, the sensor cells with different buffer gas pressures could be easily exchanged. For these measurements, the CSES EM cells listed in table A.2 were used. All of the cells contained neon as buffer gas.
The measurements were performed at an intensity of $I \approx 180\,\mu\text{W/cm}^2$. The transmitted laser intensity varied for the different vapour cells due to deposition of Rb atoms on the inside of the optical windows which influenced the amount of reflected light.

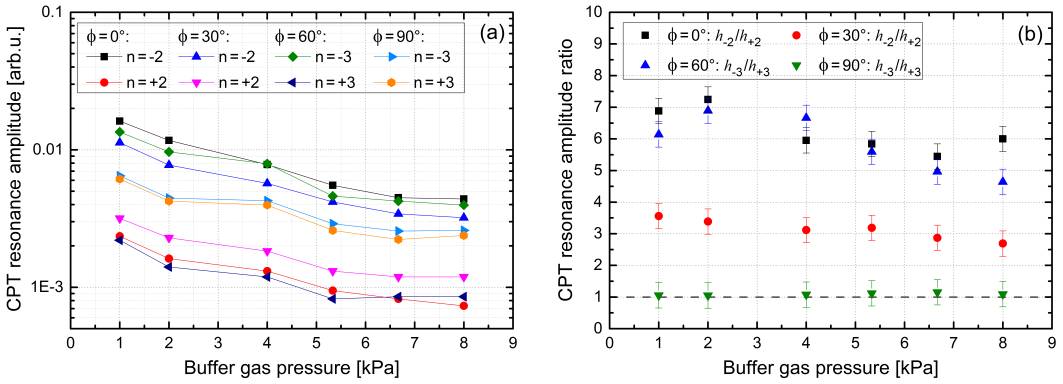

Figure 4.27.: Dependence of the CPT resonance amplitudes and their ratios on the buffer gas pressure: In (a) the CPT resonance amplitudes of $n = -2$, $+2$, -3 and $+3$ are depicted. The CPT resonance amplitudes reduced with increasing buffer gas pressure. In (b) the amplitude ratios of h_{-2}/h_{+2} and h_{-3}/h_{+3} are shown. At $\phi = 90°$ the ratio h_{-3}/h_{+3} is close to the ideal ratio of one which indicates equal CPT resonance amplitudes. At all other angles the ratios deviated from the ideal ratio. For different CPT resonance amplitudes the CDSM-based compensation is reduced. A magnetic field of $B = 40.0\,\mu\text{T}$ was applied and the laser intensity was about $180\,\mu\text{W/cm}^2$. The CSES EM electronics was used in combination with the CSES EM cells (see appendix A.2).

In figure 4.27(a) the CPT resonance amplitudes of $n = -2$ and $n = +2$ are shown for the sensor angles $\phi = 0°$ and $\phi = 30°$. Additionally, the CPT resonance amplitudes of

$n = -3$ and $n = +3$ are depicted for the sensor angles $\phi = 60°$ and $\phi = 90°$. The trend of the amplitudes with increasing buffer gas pressure was similar for all CPT resonances and sensor angles. The CPT resonance amplitudes reduced by about a factor of three when increasing the buffer gas pressure from $P_{BG} = 1.0\,\text{kPa}$ to $P_{BG} = 8.0\,\text{kPa}$. The decrease of the CPT resonance amplitude was caused by the mentioned reduction of the excitation strength due to the broadening of the optical transitions (see also section 4.1.3).
In figure 4.27(b) the amplitude ratios of the CPT resonances h_{-2}/h_{+2} and h_{-3}/h_{+3} are depicted. The ratio of h_{-3}/h_{+3} at $\phi = 90°$ was about one for all buffer gas pressures. This result was expected, since the transition strengths as well as the influence of the optical pumping effect should be balanced at this sensor angle. For $\phi = 0°$, the amplitude ratio h_{-2}/h_{+2} showed a value of about seven. At this sensor angle, the CPT resonances $n = -2$ and $n = +2$ should experience the highest impact of the optical pumping effect. As a result, the amplitude ratios were reduced at the sensor angle of $\phi = 30°$.
The amplitude ratios of the CPT resonances at $\phi = 0°$, $30°$ and $60°$ showed no distinct trend with increasing buffer gas pressure. There might be a slight equalisation at higher buffer gas pressures but the obvious amplitude difference between the single CPT resonance was not removed.
Additionally, the amplitude ratios h_{-2}/h_{+2} were measured within a magnetic shielding can at $\phi = 0°$ for three different buffer gas pressures: $P_{BG} = 1.0\,\text{kPa}$ (15 Torr), $P_{BG} = 5.3\,\text{kPa}$ (40 Torr) and $P_{BG} = 8.0\,\text{kPa}$ (60 Torr). For these measurements, the CSES EM cells were mounted in the CSES sensor unit. The intensity was about $160\,\mu\text{W/cm}^2$ which is very similar to the intensity used for the measurements in the coil system ($I \approx 180\,\mu\text{W/cm}^2$). The CPT resonance amplitude ratios are listed in table 4.9. The amplitude ratios for $P_{BG} = 5.3\,\text{kPa}$ (40 Torr) and $P_{BG} = 8.0\,\text{kPa}$ (60 Torr) were measured several times. Thus, the listed values for these two buffer gas pressures are the mean amplitude ratio plus the standard deviation.

Table 4.9.: Amplitude ratio h_{-2}/h_{+2} for three different buffer gas pressures P_{BG}: The measurements were performed with the CSES EM within a magnetic shielding can. The sensor angle was set to $\phi = 0°$.

P_{BG} [kPa]	P_{BG} [Torr]	h_{-2}/h_{+2}
1.0	15	3.6
5.3	40	3.0 ± 0.3
8.0	60	3.00 ± 0.09

The amplitude ratios in the magnetic shielding can were much more balanced compared to the measurement results obtained within the Helmholtz coil system. The large difference of the CPT amplitude ratios measured in the magnetic shielding can and in the coil system for $\phi = 0°$ remains unclear. The ration in figure 4.23 was also measured in the coil system but the results showed nearly the same ratio compared to the measurements in the

magnetic shielding can. However, the Helmholtz coil system had been relocated between the measurements in figures 4.23 and 4.27. Since almost the identical setup was used for both measurements, the difference is assumed to result from the new measurement environment by, e.g., disturbing AC and DC magnetic fields but further measurements will be required for confirmation.
Nevertheless, the CPT resonance amplitude ratio measured in the magnetic shielding can showed a clear imbalance between the single CPT resonance amplitudes and the ratio did not improve significantly for increasing buffer gas pressures. In reference [91] a clear reduction of the optical pumping effect as well as a balancing of the CPT resonance spectrum was visible either by using a buffer gas or by reducing the laser intensity. The difference between the obtained results in this section and those in reference [91] might be caused by the different atomic structure used for the CPT resonance preparation. In reference [91] the CPT resonances were established in the Cs D_2 line. The excited state of the Cs D_2 line consists of four sublevels with frequency separations between 151 MHz and 251 MHz [123]. For our experiments, the ^{87}Rb D_1 line was selected. Here the two excited states are separated by $\Delta\nu_{D_1} \approx 815\,\text{MHz}$ which is greater than the frequency distances of the excited states in the Cs D_2 line. Therefore, higher buffer gas pressures may be required for the ^{87}Rb D_1 line to reach the regime where the overlap of the excited states is sufficient enough to result in a balancing of the CPT resonance spectrum. The drawback of further increasing the buffer gas pressure is that the CPT resonance amplitudes are decreased as well (see figure 4.27(a)). This results in a further reduction of the signal-to-noise ratio. Therefore, the usage of much higher buffer gas pressures is not planned.

4.2.3. Compensation Effects for Single and Dual Laser Beam Pass

An equalisation of the CPT resonance line shapes is targeted by the dual pass sensor (see section 3.3.3). Both the influence of the optical pumping effect as well as the different transition strengths should be balanced over the sensor angle ϕ. Especially, the line shapes of the CPT resonances $n = \pm 2$ and $n = \pm 3$, which build the CDSM resonances $n = 2$ and $n = 3$ respectively, should be identical to obtain the best CDSM-based compensation (see section 4.2.1).
In figure 4.28 the CPT resonance amplitude ratios of h_{-2}/h_{+2} and h_{-3}/h_{+3} were determined in dependence of the sensor angle for a single and a dual laser beam pass through the sensor cell.

For these measurements, the CSES FS electronics and the dual pass sensor were used. The sensor cell contained neon as buffer gas at a pressure of $P_{BG} = 8.0\,\text{kPa}$ (60 Torr). For the single pass measurements, the laser beam was coupled into the inbound fibre after one pass of the sensor cell. The measurements were performed in a magnetic shielding can. The drawback of the magnetic shielding can is that the optical fibres have to be moved

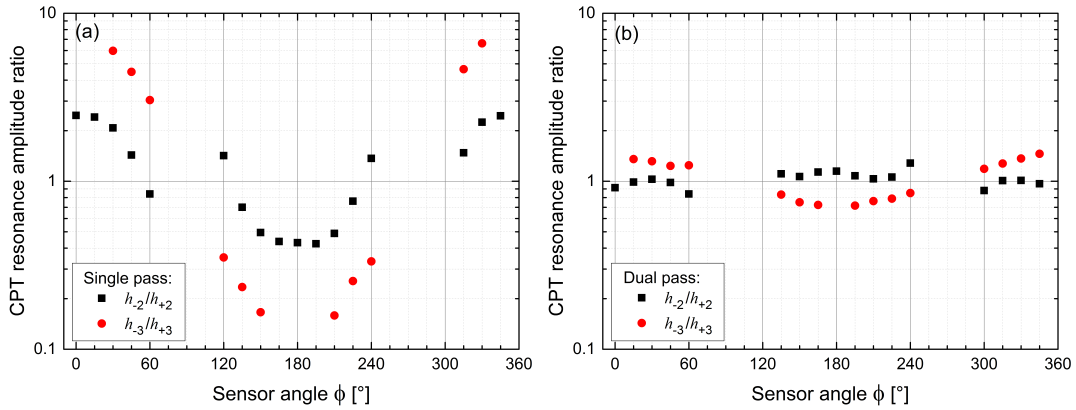

Figure 4.28.: Angular dependence of the CPT resonance amplitude ratios h_{-2}/h_{+2} and h_{-3}/h_{+3}: In (a) the ratios are depicted for a single pass and in (b) for a dual pass of the laser beam through the sensor cell. A magnetic field of $B = 19.9\,\mu T$ was applied. The CSES FS electronics and the dual pass sensor were used. The dual pass cell contained a buffer gas (Ne) at a pressure of $P_{BG} = 8.0\,kPa$ (60 Torr).

when the sensor is rotated in order to obtain different sensor angles. Additionally, they are also bent differently at the sensor angle positions. At the sensor angle of $\phi = 90°$ or $\phi = 270°$ the bending radius is too tight for the inbound fibre with a core diameter of $d = 400\,\mu m$. Therefore, no measurements were performed around $\phi = 90 \pm 15°$ and $\phi = 270 \pm 15°$.

In figure 4.28(a) the CPT resonance amplitude ratios are shown for a single laser beam pass through the sensor cell. Ideally, the CPT resonance amplitude ratios should be one, in order to obtain the best CDSM-based compensation (see section 4.2.1).

The ratios for the single pass in figure 4.28(a) showed a similar behaviour as the measurement results depicted in figure 4.23 which were obtained with a lower buffer gas pressure ($P_{BG} = 4.0\,kPa$ (30 Torr)). In contrast to the previous measurements, the amplitude ratios h_{-2}/h_{+2} and h_{-3}/h_{+3} became more balanced with increasing the buffer gas pressure from 4.0 kPa to 8.0 kPa. At $\phi = 0°$, the ratio of h_{-2}/h_{+2} was about 3.5 for $P_{BG} = 4.0\,kPa$ which is higher compared to a ratio of 2.5 for $P_{BG} = 8.0\,kPa$. Further, at $\phi = 60°$ the ratio of h_{-3}/h_{+3} decreased from about 4.4 to about 3.0 with increasing the buffer gas pressure. Since different electronic models (CSES EM and CSES FS) were used for these tests, the settings of the laser operational parameters or the modulation indices could have influenced the intensities in the laser sideband structure and thus affect the measured amplitude ratio. Thus, the reduced amplitude ratio is supposed to result from the changed intensity distribution and not from the higher buffer gas pressure.

In figure 4.28(b) the ratios of h_{-2}/h_{+2} and h_{-3}/h_{+3} are depicted for a dual pass. The amplitude ratios for the dual pass were much more balanced within the whole sensor angle range compared to the amplitude ratios obtained by the single pass. At $\phi = 0°$ the ratio

h_{-2}/h_{+2} improved from 2.5 for the single pass to 0.92 for the dual pass. At $\phi = 60°$ the ratio h_{-3}/h_{+3} changed from 3.0 for the single pass to 1.2 for the dual pass.
A residual deviation from the ideal ratio of one remained for the dual pass which is intended to be further reduced by an optimisation of the operational parameters which affect the laser intensity distribution,e.g., laser operational parameters in combination with the microwave power level and modulation indices.

Due to the fact that the CPT resonance line shapes are much more balanced for a dual laser beam pass through the sensor cell, the CDSM resonances obtained with the dual pass sensor should be able to compensate much higher disturbing frequency shifts without an influence on the measured magnetic field strength compared to the single pass sensor design (CSES sensor). As shown in figure 4.24, disturbing frequency shifts introduce a detuning Δ between the single CPT resonances.
In figure 4.29 the influence of a detuning Δ on the determined magnetic field strength is depicted for a single and a dual laser beam pass through the sensor cell. The CSES FS electronics and the dual pass sensor were used. The sensor cell contained neon as buffer gas at a pressure of $P_{BG} = 4.0\,\text{kPa}$ (30 Torr).
These measurements were performed with respect to the JUICE mission. During the JUICE mission, magnetic field strengths in the range of $B = 350 - 1\,500\,\text{nT}$ are of special interest (see section 4.3). Additionally, a measurement accuracy of 0.2 nT (1 sigma) has to be achieved. To measure such low magnetic field strengths with this accuracy, the CDSM resonance line widths should be about 200 Hz or even less (see discussion in section 4.3.2). The detuning, which can be compensated by the formed CDSM resonance, depends on the CPT resonance line widths (see equation 2.47). Therefore, the CDSM resonances line width was set to $\Delta\nu_{CDSM} \approx 200\,\text{Hz}$ in order to get representative results with respect to the JUICE mission. The CDSM resonance line width was narrowed by reducing the laser intensity in front of the sensor cell. Therefore, an additional polarising beam splitter cube was mounted after the first fibre coupler in the sensor unit (see section 3.3.3). The laser intensity reduction was obtained by rotating the additional polariser relative to the fixed polarisation optics mounted in the sensor.
A sensor angle of $\phi = 60°$ and the CDSM resonance $n = 3$ were chosen for these measurements. The CDSM resonance $n = 3$ is typically selected for the magnetic field measurement in the sensor angle ranges from $\phi = 60°$ to $\phi = 120°$ and $\phi = 240°$ to $\phi = 300°$. The CDSM resonances are switched at the sensor angles 60°, 120°, 240° and 300° to obtain an omnidirectional magnetic field measurement (see section 4.1.7). At these angles the line shapes of the single CPT resonances $n = \pm 3$, which form $n = 3$, have the highest line shape imbalance of the operational angular range (see figure 4.23). As a consequence, a detuning has the highest impact on the determined magnetic field strength in this measurement configuration.
First, the microwave generator frequency was stabilised to the zero crossing frequency of $n = 0$ in order to obtain $\Delta = 0\,\text{Hz}$ and then the external magnetic field was measured.

Afterwards, a defined detuning was introduced ($\Delta \neq 0\,\mathrm{Hz}$) by shifting the microwave frequency by a certain value. Subsequently, the respective measured magnetic field was recorded. The shift of the measured magnetic field with various detunings is compared in figure 4.29 for a single and a dual laser beam pass through the sensor cell.

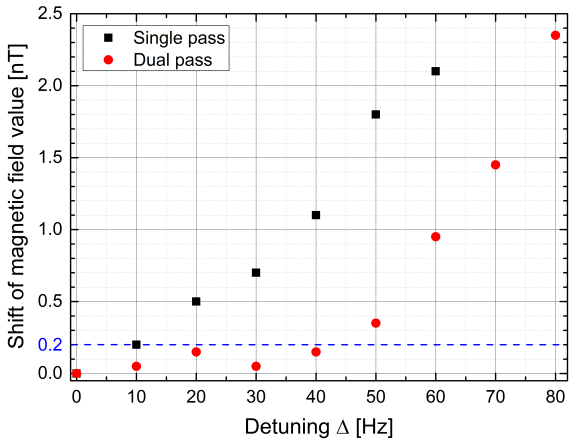

Figure 4.29.: Influence of a detuning Δ on the measured magnetic field strength for a single and a dual laser beam pass through the sensor cell: A sensor angle of ϕ=60° and the CDSM resonance $n = 3$ were selected for the magnetic field measurement because the single CPT resonances $n = \pm 3$ have the highest imbalance for these settings within the CDSM's operational range. At this angle, the highest influence of a detuning on the measured magnetic field strength is expected. The accuracy limit for JUICE (0.2 nT) is marked by the dashed line. The measurement was performed with the CSES FS electronics and the dual pass sensor. A magnetic field of $B = 5.00\,\mu\mathrm{T}$ was applied. The sensor cell contained a buffer gas with a pressure of $P_{BG} = 4.0\,\mathrm{kPa}$ (30 Torr). The laser intensity was about $6\,\mu\mathrm{W/cm^2}$. The sensor temperature was $T = 26°\mathrm{C}$.

As can be seen in figure 4.29, for single laser beam pass through the sensor cell, only a detuning of $\Delta \approx 10\,\mathrm{Hz}$ could be accepted in order to achieve the accuracy limit of 0.2 nT. The dual pass configuration tolerated more than $\Delta \approx 40\,\mathrm{Hz}$ before the measured magnetic field strength exceeds the accuracy limit. Thus, the dual pass design enabled the compensation of a four times higher detuning compared to the single pass design by keeping the required accuracy.
For identical CPT resonance line shapes with a line width of $\Delta\nu_{CPT} = 200\,\mathrm{Hz}$, a theoretical compensation limit of $\Delta_{max} = 58\,\mathrm{Hz}$ can be achieved (see equation 2.47). The deviation of the obtained compensation from the theoretical compensation limit results from the remaining imbalance between the single CPT resonance line shapes. A further equalisation of the CPT resonance line shapes is targeted by optimising the operational parameters of the magnetometer (see section 4.1) by using a higher buffer gas pressure (see discussion above).

4.3. Accuracy at Low Magnetic Field Strengths

During the JUICE mission, magnetic fields are investigated within the Jupiter system which can become lower than $B < 150\,\mathrm{nT}$. Particular attention will be on the magnetic field of the Jupiter moon Ganymede which is supposed to have a subsurface ocean [13]. In order to get information on the inner structure of Ganymede, the JUICE spacecraft will orbit Ganymede at a distance of 500 km where magnetic fields in the range from 350 to 1500 nT are expected. As a consequence, magnetic fields lower than $B < 2\,000\,\mathrm{nT}$ are of special interest. In this context, the magnetic field range from 0 to 2000 nT is defined as the low magnetic field range. This magnetic field range has the benefit that the non-linear dependence of the CPT resonance positions on the external magnetic field can be neglected (see section 4.1.6) for the operation of the CDSM.
However, in this magnetic field range, the influence of the CPT and CDSM resonances on each other can affect the magnetic field measurement. This is due to the fact that for decreasing magnetic field strengths the resonances converge (see figure 4.30) and at a certain magnetic field strength they start to shift each others zero crossing frequency depending on their resonance structures. If the magnetic field is further reduced, the resonances finally overlap and become undistinguishable.

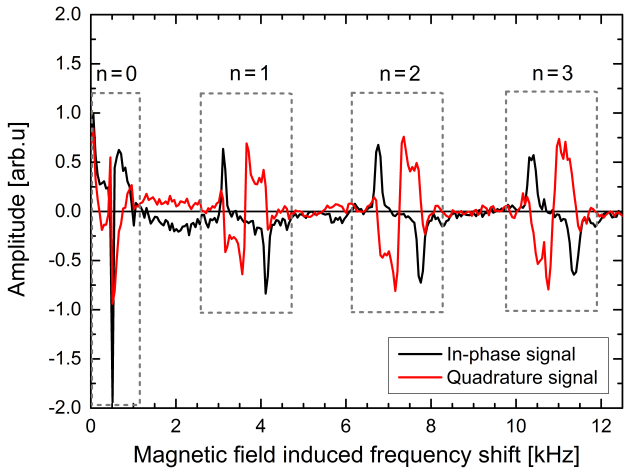

Figure 4.30.: CPT and CDSM resonances for $B = 0.50\,\mu\mathrm{T}$ at a sensor angle of $\phi = 45°$: All three CDSM resonances as well as parts of the CPT resonance $n = 0$ are visible but still separated. The measurement was performed with the CSES LM. The optical power at the photodiode was $P = 2.5\,\mu\mathrm{W}$ which corresponds to $I \approx 8\,\mu\mathrm{W/cm^2}$ in front of the sensor cell. A modulation frequency of $\nu_{B_{FMS}} = 500\,\mathrm{Hz}$ was applied.

In this context, the low magnetic field measurement limit is defined as the magnetic field strength at which the influence of the converging resonances on the CDSM resonance, which is selected for the magnetic field measurement, is so high that its zero crossing

frequency is shifted above the defined accuracy limit. For the JUICE mission, the requirement on the accuracy is 0.2 nT (1 sigma).

As shown in section 4.1, the CPT and CDSM resonance structures are influenced by several operational parameters of the magnetometer. Especially, the setting of the modulation frequency $\nu_{B_{FMS}}$ for the detection of the CDSM resonance (see section 2.2.2), the laser intensity and the buffer gas pressure affect the lower measurement limit. The influence of these parameters and their proper selection for the low magnetic field range are discussed in section 4.3.1.
Moreover, the low magnetic field measurement limit varies for the different CDSM resonances and sensor angles because not all resonances are present at all sensor angles (see section 4.1.7). For example, at $\phi = 0°$ or $\phi = 180°$, only the CDSM resonance $n = 2$ and half of the CPT resonance $n = 0$ are detectable in the measurement range. Then, the lower measurement limit is reached when the CDSM resonance $n = 2$ gets shifted by the CPT resonance $n = 0$ above the accuracy limit. At $\phi = 90°$ or $\phi = 270°$, just the CDSM resonances $n = 1$ and $n = 3$ are visible in the measurement range. Thus, the lower measurement limit is determined by the frequency distance between the resonances $n = 1$ and $n = 3$. In the intermediate case all resonances are present. Therefore, the low magnetic field limit is typically higher than for the two extreme cases discussed above. Measurements on the low magnetic field measurement limit for several sensor angles are summarised in section 4.3.2.

4.3.1. Settings of Operational Parameters for the Low Magnetic Field Range

The operational parameters of the magnetometer influence the CPT and CDSM resonance structures (see figure 4.1(a)) and their line widths. The choice of the modulation frequency $\nu_{B_{FMS}}$ (see section 2.2.2) is crucial for the low magnetic field range. Typically, a modulation frequency $\nu_{B_{FMS}}$ of several kHz is selected (see sections 2.2.2 and 2.4.2). In the low magnetic field range, the distinct sideband structure can be disturbing and increase the lower measurement limit due to the large overall extent of the CDSM resonance structure. The CDSM resonance structure consists of the carrier structure and sidebands at the frequency distance of the modulation frequency $\nu_{B_{FMS}}$ which also influence the zero crossing frequencies of the other resonances. Thus, the zero crossing frequencies of the carrier structure, which is used for the magnetic field measurement, already experience a shift due to the sidebands.
In order to reduce the influence of the converging resonances on each other, two different options can be selected to set the modulation frequency $\nu_{B_{FMS}}$. The first option is to decrease the overall CDSM resonance structures by choosing a modulation frequency less or equal to the CDSM resonance line width. Thus, the frequency spacing between the CDSM resonances is increased. The second option is to increase the modulation frequency $\nu_{B_{FMS}}$

such that the sidebands are located outside of the measurement range. In this case, just the carrier structures of the CDSM resonances remain in the measurement range. Then, the lower measurement limit depends on the line widths of the carrier structures.
In figure 4.31 the CDSM resonance $n = 2$ is shown for four different modulation frequencies $\nu_{B_{FMS}}$.

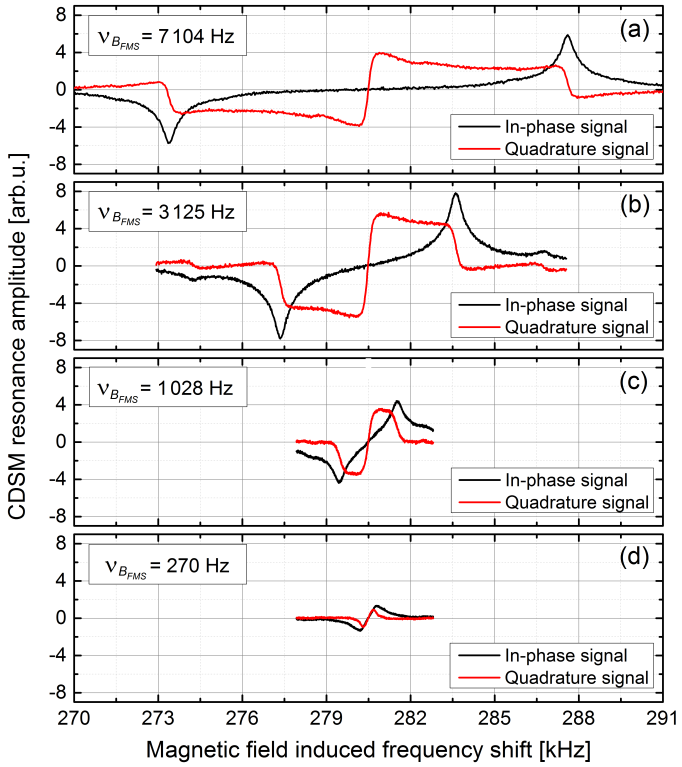

Figure 4.31.: CDSM resonance $n = 2$ for different modulation frequencies $\nu_{B_{FMS}}$: (a) $\nu_{B_{FMS}} = 7\,102\,\text{Hz}$, (b) $\nu_{B_{FMS}} = 3\,125\,\text{Hz}$, (c) $\nu_{B_{FMS}} = 1\,028\,\text{Hz}$ and (d) $\nu_{B_{FMS}} = 270\,\text{Hz}$. Decreasing the modulation frequency results in a reduction of the overall CDSM resonance structure. The measurements were performed with the CSES FS electronics and the dual pass sensor. The long dual pass cell was mounted which contained Ne as buffer gas at a pressure of $P_{BG} = 8.0\,\text{Pa}$ (60 Torr) (see appendix A.2). A magnetic field of $B = 19.9\,\mu\text{T}$ was applied. The sensor angle was set to $\phi = 0°$. The intensity was about $180\,\mu\text{W/cm}^2$.

In figure 4.31(a) a modulation frequency of $\nu_{B_{FMS}} = 7\,102\,\text{Hz}$ was applied for detection, which is the default setting for the CSES mission (see section 2.2.2). In this case, the carrier structure and the sidebands are well separated. For lower modulation frequencies, the distance between the sidebands and the carrier structure reduces and the overall expansion of the resonance decreases (see figure 4.31 (b), (c) and (d)). Additionally, the resonance amplitude starts to decline for modulation frequencies lower than the CDSM resonance line width, since the contribution of the sidebands and the carrier are getting

more and more equal and thus the similar contributions cancel the detected signal (see equation 2.24).
The line width of the CDSM resonance $\Delta\nu_{CDSM}$ detected by using the modulation frequency $\nu_{B_{FMS}} = 7\,102\,\text{Hz}$ was about 800 Hz. For high modulation frequencies ($\nu_{B_{FMS}} >> \Delta\nu_{CDSM}$), the line width is defined as the line width of the carrier structure (see figure 4.1). In contrast, for modulation frequencies close to the line width or undergoing it, the carrier structure and the sideband structures overlap. Thus, the definition of line width refers to the line width of the dispersion shaped overall resonance structure. For the modulation frequency of $\nu_{B_{FMS}} = 270\,\text{Hz}$ (see figure 4.31(d)), the line width of the overall resonance structure $\Delta\nu_{CDSM,all}$ was about 350 Hz. Thus, the line width of the overall resonance structure can be narrower than the original line width of the CDSM resonance. Nevertheless, the resonance amplitude reduced by about a factor of four comparing the resonances detected by applying $\nu_{B_{FMS}} = 7\,102\,\text{Hz}$ and $\nu_{B_{FMS}} = 270\,\text{Hz}$ (see figure 4.31(a) and (d)).

In figure 4.32, the CDSM resonances $n = 1$ and $n = 3$ are compared for (a) a low modulation frequency of $\nu_{B_{FMS}} = 100\,\text{Hz}$ and (b) for a high modulation frequency $\nu_{B_{FMS}} = 15\,600\,\text{Hz}$.

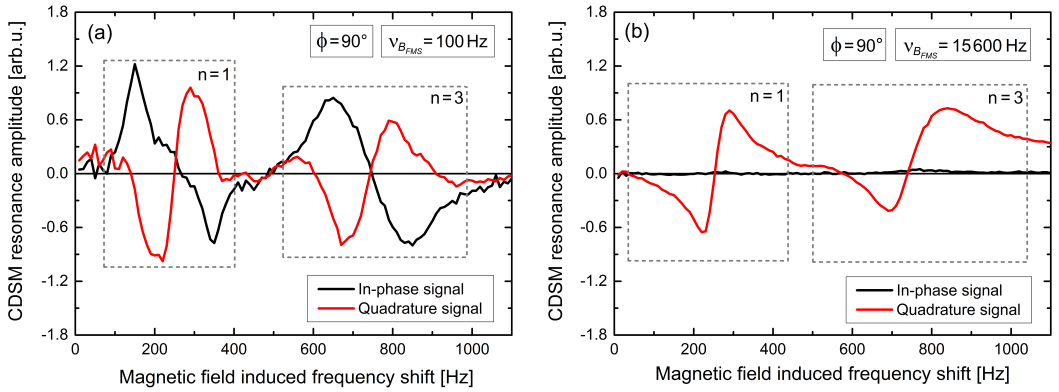

Figure 4.32.: Comparison of the CDSM resonances $n = 1$ and $n = 3$ at a sensor angle of $\phi = 90°$ for two different modulation frequencies $\nu_{B_{FMS}}$: Modulation frequencies of (a) $\nu_{B_{FMS}} = 100\,\text{Hz}$ and (b) $\nu_{B_{FMS}} = 15\,600\,\text{Hz}$ were applied. The measurements were carried out with the CSES LM. The sensor cell contained a buffer gas (Ne) at a pressure of $P_{BG} = 4.0\,\text{kPa}$ (30 Torr). The intensity was $I \approx 10\,\mu\text{W/cm}^2$ in front of the sensor cell. The magnetic field in the magnetic shielding can was about 35 nT.

The benefit of the low modulation frequency is that there are no disturbing sidebands in the measurement range but the modulation frequency has to be adapted carefully in order to keep the highest possible CDSM resonance amplitude. When the modulation frequency $\nu_{B_{FMS}}$ gets much lower than the line width of the CDSM resonance, the signal amplitude decreases. Thus, the obtained signal-to-noise ratio is reduced compared to the case of

$\nu_{B_{FMS}} >> \Delta\nu_{CDSM}$.
In contrast, the benefit of choosing a high modulation frequency relative to the CDSM resonance line width is that the CDSM resonance amplitude and width are not affected by the selected modulation frequency (see figure 4.32(b)). Again, the modulation frequency has to be carefully adapted to the measurement range to avoid a disturbing influence of the sidebands. Furthermore, in case that the external magnetic field induced frequency shift $2 \cdot |\nu_{B_n}|$ is lower than the modulation frequency $\nu_{B_{FMS}}$, the lower sideband appears in the measurement range at the frequency $\nu_{B_{FMS}} - 2 \cdot |\nu_{B_n}|$ and can again disturb the magnetic field measurement.

Besides these considerations of a proper modulation frequency $\nu_{B_{FMS}}$, the modulation of the microwave frequency stabilisation control loop with the frequency $\nu_{MW_{FMS}}$ can affect the magnetic field measurement in the low magnetic field range. Since the modulations of the two control loops (microwave frequency stabilisation and magnetic field detection control loop) interact, disturbances are created at several mixed frequency combinations of $\nu_{B_{FMS}}$ and $\nu_{MW_{FMS}}$ (see figure 4.33). The frequency range depicted on the x-axis of figure 4.33 corresponds to a magnetic field range of 0 to 1284 nT, if the CDSM resonance $n = 2$ ($\delta_{CDSM_n} \approx 14\,\mathrm{Hz/nT}$) or 0 to 857 nT, if the CDSM resonance $n = 3$ ($\delta_{CDSM_n} \approx 21\,\mathrm{Hz/nT}$) is used for the magnetic field measurement.
In figure 4.33(a) both modulation frequencies were applied. The default values of the CSES mission were set: $\nu_{B_{FMS}} = 7\,102\,\mathrm{Hz}$ and $\nu_{MW_{FMS}} = 1\,905\,\mathrm{Hz}$. Several disturbances appeared at different combinations of the modulation frequencies within the measurement range.
In figure 4.33(b) the microwave frequency stabilisation control loop was stopped and the modulation frequency $\nu_{MW_{FMS}}$ turned off. In this case, the highest signal in the measurement range resulted from the sideband of the CPT resonance $n = 0$ at the frequency of $\nu_{B_{FMS}} = 7\,102\,\mathrm{Hz}$. In order to remove this sideband from the intended measurement range, either a lower modulation frequency $\nu_{B_{FMS}}$ can be set to shift the sideband to lower frequencies or a higher modulation frequency can be selected to shift the sideband outside of the measurement range.
In figure 4.33(c) the modulation frequency was reduced to $\nu_{B_{FMS}} = 270\,\mathrm{Hz}$, the microwave frequency stabilisation control loop was stopped and the modulation frequency $\nu_{MW_{FMS}}$ turned off. Thus, the sideband of $n = 0$ was shifted to a lower frequency. As a result, the frequency range above 2 kHz was almost undisturbed. A magnetic field induced frequency of 2 kHz corresponds to a magnetic field strength of $B = 143\,\mathrm{nT}$ for $n = 2$ and $B = 95\,\mathrm{nT}$ for $n = 3$. Therefore, the selection of a lower modulation frequency is favourable to reduce disturbances in the low magnetic field measurement range and thus enable accurate magnetic field measurements in this magnetic field range.
Further tests with different values of $\nu_{MW_{FMS}}$ are planed in order to find a proper setting which allows the operation of both control loops without disturbances on the magnetic field measurement.

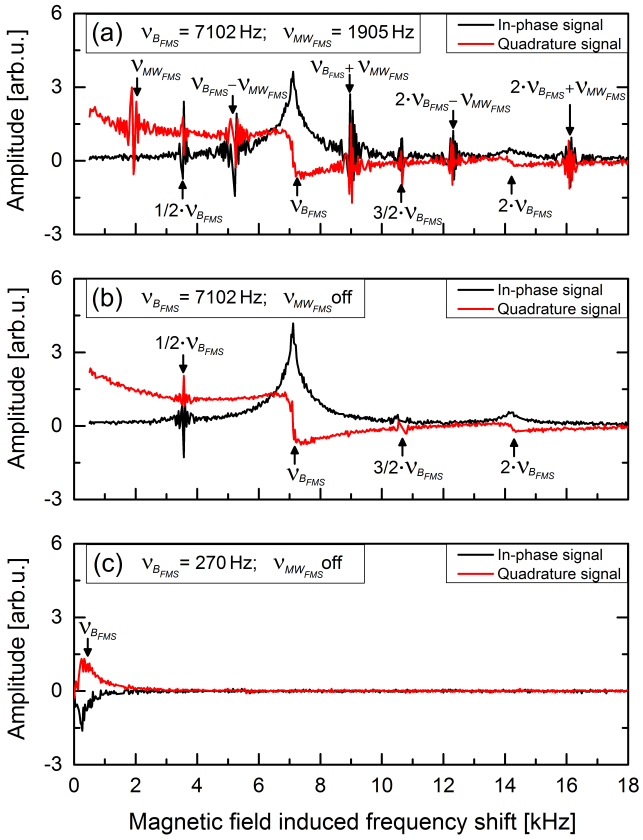

Figure 4.33.: Disturbing frequency components caused by the interaction of the modulation frequencies $\nu_{MW_{FMS}}$ and $\nu_{B_{FMS}}$ from the microwave frequency stabilisation and the magnetic field detection control loops: In (a) both modulation frequencies were applied. The default values for the CSES mission were set: $\nu_{B_{FMS}} = 7\,102\,\text{Hz}$ and $\nu_{MW_{\text{FMS}}} = 1\,905\,\text{Hz}$. In the depicted frequency range, several disturbances are detectable at different combinations of the modulation frequencies. In (b) the modulation frequency $\nu_{MW_{FMS}}$ was turned off. In (c) the modulation frequency $\nu_{B_{FMS}}$ was reduced to 270 Hz. The modulation frequency $\nu_{MW_{FMS}}$ was turned off again. Thus, the frequency range above 2 kHz was almost unaffected by disturbances.

In addition to the proper setting of the modulation frequencies $\nu_{MW_{FMS}}$ and $\nu_{B_{FMS}}$, a narrow CDSM resonance is advantageous in the low magnetic field range. The typical CDSM resonance line widths are several hundreds of Hz. However, in the low magnetic field range line widths of less than 200 Hz are preferable to keep the accuracy and a sufficient signal-to-noise ratio in this field range (see discussion in section 4.3.2 below).
In order to obtain such narrow line widths, the maximum laser intensity at the sensor cell (typically $< 200\,\mu\text{W/cm}^2$) has to be decreased, since the line width significantly reduces with the laser intensity (see section 4.1.1). A laser intensity reduction is obtained, e.g., by decreasing the total laser power or by increasing the cross section of the laser beam in

the sensor cell. However, lowering the intensity below the optimum laser intensity reduces the signal-to-noise ratio. Here a compromise between the signal-to-noise ratio and the obtained low magnetic field measurement limit has to be made.
Additionally, the line width can be optimised by the buffer gas pressure in the sensor cell. Higher buffer gas pressures are preferable in the low magnetic field range because the CPT resonances have narrower line widths due to the reduction of time-of-flight broadening (see section 4.1.3). However, increasing the buffer gas pressure has the disadvantage of reducing the CPT resonance amplitudes (see figure 4.27) which lowers the signal-to-noise ratio.

4.3.2. Measurements on the Lower Magnetic Field Measurement Limit

As already discussed in the previous sections, the lower magnetic field measurement limit critically depends on the CDSM resonance structure and on the sensor angle ϕ. Therefore, measurements at several sensor angles were performed for the CDSM resonances $n = 2$ and $n = 3$. For these measurements, the sensor unit was mounted in a magnetic shielding can containing a solenoid coil (see appendix A.4.1). A defined magnetic field value S_B was set via a constant current source. The set magnetic field strength S_B is determined by the coil factor: $\Delta B/\Delta I = 1244\,\mathrm{nT/mA}$.
The magnetic field strength S_B and the measured magnetic field strength M'_B typically differ due to several systematic effects. In order to characterise the shift of the magnetic field strength due to the converging resonances, measurements and evaluations were performed as follows.
The magnetic field S_B was varied starting at $B = 2.00\,\mu\mathrm{T}$, where no influence of the resonances on each other was measurable, to lower magnetic field strengths. At each value of S_B, the magnetic field direction was inverted by reversing the direction of the current through the solenoid coil. For both field directions, the magnetic field strength was measured with the CDSM in order to subtract an remanent offset magnetic field O_B inside of the shielding can from the measured magnetic field strength M'_B. The offset corrected field is $M_B = M'_B - O_B$.
The ratio $R_B = M_B/S_B$ of the measured magnetic field strength M_B, which was corrected by the remanent offset field, to the set magnetic field strength is assumed to remain constant for $B \leq 2\,\mu\mathrm{T}$, if there is no influence from the converging resonances, but changes when the resonances influenced each other.
For the further evaluation, the ratio $R_{2\mu\mathrm{T}} = M_{2\mu\mathrm{T}}/S_{2\mu\mathrm{T}}$ at $B = 2\,\mu\mathrm{T}$ was determined. At this magnetic field strength no influence of the converging CDSM resonances on the measured magnetic field was detected. In order to determine the resulting shift ΔB_{lf}, which is introduced by the converging resonances, the set magnetic field $S_{\leq 2\mu\mathrm{T}}$ at $B \leq 2\,\mu\mathrm{T}$ is corrected by $R_{2\mu\mathrm{T}}$. This yields the magnetic field strength which is expected to be measures in the magnetic shielding can without influence of the converging resonances. Then,

the difference from the measured magnetic field $M_{\leq 2\mu T}$ was calculated according to

$$\Delta B_{lf} = M_{\leq 2\mu T} - R_{2\mu T} \cdot S_{\leq 2\mu T} \,. \tag{4.22}$$

The low magnetic field measurement limit $B_{lf,lim}$ was reached, when the shift ΔB_{lf} exceeded the defined accuracy limit (0.2 nT for JUICE). In the following discussion the zero crossing frequency shift of the CDSM resonance by the approaching resonances is referred to as low field induced shift.

In figure 4.34 the low field induced shifts of the CDSM resonances $n = 2$ and $n = 3$ are summarised for different sensor angles ϕ. These measurements were performed with the CSES EM with inactive microwave frequency stabilisation control loop. Since this control loop was not operated, less disturbing frequency components were present in the measurement range (see figure 4.33). For this test, the targeted optical power was $P_{PD} = 15\,\mu W$ at the photodiode, which corresponds to a laser intensity of $I \approx 60\,\mu W/cm^2$ in front of the sensor cell. The sensor cell contained neon as buffer gas at a pressure of $P_{BG} = 2.0\,kPa$ (15 Torr). The modulation frequency $\nu_{B_{FMS}}$ was set to the same value as the CDSM resonance line width $\nu_{B_{FMS}} = \Delta\nu_{CDSM} = 350\,Hz$.

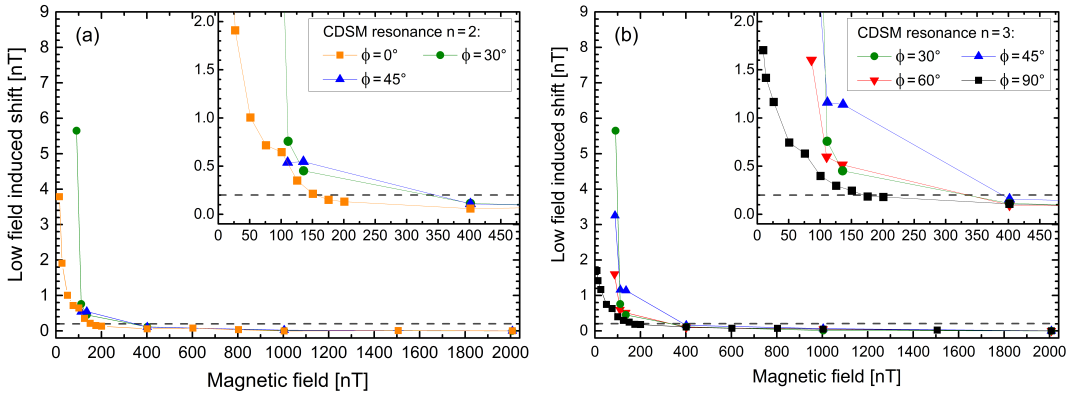

Figure 4.34.: Low field induced shifts for $n = 2$ and $n = 3$ with the CSES EM using a buffer gas pressure of $P_{BG} = 2.0\,kPa$ (15 Torr): In (a) the results at $\phi = 0°$, 30° and 45° are shown for $n = 2$. In (b) the results are depicted for $n = 3$ at $\phi = 30°$, 45°, 60° and 90°. At the sensor angles 0° and 90° the lowest measurement limit of $B_{lf,lim} \approx 150\,nT$ was obtained by keeping the influence of the converging resonances below 0.2 nT. The laser intensity was $I \approx 60\,\mu W/cm^2$.

As shown in figure 4.34(a), at ϕ=0° the zero crossing frequency of the CDSM resonance $n = 2$ showed, starting from higher magnetic fields, just a small shift until a set magnetic field strength of 200 nT. However, a significant shift was visible for lower magnetic field strengths. The low magnetic field measurement limit was reached at an applied magnetic field of $B_{lf,lim} \approx 150\,nT$ at $\phi = 0°$. At the other sensor angles $\phi = 30°$ and $\phi = 45°$, a higher low magnetic field measurement limit was obtained. This angular behaviour was

expected, since only the CPT resonance $n = 0$ was present in the measurement range at $\phi = 0°$ and all other resonances were not detectable. At $\phi = 30°$ the CDSM resonances $n = 1$ and $n = 3$ are already clearly visible in the CDSM resonance spectrum (see, e.g., figure 4.22) and therefore affect the zero crossing frequency of the CDSM resonance $n = 2$ depending on their resonance line widths and the set magnetic field strength.
In 4.34(b) the low field induced shift is depicted for the CDSM resonance $n = 3$. At $\phi = 90°$ the lower measurement limit was $B_{lf,lim} \approx 150\,\text{nT}$ for $n = 3$. At this sensor angle only the CDSM resonance $n = 1$ and $n = 3$ are present in the measurement range. At the other sensor angles ($\phi = 30°$, 45° and 60°) the lower measurement limit was reached at higher magnetic field strengths due to the appearance of the additional resonances $n = 0$ and $n = 2$.

Similar measurements as in figure 4.34 were performed with the CSES EM and a sensor cell containing a higher buffer gas pressure of $P_{BG} = 5.3\,\text{kPa}$ (40 Torr). The higher buffer gas pressure narrowed the CDSM resonance line widths of $n = 2$ from $\Delta\nu_{CDSM} \approx 350\,\text{Hz}$ for $P_{BG} = 2.0\,\text{kPa}$ to 155 Hz. Thus, a smaller modulation frequency of $\nu_{B_{FMS}} = \Delta\nu_{CDSM} = 155\,\text{Hz}$ was used.

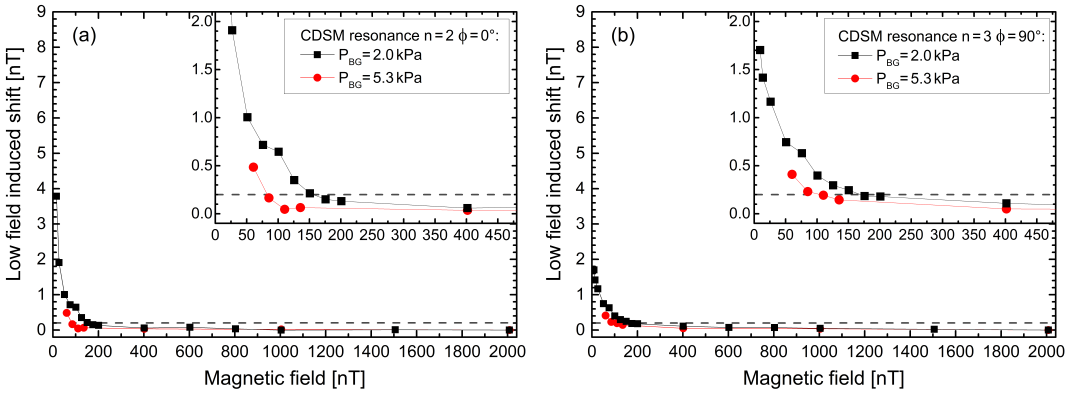

Figure 4.35.: Comparison of the low field induced shift measured with the CSES EM for two different buffer gas pressures: $P_{BG} = 2.0\,\text{kPa}$ (15 Torr) and $P_{BG} = 5.3\,\text{kPa}$ (40 Torr). In (a) the low field induced shifts are depicted for $n = 2$ at $\phi = 0°$. In (b) the low field induced shifts of $n = 3$ are shown at $\phi = 90°$. The lower measurement limit was reduced using a higher buffer gas pressure. The laser intensity was $I \approx 60\,\mu\text{W/cm}^2$.

As depicted in figure 4.35(a), the increase of the buffer gas pressure resulted in a reduced lower magnetic field limit of $B_{lf,lim} \approx 85\,\text{nT}$ for $n = 2$ at $\phi = 0°$. Further, as can be seen in figure 4.35(b), at $\phi = 90°$ the limit was lowered from $B_{lf,lim} \approx 150\,\text{nT}$ for $P_{BG} = 2.0\,\text{kPa}$ (15 Torr) to $B_{lf,lim} \approx 100\,\text{nT}$ for $n = 3$ for $P_{BG} = 5.3\,\text{kPa}$ (40 Torr). The reduced low field measurement limit was simply a result of the narrower resonance line width due to the increase of the buffer gas pressure.

In figure 4.36 further measurements on the lower measurement limit are summarised for the CSES FS electronics and the dual pass sensor. These measurements were performed with the goal to enable the highest possible optical power in the inbound fibre. A high optical power in the inbound fibre is desirable for the JUICE mission in order to reduce radiation induced attenuation in the optical fibre (see section 3.4.2).
The typical line widths at the highest possible optical intensities were $\Delta\nu_{CDSM} \approx 800 - 1\,000\,\text{Hz}$. These line widths were too high to keep the accuracy limit of 0.2 nT within the whole low magnetic field measurement range for JUICE ($B \approx 150 - 2\,000\,\text{nT}$). Therefore, the option was tested to reduce the CDSM resonance line width by applying modulation frequencies $\nu_{B_{FMS}}$ much lower than the CDSM resonance line width $\Delta\nu_{CDSM}$. A modulation frequency of $\nu_{B_{FMS}} = 123\,\text{Hz}$ was selected. As a result, the total line width $\Delta\nu_{CDSM,all}$ reduced below the CDSM resonance line width $\Delta\nu_{CDSM}$ (see section 4.3.1). The line widths of the whole CDSM resonance structure were $\Delta\nu_{CDSM,all} \approx 200\,\text{Hz}$ for $n = 2$ and $\Delta\nu_{CDSM,all} \approx 250\,\text{Hz}$ for $n = 3$.
For the following measurements, the microwave frequency stabilisation control loop was operated until a magnetic field strength of $B = 300\,\text{nT}$. For lower magnetic field strengths, the microwave frequency stabilisation control loop was stopped, the last controller value preserved and the modulation frequency $\nu_{MW_{FMS}}$ turned off. Otherwise disturbances would have influenced the low field measurement (see figure 4.33).
The buffer gas pressure and the laser intensity were higher for the measurements with the CSES FS electronics in combination with the dual pass sensor ($P_{BG} = 8.0\,\text{kPa}$ (60 Torr) and $I \approx 180\,\mu\text{W/cm}^2$) compared to the measurements with the CSES EM ($P_{BG} = 2.0\,\text{kPa}$ or $P_{BG} = 5.3\,\text{kPa}$ and $I \approx 60\,\mu\text{W/cm}^2$).

In figure 4.36(a) measurements on the lower measurement limit are summarised for the CDSM resonance $n = 2$ at the sensor angles $\phi = 0°$, 30°, 45° and 60°. At $\phi = 0°$ the lower measurement limit was $B_{lf,lim} \approx 150\,\text{nT}$ for $n = 2$. With the default modulation frequency ($\nu_{B_{FMS}} = 7.102\,\text{kHz}$) only magnetic fields down to about 1 000 nT could be measured by keeping the required measurement accuracy. Unexpectedly, at the sensor angle $\phi = 30°$ the lowest measurement limit of $B_{lf,lim} < 100\,\text{nT}$ was obtained for $n = 2$.
In figure 4.36(b) the results on the lower measurement limit are depicted for the CDSM resonance $n = 3$. At $\phi = 90°$ the lower measurement limit was $B_{lf,lim} \approx 400\,\text{nT}$ for $n = 3$. The lower measurement limit was even higher at the sensor angles $\phi = 45°$ and $\phi = 60°$.

Comparing the results obtained in figures 4.35 and 4.36, the measurements with the CSES FS electronics and the dual pass sensor showed a higher lower measurement limit compared to measurements with the CSES EM. At $\phi = 0°$ the lower measurement limit of the CSES FS electronics and the dual pass sensor exceeded the results with the CSES EM by about a factor of two. At $\phi = 90°$ the limit was even a factor of four higher.
The line widths of the CDSM resonances measured with the CSES FS electronics and the dual pass sensor were $\Delta\nu_{CDSM,all} \approx 200\,\text{Hz}$ for $n = 2$ and $\Delta\nu_{CDSM,all} \approx 250\,\text{Hz}$ for $n = 3$.

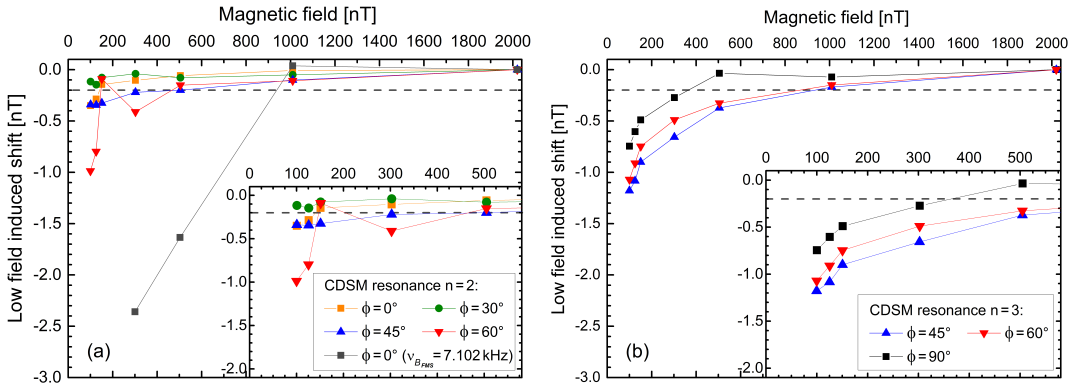

Figure 4.36.: Lower measurement limit for $n = 2$ and $n = 3$ with the CSES FS electronics and dual pass sensor for a modulation frequency much lower than the resonance line width: The resonance line width was $\Delta\nu_{CDSM} \approx 800\,\mathrm{Hz}$. A modulation frequency of $\nu_{B_{FMS}} = 123\,\mathrm{Hz}$ was applied. In (a) the low field induced shifts of $n = 2$ are depicted for the sensor angles $\phi = 0°$, 30°, 45° and 60°. In (b) the low field induced shiftd of the CDSM resonance $n = 3$ are shown for the sensor angles $\phi = 45°$, 60° and 90°. The buffer gas pressure was $P_{BG} = 8.0\,\mathrm{kPa}$ (60 Torr). The intensity in front of the cell was $I \approx 180\,\mu\mathrm{W/cm^2}$.

The CDSM resonance line widths obtained with the CSES EM using a buffer gas pressure of $P_{BG} = 2.0\,\mathrm{kPa}$ (15 Torr) were higher (about 350 Hz) but a lower measurement limit was achieved. Additionally, the resonances seemed rather well separated for the resonance measurements with the dual pass sensor. Nevertheless, the line width of the CDSM resonance measured with the dual pass sensor is the mean line width over twice the optical path compared to the CSES sensor (single pass design). Thus, the line width in the first path is typically higher. As a consequence, the zero crossing frequency should experience a higher low field induced shift in the first pass. Therefore, it is assumed that the overall resonance line width has to be further reduced to decrease the lower measurement limit for the dual pass sensor.

The drawback of using modulation frequencies lower than the resonance line width in combination with the high optical power was that the resonance amplitude reduced significantly by a factor of about eleven compared to the default modulation frequency of $\nu_{B_{FMS}} = 7.102\,\mathrm{kHz}$.

Another option to reduce the line widths would be to reduce the optical intensity. In order to reach the same line width, the optical intensity would have to be reduced by about a factor of seven which would also reduce the CDSM resonance amplitude by about the same factor. Therefore, with regard to the signal-to-noise ratio, the better option would be to reduce the laser intensity than to use a modulation frequency much less than the line width.

Nevertheless, the laser intensity in the sensor unit can be reduced without lowering the total optical power in the inbound fibre by increasing the laser beam cross section. The

laser beam cross section can be enlarged by selecting a lens with a higher focal length. Additionally, measurements with a higher buffer gas pressure ($P_{BG} = 10.7\,\text{kPa}$ (80 Torr)) are planned which may further narrow the resonance line widths. Thus, a further reduction of the lower measurement limit is expected.
Moreover, the influence of the microwave frequency stabilisation control loop on the lower measurement limit has to be further investigated. Since the microwave frequency stabilisation control loop uses the CPT resonance position of $n = 0$ to stabilise the frequency ν_{mod_1} (see section 2.4.2), the control loop is also affected by the overlapping CPT resonances at low magnetic field strengths. That was also the reason why the microwave frequency stabilisation control loop was only operated until $B = 300\,\text{nT}$. For lower magnetic field strengths, an additional shift of the measured magnetic field strength was detectable. The mentioned increase of the buffer gas pressure and the reduction of the laser intensity would also help to reduce the influence of the overlapping CPT resonances on the CPT resonance position of $n = 0$. Thus, the operation of the microwave frequency stabilisation control loop should be possible for lower magnetic field strengths than $B = 300\,\text{nT}$.

5. Summary and Discussion

This thesis describes several investigations and development steps for a compact optical magnetometer instrument which aims at magnetic field measurements in space. In this context, the optical path of the Coupled Dark State Magnetometer (CDSM) was characterised and the performance of the CDSM evaluated. The first CDSM instrument was designed for the China Seismo-Electromagnetic Satellite (CSES) mission launched in February 2018. Currently, a further CDSM instrument is under development for the JUpiter ICy moon Explorer (JUICE) mission of the European Space Agency. For this mission, several evaluation tests were carried out with special emphasis on the required accuracy of 0.2 nT (1 sigma).

The optical path of the CDSM consists of the laser unit, the sensor unit and a pair of optical fibres. A Vertical-Cavity Surface-Emitting Laser (VCSEL) is used as light source. VCSELs fulfil both the requirements for a space application and for the CPT resonance preparation. However, the ageing behaviour of its electro-optical parameters and their operational lifetime were unknown. Therefore, VCSELs from three different suppliers were procured and the change of their electro-optical parameters investigated during a more than a one-year long endurance test. These lasers showed distinct differences in their performance ,e.g., polarisation jumps, optical power variations and operational lifetimes. But most importantly, the results showed that VCSELs can be operated for more than 17 years, which is an essential requirement for the JUICE mission.

Furthermore, the modulation capability of a selected VCSEL was investigated with the help of a Fabry-Pérot interferometer. A modulation signal with a frequency of about 3.4 GHz was superimposed on the laser current. Ideally, most of the intensity should be contained in the first-order sidebands used for the CPT resonance preparation, which is achieved at a modulation index of about 1.85. Such a modulation index could only be reached for laser currents lower than 2.4 mA with a maximal microwave power level of $P_{MW} = -5.4\,\mathrm{dBm}$ for the CSES model, while the operational laser current ranges from about 1.5 mA to 4.0 mA. In contrast, the JUICE CDSM models provide higher microwave power levels ($P_{MW} \approx 2\,\mathrm{dBm}$). Thus, the ideal modulation index can also be achieved at higher laser currents. However, the intensities of the sidebands were unbalanced for laser currents less than 2.75 mA. This imbalance can affect the measurement accuracy by CPT resonance line shape asymmetries or the light shift. For equal laser sideband intensities, the CPT resonance line shapes are symmetric, if the two transitions required for the CPT

resonance preparation have the same transition strength. Therefore, a laser current around 2.75 mA, where both first-order sidebands have the same amplitude, is preferred for the operation of the magnetometer, although a lower modulation index is reached ($M = 1.2$). The sensor unit developed for the CSES mission is based on a single pass of the laser beam through the sensor cell. Measurements with this sensor unit revealed an imbalance between the single CPT resonance line shapes, which reduced the efficiency of the CDSM-based compensation of disturbing frequency shifts. As a result, a new sensor unit was designed which enables a dual laser beam pass through the sensor cell. These two different sensor designs were evaluated and measurements were compared as part of this thesis.

The CDSM operates using a graded-index multi-mode fibre as outbound fibre and a step-index multi-mode fibre as inbound fibre. The larger fibre core diameters enable a higher coupling reliability. Nevertheless, the selection of a multi-mode fibre and polarisation optics in the sensor unit instead of a polarisation-maintaining single-mode fibre as outbound fibre resulted in less stable operational parameters for the CPT resonance preparation, e.g., the laser beam profile and optical intensity at the sensor cell.

Besides the evaluation of the magnetometer's optical path, a large part of this thesis focuses on the influences of the operational parameters on the coupled CPT resonances (CDSM resonance) and investigations of the accuracy of the magnetometer. Before this thesis, the dependence of the CDSM resonances on the operational parameters had not been investigated. Therefore, the most important parameters which affect the line shapes and the zero crossing frequency were studied. This includes the following parameters: laser intensity, magnetic field inhomogeneity, buffer gas pressure, sensor cell temperature, combinations of laser current, laser temperature and microwave power level, optical detuning, non-linear dependence of the CPT resonance positions on the external magnetic field and the sensor angle ϕ, which is the angle between the laser propagation direction in the sensor unit of the first laser beam pass and the external magnetic field direction.

Measurements of the CPT and CDSM resonance line shapes in dependence of the laser intensity revealed a deviation from the predictions of the simple three level system. The amplitudes and line widths of the CPT and CDSM resonances are assumed to be affected by the optical pumping effect within the hyperfine structure of the ^{87}Rb D_1 line.

Comparing measurements for single and dual laser beam pass through the sensor cell, the dual pass resulted in an increase of the CDSM resonance amplitudes and the line widths were reduced. As a result, the slope of the dispersive CDSM resonance signals, which are used to determine the external magnetic field, increased by about a factor of two for dual pass.

Moreover, the CPT resonance line widths varied for repeated measurements. Initially, an inhomogeneity of the applied magnetic field in the magnetic shielding can, which is used for most tests in the laboratory, was assumed to cause this variations. However, it was shown then that the line width of the CPT resonances can be influenced by a magnetic field gradient, but that this influence can be neglected for most of our measurement con-

figurations in the magnetic shielding can. Additionally, the CPT resonance $n = 0$, which is far less influenced by a magnetic field inhomogeneity, revealed this broadening as well. Instead, this random broadening is believed to result from the changing laser beam profiles within the sensor unit due to the use of multi-mode fibres, which is a topic for future investigations.
Further, as discussed in literature, the light shift can change the CPT resonance positions depending on the laser intensity and intensity distribution within the laser sideband structure as well as the optical detuning. Test measurements of the determined magnetic field showed no significant shift with varying intensity ($\Delta B < 0.2\,\mathrm{nT}$).
Another important operational parameter is the buffer gas pressure. The usage of a buffer gas causes a broadening of the optical transition which affects the laser frequency stabilisation and reduces the CPT resonance amplitudes. However, the collisions of the Rb atoms with the buffer gas atoms narrow the CPT resonance line widths which is especially important for measurements at magnetic field strengths of $B < 2\,\mu\mathrm{T}$ in order to keep the required measurement accuracy of 0.2 nT (1 sigma) for JUICE. Therefore, the use of buffer gas pressures higher than $P_{BG} = 60\,\mathrm{Torr}$ (8.0 kPa) is favourable for the operation of the magnetometer, although the increase of the buffer gas pressure causes a reduction of the CPT resonance amplitudes.
Additionally, the usage of a buffer gas introduces shifts of the CPT resonance positions, another effect that needs to be taken into account. These shifts depend on the selected buffer gas pressure and the sensor cell temperature. With a higher buffer gas pressure, the CPT resonance positions experience higher shifts with a change of the sensor cell temperature.
For a buffer gas pressure of $P_{BG} = 30\,\mathrm{Torr}$ (4.0 kPa), the temperature shift coefficients of the CPT resonance positions $n = 0$, $n = \pm 2$ and $n = \pm 3$ were determined. The results showed that the shift coefficients are very similar and close to the calculated value of 7.8 Hz/°C. The deviations of the temperature shift coefficients are assumed to result from the measurement method which resulted in lower accuracy for the determination of the CPT resonance positions at higher temperatures.
Furthermore, the sensor cell temperature was used to optimise the CDSM resonance amplitudes at $\phi = 45°$. A maximum of the CDSM resonance amplitudes was found at about $T = 45°\mathrm{C}$. Increasing the sensor cell temperature from $T = 26°\mathrm{C}$ to $T = 45°\mathrm{C}$ resulted in a rise of the CDSM resonance amplitudes of $n = 2$ and $n = 3$ by a factor of about 3.5. In contrast, the CDSM resonance line widths of $n = 2$ and $n = 3$ showed no dependence on the sensor temperature.
Next, the combination of laser current, laser temperature and microwave power level was used to increase the CPT and CDSM resonance amplitudes. Due to the limited microwave power of the selected microwave oscillator for the CSES CDSM models, it was not possible to optimise the resonance amplitude over the whole operational laser current range. As mentioned above, a higher microwave power level is available for the JUICE CDSM models. Thus, optimisation of the amplitudes will also be possible for higher laser currents.

Further, it was shown that the selected operational parameters of the laser and microwave power level could influence the symmetry of the CPT and CDSM resonances, most likely due to the changing intensity distribution of the laser sideband structure. The symmetry of the CPT resonances is affected by the Rabi frequencies of the two transitions forming the Λ excitation scheme. The Rabi frequency depends on the intensity of the laser sideband and the transition strength. Both Rabi frequencies of the CPT resonance excitation scheme should ideally be equal to obtain a symmetric CPT resonance line shape. However, the single transitions used to build the CPT resonances ($n = \pm 2$ or $n = \pm 3$) do not have the same transition strengths for most sensor angles. As a result, the Rabi frequencies are not equal when the laser sidebands have the same intensity and the line shapes are asymmetric.
Additionally, the CPT resonance line shapes are influenced by an optical detuning. Although the asymmetric CPT resonance structures are largely compensated when forming the CDSM resonances, shifts of the zero crossing frequencies are still possible. Furthermore, the optical detuning can influence the magnetic field measurement by changing the light shift. Moreover, the quadratic magnetic field induced shift of the CPT resonance positions can influence the measured magnetic field, when the control loop for the stabilisation of the microwave frequency is operated. This results from the different quadratic magnetic field shift coefficients of the CPT resonance position of $n = 0$, which is selected for the operation of the microwave frequency stabilisation control loop, and the CPT resonance positions of $n = \pm 2$ and $n = \pm 3$, which are used for the magnetic field measurement. Therefore, the quadratic shift is corrected by the microwave frequency stabilisation control loop during the CSES mission. In contrast, for the JUICE mission, where mainly magnetic fields below $B < 2\,\mu\mathrm{T}$ are measured, the influence of the quadratic shift can be neglected.
Furthermore, the CPT and CDSM resonance line shapes depend on the sensor angle ϕ. The amplitudes and line widths of the CPT and CDSM resonances were measured in the angular range from 0° to 180°. The amplitude of the CDSM resonance $n = 2$ showed two maxima at $\phi = 30°$ and $\phi = 150°$ and vanished close to $\phi = 90°$. In contrast, the amplitude of the CDSM resonance $n = 3$ revealed a maximum at $\phi = 90°$ and was close to zero at $\phi = 0°$ and $\phi = 180°$. The different angular dependence of the CDSM resonances and switching between the resonances at a certain sensor angle enable an omni-directional magnetic field measurement.
For the CSES sensor design, which is based on a single pass of the sensor cell, the single CPT resonance amplitudes, which form the CDSM resonance, had different amplitudes for most sensor angles. The imbalance between the single CPT resonance line shapes influences the obtained compensation behaviour when building the CDSM resonance. The CDSM-based compensation of a disturbing frequency shift performs best when the single CPT resonances have the same line shape. If the single CPT resonances have different line shapes then the compensation effect is reduced. Especially, at sensor angles where the microwave control loop cannot be operated, the compensation effect of the CDSM has

to work properly to reduce the influence of disturbing frequency shifts, e.g., by a sensor temperature change or a drift of the reference oscillator frequency, on the magnetic field measurement.
As indicator of the equality of the single CPT resonances, the single CPT resonance amplitudes were compared for the single and dual pass configuration. The amplitude ratios h_{-2}/h_{+2} and h_{-3}/h_{+3} of the CPT resonances $n = -2$ and $n = +2$ as well as $n = -3$ and $n = +3$ were much more balanced for the dual pass compared to the single pass of the laser beam through the sensor cell. At $\phi = 0°$ the ratio h_{-2}/h_{+2} improved from 2.5 for the single pass to 0.92 for the dual pass and at $\phi = 60°$ the ratio h_{-3}/h_{+3} changed from 3.0 for the single pass to 1.2 for the dual pass. As a result, the dual pass sensor enhances the performance of the magnetometer compared to the single pass design by improving the CDSM-resonance-based compensation of a disturbing frequency shift. For the example of $\phi = 60°$ and the CDSM resonance $n = 3$, the dual pass sensor enabled the compensation of a four times larger disturbing frequency shift compared to the single pass design.
For the JUICE mission, the accuracy of the CDSM was investigated for magnetic field strengths $B < 2\,\mu\text{T}$. In this range, the CPT and CDSM resonances start to converge. Consequently, the resonance structures start to overlap and the zero crossing frequencies of the CDSM resonances are shifted. The overlap of the resonances depends on the external magnetic field strength and the overall resonance structures consisting of the centre structure and both sidebands. The overall resonance structure is mainly determined by the modulation frequency $\nu_{B_{FMS}}$ used for the detection of the CDSM resonances. For this reason, the use of high modulation frequencies (several kHz) is not an option for the low magnetic field range, since the overall CDSM structures were too large to keep the required accuracy limit. Therefore, the modulation frequency was selected such that the first-order sidebands vanished within the centre structures of the CDSM resonances and the resulting resonance structures had about the same line width as the original CDSM resonance centre structures. Thus, the disturbing influence of the sidebands on the magnetic field measurement was removed.
Further, a high optical power of $P > 15\,\mu\text{W}$ is targeted within the optical fibres for the JUICE mission in order to reduce radiation induced attenuation. However, the typical CDSM resonance line widths at this optical power were too broad to keep the required accuracy for magnetic field strengths as low as 150 nT. Thus, tests were conducted in order to reduce the overall CDSM resonance line widths by selecting a modulation frequency for the detection much lower than the line widths of the CDSM resonances. Measurements showed that the accuracy within the low magnetic field range could be improved at the expense of the CDSM resonance amplitudes.
The reduction of the CDSM resonance amplitudes depends on the CDSM resonance line widths and the selected modulation frequency $\nu_{B_{FMS}}$. For modulation frequencies much lower than the line width, the CDSM resonance amplitudes started to decline rapidly. For example, with the dual pass sensor at a sensor angle of $\phi = 0°$, the CDSM resonance line widths were typically in the range of $800 - 1000\,\text{Hz}$ for the selected operational parameters.

In this case, the magnetic field, which could be measured with an influence less than 0.2 nT from the other resonances, could be reduced from about 1000 nT for $\nu_{B_{FMS}} = 7.102\,\mathrm{kHz}$ (default for CSES mission) to 150 nT for $\nu_{B_{FMS}} = 123\,\mathrm{Hz}$ at the expense of a reduction of the amplitudes by about a factor of eleven.
A further reduction of the CDSM resonance line widths is targeted to prevent such a large amplitude reduction while keeping the accuracy limit for magnetic field strengths as low as 150 nT. This goal can be achieved by further increasing the buffer gas pressure or reducing the laser intensity by enlarging the laser beam profile.

6. Conclusion and Outlook

The performance of the CDSM instrument was evaluated with special focus on the upcoming Jupiter mission of the European Space Agency. This mission requires a measurement accuracy of 0.2 nT (1 sigma), an operational instrument lifetime of 17 years and the ability to measure magnetic fields as low as 150 nT.
The results from the endurance test in this thesis proved that vertical-cavity surface-emitting lasers can be operated for more than 17 years with properties suitable for accurate CDSM measurements. Further, the operational parameters of the CDSM were studied in order to optimise performance with respect to signal-to-noise ratio and accuracy. The sensor design developed in this thesis, can compensate for up to four times higher disturbing frequency shifts compared to the original sensor design for the CSES mission. Furthermore, the optimised operational magnetometer parameters developed in this work enable measurements of the magnetic field strengths as low as 150 nT, meeting the requirements of the Jupiter mission
With respect to the Jupiter mission, an upcoming task is the further optimisation of the CSDM-resonance-based compensation of disturbing frequency shifts with the new sensor design. For certain sensor angles, ideal compensation has not yet been achieved. Optimising those operational parameters that affect the intensity distribution, e.g., the laser operational parameters in combination with the microwave power level and modulation indices, is expected to result in a further improvement.
Another open issue concerns the light shift. Changes in laser intensity could potentially impact the measured magnetic field, resulting in a violation of the required 0.2 nT accuracy. Thus far, no sizeable influence of laser intensity on magnetic field strength has been observed. However, a more detailed study of the light shift is planned, which will also account for the influence of an optical detuning on the light shift and the magnetic field.
Moreover, calibration and verification tests of the optimised new sensor unit introduced in this thesis are planned at magnetic field strengths below 2 µT, which is required for the Jupiter mission. These measurements will be performed at the Conrad Observatory where the sensor unit will be mounted in the centre of the newly installed three-meter Merritt coil system at homogeneous magnetic field.

Bibliography

1. Lammegger, R. *pat.* WO/2008/151344. Method and Device for Measuring Magnetic Fields (2008).
2. Budker, D. & Romalis, M. Optical magnetometry. *Nature Physics* **3,** 227 (2007).
3. Arimondo, E. in (ed Wolf, E.) Coherent Population Trapping in Laser Spectroscopy, 257 (Elsevier, 1996).
4. Shah, V. & Kitching, J. in *Advances In Atomic, Molecular, and Optical Physics* (eds Arimondo, E., Berman, P. R. & Lin, C. C.) 21 (Academic Press, 2010).
5. Zhong, W. Review of chip-scale atomic clocks based on coherent population trapping. *Chinese Physics B* **23,** 030601 (2014).
6. Nagel, A., Graf, L., Naumov, A., Mariotti, E., Biancalana, V., Meschede, D. & Wynands, R. Experimental realization of coherent dark-state magnetometers. *Europhysics Letters* **44,** 31 (1998).
7. Schwindt, P. D. D., Knappe, S., Shah, V., Hollberg, L., Kitching, J., Liew, L.-A. & Moreland, J. Chip-scale atomic magnetometer. *Applied Physics Letters* **85,** 6409 (2004).
8. Acuña, M. H. Space-based magnetometers. *Review of Scientific Instruments* **73,** 3717 (2002).
9. Balogh, A. Planetary magnetic field measurements: Missions and instrumentation. *Space Science Reviews* **152,** 23 (2010).
10. Pollinger, A., Ellmeier, M., Magnes, W., Hagen, C., Baumjohann, W., Leitgeb, E. & Lammegger, R. *Enable the inherent omni-directionality of an absolute coupled dark state magnetometer for e.g. scientific space applications* in. 2012 IEEE International Instrumentation and Measurement Technology Conference Proceedings (Graz, Austria, 2012), 33.
11. Léger, J.-M., Jager, T., Bertrand, F., Hulot, G., Brocco, L., Vigneron, P., Lalanne, X., Chulliat, A. & Fratter, I. In-flight performance of the Absolute Scalar Magnetometer vector mode on board the Swarm satellites. *Earth, Planets and Space* **67,** 57 (2015).

12. Pollinger, A., Lammegger, R., Magnes, W., Hagen, C., Ellmeier, M., Jernej, I., Leichtfried, M., Kürbisch, C., Maierhofer, R., Wallner, R., Fremuth, G., Amtmann, C., Betzler, A., Delva, M., Prattes, G. & Baumjohann, W. Coupled dark state magnetometer for the China Seismo-Electromagnetic Satellite. *Measurement Science and Technology* **29,** 095103 (2018).
13. European Space Agency. *JUICE definition study report (Red Book)* 1 (2014).
14. Pollinger, A. *Developement and evaluation of a control unit for the coupled dark state magnetometer* PhD thesis (Graz University of Technology, Graz, Austria, 2013).
15. Knappe, S., Wynands, R., Kitching, J., Robinson, H. G. & Hollberg, L. Characterization of coherent population-trapping resonances as atomic frequency references. *Journal of the Optical Society of America B* **18,** 1545 (2001).
16. Orriols, G. Nonabsorption resonances by nonlinear coherent effects in a three-level system. *Il Nuovo Cimento B* **53,** 1 (1979).
17. Erhard, M. & Helm, H. Buffer-gas effects on dark resonances: Theory and experiment. *Physical Review A* **63,** 043813 (2001).
18. Wynands, R. & Nagel, A. Precision spectroscopy with coherent dark states. *Applied Physics B* **68,** 1 (1999).
19. Ficek, Z. & Swain, S. *Quantum Interference and Coherence - Theory and Experiments* 1st ed. (Springer-Verlag New York, 2005).
20. Lambropoulos, P. & Petrosyan, D. *Fundamentals of Quantum Optics and Quantum Information* 1st ed. (Springer-Verlag Berlin Heidelberg, 2007).
21. Lammegger, R. *Coherent Population Trapping - Ein Quanteninterferenzeffekt als Basis optischer Magnetometer* PhD thesis (Graz University of Technology, Graz, Austria, 2006).
22. Loudon, R. *The Quantum Theory of Light* 2nd ed. (Oxford University Press, 1983).
23. Vanier, J., Godone, A. & Levi, F. Coherent population trapping in cesium: Dark lines and coherent microwave emission. *Physical Review A* **58,** 2345 (1998).
24. Agap′ev, B. D., Gornyĭ, M. B., Matisov, B. G. & Rozhdestvenskiĭ, Y. V. Coherent population trapping in quantum systems. *Physics-Uspekhi,* 763 (1993).
25. Corney, A. *Atomic and Laser Spectroscopy* (Clarendon Press, Oxford, 1977).
26. Breit, G. & Rabi, I. I. Measurement of Nuclear Spin. *Physical Review* **38,** 2082 (1931).
27. Kusch, P., Millman, S. & Rabi, I. I. The radiofrequency spectra of atoms hyperfine structure and Zeeman effect in the ground state of Li^6, Li^7, K^{39} and K^{41}. *Physical Review* **57,** 765 (1940).
28. Steck, D. A. *Rubidium 87 D Line Data* available online at http://steck.us/alkalidata (revision 2.1.5, 13 January 2015).

29. Vanier, J. & Audoin, C. *The Quantum Physics of Atomic Frequency Standards* (Adam Hilger, 1989).

30. Ellmeier, M. *Influence of characteristic parameters on the performance of a coupled dark state magnetometer* Diploma thesis (unpublished) (University of Graz, Graz, Austria, 2011).

31. Stähler, M., Wynands, R., Knappe, S., Kitching, J., Hollberg, L., Taichenachev, A. & Yudin, V. Coherent population trapping resonances in thermal ^{85}Rb vapor: D_1versus D_2 line excitation. *Optics Letters* **27,** 1472 (2002).

32. Knappe, S., Kemp, W., Affolderbach, C., Nagel, A. & Wynands, R. Splitting of coherent population-trapping resonances by the nuclear magnetic moment. *Physical Review A* **61,** 012508 (1999).

33. Knappe, S. *Dark Resonance Magnetometers and Atomic Clocks* PhD thesis (University of Bonn, Bonn, Germany, 2001).

34. Affolderbach, C., Nagel, A., Knappe, S., Jung, C., Wiedenmann, D. & Wynands, R. Nonlinear spectroscopy with a vertical-cavity surface-emitting laser (VCSEL). *Applied Physics B* **70,** 407 (2000).

35. Bjorklund, G. C., Levenson, M. D., Lenth, W. & Ortiz, C. Frequency modulation (FM) spectroscopy. *Applied Physics B* **32,** 145 (1983).

36. Bjorklund, G. C. Frequency-modulation spectroscopy: a new method for measuring weak absorptions and dispersions. *Optics Letters* **5,** 15 (1980).

37. Whitaker, J. C. *The Electronics Handbook* 2nd (CRC Press, 2005).

38. Supplee, J. M., Whittaker, E. A. & Lenth, W. Theoretical description of frequency modulation and wavelength modulation spectroscopy. *Applied Optics* **33,** 6294 (1994).

39. Knappe, S., Stähler, M., Affolderbach, C., Taĭchenachev, A. V., Yudin, V. I. & Wynands, R. Simple parameterization of dark-resonance line shapes. *Applied Physics B* **76,** 57 (2003).

40. Shen, X., Zhang, X., Wang, L., Chen, H., Wu, Y., Yuan, S., Shen, J., Zhao, S., Qian, J. & Ding, J. The earthquake-related disturbances in ionosphere and project of the first China seismo-electromagnetic satellite. *Earthquake Science* **24,** 639 (2011).

41. Cheng, B., Zhou, B., Magnes, W., Lammegger, R. & Pollinger, A. High precision magnetometer for geomagnetic exploration onboard of the China Seismo-Electromagnetic Satellite. *Science China Technological Sciences* **61,** 659 (2018).

42. Pollinger, A., Lammegger, R., Magnes, W., Ellmeier, M., Baumjohann, W. & Windholz, L. *Control loops for a Coupled Dark State Magnetometer* in. SENSORS, 2010 IEEE (Kona, USA, 2010), 779.

43. Ellmeier, M., Hagen, C., Piris, J., Lammegger, R., Jernej, I., Woschank, M., Magnes, W., Murphy, E., Pollinger, A., Erd, C., Baumjohann, W. & Windholz, L. Accelerated endurance test of single-mode vertical-cavity surface-emitting lasers under vacuum used for a scalar space magnetometer. *Applied Physics B* **124,** 18 (2018).

44. Knappe, S., Kitching, J., Hollberg, L. & Wynands, R. Temperature dependence of coherent population trapping resonances. *Applied Physics B* **74,** 217 (2002).

45. Aguirre, M. A. *Introduction to Space Systems: Design and Synthesis* 1st (Springer-Verlag New York, 2013).

46. Soda, H., Iga, K., Kitahara, C. & Suematsu, Y. GaInAsP/InP Surface Emitting Injection Lasers. *Japanese Journal of Applied Physics* **18,** 2329 (1979).

47. Jewell, J. L., Harbison, J. P., Scherer, A., Lee, Y. H. & Florez, L. Vertical-cavity surface-emitting lasers: Design, growth, fabrication, characterization. *IEEE Journal of Quantum Electronics* **27,** 1332 (1991).

48. *Vertical-Cavity Surface-Emitting Laser Devices* (eds Li, H. & Iga, K.) 1st ed. (Springer Berlin Heidelberg, 2003).

49. Michalzik, R. *VCSELs - Fundamentals, Technology and Applications of Vertical-Cavity Surface-Emitting Lasers* 1st ed. (Springer-Verlag Berlin Heidelberg, 2013).

50. Melentiev, P. N., Subbotin, M. V. & Balykin, V. I. Simple and effective modulation of diode lasers. *Laser Physics* **11,** 891 (2001).

51. Panter, P. F. *Modulation, Noise, and Spectral Analysis: Applied to Information Transmission* (McGraw-Hill, 1965).

52. Lenth, W. Optical heterodyne spectroscopy with frequency- and amplitude-modulated semiconductor lasers. *Optics Letters* **8,** 575 (1983).

53. Piris, J., Ferreira, L. & Sarti, B. *Characterization and endurance testing of High Power Laser Diodes at ESTEC's laser diode laboratory* in. 52nd Electronic Components and Technology Conference (Noordwijk, Netherlands, 2012), 30.

54. Piris, J., Murphy, E. M., Levy, M., Klumel, G., Diamant, R. & Sarti, B. *Evaluation of high power laser diodes for space applications: Effects of the gaseous environment and mechanical stress in their long term performance* in. Proceedings of SPIE, International Conference on Space Optics - ICSO 2014 (Tenerife, Spain, 2014). **10563** (2017), 105633A.

55. Breschi, E., Kazakov, G., Lammegger, R., Mileti, G., Matisov, B. & Windholz, L. Quantitative study of the destructive quantum-interference effect on coherent population trapping. *Physical Review A* **79,** 063837 (2009).

56. Breschi, E., Kazakov, G., Lammegger, R., Matisov, B., Windholz, L. & Mileti, G. Influence of laser sources with different spectral properties on the performance of vapor cell atomic clocks based on lin||lin CPT. *IEEE Transactions on Ultrasonics, Ferroelectrics and Frequency Control* **56,** 926 (2009).

57. Hagen, C., Ellmeier, M., Piris, J., Lammegger, R., Jernej, I., Magnes, W., Murphy, E., Pollinger, A., Erd, C. & Baumjohann, W. *Long-term vacuum tests of single-mode vertical cavity surface emitting laser diodes used for a scalar magnetometer* in. Proceedings of SPIE, International Conference on Space Optics - ICSO 2014 (Tenerife, Spain, 2014). **10563** (2017), 105634Y.

58. Herrick, R. W. Reliability of Vertical-Cavity Surface-Emitting Lasers. *Japanese Journal of Applied Physics* **51,** 11PC01 (2012).

59. Hawkins, B. M., Hawthorne, R. A., Guenter, J. K., Tatum, J. A. & Biard, J. R. *Reliability of various size oxide aperture VCSELs* in. 52nd Electronic Components and Technology Conference 2002. (Cat. No.02CH37345) (San Diego, USA, 2002), 540.

60. Kim, H.-D., Jeong, W.-G., Shin, H.-E., Ser, J.-H., Shin, H.-K. & Ju, Y.-G. Reliability in the oxide vertical-cavity surface-emitting lasers exposed to electrostatic discharge. *Optics Express* **14,** 12432 (2006).

61. *Materials and Reliability Handbook for Semiconductor Optical and Electron Devices* (eds Ueda, O. & Pearton, S. J.) 1st ed. (Springer-Verlag New York, 2013).

62. Camparo, J., Huang, M. & Driskell, T. *The influence of laser polarization noise on the short-term stability of CPT atomic clocks* in (Joint European Frequency, Time Forum, and International Frequency Control Symposium (EFTF/IFC), Prague, Czech Republic, 2013), 612.

63. Huang, M. & Camparo, J. *The influence of laser polarization variations on CPT atomic clock signals* in (Joint Conference of the IEEE International Frequency Control, the European Frequency, and Time Forum Proceedings, San Francisco, USA, 2011).

64. Kim, T., Kim, T., Kim, S. & Kim, S. B. Degradation behavior of 850 nm AlGaAs/GaAs oxide VCSELs suffered from electrostatic discharge. *ETRI Journal* **30,** 833 (2008).

65. Lytkine, A., Jäger, W. & Tulip, J. Frequency tuning of long-wavelength VCSELs. *Spectrochimica Acta Part A: Molecular and Biomolecular Spectroscopy* **63,** 940 (2006).

66. Davim, J. P., Reis, P., Lapa, V. & António, C. C. Machinability study on polyetheretherketone (PEEK) unreinforced and reinforced (GF30) for applications in structural components. *Composite Structures* **62,** 67 (2003).

67. Victrex. *VICTREX PEEK - Properties Guide* 2002.

68. Al-Azzawi, A. *Fiber Optics: Principles and Advanced Practices* 2nd ed. (CRC Press, 2017).

69. Haar, L., Gallagher, J. S. & Kell, G. S. *NBS/NRC Wasserdampftafeln* 1st ed. (Springer-Verlag Berlin Heidelberg, 1988).

70. Henson, T. D. & Torrington, G. K. *Space radiation testing of radiation-resistant glasses and crystals* in. Proceedings od SPIE, Inorganic Optical Materials III. **4452** (San Diego, USA, 2001), 54.

71. *The Properties of Optical Glass* (eds Bach, H. & Neuroth, N.) 1st ed. (Springer-Verlag Berlin Heidelberg, 1998).

72. *Advanced Fiber Optics* (ed Thévenaz, L.) 1st ed. (EPFL Press, 2011).

73. Mathur, K. S. *Fundamentals of Fiber Optics Communications* (Zorba Books, 2018).

74. *Specialty Optical Fibers Handbook* (eds Mendez, A. & Morse, T.) 1st ed. (Academic Press, 2006).

75. Nikolić, S. N., Radonjić, M., Krmpot, A. J., Lučić, N. M., Zlatković, B. V. & Jelenković, B. M. Effects of a laser beam profile on Zeeman electromagnetically induced transparency in the Rb buffer gas cell. *Journal of Physics B: Atomic, Molecular and Optical Physics* **46,** 075501 (2013).

76. Buck, J. A. *Fundamentals of Optical Fibers* 2nd ed. (John Wiley & Sons, 2004).

77. Demtröder, W. *Laser Spectroscopy* 4th ed. (Springer-Verlag Berlin Heidelberg, 2008).

78. For Standardization (ISO), I. O. *Lasers and laser-related equipment - Test methods for laser beam widths, divergence angles and beam propagation ratios (ISO Standard No.11146)* 2005.

79. Lee, M. *Laser beam profiling* Bachelor Thesis (unpublished) (Graz University of Technology, Graz, Austria, 2018).

80. Girard, S., Morana, A., Ladaci, A., Robin, T., Mescia, L., Bonnefois, J. J., Boutillier, M., Mekki, J., Paveau, A., Cadier, B., Marin, E., Ouerdane, Y. & Boukenter, A. Recent advances in radiation-hardened fiber-based technologies for space applications. *Journal of Optics* **20,** 093001 (2018).

81. Girard, S., Kuhnhenn, J., Gusarov, A., Brichard, B., Van Uffelen, M., Ouerdane, Y., Boukenter, A. & Marcandella, C. Radiation effects on silica-based optical fibers: Recent advances and future challenges. *IEEE Transactions on Nuclear Science* **60,** 2015 (2013).

82. Ott, M. N. *Fiber optic cable assemblies for space flight: II. Thermal and radiation effects* in. Proceedings of SPIE, Photonics for Space Environments VI. **3440** (1998), 37.

83. Kuhnhenn, J., Hoeffgen, S. K., Köhn, O., Schumann, O., Weinand, U. & Wolf, R. *Irradiation tests on optical fibers below 20 k* in. Proceedings of SPIE, International Conference on Space Optics - ICSO 2014 (Tenerife, Spain, 2014). **10563** (2018), 105632A.

84. Friebele, E. J. & Gingerich, M. E. Photobleaching effects in optical fiber waveguides. *Applied Optics* **20,** 3448 (1981).

85. Alam, M., Abramczyk, J., Farroni, J., Manyam, U. & Guertin, D. *Passive and active optical fibers for space and terrestrial applications* in. Proceedings of SPIE, Photonics for Space Environments XI. **6308** (San Diego, USA, 2006), 630808.

86. Friebele, E. J., Gingerich, M. E. & Long, K. J. Radiation damage of optical fiber waveguides at long wavelengths. *Applied Optics* **21,** 547 (1982).

87. Friebele, E. J., Askins, C. G., Gingerich, M. E. & Long, K. J. Optical fiber waveguides in radiation environments, II. *Nuclear Instruments and Methods in Physics Research Section B: Beam Interactions with Materials and Atoms* **1,** 355 (1984).

88. Friebele, E. J., Schultz, P. C. & Gingerich, M. E. Compositional effects on the radiation response of Ge-doped silica-core optical fiber waveguides. *Applied Optics* **19,** 2910–2916 (1980).

89. Erhard, M., Nu„mann, S. & Helm, H. Power broadening and Doppler effects of coherent dark resonances in Rb. *Physical Review A* **62,** 061802 (2000).

90. Amtmann, C. *Measurement of the laser sideband structure with a Fabry-Pérot interferometer* (unpublished) (Graz University of Technology, Graz, Austria, 2018).

91. Wynands, R., Nagel, A., Brandt, S., Meschede, D. & Weis, A. Selection rules and line strengths of Zeeman-split dark resonances. *Physical Review A* **58,** 196 (1998).

92. Vanier, J., Levine, M. W., Janssen, D. & Delaney, M. Contrast and linewidth of the coherent population trapping transmission hyperfine resonance line in ^{87}Rb: Effect of optical pumping. *Physical Review A* **67,** 065801 (2003).

93. Vanier, J. Atomic clocks based on coherent population trapping: A review. *Applied Physics B* **81,** 421 (2005).

94. Nagel, A., Affolderbach, C., Knappe, S. & Wynands, R. Influence of excited-state hyperfine structure on ground-state coherence. *Physical Review A* **61,** 012504 (1999).

95. Mathur, B. S., Tang, H. & Happer, W. Light shifts in the alkali atoms. *Physical Review* **171,** 11 (1968).

96. Vanier, J., Godone, A. & Levi, F. *Coherent microwave emission in coherent population trapping: origin of the energy and of the quadratic light shift* in. Proceedings of the 1999 Joint Meeting of the European Frequency and Time Forum and the IEEE International Frequency Control Symposium (Cat. No.99CH36313). **1** (Besancon, France, 1999), 96.

97. Levi, F., Godone, A. & Vanier, J. The light shift effect in the coherent population trapping cesium maser. *IEEE Transactions on Ultrasonics, Ferroelectrics and Frequency Control* **47,** 466 (2000).

98. Gerginov, V., Knappe, S., Shah, V., Schwindt, P. D. D., Hollberg, L. & Kitching, J. Long-term frequency instability of atomic frequency references based on coherent population trapping and microfabricated vapor cells. *Journal of the Optical Society of America B* **23,** 593 (2006).

99. Shah, V., Gerginov, V., Schwindt, P. D. D., Knappe, S., Hollberg, L. & Kitching, J. Continuous light-shift correction in modulated coherent population trapping clocks. *Applied Physics Letters* **89,** 151124 (2006).

100. Nagel, A., Brandt, S., Meschede, D. & Wynands, R. Light shift of coherent population trapping resonances. *Europhysics Letters* **48,** 385 (1999).

101. Nagel, A. *Precision Spectroscopy of Coherent Dark States in Thermal Cesium Vapour* PhD thesis (University of Bonn, Bonn, Germany, 1999).

102. Thomas, J. E. & Quivers Jr., W. W. Transit-time effects in optically pumped coupled three-level systems. *Physical Review A* **22,** 2115 (1980).

103. Brandt, S., Nagel, A., Wynands, R. & Meschede, D. Buffer-gas-induced linewidth reduction of coherent dark resonances to below 50 Hz. *Physical Review A* **56,** R1063 (1997).

104. Happer, W. Optical pumping. *Reviews of Modern Physics* **44,** 169 (1972).

105. Rotondaro, M. D. & Perram, G. P. Collisional broadening and shift of the rubidium D_1 and D_2 lines ($5^2S_{1/2} \rightarrow 5^2P_{1/2}$, $5^2P_{3/2}$) by rare gases, H_2, D_2, N_2, CH_4 and CF_4. *Journal of Quantitative Spectroscopy and Radiative Transfer* **57,** 497 (1997).

106. Demtröder, W. *Atoms, Molecules and Photons* 2nd ed. (Springer-Verlag Berlin Heidelberg, 2010).

107. Alcock, C. B., Itkin, V. P. & Horrigan, M. K. Vapour pressure equations for the metallic elements: 298-2500K. *Canadian Metallurgical Quarterly* **23,** 309 (1984).

108. Dicke, R. H. The effect of collisions upon the Doppler width of spectral lines. *Physical Review* **89,** 472 (1953).

109. Firstenberg, O., Shuker, M., Ben-Kish, A., Fredkin, D. R., Davidson, N. & Ron, A. Theory of Dicke narrowing in coherent population trapping. *Physical Review A* **76,** 013818 (2007).

110. Boudot, R., Dziuban, P., Hasegawa, M., Chutani, R. K., Galliou, S., Giordano, V. & Gorecki, C. Coherent population trapping resonances in Cs-Ne vapor microcells for miniature clocks applications. *Journal of Applied Physics* **109,** 014912 (2011).

111. Bradley, M. P., Porto, J. V., Rainville, S., Thompson, J. K. & Pritchard, D. E. Penning trap measurements of the masses of ^{133}Cs, ^{87,85}Rb, and ^{23}Na with uncertainties $\leq$l0.2 ppb. *Physical Review Letters* **83,** 4 (1999).

112. *CRC Handbook of Chemistry and Physics* (ed Haynes, W. M.) 97th ed. (CRC Press, 2016).

113. Vanier, J. Relaxation in rubidium-87 and the rubidium maser. *Physical Review* **168,** 129 (1968).

114. Bender, P. L., Beaty, E. C. & Chi, A. R. Optical detection of narrow Rb^{87} hyperfine absorption lines. *Physical Review Letters* **1,** 311 (1958).

115. Vanier, J., Kunski, R., Cyr, N., Savard, J. Y. & Têtu, M. On hyperfine frequency shifts caused by buffer gases: Application to the optically pumped passive rubidium frequency standard. *Journal of Applied Physics* **53,** 5387 (1982).

116. Cooper, D. E. & Gallagher, T. F. Double frequency modulation spectroscopy: High modulation frequency with low-bandwidth detectors. *Applied Optics* **24,** 1327 (1985).

117. Taĭchenachev, A. V., Yudin, V. I., Wynands, R., Stähler, M., Kitching, J. & Hollberg, L. Theory of dark resonances for alkali-metal vapors in a buffer-gas cell. *Physical Review A* **67,** 033810 (2003).

118. Hobbs, P. C. D. *Building Electro-Optical Systems: Making It all Work* 2nd (Wiley, 2009).

119. Benumof, R. Optical pumping theory and experiments. *American Journal of Physics* **33,** 151 (1965).

120. Kargapoltsev, S. V., Kitching, J., Hollberg, L., Taichenachev, A. V., Velichansky, V. L. & Yudin, V. I. High-contrast dark resonance in σ_+- σ_- optical field. *Laser Physics Letters* **1,** 495 (2004).

121. Levi, F., Godone, A., Vanier, J., Micalizio, S. & Modugno, G. Line-shape of dark line and maser emission profile in CPT. *The European Physical Journal D* **12,** 53 (2000).

122. Shah, V., Knappe, S., Schwindt, P. D. D., Gerginov, V. & Kitching, J. Compact phase delay technique for increasing the amplitude of coherent population trapping resonances in open Λsystems. *Optics Letters* **31,** 2335 (2006).

123. Steck, D. A. *Cesium D Line Data* available online at http://steck.us/alkalidata (revision 2.1.4, 23 December 2010).

124. Farrell, P. M. & MacGillivray, W. R. On the consistency of Rabi frequency calculations. *Journal of Physics A: Mathematical and General* **28,** 209 (1995).

125. Meinert, F., Basler, C., Lambrecht, A., Welte, S. & Helm, H. Quantitative analysis of the transient response of the refractive index to conditions of electromagnetically induced transparency. *Physical Review A* **85** (2012).

126. Radonjić, M., Arsenović, D., Grujić, Z. & Jelenković, B. M. Coherent population trapping linewidths for open transitions: Cases of different transverse laser intensity distribution. *Physical Review A* **79,** 023805 (2009).

127. *Space Research Institute of the Austrian Academy of Sciences - Test Facilities. (2019-05-16). Retrieved from* `https://www.iwf.oeaw.ac.at/en/institute/infrastructure/test-facilities`.

128. *Conrad Observatory - Geomagnetic Observatory. (2019-05-16). Retrieved from* `http://www.conrad-observatory.at/zamg/index.php/`.

129. *Magnetsrode by Technische Universität Braunschweig. (2019-05-16). Retrieved from* `http://www.igep.tu-bs.de/institut/einrichtungen/magnetsrode`.

A. Appendix

A.1. Calculation of the Rabi Frequencies and Decay Rates

The Rabi frequency g was calculated for the transition from the lower state $|F\, m_F\rangle$ to the upper state $|F'\, m'_F\rangle$ via the relation [124]

$$g(F, m_F, F', m'_F, q) = (-1)^{1/2(q(1+q))+1} \sqrt{\frac{2I}{\epsilon_0 c \hbar^2}} \langle F'\, m'_F|\, d_q\, |F\, m_F\rangle \ . \tag{A.1}$$

d_q is the component q of the dipole operator $\hat{d}$ which is commonly stated in a spherical basis [124] where $q = -1,\ 0,\ +1$ is used respective for σ^-, π and σ^+ transitions. Further, I is the optical intensity and ϵ_0 gives the vacuum permittivity.
The transition matrix element from level $|F\, m_F\rangle$ to level $|F'\, m'_F\rangle$ was calculated from [125]

$$\langle F' m'_F | d_q | F m_F \rangle = c_{F', m'_F, F, m_F, q} \langle J' || d || J \rangle \ ,$$

where $\langle J' || d || J \rangle = \sqrt{2} \times 2.5377(17) \times 10^{-29}$ Cm [28] for the ^{87}Rb D_1 line.
The coefficients $c_{F', m'_F, F, m_F, q}$ were determined by the relation

$$c_{F', m'_F, F, m_F, q} = (-1)^{2F' - m'_F + I + J + 1} \sqrt{(2F'+1)(2F+1)} \begin{pmatrix} F' & 1 & F \\ -m'_F & q & m_F \end{pmatrix} \begin{Bmatrix} J' & F & I \\ F & J & 1 \end{Bmatrix},$$

where in this context I stands for the nuclear spin. The term in the parenthesis is the Wigner 3-j symbol and the bracket on the right-hand side is a Wigner 6-j symbol.

The decay rate from the excited state F' into the ground state F can be calculated with [126]:

$$\Gamma_{\mathrm{F'\to F}} = (2J'+1)(2F+1) \begin{Bmatrix} J & J' & 1 \\ F' & F & I \end{Bmatrix}^2 \Gamma \, . \tag{A.2}$$

From this equation the decay rates of the excited states into the ground states were calculated which are summarised in table A.1.

Table A.1.: Decay rates from the excited states to the ground states $\Gamma_{F' \to F}$ in the hyperfine structure of the ^{87}Rb D_1 line.

F	F'	$\Gamma_{F' \to F}$
1	1	$\frac{1}{6} \cdot \Gamma$
2	1	$\frac{5}{6} \cdot \Gamma$
1	2	$\frac{1}{2} \cdot \Gamma$
2	2	$\frac{1}{2} \cdot \Gamma$

A.2. List of Applied Rb Vapour Cells

During this thesis several Rb vapour cells were used with different shapes and buffer gas pressures. In table A.2 the utilised sensor cells are listed and their properties compared. The described cells were all filled with isotopically pure ^{87}Rb and neon as buffer gas. In column one the sensor cell type is stated. The main two cell types were the CSES sensor cells and the dual pass sensor cells. The CSES sensor cells have a lower diameter than the dual pass cells. An exception was the sensor cell of the CSES LM which had a higher diameter than the common sensor cells used for the CSES sensor. In the second and third column the buffer gas pressure P_{BG} of the respective sensor cell is given. The fourth and fifth column include the length and the diameter of the sensor cells. The stated length equals the optical path length within the sensor cell. The last two columns contain information on the coating of the sensor cell windows. Several cell windows have Anti-Reflection (AR) coating in order to reduce reflections. The windows of the dual pass sensor cells are not coated but have a wedged shape to reduce reflections.

Table A.2.: List of different types of Rb vapour cells for the CDSM operation and test measurements: The cells differ by their dimensions, buffer gas pressure, AR coating and Window Shape (WS). The selected buffer gas was neon for all listed cells.

Cell type	P_{BG}		Length	Diameter	AR	WS
	[kPa]	[Torr]	[mm]	[mm]		
CSES LM	4	30	36	25	yes	plane
CSES EM	1	7.5	25.2	12.7	no	plane
	2	15	25.2	12.7	no	plane
	4	30	25.2	12.7	no	plane
	5.3	40	25.2	12.7	no	plane
	6.7	50	25.2	12.7	no	plane
	8	60	25.2	12.7	no	plane
CSES QM/FM/FS	5.3	40	25.2	12.7	yes	plane
Dual pass	4	30	25	25	no	wedge
Dual pass	8	60	25	25	no	wedge
Dual pass (long)	8	60	28.2	25	no	wedge

A.3. CPT Resonance Amplitude Ratio and Slope Ratio

The compensation behaviour of the CDSM magnetometer depends on the slope of the single CPT resonances. For simplicity, the CPT resonance amplitude ratio is often used instead of the slope to describe the compensation behaviour. In figure A.1 the CPT resonance amplitude ratio and the CPT resonance slope ratio are compared in dependence of the sensor angle for a single and a dual laser beam pass.

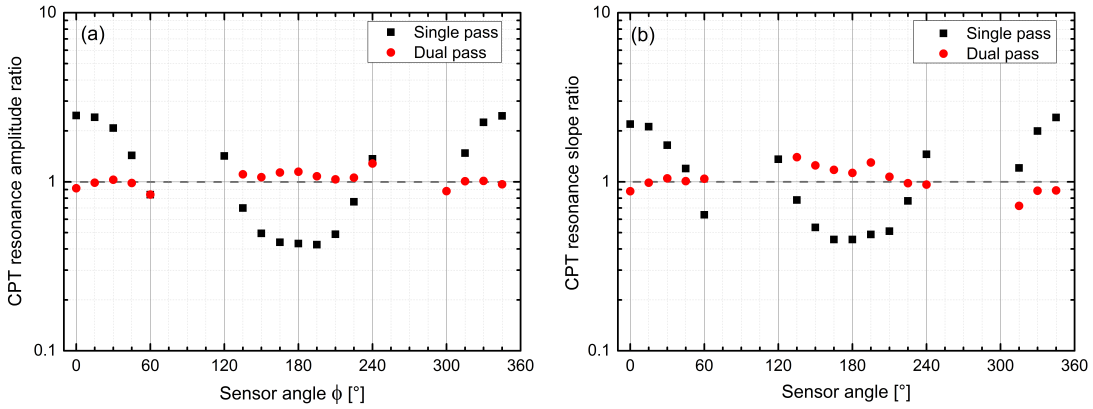

Figure A.1.: Angular dependence of the CPT resonance amplitude ratios and slope ratios of the CPT resonances $n = -2$ and $n = +2$ for a single and a dual pass of the laser beam through the sensor cell: In (a) the ratio of the CPT resonance amplitudes $h_{n=-2}/h_{n=+2}$ is depicted. In (b) the slope ratios for the same resonances is shown for the identical measurement. A magnetic field of $B = 19.9\,\mu\mathrm{T}$ was applied. The CSES FS electronics was used and the dual pass sensor. The sensor cell contained a buffer gas pressure of $P_{BG} = 8.0\,\mathrm{kPa}$ (60 Torr). For the single pass measurements, the laser light was coupled into the inbound fibre after the first sensor cell pass.

The slopes of the single CPT resonances were determined by a linear fit through the zero crossing. Comparing the results revealed an almost identical trend for the amplitude ratio and the slope ratio for the CPT resonance. Since it is easier to determine the CPT resonance amplitudes than the slope of the CPT resonances, the amplitude ratio was commonly used to evaluate the compensation behaviour. The difficulty of determining the slope is that it depends significantly on the number of measurement points included in the fitting procedure. Therefore, the slopes get inaccurate for small CPT resonance amplitudes.

A.4. Test Facilities

A.4.1. Space Research Institute of the Austrian Academy of Sciences

Magnetic field measurements with the CDSM are commonly performed in a magnetic shielding can at the Space Research Institute of the Austrian Academy of Sciences [127]. The magnetic shielding can consists of three layers of mu-metal and a solenoid coil (coil windings $N = 640$) within the innermost layer which allows the application of defined magnetic field strengths.
Magnetic field measurements can also be carried out in a triaxial Helmholtz coil system. The benefit of the coil system compared to the magnetic shielding can is that the direction of the applied magnetic field can be changed via the current through the respective coils. Therefore, measurements in dependence of the sensor angle (see section 4.1.7) can be performed without moving the sensor unit nor the optical fibres. As a result of fibre movements, the transmitted optical power through the optical fibre and the mode distribution is altered which influences the polarisation state at the sensor input (see section 3.3.2.1) as well as the intensity distribution of the laser beam profile (see section 3.4.1).
The drawback of the coil system compared to the magnetic shielding can is that disturbing external magnetic fields are not shielded. Thus, they can influence the magnetic field measurement or affect the CPT and CDSM resonance line shapes.
The institute also owns a temperature facility, which consists of a temperature controlled test volume within a magnetic shielding can. It allows heating of the sensor unit without the resistive sensor cell heater. Thus, measurements can be performed without disturbing influences from the resistive cell heating.

A.4.2. Conrad Observatory of the Central Institute for Meteorology and Geodynamics

The Conrad observatory is a geophysical observatory in Austria [128]. One of its facilities is the geomagnetic observatory which has a several hundred meter long tunnel system designed for several types of magnetic field measurements including an absolute tunnel which was built for absolute magnetic field measurements.
A number of magnetometers are operated at this observatory. Typically, an Overhauser magnetometer was used to evaluate the magnetic field strength measured with the CDSM. The measurements were performed in Earth's magnetic field which is about 48.5 µT at the observatory. The temperature in the tunnel system is constant and around 6 °C. Therefore, the sensor cell of the CDSM has to be heated for test measurements, since the CPT resonance amplitudes are typically too low at this temperature (see section 4.1.3.4).

A.4.3. Magnetsrode of Technische Universität Braunschweig

Test measurements with the CDSM were also performed in Magnetsrode [129]. Magnetsrode is a test facility operated by Technische Universität Braunschweig in Germany. This test facility comprises a triaxial Braunbek coil system in a magnetic clean environment. The system can compensate the Earth's magnetic field dynamically. The dynamic compensation is realised with a fluxgate magnetometer which detects the variation of the external magnetic field and the applied current at the coil system is adjusted accordingly. Further, an defined magnetic field can be applied with the magnetic field set to any direction.